

High Enthalpy Effects on Two Boundary Layer Disturbances
in Supersonic and Hypersonic Flow

A DISSERTATION
SUBMITTED TO THE FACULTY OF THE GRADUATE SCHOOL
OF THE UNIVERSITY OF MINNESOTA
BY

Ross Martin Wagnild

IN PARTIAL FULFILLMENT OF THE REQUIREMENTS
FOR THE DEGREE OF
Doctor of Philosophy

Graham V. Candler, Advisor

May, 2012

Report Documentation Page

Form Approved
OMB No. 0704-0188

Public reporting burden for the collection of information is estimated to average 1 hour per response, including the time for reviewing instructions, searching existing data sources, gathering and maintaining the data needed, and completing and reviewing the collection of information. Send comments regarding this burden estimate or any other aspect of this collection of information, including suggestions for reducing this burden, to Washington Headquarters Services, Directorate for Information Operations and Reports, 1215 Jefferson Davis Highway, Suite 1204, Arlington VA 22202-4302. Respondents should be aware that notwithstanding any other provision of law, no person shall be subject to a penalty for failing to comply with a collection of information if it does not display a currently valid OMB control number.

1. REPORT DATE MAY 2012	2. REPORT TYPE	3. DATES COVERED 00-00-2012 to 00-00-2012	
4. TITLE AND SUBTITLE High Enthalpy Effects on Two Boundary Layer Disturbances in Supersonic and Hypersonic Flow		5a. CONTRACT NUMBER	
		5b. GRANT NUMBER	
		5c. PROGRAM ELEMENT NUMBER	
6. AUTHOR(S)		5d. PROJECT NUMBER	
		5e. TASK NUMBER	
		5f. WORK UNIT NUMBER	
7. PERFORMING ORGANIZATION NAME(S) AND ADDRESS(ES) The University of Minnesota, 240 Williamson Hall, 231 Pillsbury Drive S.E., Minneapolis, MN, 55455-		8. PERFORMING ORGANIZATION REPORT NUMBER	
9. SPONSORING/MONITORING AGENCY NAME(S) AND ADDRESS(ES)		10. SPONSOR/MONITOR'S ACRONYM(S)	
		11. SPONSOR/MONITOR'S REPORT NUMBER(S)	
12. DISTRIBUTION/AVAILABILITY STATEMENT Approved for public release; distribution unlimited			
13. SUPPLEMENTARY NOTES			
14. ABSTRACT			
15. SUBJECT TERMS			
16. SECURITY CLASSIFICATION OF:			17. LIMITATION OF ABSTRACT Same as Report (SAR)
a. REPORT unclassified	b. ABSTRACT unclassified	c. THIS PAGE unclassified	
19a. NAME OF RESPONSIBLE PERSON			

© Ross Martin Wagnild 2012
ALL RIGHTS RESERVED

Acknowledgements

I would first like to thank my advisor, Graham Candler, for all of his support, his guidance concerning the path of my research, and wisdom concerning the fields of CFD, hypersonics, and boundary layer stability as well as the scientific community. I would also like to thank the entire Candler group for all of their help with the current work, but also making graduate school an interesting and fun environment in which to learn. In particular, Dr. Dave Peterson helped greatly with my understanding gridding software and techniques, US3D, and the application of chemistry in simulation. Dr. Michael Barnhardt mentored me both at the University of Minnesota as well as during my internships at NASA Ames research center. Dr Travis Drayna helped with understanding complex gridding techniques. Dr. Ioannis Nompelis helped a great deal with my understanding of the numerical workings of US3D as well as the general application of chemistry and molecular vibration in numerical methods. In addition to this, Dr. Nompelis fielded numerous questions concerning mathematics, fluid mechanics, and the field of hypersonics as a whole. Dr. Pramod Subbareddy also fielded numerous questions and provided endless guidance concerning numerical simulation, fluid mechanics, and mathematics. He provided helpful insight into much of this work as well as a critical eye to ensure that I always attempted to achieve excellence in my work. Dr. Sriram Doraiswamy helped with my understanding of the mechanics of molecular vibration, acoustic damping, and reflected shock tunnels. Chris Alba introduced me to PSE analyses and helped me learn to use the STABL software. Dr. Heath Johnson fielded numerous questions concerning boundary layer stability theory and second mode disturbances. Dr. Johnson also provided a much needed critical eye on my work concerning second mode disturbances. Joel Gronvall helped with the use of the STABL software and engaged in many helpful discussion concerning boundary layer disturbances. Dr. Matthew Bartkowicz was a constant pillar of support throughout graduate school, providing help and engaging in discussion with all aspects of hypersonic CFD, boundary layer disturbance, and classwork.

I also need to thank the entire T5 tunnel group, Dr. Hans Hornung, Dr. Joseph Shepherd, Dr. Ivett Leyva, Bahram Valiferdowsi, Joe Jewell, and Nick Parziale, without them much of this work would not be possible. They provided essential guidance and discussion in both theoretical and experimental high enthalpy fluid mechanics and second mode disturbances. Much of the experimental data used in this work was shared by Joe Jewell, allowing for the comparison between computation and experiment. Only through such comparisons can a computational scientist know his work is relevant. I am greatly indebted to Dr. Ivett Leyva, who worked very hard to maintain the collaboration from which I owe so much of my understanding of high enthalpy flow as well as provided guidance with numerous aspects of being a member of the scientific community.

I would also like to thank Dr. Eli Reshotko and Dr. Anatoli Tumin for all of their helpful discussions of transient growth theory and tips in the development of the compressible optimal disturbance solver.

Finally, I would like to thank my family, who have supported me throughout graduate school as well as throughout my life. I would especially like to thank my parents, who have encouraged me to work hard to achieve my goals. My wife, Tessa, supported me for several years as well as provided so much help with improving my technical writing.

This work was sponsored by the Air Force Office of Scientific Research under grants FA9550-04-1-0341 and FA9550-10-1-0352 as well as the Department of Defense National Security Science & Engineering Faculty Fellowship. A partial amount of the computation time for the simulations in this work was provided by the Minnesota Supercomputing Institute (MSI) cluster, Itasca.

Dedication

For my wife, Tessa, and my daughter, Andie.

Abstract

The fluid flow phenomenon of boundary layer transition is a complicated and difficult process to model and predict. The importance of the state of the boundary layer with regard to vehicle design cannot be understated. The high enthalpy environment in which high speed vehicles operate in further complicates the transition process by adding several more degrees of freedom. In this environment, the internal properties of the gas can stabilize or destabilize the boundary layer as well as modify the disturbances that cause transition. In the current work, the interaction of two types of disturbances with the high enthalpy flow environment are analyzed. The first is known as a second mode disturbance, which is acoustic in nature. The second type is known as a transient growth disturbance and is associated with flows behind roughness elements. Theoretical analyses, linear stability analyses, and computation fluid dynamics (CFD) are used to determine the ways in which these disturbances interact with the high enthalpy environment as well as the consequences of these interactions. First, acoustic wave are directly studied in order to gain a basic understanding of the response of second mode disturbances in the high enthalpy boundary layer. Next, this understanding is used in interpreting the results of several computations attempting to simulate the flow through a high enthalpy flow facility as well as experiments attempting to take advantage of the acoustic interaction with the high enthalpy environment. Because of the difficulty in modeling these experiments, direct simulations of acoustic waves in a hypersonic flow of a gas with molecular vibration are performed. Lastly, compressible transient growth disturbances are simulated using a linear optimal disturbance solver as well as a CFD solver. The effect of an internal molecular process on this type of disturbance is tested through the use of a vibrational mode. It is the goal of the current work to reinforce the critical importance of accurately capturing the physics of the “real” gas effects in the high enthalpy flow environment in order to understand and predict transition on high speed vehicles.

Contents

Acknowledgements	i
Dedication	iii
Abstract	iv
List of Tables	xi
List of Figures	xii
1 Introduction	1
1.1 Boundary Layer Transition	1
1.2 Paths to Turbulence	4
1.3 High Enthalpy Flows	6
1.4 Motivation for the Current Work	8
1.5 Objectives and Scope of the Current Work	10
2 Background	12
2.1 Second Mode Disturbances	12
2.1.1 Development and Application of LST and PSE	13
2.1.2 Acoustic Damping	15
2.1.3 Direct Numerical Simulations of Acoustic Waves	18
2.1.4 Review of Experimental Work at the GALCIT T5 Tunnel	18
2.2 Transient Growth and Roughness Transition	20
2.2.1 Roughness Transition	20
2.2.2 Theoretical Basis of Transient Growth	24

2.2.3	Optimal Disturbances	28
2.2.4	Theoretical development	28
2.3	Modern Developments of Transient Growth and Roughness Transition	30
3	Mathematical Models	32
3.1	Governing Equations	32
3.1.1	State Equations	33
3.1.2	Diffusive Relations	35
3.1.3	Chemical Source Terms	36
3.1.4	Vibrational Source Terms	38
3.2	Review of Parabolized Stability Equations	39
3.3	General Procedure for Acoustic Wave Equations	41
3.3.1	Fujii's method : Streamfunction Approach	43
3.3.2	Balakumar's Formulation : Frozen Acoustic Wave	46
3.4	Generalization of Balakumar's Formulation	49
3.5	Transient Growth Formulation	51
3.5.1	Disturbance Equations	51
3.5.2	Non-Dimensionalization	54
3.5.3	Optimization Method	55
4	Numerical Methods	60
4.1	Flow Solver : The Finite Volume Method	60
4.1.1	Inviscid Fluxes	62
4.1.2	Viscous Fluxes	66
4.1.3	Time Advancement	67
4.1.4	Higher-order Inviscid Flux Methods	70
4.2	Optimal Disturbance Solver	71
5	Properties of Acoustic Damping	74
5.1	Theoretical Results of Acoustic Damping	74
5.1.1	Properties of Acoustic Damping	74
5.1.2	Acoustic Damping for Mixtures of Air and CO_2	81
5.1.3	Acoustic Damping in a Flow with a Mean Velocity	83

5.2	Acoustic Wave Simulations	85
5.2.1	Static Gas Simulations	85
5.2.1.1	Problem Setup	85
5.2.1.2	Results	86
5.2.2	Mean Flow Simulations	94
5.2.2.1	Problem Setup	94
5.2.2.2	Results	94
5.3	Conclusion	96
6	2nd Mode Transition Delay	98
6.1	T5 Smooth Cone Simulations	98
6.1.1	Problem Setup	98
6.1.2	Derivation of Freestream Conditions for T5 Cone Simulations	99
6.1.2.1	The T5 Tunnel and Assumptions	99
6.1.2.2	Nozzle Simulation	100
6.1.2.3	Heat Flux Comparisons	105
6.1.3	Simulation and Stability Analyses	107
6.1.3.1	Transition N Factor	107
6.1.3.2	Transition Reynolds Number	110
6.1.3.3	The Effect of Internal Processes	112
6.1.3.4	Realistic Nozzle Flow Effects	114
6.1.4	Conclusion	116
6.2	Theoretical Injection	116
6.2.1	Nitrogen Freestream	116
6.2.2	Smooth Cone and Cold Carbon Dioxide Injection	118
6.2.3	Alternate Injection Gases	119
6.2.4	Heated Gas Injection	120
6.2.5	Effect of Relaxation Processes	122
6.2.6	Air Freestream	124
6.2.7	Smooth Cone and Cold Carbon Dioxide Injection	125
6.2.8	Alternate Injection Gases	125
6.2.9	Heated Gas Injection	127

6.2.10	Conclusion	128
6.3	Porous Injection	129
6.3.1	Model and Simulation Parameters	129
6.3.2	Cold Carbon Dioxide Injection	130
6.3.3	Alternate Injection Gases	132
6.3.4	Heated Carbon Dioxide Injection	133
6.3.5	Conclusion	135
7	Direct Simulation of Acoustic Waves Over a Cone	136
7.1	Introduction	136
7.2	Sharp Cone Model	137
7.3	Stability Analysis	138
7.4	Stability Analysis of the Mean Flow	139
7.5	Sharp Cone Simulations	143
7.5.1	Validation	143
7.5.2	Vibrational Relaxation Effects	150
7.6	Conclusion	158
8	Transient Growth Disturbances	160
8.1	Optimal Compressible Disturbances	160
8.1.1	Base Flow	160
8.1.2	Validation	161
8.2	Full Simulations	167
8.2.1	Single Vortex Test	175
8.3	Internal Relaxation Effects	177
8.3.1	Base Flow	177
8.3.2	Simulation Results	178
8.3.3	Non-equilibrium Freestream	183
8.4	Conclusion	184
9	Summary and Conclusions	186
9.1	Recommendations for Future Work	189

Bibliography	191
Appendix A. Fujii’s Method : Full Problem Derivation	203
A.1 Definitions of Variables and Description of the System	203
A.2 Calculation of derivative values	204
A.2.1 Extent of Reaction	204
A.2.2 Vibrational Energy	206
A.2.3 Enthalpy Derivatives	207
A.2.4 Relaxation Time	208
A.3 Proof of frozen speed of sound formula	210
A.4 Derivation of single mode formula	210
A.5 Acoustic absorption rate for a single mode	214
A.5.1 Dissipation per wavelength for a single vibrational mode	218
A.5.2 Dissipation per wavelength for an dissociating gas	220
A.5.3 Frozen Wave Dispersion Relation from Disturbance Energy	225
A.5.4 The nature of the acoustic dispersion relation with a mean flow	226
Appendix B. Transient Growth Formulation	229
B.1 Definition of the Derivatives for the Species Density Equations	229
B.2 Definition of the Derivatives for the Temperature Equation	230
B.3 Non-dimensional Disturbance Equations	231
B.4 Transient Growth Disturbance Equations	235
B.5 Optimization Equations	237
Appendix C. Chemistry Models and Test Cases	242
C.1 Chemistry Sets	242
C.1.1 Five Species Air Model	242
C.1.2 Six Species Air Model	243
C.1.3 Seven Species Air Model	245
C.1.4 Five Species CO_2 Model	247
C.2 Modified Vibrational Relaxation Parameters	249
C.3 T5 Shots Simulated	249
C.4 Injection Conditions	251

C.4.1	Theoretical Injection Conditions	251
C.4.1.1	Nitrogen Freestream	251
C.4.1.2	Air Freestream	252
C.4.2	Porous Injection Conditions	252
Appendix D. Useful Second Mode Disturbance Trends		253
D.1	Disturbance Bandwidth	254
D.2	Relative Amplification	255

List of Tables

6.1	Edge and Stagnation conditions for shot 2540 extracted from a US3D simulation. . .	107
6.2	Comparison of conditions for the CO_2 cases.	112
6.3	Comparison of conditions for the air cases.	112
6.4	Freestream Conditions for the first set of theoretical injections cases.	118
6.5	Freestream Conditions for the second set of theoretical injections cases.	125
7.1	Table of freestream conditions for the sharp cone case.	137
7.2	Upstream phase shift in degrees versus the height above the wall in boundary layer thicknesses. A negative value indicates a downstream phase shift.	157
8.1	This table contains the freestream conditions used in the validation of the optimal disturbance solver.	161
8.2	This table contains the freestream conditions used in the full simulations.	169
8.3	Vibrational parameters for the vibrationally active simulations	178
8.4	This table contains the freestream conditions used in the vibrationally active simulations.	178
C.1	Modified Millikan and White relaxation times	249
C.2	List of T5 Tunnel shots simulated in Chapter 6.1.	250
C.3	Injection conditions for the theoretical injection cases with a freestream of N_2	251
C.4	Injection conditions for the theoretical injection cases with a freestream of Air	252
C.5	Injection conditions for the porous injection cases with a freestream of Air	252

List of Figures

1.1	Example cases demonstrating the heating difference between laminar and turbulent boundary layers.	2
1.2	Diagram showing the known paths to turbulence[1], taken from Fedorov[2].	5
1.3	Diagram of boundary layer transition following path A in Figure 1.2 taken from White[3].	6
1.4	Plot of velocity versus altitude of relevant vibrational excitation, dissociation, and ionization with the flight envelopes of NASP and AOTV taken from Fujii[4].	7
2.1	Diagram showing how a second mode disturbance is an acoustic wave trapped in a boundary layer. Taken from Fedorov[2].	13
2.2	This plot shows the typical acoustic damping properties of a gas with a single relaxation mode versus frequency. The most effective damping occurs when the frequency is of similar scale to the relaxation time of the gas. Also in the plot is the ratio of the speeds of sound. This is an important factor in the acoustic analysis. Taken from Fujii and Hornung[5]	16
2.3	These plots demonstrate the acoustic damping properties of carbon dioxide and the amplification of second mode disturbances in attachment line transition. Taken from Fujii and Hornung[6]	17
2.4	These plots show recent test data from the T5 tunnel. Figure 2.4a shows the variation with transition Reynolds number with mole fraction of carbon dioxide. As the mole fraction of carbon dioxide is increased, the transition Reynolds number is increased, thus delaying transition until further back on the cone. Figure 2.4b shows the variation of transition Reynolds number with injection mass of carbon dioxide. Increasing the injection mass of carbon dioxide further delays transition until causing too large a disturbance to the boundary layer and moving transition forward.	20

2.5	This plot shows the classes of horseshoe vortex systems that develop in front of isolated roughness elements. The results are plotted based on element diameter over boundary layer displacement thickness versus Reynolds number based on the element diameter. This figure was taken from Baker[7].	21
2.6	A reproduction of Fig. 4a from Bartkowicz et al.[8] that demonstrates the vortex system that forms around an isolated roughness element. The iso-surfaces are of the Q criterion and indicate the presence of a vortex. The contours are the wall heat flux. The flow is from the lower left to upper right of the figure.	22
2.7	Comparison of the numerical simulation performed by Fischer and Choudhari[9] and the experimental data from White and Ergin[10]. Both studies show similar trends, however, the magnitude of disturbances is not equal.	23
2.8	This plot demonstrates the progression of the transition location due to three dimensional roughness elements. This image was taken from Schneider[11].	24
2.9	A pair of streamwise vortices undergoing transient growth in a flat plate boundary layer with a freestream Mach number of approximately three. The iso-surface indicates the presence of one of the vortices. The contours are on five spanwise slices as well as one streamwise slice and depict a normalized temperature. The flat plate is indicated by the gray surface below and the flow velocity is indicated with the black arrow.	25
4.1	The plot shows an arbitrary mesh that discretizes a flow domain.	66
5.1	Damping per wavelength versus frequency over a range of temperatures for a fictitious diatomic molecule.	77
5.2	A plot showing the damping rate per wavelength at a constant temperature with an increasing number of degeneracies (indicated in the plot by the arrow) starting with a degeneracy of one. A doubling in damping rate per wavelength from a single vibrational mode (green) requires a degeneracy of three (blue) and another doubling of damping rate per wavelength require a degeneracy of seven (red).	78
5.3	Chemical damping processes examples	80

5.4	Damping per wavelength versus frequency for an equilibrium mixture of gas starting from CO_2 with a final density of 0.1 kg/m^3 and at two different temperatures. The vibrational mode responsible for each peak in vibrational damping is noted on each plot.	81
5.5	Damping per wavelength for various mixtures of air and carbon dioxide at two different temperatures (indicated in the sub-figure caption). As the mass fraction of carbon dioxide increases, the damping per wavelength profile shifts toward the pure carbon dioxide case.	83
5.6	Damping per wavelength for various mixtures of air and carbon dioxide at a frequency of 1.0 MHz . The temperature ranges from 500 K to 4000 K with a density of 0.1 kg/m^3	83
5.7	Damping per wavelength of the vibrational modes of carbon dioxide at $T = 1000 \text{ K}$ for various Mach numbers. The behavior of the optimum damping frequency is described by Eq. 5.4. Interestingly, the damping rate on the right of the optimum is not affected by the mean flow.	85
5.8	A frozen acoustic wave at $T = 1000 \text{ K}$ and a frequency of 100 kHz in carbon dioxide. The amplitude of the wave is essentially constant throughout the domain.	87
5.9	A comparison of the damping rate per wavelength for a range of temperatures in nitrogen. US3D matches Fujii's calculation almost exactly.	87
5.10	A comparison of the damping rate per wavelength for a range of temperatures in oxygen (a) and carbon dioxide (b). The temperature range dominated by vibration show excellent agreement, while the agreement in the region dominated by chemical damping is moderate for oxygen and decent for carbon dioxide.	88
5.11	The damping rate per wavelength for three different temperatures of carbon dioxide. The black dashed line indicates the frequency used in the simulation, 100 kHz . The three temperatures indicated are chosen to demonstrate the properties of an equilibrium wave, a frozen wave, and a wave with near optimal damping.	89
5.12	An Acoustic wave traveling through carbon dioxide with a frequency of 100 kHz and a temperature of 2500 K . This case demonstrates an equilibrium wave.	90
5.13	An acoustic wave traveling through carbon dioxide in equilibrium with a frequency of 100 kHz and a temperature of 1000 K . This case demonstrates a wave with near optimal damping.	90

5.14	Acoustic wave traveling through carbon dioxide in equilibrium with a frequency of 100 kHz and a temperature of 300 K	90
5.15	The extent of reaction and pressure disturbance waves versus distance. The approximate equilibrium temperature is of each curve is given in the legend. The extent of reaction is plotted using solid lines with the ordinate on the left. The pressure disturbance is plotted using dash-dot lines with the ordinate on the right.	93
5.16	Normalized disturbance quantities from an acoustic wave of 20 kHz traveling through an equilibrium mixture of oxygen at a temperature of 3500 K and a density of 0.1 kg/m^3 . In order to clarify the phase shift between each of the components, a dashed line with the same color as the disturbance quantity has been drawn from the peak amplitude to the abscissa axis.	93
5.17	Normalized disturbance quantities from an acoustic wave of 100 kHz traveling through an equilibrium mixture of carbon dioxide at a temperature of 4500 K and a density of 0.1 kg/m^3 . In order to clarify the phase shift between each of the components, a dashed line with the same color as the disturbance quantity has been drawn from the peak amplitude to the abscissa axis.	94
5.18	Damping rate per wavelength in carbon dioxide with a temperature of 1000 K , a density of 0.1 kg/m^3 , and a mean flow Mach number of 1.15 for both slow and fast acoustic waves. The excellent agreement between the theoretical and computational codes indicate that the theory accurately describes the physics behind acoustic damping. The two data points at 1 MHz overlay each other at the scale of the plot, however, they each lie on top of the corresponding theoretical curve.	95
5.19	A fast acoustic wave traveling through carbon dioxide in equilibrium with a frequency of 100 kHz and a temperature of 1000 K , a density of 0.1 kg/m^3 , and a mean flow Mach number of 1.15. The wave propagates in a similar fashion as in the static cases with the vibrational temperature disturbance lagging the translational temperature disturbance in the upstream direction.	96
5.20	A slow acoustic wave traveling through carbon dioxide in equilibrium with a frequency of 8.6 kHz and a temperature of 1000 K , a density of 0.1 kg/m^3 , and a mean flow Mach number of 1.15.	96
6.1	A diagram of the T5 tunnel taken from Fujii[4].	99

6.2	Mach contours of shot 2540 in the T5 tunnel based on a Nozzle code simulation.	101
6.3	Variations in the gas properties near the end of the nozzle based on the Nozzle code simulation.	102
6.4	Mach contours of shot 2540 in the T5 tunnel based on a US3D simulation.	103
6.5	Comparisons of various gas properties in the radial direction across the nozzle at a streamwise location of 0.45 m.	104
6.6	Contours of the density gradient magnitude for shot 2540.	105
6.7	Comparison of laminar heat flux between the US3D nozzle simulation, the STABL mean flow calculation, and the experiment	106
6.8	Comparison of the laminar and turbulent wall heating from the US3D nozzle simulation, experiment, and theoretical estimates. The theoretical turbulent estimates include the van Driest II (VD) model and the White and Christoph (WhCh) model.	107
6.9	Linear stability diagram and maximum N factors from the stability analysis of shot 2540.	108
6.10	Figure depicting the qualitative method for determining the transition location.	110
6.11	Transition N factor versus the flow total enthalpy for flows of Air and CO_2 . The transition location is determined based on the method given in the legend of each plot. “Adam” implies that the transition location was determined from Adam’s data[12]. “Qual” implies the qualitative method of determining the transition location. “Inter” implies the intermittancy method for determining the transition location described by Jewell et. al[13]. The error bars on each datum are calculated as the maximum change in N factor when shifting the transition location by ± 4 cm.	110
6.12	Comparisons of Re_{tr}^* versus the flow total enthalpy for flows of air and CO_2 . The data for the CO_2 cases are based on the same shots, while the air cases are based on two different shot series.	112
6.13	Transition N factor versus total enthalpy based on a stability analysis with chemical reactions and vibrational relaxation (‘Full’) and a stability analysis without any internal processes (‘Frozen’) for two cases of air and two cases of carbon dioxide.	114

6.14	Damping per wavelength versus total enthalpy for three cases of air and three cases of carbon dioxide with and without a freestream velocity. The flow properties for these cases are taken from a location based on following the acoustic characteristics from the cone nose to the boundary layer edge on the tunnel wall.	114
6.15	Comparison of the maximum N factor versus distance along the cone between the stability analysis based on the Nozzle code simulation ('Nozzle & STABL') and the stability analysis based on the US3D simulation ('US3D').	115
6.16	Comparison of the transition N factor and Re_{tr}^* versus total enthalpy between the stability analysis based on the Nozzle code simulation and the stability analysis based on the US3D simulation.	116
6.17	These plots show the stability analysis results for the smooth cone, a), and cold carbon dioxide injection, b), with a free-stream composed of nitrogen. The free-stream conditions for these cases are contained in Table 6.4. The case with f_w set to 0.1 shows the maximum transition delay. Cases with higher mass flux result in more amplification.	119
6.18	This plot shows the stability analysis results for select cases of alternate gas injection. The injection of the alternate gases results in larger disturbance amplification than in the smooth cone case.	120
6.19	This plot shows the stability analysis results for select cases of heated CO_2 injection. The wall temperature in each case is indicated in the legend. The transition delay occurs for all cases tested.	121
6.20	The show the stability analysis results for two smooth cone cases and two cases of injection with different gases. All wall temperatures are indicated in the legend. . . .	121
6.21	This plot is a summary of the transition locations for the theoretical injection cases based on the critical N factor of 9.2. The injection of carbon dioxide shows an optimum amount of mass injected.	122
6.22	This plot shows the effect of non-equilibrium processes on the disturbances for cold carbon dioxide with f_w set to 0.1. The vibrational modes of carbon dioxide results in a transition delay relative to the smooth case due to boundary layer heating and acoustic damping.	123

6.23	Boundary layer profiles of translational and vibrational temperature for the different injection cases. The location for the data extraction is indicated at the top of each plot. This comparison makes evident the heating of the boundary layer gas caused by the vibrational energy.	124
6.24	This plots shows the stability analysis results for the smooth cone and cold carbon dioxide injection cases. For these freestream conditions, injection of carbon dioxide only results in transition promotion.	125
6.25	The plot shows the stability analysis results for select cases of gas injection. For these freestream conditions, gas injection for all gases decreases the stability of the boundary layer. The injection of carbon dioxide results in greater amplification of second mode disturbances than other gases.	126
6.26	Boundary layer profiles of translational and vibrational temperature for the different injection cases. The location for the data extraction is indicated at the top of each plot. This comparison makes evident the heating of the boundary layer gas caused by the vibrational energy.	127
6.27	This plot shows the stability analysis results for select cases of heated CO_2 injection. The wall temperature in each case is indicated in the legend. The injection of heated carbon dioxide results in transition promotion.	128
6.28	This plot is a summary of the transition locations for the theoretical injection cases based on the critical N factor of 9.5. These data show for these freestream conditions, gas injection of any kind results in a promotion of transition.	128
6.29	These plots show the results from the stability analyses of cold carbon dioxide injection. The free-stream conditions for these cases are contained in Table6.5. The low mass flux cases are shown in a). The high mass flux cases are shown in b). The 3 g/s case is in a borderline state of transition, while all other cases reach an N factor sufficient to cause transition immediately following the injection region.	131
6.30	This plot shows the LST stability diagram for the case of cold carbon dioxide injection at a rate of 6 g/s. The sharp drop in amplified frequencies is due to the rapid increase in boundary layer thickness. The frequencies rise as the boundary layer recovers from the injection until resuming its natural growth. Also visible is the amplification of higher modes of disturbances.	132

6.31	The plot on the left, a), shows the N factors that result from the injection of various gases while preserving the penetration height of transpiration. The plot on the right, b), shows the normalized boundary layer profiles of mass fraction of carbon dioxide (dashed dot), translational temperature (solid), and vibrational temperature (dashed). This plot shows a layer of cold carbon dioxide that is inefficient for absorbing energy from acoustic disturbances. The free-stream conditions for these cases are contained in Table 6.5. Each case has a different total mass flux in order to match the penetration height of the injection. The variable y_n indicates the wall-normal direction.	134
6.32	This plot shows the results from the stability analyses of heated carbon dioxide injection. The free-stream conditions for these cases are contained in Table 6.5. As expected, an increase in temperature of the injected gas further reduces the amplification experienced in the post-injection region.	134
7.1	Acoustic absorption rate versus enthalpy for the approximated most amplified frequencies over a 5° half-angle cone in the T5 tunnel. This plot has been reproduced from Fig. 3 in Fujii and Hornung.[6]	138
7.2	Boundary layer profiles of streamwise velocity (U), translational temperature (T), and vibrational temperature (Tv) versus wall-normal distance at length of 30 cm from the nose of the cone. The boundary layer is essentially in thermal equilibrium. The wall-normal distance has been normalized by the boundary layer thickness, δ	140
7.3	N factor and most amplified disturbance frequency versus distance along the cone for conditions in Table 7.1 using only the first bending vibrational mode of CO_2	141
7.4	Boundary layer profiles of streamwise velocity (U), translational temperature (T), and vibrational temperature (Tv) versus wall-normal distance at length of 30 cm from the nose of the cone. With all vibrational modes of CO_2 present in the flow, the boundary layer has a larger degree of non-equilibrium. The wall-normal distance has been normalized by the boundary layer thickness, δ	142
7.5	Comparison of N factor most amplified disturbance frequency versus distance along the cone for conditions in Table 7.1 using only the all of the vibrational mode of CO_2	142
7.6	Comparison of the percent change in N factor versus distance along the cone due to the addition of various vibrational relaxation modes to the PSE stability analysis.	143

7.7	Comparison of the mean flow boundary layer profiles of streamwise velocity (Fig. 7.7a), translational temperature, and vibrational temperature (Fig. 7.7b). The boundary layer profiles between the two mean flows are nearly identical.	144
7.8	A view of the disturbance field using contours of normalized density disturbance at an approximate streamwise location of 21 <i>cm</i> from the nose of the cone for the 1.4 <i>MHz</i> , slow-wave case. The disturbance field contains the same four regions described in Balakumar and Kegerise[14]; freestream, shock, shock layer and boundary layer. . . .	145
7.9	Comparison of the normalized wall pressure disturbance between the acoustic wave simulations and the linear PSE analysis for a frequency of 1.4 <i>MHz</i> . The type of acoustic wave used to generate the boundary layer disturbance is indicated in the sub-figure caption.	146
7.10	Comparison of the normalized wall pressure disturbance between the acoustic wave simulations and the linear PSE analysis for frequencies of 1.05 <i>MHz</i> and 2.2 <i>MHz</i> as indicated in the sub-figure caption. Both cases use a slow acoustic wave to generate the boundary layer disturbance.	147
7.11	Comparison of the normalized wall pressure disturbance between the acoustic wave simulation and the linear PSE analysis for a frequency of 1.2 <i>MHz</i>	148
7.12	Plots of the normalized density disturbance at several locations on the cone from the 1.4 <i>MHz</i> , slow-wave case. The contours are chosen such that the shape of the boundary layer disturbance is easily visible. The boundary layer edge is indicated with the solid white line and the approximate disturbance sonic line is indicated by the dashed white line that run roughly parallel to the wall. For this flow, the boundary layer edge is determined by the location at which the total enthalpy is 99.5 percent of the freestream enthalpy. The disturbance sonic line is calculated as part of the linear PSE analysis	149
7.13	Power spectral density versus frequency for the 1.4 <i>MHz</i> , slow-wave case. The black line indicates the location of 1.4 <i>MHz</i>	150
7.14	Contours of the density disturbance over the cone with the sampling locations to determine the presence of vibrational temperature lag. Each sampling line is indicated with a number in order to identify where the data are taken from in further figures. .	153

7.15	Translational and vibrational temperature disturbances versus streamwise distance. The number below each plot corresponds to the sample location indicated in Fig. 7.14.	154
7.16	Close up view of one wavelength from sample location 5. The data show a slight lag of the vibrational temperature disturbance from the translational temperature disturbance in the upstream direction.	155
7.17	Normalized disturbance quantities versus distance along the cone for half of a disturbance wavelength at a wall-normal height of 0.3 boundary layer thicknesses. These data are sampled from a location where the disturbance is amplifying.	156
7.18	Contours of the normalized vibrational temperature disturbance field at an approximate streamwise location of 25 <i>cm</i> from the nose of the cone for the slow wave case. The vibrational temperature disturbance amplifies behind the shock due to the transfer of energy from molecular translation to molecular vibration. The line of sample data taken is indicated by the black line.	158
7.19	Mean (dashed lines) and disturbance (solid lines) temperatures versus streamwise distance sampled in a direction perpendicular to the wavefronts of the acoustic disturbance.	158
8.1	Comparison of the growth factor as calculated by the current method to the published result of Tumin and Reshotko[15] (indicated by Tumin in the plot legend). The two profiles are nearly identical, showing the agreement between the two methods. The growth factor is independent of Reynolds number and the x distance has been scaled by the length L	162
8.2	Comparison of the v and w disturbances at $x = x_{in}$ (a) as calculated by the current method to the published result of Tumin and Reshotko[15]. Both disturbance velocity components are nearly identical, showing the agreement between the two methods. The wall-normal distance has been scaled by εL and both velocity components have been scaled by εU_∞ . To demonstrate that these profiles represent a pair of streamwise vortices, the disturbance velocity vectors have been plotted at $x = x_{in}$ in sub-figure b.	163
8.3	Comparison of the u and θ disturbances at $x = x_{out}$ as calculated by the current method to the published result of Tumin and Reshotko[15]. Both disturbance quantities are in good agreement between the two methods. The u disturbance has been scaled by U_∞ and the θ disturbance has been scaled by T_∞	163

8.4	Comparison of the growth factor at $x = x_{out}$ over a range of β 's for three different wall temperatures. The two methods produce nearly identical results over the range of conditions.	164
8.5	Grid convergence study on the shape of the initial disturbance quantities, v and w . Both quantities show grid dependence until approximately 3200 streamwise points. In the plot, the number of points used is given in the plot legend as the number of streamwise points by the number of wall-normal points. The v velocity disturbance is plotted with the solid line, while the w velocity disturbance is plotted with the dashed-dot line.	165
8.6	Results from the grid convergence study. The growth factor shows no noticeable grid dependence past 200 streamwise points. The output disturbance quantities are least sensitive to the grid.	165
8.7	Comparison of θ disturbance at $x = x_{out}$ between the isothermal wall and adiabatic wall boundary conditions. The adiabatic wall case allows a non-zero value of θ at the wall.	166
8.8	Comparisons of growth factor over the domain and u disturbance at $x = x_{out}$ between the isothermal wall and adiabatic wall boundary conditions.	166
8.9	Effect of Prandtl number on the growth factor and θ disturbance. Increasing the Prandtl results in a greater temperature disturbance and a larger growth factor over the domain.	167
8.10	Effect of Prandtl number on v , solid line, and w , dash-dot line, disturbances at $x = x_{in}$. A change in the Prandtl number has a minimal effect on the input disturbance.	167
8.11	Comparison of growth factor between linear theoretical code and US3D. The growth factor curves are similar indicating reasonable agreement. The growth factor from the similarity solution is also plotted to show how the different base flowfields affect the optimal growth factor.	170
8.12	Comparison of θ and u disturbances at $x = x_{out}$ between US3D and linear theory. Although differences exist between the maximum amplitudes of both quantities, the curves are similar for a majority of the wall-normal distance. US3D also shows a smaller θ disturbance at the wall as compared to the linear theory.	170

- 8.13 The effect of non-linearities on the normalized disturbance energy and transient growth disturbance amplitude. The input energies plotted are $E_{in} = 4.725 \cdot 10^{-5}$, $E_{in} = 1.890 \cdot 10^{-4}$, $E_{in} = 7.560 \cdot 10^{-4}$, $E_{in} = 1.512 \cdot 10^{-3}$, $E_{in} = 3.024 \cdot 10^{-3}$, $E_{in} = 6.048 \cdot 10^{-3}$, $E_{in} = 1.210 \cdot 10^{-2}$, $E_{in} = 2.419 \cdot 10^{-2}$, and $E_{in} = 4.839 \cdot 10^{-2}$. The arrow indicates the direction of increasing energy in both figures. The first noticeable departure from linear growth begins when $E_{in} = 3.024 \cdot 10^{-3}$. The amplitude function was found to be an important factor in streak breakdown due to secondary instabilities.[16] 172
- 8.14 Comparison of θ and u disturbances at $x = x_{out}$ for the input energies indicated in each figure's legend. In addition to the disturbance values, the base flow quantity's amplitude has been scaled arbitrarily to show the height at which various features of the disturbances occur. 172
- 8.15 Evolution of the u disturbance for three different input energies. The top sequence of plots is $E_{in} = 4.725 \cdot 10^{-5}$, followed by $E_{in} = 3.024 \cdot 10^{-3}$ in the middle, and $E_{in} = 4.839 \cdot 10^{-2}$ at the bottom. The top sequence shows linear growth, the middle sequence shows growth that departs from linear theory, and the bottom sequence shows very non-linear behavior. In the bottom sequence, the vortices have sufficient strength to form a low momentum fluid lobe above the base flow boundary layer edge.173
- 8.16 Evolution of the θ disturbance for three different input energies. The top sequence of plots is $E_{in} = 4.725 \cdot 10^{-5}$, followed by $E_{in} = 3.024 \cdot 10^{-3}$ in the middle, and $E_{in} = 4.839 \cdot 10^{-2}$ at the bottom. The top sequence shows linear growth, the middle sequence shows growth that departs from linear theory, and the bottom sequence shows very non-linear behavior. In the bottom sequence, the vortices have sufficient strength to form a high temperature fluid lobe above the base flow boundary layer edge. Each case reaches its maximum growth near $x = 1.5$ 174

8.17	Comparison of the temporal rms value of streamwise velocity for $E_{in} = 9.677 \cdot 10^{-2}$ to that of previous studies[16, 17]. Although the unsteadiness in the current study is due to an uncontrolled disturbance, the temporal rms values are very similar in shape to the sinuous disturbance seen in Andersson et al.[16] and Denissen and White.[17] For Fig. 8.17a and Fig. 8.17b, the color contours show streamwise velocity rms and each black line represents a 10% change in velocity relative to the freestream velocity. Denissen and White[17] are plotting the flowfield behind a roughness element. In Fig. 8.17c, Andersson et al.[16] are plotting contours of the sinuous disturbance amplitude in solid lines and the dashed line shows the shape of the streamwise streak resulting from an optimal disturbance.	175
8.18	Disturbance velocity vectors at $x = x_{in}$ for the single vortex case. The vortex is generated by applying a Gaussian variation to the initial velocity disturbances from the optimal transient growth problem in the spanwise direction.	176
8.19	Growth factor versus streamwise distance for the single vortex problem.	177
8.20	Disturbance energy of the streamwise velocity disturbance versus normalized streamwise distance and the mean streamwise velocity versus wall-normal distance at a normalized streamwise distance of 2.	179
8.21	Disturbance energy of the translational temperature disturbance versus normalized streamwise distance and the mean translational temperature versus wall-normal distance at a normalized streamwise distance of 2.	180
8.22	Disturbance energy of the vibrational temperature disturbance versus normalized streamwise distance and the mean vibrational temperature versus wall-normal distance at a normalized streamwise distance of 2.	181
8.23	Total disturbance energy versus normalized streamwise distance without and with the contribution of the vibrational disturbance energy.	182
8.24	Growth factor and the disturbance amplitude function versus normalized streamwise distance.	183
8.25	Growth factor and disturbance amplitude versus normalized streamwise distance. . .	184
D.1	Amplification rate and boundary layer thickness versus distance along a sharp cone surface. The amplification rate of a particular frequency is approximately a concave-down parabola with respect to boundary layer thickness.	254

D.2 N factor versus frequency for several locations along a sharp cone boundary layer. . . 255

Chapter 1

Introduction

1.1 Boundary Layer Transition

In fluid mechanics, a boundary layer is a thin region of fluid surrounding a solid surface where the consideration of viscous forces is essential. This layer develops due to a “no-slip” condition between the fluid and the solid surface causing the relative fluid velocity to vanish at the surface. A boundary layer flow has three main types; laminar, turbulent, and transitional. A laminar boundary layer is characterized by fluid traveling roughly parallel to the surface in several lamina of constant velocity. In this case, the presence of the surface is transmitted into the fluid only by means of the intermolecular viscous properties of the fluid. In a turbulent boundary layer, a fluid element travels with a seemingly random motion caused by vortices of varying size. In this case, the fluid motion transmits the presence of the surface in addition to the fluid’s viscous properties. Each flow type has its disadvantages, laminar flows are more susceptible to separation, while turbulent flows have higher skin friction drag and heat transfer. A transitional boundary layer is neither laminar nor turbulent and occurs when a laminar boundary layer becomes unstable and is in the process of becoming fully turbulent. To demonstrate the difference in heat transfer rates between laminar and turbulent flow, two data sets have been plotted in Figure 1.1. In the first example, heat transfer data from a wind tunnel test of the Crew Exploration Vehicle (CEV) as well as the computational predictions are plotted versus surface location. The difference between the estimated laminar heating near the shoulder of the vehicle differs from the predicted and measured values of turbulent heating by a factor of four. In the second example, thermocouple data from a wind tunnel test of a sharp cone are plotted along with laminar and two different kinds of turbulent heating

estimates. As seen in the figure, the flow follows the laminar heating until transitioning to turbulent flow and increasing the heat transfer rate to the wall by also a factor of five. In general, this increase in heating could be as much as an order of magnitude.

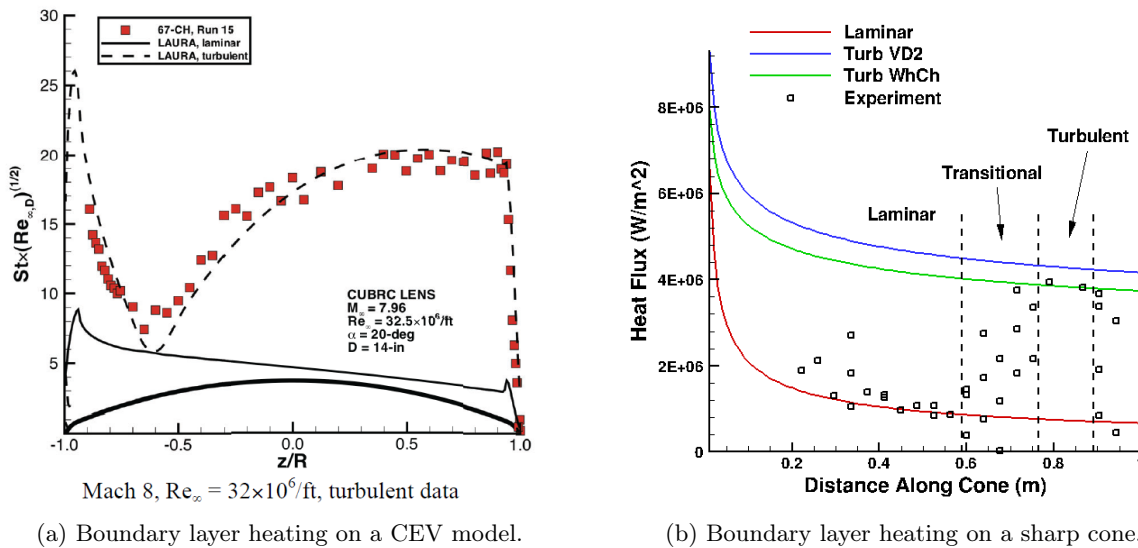


Figure 1.1: Example cases demonstrating the heating difference between laminar and turbulent boundary layers.

Laminar to turbulent boundary layer transition has been the focus of study for several decades. Despite all of the progress that has been made, the scientific community still has much to learn about the transition process. Predicting boundary layer transition is difficult because it can vary depending on numerous factors such as vehicle geometry and flight conditions. This variation is partly due to the number of mechanisms that cause transition. Tollmein[18] and Schlichting[19] were among the first to identify a viscous flow transition mechanism by finding a solution to the Orr-Sommerfeld equation, a linear disturbance equation of incompressible viscous fluid flow. These disturbances now bear their names and are called Tollmein-Schlichting waves, which are a common transition mechanism for subsonic flow. A first mode disturbance[20] is the extension of a Tollmein-Schlichting waves to compressible flow and is a viscous instability at low Mach number and, as the Mach number increases, becomes an inviscid instability operating on the generalized momentum inflection point as first predicted by Rayleigh[21] for incompressible flows[22]. It is well known in the transition community that this first mode is stabilized by increasing the mach number, wall cooling, and certain configuration of roughness elements. Mack[23] also hypothesized the existence of an infinite number of higher modes that occur when the boundary layer contains supersonic

flow, with the first of these higher modes, named the second mode, usually undergoing the largest amplification. The presence of these higher modes was later proved to exist in the experiments of Demetriades[24], Kendall[25], and Stetson et al.[26]. For many hypersonic vehicles with a slender forebody, second mode disturbances are the dominant mechanism that causes transition. Second mode disturbances can be stabilized by adding nose bluntness[27] and wall heating[22]. Another transition mechanism seen in supersonic flows is caused by a Görtler instability, which occurs over concave walls. This instability results in the formation of streamwise vortices that become unstable and was predicted by Görtler[28]. Lastly, depending on a vehicle's geometry or angle of attack, a cross-flow instability may develop due to pressure gradients in the boundary layer causing the fluid velocity direction to differ from the boundary layer edge fluid velocity direction. This change in flow velocity results in an inflection point in the boundary layer, thus causing the instability.

In addition to these known mechanisms, surface roughness can also be an important factor in boundary layer transition in all flow regimes. Surface roughness is generally divided into two groups; isolated and distributed. Isolated roughness elements are considered to act independently from other roughness in the flow and include surface irregularities in vehicle construction such as bolts, screws, and rivets as well as steps and gaps that occur at joints of surface materials. Distributed roughness occurs when several roughness elements are of similar size and are sufficiently close to interact with each other and have a combined effect on the fluid flow. Examples of distributed roughness include surface paints, a laminar-ablated surface, or machining patterns. On ablative surfaces, large protrusions may form as a result of irregular burning of the surface and act as isolated roughness elements. A significant amount of research has been done on the effect of both isolated and distributed roughness which includes the shape, orientation, size, fluid composition and location. From this research, the basic flow features around roughness elements have been identified for different flow regimes and will be discussed later. One of the main features is the presence of a set of counter-rotating streamwise vortices that develop immediately behind the roughness element. These vortices are remarkably similar to a shear flow disturbance described by transient growth theory. Due to this similarity, several researches have focused their efforts into identifying the properties and trends of transient growth disturbances as a means of analyzing transition due to roughness elements.

Transient growth theory differs from the previously mentioned transition mechanisms in that disturbance growth occurs as a result of disturbances interacting as opposed to single disturbances

evolving independently. Because transient growth requires disturbance interaction, its application was largely overlooked because a traditional laminar flow stability analysis relies on finding solutions to the linearized Navier-Stokes equations, which only model the evolution of a single disturbance mode. Since scientists realized the relevance of transient growth in fluid flows, transient growth theory has been successfully applied to some cases of “bypass transition”[29, 30, 31, 32, 33, 34], named so because these cases of boundary layer transition bypass the traditional method of stability analysis. Transient growth disturbances often develop streaky structures in boundary layers, which have since been named Klebanoff modes[35] started by Kendall[36].

1.2 Paths to Turbulence

Given an understanding of all of these transition mechanisms, it is instruction to understand the path a boundary layer takes as it transforms from laminar flow to turbulent flow. To aid in this goal, the diagram in Fig. 1.2 was first created by Morkovin and later edited to include transient growth by Morkovin, Reshotko, and Herbert[1]. As shown in the diagram, the path taken to transition depends on the intensity of freestream disturbances. As these freestream disturbances encounter a vehicle, they become entrained in the boundary layer by a receptivity process that may be non-linear. Once in the boundary layer, these disturbances are then amplified according to their type. In path A, the individual disturbances governed by modal growth (1st mode, 2nd mode, Görtler instability, and crossflow instability) are able to amplify from infinitesimal levels to levels sufficiently large to distort the mean flow. This new mean state may develop further instabilities, called a secondary instability, which allows other modal disturbances to amplify. The result of this interaction can be large disturbance growth that leads to a breakdown of the laminar state that eventually develops into turbulence. At higher levels of freestream disturbances, path B, a transient growth type disturbance could provide high initial amplitudes to modal disturbances before modal growth occurs. Disturbance evolution in path C does not include modal growth. Transition cases following this path were previously grouped into bypass transition. However, after the application of transient growth theory[31], an explanation was found for the disturbance growth leading to transition. It is thought that transition due to distributed roughness would follow path C due to the combined flow effects of distributed roughness[37]. Transition cases that follow path D contain moderate levels of freestream turbulence. This results in the boundary layer containing weak turbulent spectrum of disturbances although the flow is laminar[38]. In these transition cases, transient growth theory

has also supplied an explanation for transition without modal disturbances[30]. Finally, path E represents situations where the disturbance level of the freestream is sufficiently strong to cause transition by means other than those described by linear analysis.

A visual diagram of the transition process following path A is given in White[3] and is shown in Fig. 1.3. Initially, the boundary layer begins in a laminar state and, as the boundary layer grows, freestream disturbances of various frequencies begin modal amplification. In the incompressible case considered in White's diagram, these modal disturbances are Tollmein-Schlichting waves. As the mean flow begins to distort, the boundary layer takes on a three dimensional character, leading to further instabilities. Finally, turbulent spots begin to appear as the precursor to a fully developed turbulent boundary layer.

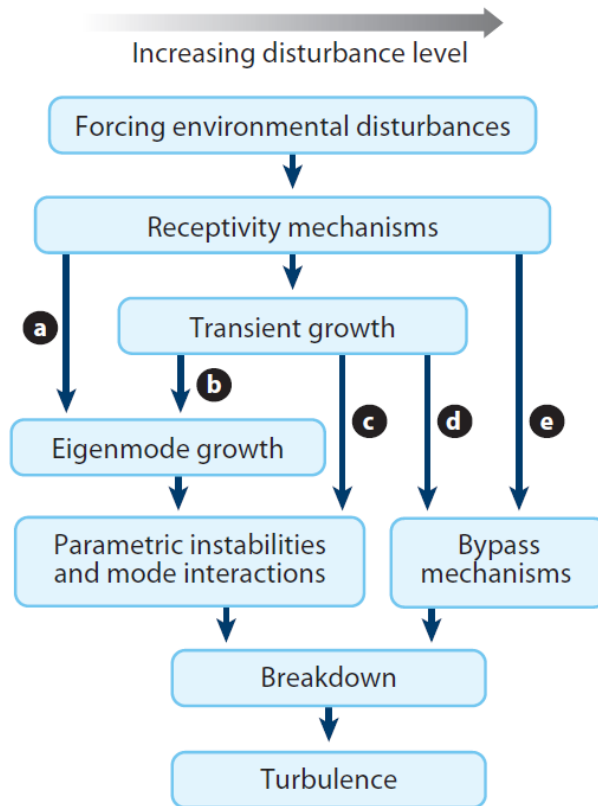


Figure 1.2: Diagram showing the known paths to turbulence[1], taken from Fedorov[2].

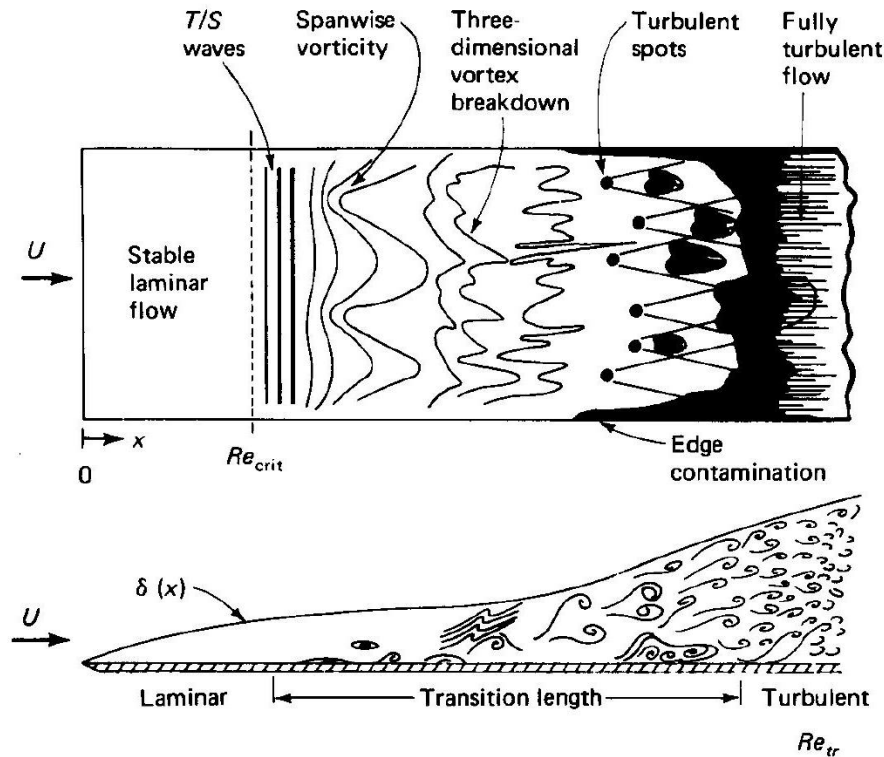


Figure 1.3: Diagram of boundary layer transition following path A in Figure 1.2 taken from White[3].

1.3 High Enthalpy Flows

To further complicate the transition process, realistic supersonic and hypersonic flight vehicles operate in an enthalpy range where “real gas” effects occur. Real gas effects can be considered internal energy modes through which a gas can absorb, store, and release energy. These modes include molecular rotation, molecular vibration, chemical dissociation and exchange, electronic excitation, radiation, and ionization. Unless considering the release of stored energy, as in combustion, internal energy modes generally function as dampers, resisting change from the current state of the gas. In external fluid flows, the energy contained in a fluid’s momentum is converted into heat, an increase in the fluid’s translational temperature, at stagnation points and in the boundary layer as the fluid is decelerated by the presence of the wall. Real gas effects function as heat sinks, reducing the energy load on the translation temperature. The more internal energy modes a gas has, the greater the distribution of energy can be, thus resulting in a smaller change in the translational temperature.

A good example of this effect is given by Anderson[39] (page 364), where he determines the stagnation temperature of the Apollo 11 vehicle during re-entry to be 58,000 K based on a gas without internal energy modes. Upon repeating the analysis with real gas effects included, he finds the new stagnation temperature to be 11,600 K, which is a still a high temperature, however, it is drastically reduced from his previous estimate.

The internal energy modes that are accessible to the gas depend on the enthalpy range of a vehicle's flight conditions. Each mode requires a different energy level before it is able to absorb energy, which is sometimes referred to as being activated. To demonstrate this, Hansen and Heims[40] laid out the flight velocities corresponding to the activation of various internal energy modes of air, seen in Fig. 1.4 taken from Fujii[4]. Because a majority of a flow's enthalpy lies in the momentum, the plot's abscissa is based on the velocity of a vehicle. However, the initial state of the gas is also important for determining the relevance of various internal energy modes, which is fixed for a given altitude, thus Hansen and Heims have plotted the altitude on the ordinate axis. Overlaid on this plot are the flight envelopes of the National Aero-Space Plane (NASP) and the Aeroassisted Orbital Transfer Vehicle (AOTV), thus demonstrating that supersonic and hypersonic flight vehicles are exposed to real gas effects and that the effects vary with enthalpy.

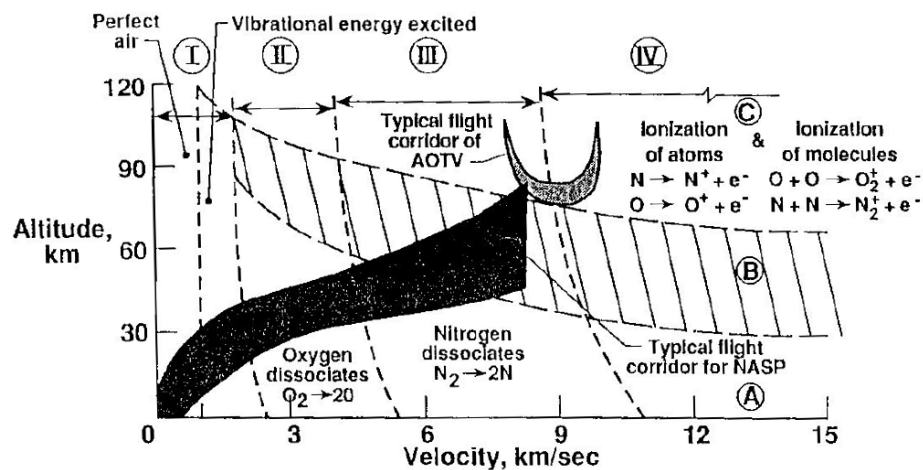


Figure 1.4: Plot of velocity versus altitude of relevant vibrational excitation, dissociation, and ionization with the flight envelopes of NASP and AOTV taken from Fujii[4].

Another important factor governing real gas effects are the rates at which energy can transfer. At the molecular level, energy is transferred from molecular translation to molecular rotation, vibration,

and dissociation through molecular collisions. Even with the high density of molecules required to satisfy the continuum approximation made in fluid flow, the transfer processes take a finite amount of time. Calculating the rate of transfer requires very detailed experiments followed by computations to verify physical models and constants. Many aspects of supersonic and hypersonic flow require nearly exact modeling of these internal energy modes to properly model the flow. Examples demonstrating this sensitivity include bow shock stand-off distances[41], wall heating and flow separation[42], as well as boundary layer thickness[22]. Because flow velocity time scales may be shorter than those that govern the energy transfer between internal modes, energy may be pushed and pulled from the translational temperature faster than the energy can be distributed to all of the internal modes. When the gas is in this state, it is considered to be in non-equilibrium as opposed to a state of equilibrium in which the energy transfer between modes is balanced and the energy contained in each mode is constant. Due to the large velocities encountered in supersonic and hypersonic flows, the fluid is frequently in non-equilibrium. One example of this is a shock, through which the gas's translation temperature may rise drastically over a few molecular collisions, while vibrational excitation and chemical dissociation may take anywhere from hundreds to thousands of collisions. In some flows, a gas may still be in non-equilibrium as it enters the boundary layer.

As will be discussed later, disturbances are equally dependent on real gas effects as the mean flows they propagate through. Both the frequencies and amplification of disturbances depends on boundary layer characteristics[22] such as boundary layer height, boundary layer edge conditions, and the gas composition all of which can be affected by internal energy modes. In addition to dependency on mean flow changes, disturbances must also directly interact with the internal energy modes of a gas. The direct interaction differs in nature from the change in mean flow properties because disturbances may vary at timescales of similar order to internal energy modes such as vibration and dissociation. The result of this interaction depends on the state of the gas through which the disturbance is propagating. Disturbance amplification can occur in some cases of mean flow non-equilibrium such as combustor flows [43, 44], while disturbance damping can occur in other cases of non-equilibrium and also when the mean flow is in equilibrium.

1.4 Motivation for the Current Work

Understanding the transition process is important because of the state of the boundary layer has a great impact on the design parameters that govern a vehicle. In the case of high velocity flows

where the vehicle weight becomes dominated by fuel and engine mass, accurately predicting where a boundary layer will transition allows engineers to optimize design parameters such as thermal protection thickness and fuel efficiency. The increased shear forces due to turbulent boundary layer can cause spallation of an ablative material resulting in burn-through of the thermal protection system. The higher heat transfer rates of a turbulent boundary layer can require different, and possibly heavier, thermal protection materials as well as resulting in higher heating loads, which can degrade the internal structure of a vehicle if not properly accounted for in the design. Thus, maintaining laminar flow can drastically improve the payload efficiency of a particular vehicle design.

Progress has been made in the predictive capabilities through a greater understanding of transition mechanics as well as the development of more advanced analysis and modeling tools. Linear Stability Theory (LST) and the Parabolized Stability Equations (PSE) have proven to be a much more accurate and reliable means of predicting transition for a broad range of cases governed by modal disturbance growth in comparison to the previously used empirical algebraic model. With the aid of high enthalpy and high velocity test facilities, the addition of non-equilibrium vibration and chemistry models have extended the use of these tools into higher enthalpy flows. Computing power and the development of highly accurate numerical methods have also enabled the use of Direct Numerical Simulation (DNS) to efficiently simulate both linear and non-linear growth of disturbances in the high enthalpy regime. From previous research and these capabilities, it has been found that modeling real gas effects is essential to understanding the transition process in realistic high velocity flows. In order to refine our understanding and allow for vehicle optimization, these tools must be further tested and analyzed to gain a more complete picture of the transition process. Once this is done, engineers can begin to take advantage of certain aspects of high enthalpy flows and design vehicles that allow for more laminar flow and the efficient use of turbulent flow.

In the area of roughness transition, a correlation that determines when a particular roughness element or distributed roughness begins to affect the transition location and when this roughness will cause immediate transition is highly desired. This is due to prevalence of roughness in realistic flight vehicles and the difficulty of measuring flow around roughness elements as well as simulating flow around roughness elements. The roughness transition community began with empirical relationships for particular cases of roughness transition that would break down when applied to more general flows. This trend has continued with studies focusing on the determination of critical

roughness parameters for a variety of flows without a general theory as to why these critical roughness parameters need to be unique for each flow. In order to determine a more general, theoretical method for determining critical roughness parameters, the means by which roughness causes transition must be investigated and the underlying disturbances and flow physics must be understood. Once this understanding is gained, it may be possible to generate a more general law for determining critical roughness parameters.

1.5 Objectives and Scope of the Current Work

In current work, the main goal is to identify aspects of the interaction of two types of disturbances observed in supersonic and hypersonic flow with the high enthalpy environment as well as the consequences of these interactions. The first of these disturbances is acoustic waves and their manifestation in supersonic and hypersonic boundary layer transition, which is known as a second mode disturbance. The second type of disturbance is known as a transient growth disturbance, which is associated with flow over roughness elements as well as flow with moderate levels of freestream turbulence. To accomplish this goal, we use theoretical analyses, linear stability analyses, and computations fluid dynamics to study the nature of these two disturbances. In the case of second mode disturbances, we apply our computational tools to analyze the flow through the T5 reflected shock tunnel, an experimental facility capable of generating high enthalpy as well as high velocity flow. The purpose for this is to pursue agreement between computations and a set of experiments attempting to take advantage of the interaction of second mode disturbance with the high enthalpy environment. Although it is possible to approximately model transition with a perfect gas assumption, the purpose of this thesis is to demonstrate to the reader the critical importance of understanding and modeling real gas effects on the transition process for high enthalpy flows in order to accurately represent and predict the physics of transition for realistic flight applications.

After a brief introduction, the current work continues in Chapter 2 with a more focused introduction as well as more in depth historical development and modern contributions to each of the two types of disturbances considered. In Chapter 3, the mathematical models used for simulating high enthalpy flows using the reacting Navier-Stokes equations is presented. A brief review of the derivation of the linear stability equations and the parabolized stability equations is given along with some references for a more thorough understanding. Next, using the reacting Euler equations, the interaction of acoustic waves with internal molecular processes is described based on some basic

assumptions. Lastly, the models for computing compressible, transient growth disturbances in a reacting, vibrationally active flow are laid out. However, due to restrictions discussed in this chapter, the method for computing optimal transient growth disturbances is limited to perfect gas flows. In Chapter 4, the numerical methods for employing the models given in Chapter 3 are described.

The result of the current work begin in Chapter 5 with an analysis of acoustic damping. The method for determining the optimal frequency for damping as well as the magnitude of damping at this frequency is presented based on some simple assumptions. Using CFD, acoustic waves are simulated in order to verify the theory of acoustic damping as well as the ability of the CFD solver to accurately capture the propagation of acoustic waves. In Chapter 6, the understanding of acoustic damping is put into practice by attempting to simulate an experiment using gas injection to delay boundary layer transition caused by second mode disturbances. An attempt is made at simulating the flow in the experimental facility in which these experiments are performed. Next, a hypothetical gas injection case is used to gain an understanding of the injection process and its consequences. Lastly, an attempt is made at simulating the actual experiment. In Chapter 7, the ability of the CFD solver to capture the evolution of second mode disturbances generated by acoustic waves over a cone is tested against the results of linear stability analyses. Using these simulations the interaction of second mode disturbances with molecular vibration is investigated.

Lastly, in Chapter 8, the validation of a linear, optimal, compressible transient growth solver is presented. This solver is then used to validate the CFD solver for simulation of transient growth disturbances. Once validated the CFD solver is used to explore the effect of input energy on the transient growth disturbances. Finally, the effects of a general internal molecular process on transient growth disturbance is tested by creating fictitious vibrational modes.

Chapter 2

Background

2.1 Second Mode Disturbances

As stated previously, second mode disturbances are the first and often most amplified in an infinite family of disturbances that generally have a higher frequency than first mode disturbances. This class of disturbances is purely inviscid in nature. Lees and Gold[45] were the first to point out that these higher modes disturbances were simply acoustic waves trapped in the boundary layer. As discussed by Fedorov[2], these wave become trapped because the mean flow contains a supersonic region relative to the disturbance phase velocity. The location in the boundary layer for which this relative Mach number becomes unity is called the sonic line. As seen in Figure 2.1, the acoustic waves reflect off of the wall and then, rather than the waves reflecting off of the sonic line as assumed by previous analyses, the waves undergo a lensing behavior which causes them to turn and be directed back towards the wall by mean flow. Using a linear stability analysis based on LST and PSE, second mode disturbances have been well-predicted and general trends have been developed. In general, adding bluntness to vehicle nose will stabilize[27] second mode disturbances, while wall-cooling[46] will destabilize them. Second mode disturbances are most amplified when aligned with the mean flow direction as opposed to first mode disturbances which are most amplified when traveling obliquely[47]. Real gas effects on second mode disturbances will be discussed below. Based on the success of previous studies, we will use both LST and PSE to analyze transition over sharp cone.

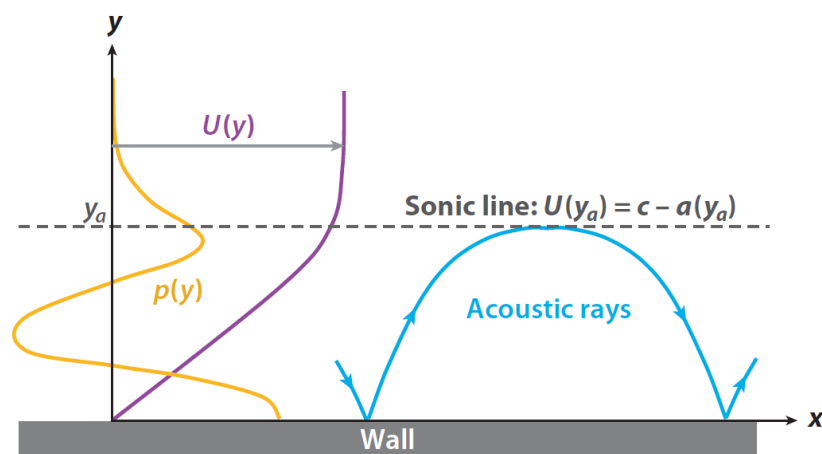


Figure 2.1: Diagram showing how a second mode disturbance is an acoustic wave trapped in a boundary layer. Taken from Fedorov[2].

2.1.1 Development and Application of LST and PSE

Mack[48] cites the first application of Linear Stability Theory occurred when Schlichting[19] calculated the amplitude growth ratios for the most amplified frequencies in a flat plate boundary layer in order to make a transition correlation. After many years of development, the transition prediction method using the semi-empirical e^N method was adopted by Smith and Gamberoni[49] for the analysis of transition over airfoils in incompressible flow. After several important contributions the field of linear flow stability[23, 20, 48], Mack[47] summarized much of this work and laid out methods for using LST for incompressible and compressible parallel flows. Herbert and Bertolotti[50] and Bertolotti and Herbert[51] improved on linear stability analysis by including the non-parallel effects of a developing boundary layer using the Parabolized Stability Equations (PSE). Several reviews of the developments in linear stability analysis can be found in the works by Herbert[52] and Fedorov[2].

Malik and Anderson[53] were among the first to add real gas effects to a linear analysis by including thermochemical equilibrium. In their study, they found real gas effects to stabilize first mode disturbances, while destabilizing second mode disturbances. Stuckert and Reed[54] added chemical non-equilibrium and found that non-equilibrium has a slight stabilizing effect. Hudson et al.[55] added thermochemical non-equilibrium to a five species air flow over a cone and found that the effect of non-equilibrium on disturbances depended on the disturbance. Their results indicated that thermochemical non-equilibrium destabilizes oblique first mode disturbances and that chemical

non-equilibrium destabilizes the second mode disturbances, while thermal non-equilibrium stabilized second mode disturbances.

Johnson et al.[56] made an important contribution by selectively applying thermochemical non-equilibrium to analyze the stability of flow over five-degree, half-angle cones that were experimentally tested in the GALCIT T5 Tunnel [57, 58]. The difference between this study and previous studies was Johnson et al. tested the effect of non-equilibrium on the mean flow and the disturbances individually. They found that the addition of non-equilibrium resulted in a stabilization of second mode disturbances. Additionally, the increase in stability was found to be greatest for flows involving carbon dioxide as opposed to air mixtures or nitrogen. What is clear from the various boundary layer stability studies including internal molecular processes can either stabilize or destabilize the boundary layer with respect to first or second mode disturbances depending on the flow conditions and the vehicle geometry.

Regardless of the models included in a numerical method, the method itself is worthless without validation to experiments. The validation process requires matching the disturbance modes and frequency as well as predicting the transition location of an experiment. As previously stated, linear stability analyses using LST and PSE have adopted the semi-empirical e^N method to predict where a boundary layer will transition. When using this prediction method, a stability analysis must be calibrated to the particular disturbance environment of the experiment. However, once the calibration has been completed, the use of LST and PSE have proven to be an accurate and reliable means of predicting transition. The e^N method has been criticized for its inability to take into account the influence of freestream disturbance levels. In practice, it is often difficult to characterize the disturbance environment in free-flight or the freestream disturbance levels in a test facility, particularly when flow enthalpies reach high levels. Oftentimes, the disturbance environment is gauged based on the transition location on similar test bodies. Another potential problem with a linear stability analysis using the e^N method is the method's inability to model the inherently non-linear modal interactions and breakdown processes leading to turbulence. The PSE do allow for the treatment of non-linear terms[51, 59], however, in many cases a majority of a modal disturbance's growth is governed by linear behavior allowing for a good estimation for the beginning of the transition process.

Several good examples of experimental validation exist in the literature. Malik[22] applied the reacting flow PSE to two high altitude flight experiments and, despite the difference in edge mach

numbers and temperatures, was able to correlate transition between the two cases to similar N factors. Alba et al.[60] performed stability analyses on the HIFiRE 1 vehicle. They used data from several wind tunnel tests between two different tunnels and were able to predict the transition location to near perfection. In another study, Alba et al. were able to match the 2nd mode disturbance frequencies between two different wind tunnel tests. Based on these and other validation cases, the N factor of transition for flight experiments and quiet wind tunnels has been found to be approximately 10 and convention wind tunnels, with higher levels of freestream disturbances, generally transition at an N factor of approximately 5.5.

2.1.2 Acoustic Damping

To better understand the results of Johnson et al.[56], work has been done studying the response of real gases to acoustic waves. The first such analysis was performed by Lighthill[61], who showed the dependency of acoustic damping on the bulk viscosity response of a gas. Vincenti and Kruger[62] also analyzed several aspects of a single internal energy mode on acoustic waves propagating through a gas in equilibrium and found the damping to be greatest when the frequency of sound is near the relaxation rate of the internal mode. Clark and McChesney[63] performed a similar analysis of the acoustic response to a single chemical reaction. A common plot used to describe the frequency response of a gas is shown in Fig. 2.2. As seen in the plot, the absorption rate is the greatest when the frequency of the sound wave, ω , is approximately equal to the relaxation rate of the gas, τ . Also plotted in Fig. 2.2, is the ratio of the frozen speed of sound to the equilibrium speed of sound. The acoustic wave speed in a real gas does not propagate at the well known speed of $\sqrt{\gamma RT}$ for all frequencies. The wave speed depends on the internal energy modes and their frequency response. As shown in the plot, if a frequency is significantly lower than the relaxation rate of the gas, the gas has enough time to adjust to the change in its state due to the acoustic wave, thus will be in equilibrium, and the wave will propagate at the equilibrium speed of sound. For higher frequencies, the gas does not have time to adjust to the change in state, thus will respond a gas without internal energy modes, a frozen gas, and the wave will travel at the frozen speed of sound.

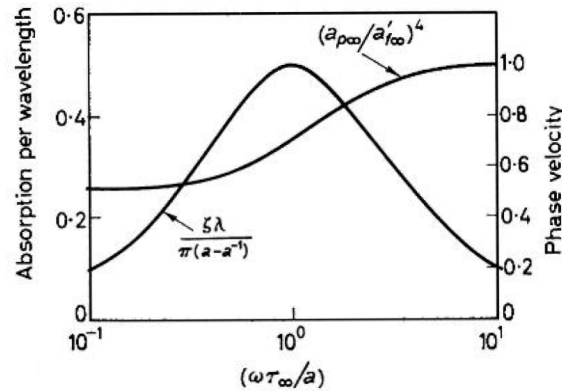


Figure 2.2: This plot shows the typical acoustic damping properties of a gas with a single relaxation mode versus frequency. The most effective damping occurs when the frequency is of similar scale to the relaxation time of the gas. Also in the plot is the ratio of the speeds of sound. This is an important factor in the acoustic analysis. Taken from Fujii and Hornung[5]

Fujii[5, 4, 6] was able to improve on the modeling of acoustic damping by including several relaxation modes. In doing this, he was able to model realistic mixtures of gases in equilibrium. For his study he considered nitrogen, air, and carbon dioxide and compared the acoustic damping properties of these gases to the second mode amplification rates on attachment line transition. Fujii found that all of the gases tested had similar damping properties at different equilibrium states and frequencies, meaning that all of the gases could be used in acoustic damping applications. A sample plot of Fujii's work is included in Fig 2.3a and shows the variation in damping properties based on the temperature range and frequency. Fujii showed that the results of Johnson et al.[56] were due to carbon dioxide's ability to damp the acoustic frequencies associated with second mode transition very well at the temperatures and pressures considered in the experiment and computation, as seen in Figure 2.3b. Another important aspect of Fujii's work was the identification of the cause for damping at different frequencies depending on the relaxation mode. As seen in Figure 2.3a, two distinct peaks in the absorption rate occur for carbon dioxide at a temperature of 3000 K. Fujii states that the peak at higher frequencies is due to vibrational relaxation, while the peak at lower frequencies is due to chemical dissociation.

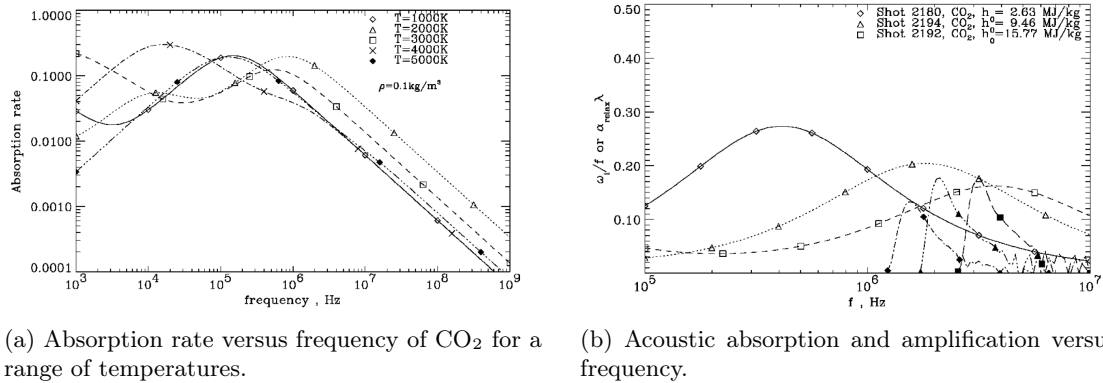


Figure 2.3: These plots demonstrate the acoustic damping properties of carbon dioxide and the amplification of second mode disturbances in attachment line transition. Taken from Fujii and Hornung[6]

Bertolotti[64] demonstrates the ability of molecular rotation to cause acoustic damping at lower flow enthalpies. At these enthalpies, he demonstrates the presence of molecular vibration results only in an increase in disturbance amplification because the relaxation rate is too slow to cause acoustic damping, but not slow enough to prevent it from affecting the mean boundary layer profile. Fujii and Hornung note that the relaxation rate of rotation begins to outpace the acoustic frequencies responsible for causing transition at higher enthalpies. However, Bertolotti's study further enforces the general effect of an internal molecular process on acoustic waves and boundary layer stability. Interestingly, Bertolotti also shows how an appropriate use of bulk viscosity produces similar damping effects seen by the internal molecular processes that result in a bulk viscosity.

Another interesting application to second mode stabilization through acoustic damping was developed by Gaponov[65] using porous surfaces. The theory involves the use of disturbance wave propagation through long, thin tubes. These tubes allow for the admittance of wall-normal disturbance velocity resulting in an absorption of disturbance energy, thus causing acoustic damping. Fedorov[66] refined this work on porous material. He found that the disturbance amplitude of certain frequencies could be drastically reduced by tailoring the radius and spacing to wall pores. The theory was verified in experiments of Rasheed [67], who showed delay in transition due to a porous surface for several test cases and with schlieren photography.

2.1.3 Direct Numerical Simulations of Acoustic Waves

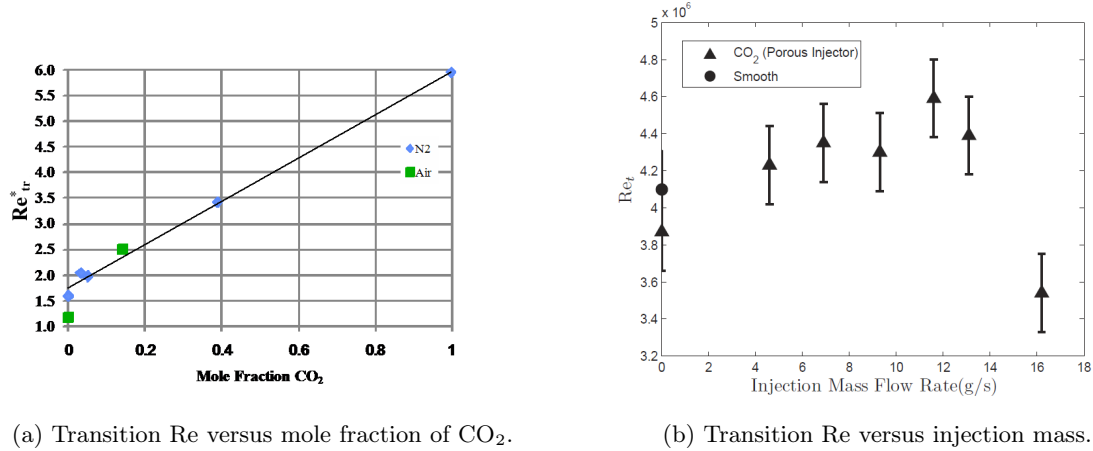
Balakumar et al.[68, 14, 69] have done a significant amount of research in the area of direct numerical simulation (DNS) of acoustic and vorticity waves and the generation of boundary layer disturbances. Balakumar[68] first showed that slow acoustic waves are more efficient than fast acoustic waves at generating disturbances over a flat plate. He also obtained excellent agreement between DNS and a linear PSE stability analysis. Balakumar and Kegerise[14] performed similar simulations over a series of experimental cones with varying geometries and were able to obtain excellent agreement between DNS, linear PSE, and experimental measurements in cold flow tunnels. Balakumar shows that this type of DNS can aid in the prediction of boundary layer transition due to wind tunnel noise by providing the receptivity of freestream disturbances to the boundary layer. This is significant because a linear stability analysis can only predict the amplification of disturbances and does not account for the initial amplitude of disturbances. Thus, this type of linear analysis cannot predict the point at which disturbances will begin to cause boundary layer transition. Balakumar and Kegerise[69] extend this work with the inclusion of an incidence angle to better approximate wind tunnel noise and vorticity waves in an attempt to model the noise environment of flight experiments.

2.1.4 Review of Experimental Work at the GALCIT T5 Tunnel

Many high speed test facilities operate in a relatively low enthalpy, “cold flow”, regime. In these facilities, high mach number is achieved by lowering the freestream temperature rather than increasing the freestream velocity. Incredible scientific advances in the understanding of fluid flow and boundary layer transition have been validated in these cold flow tunnels. However, just as numerical simulations require modeling of real gas effects, an experimental facility needs to operate at high-enthalpy conditions in order to accurately study the flow physics of realistic high speed vehicles. Generating these high-enthalpy flows is difficult and requires very high temperatures and pressures, thus flow times are relatively short due to material constraints. The T5 Free-Piston Shock Tunnel at the Graduate Aerospace Laboratories, California Institute of Technology (GALCIT) is one of the facilities capable of high-enthalpy, hypersonic flows. The method used at T5 involves rapidly compressing a column of driver gas using a piston. The driver gas generates a shock that travels through a test gas. This shock rapidly heats and pressurizes the test gas producing the high temperatures and pressures needed. In order to differentiate between low and high enthalpy hypersonic flows, the term hypervelocity flow was created.

Several important advances in understanding real gas effects have been made and verified using this facility. The first study relevant to this work was performed by Germain and Hornung[57], who studied boundary layer transition of five-degree, half-angle cones. Using mainly air and nitrogen as the freestream gas, they found that the real gas effects on transition could be correlated using Eckert's reference temperature[70]. Additionally, they found the transition Reynolds number to increase with stagnation enthalpy, more so with air than nitrogen. Germain and Hornung attributed the stabilizing effect due to non-equilibrium chemistry and the difference between the two gases to be due to the lower dissociation energy of oxygen. Adam[12], further studied this effect by studying the transition properties of carbon dioxide flows. In his work, he found the increase in transition Reynolds numbers to be greater with carbon dioxide than either air or nitrogen. Adam attributed this stabilizing effect due to non-equilibrium chemistry as Germain and Hornung had done. Fujii[6, 5, 4] analyzed real gas effects on the attachment-line transition of swept cylinders. He found similar results as Germain and Hornung and Adam, however, he utilized his understanding of acoustic damping and suggested the increase in stabilization for carbon dioxide flows was due to vibrational relaxation.

In order to begin understanding how to take advantage of carbon dioxide's stabilizing effect, the researchers at T5 began mixing carbon dioxide in with air and nitrogen test gases for hypersonic flows over five-degree, half-angle cones. The result of this work was summarized by Leyva et al.[71] and is shown in Figure 2.4a. They found that by increasing the mole fraction of carbon dioxide in the freestream, the transition Reynolds number was increased, thus delaying transition until further back on the cone. Leyva et al.[72] attempted to take this idea one step further by introducing carbon dioxide into the boundary layer by means of discrete gas injection. In this study, they found the injection method and the injector itself caused transition to occur immediately behind the injector portion of the cone. The cause of transition in these cases was not identified. Jewell et al.[13] tested a less intrusive method of injection and observed an optimum in transition delay with carbon dioxide injection, seen in Figure 2.4b. Increasing the injection mass of carbon dioxide further delays transition until causing too large a disturbance to the boundary layer and moving transition forward. To verify that the stabilizing effect was due to the relaxation modes of carbon dioxide, Jewell et al. also injected argon, which roughly matches the injection momentum, and found that argon injection only moves transition forward on the cone.

(a) Transition Re versus mole fraction of CO_2 .

(b) Transition Re versus injection mass.

Figure 2.4: These plots show recent test data from the T5 tunnel. Figure 2.4a shows the variation with transition Reynolds number with mole fraction of carbon dioxide. As the mole fraction of carbon dioxide is increased, the transition Reynolds number is increased, thus delaying transition until further back on the cone. Figure 2.4b shows the variation of transition Reynolds number with injection mass of carbon dioxide. Increasing the injection mass of carbon dioxide further delays transition until causing too large a disturbance to the boundary layer and moving transition forward.

2.2 Transient Growth and Roughness Transition

2.2.1 Roughness Transition

Research in the area of transition due to surface roughness has been ongoing for several decades in both the subsonic and supersonic regimes. These studies are so numerous that the reader is referred to the reviews of roughness research by Schneider[11], Reshotko[37], and Reda[73]. These reviews discuss how a number of different flow features and geometry can affect the transition location including the edge Mach number, M_e , boundary layer displacement thickness, δ^* , roughness height, k , roughness diameter, D , wall temperature, and the density of roughness elements. However, a brief review of roughness research is presented as well as a short discussion of the flow features of an isolated roughness element and potential mechanisms of how roughness can affect transition. Initially, studies focused on developing empirical relationships based on boundary layer properties such as the displacement thickness, roughness height, k , and various Reynolds numbers such as the roughness Reynolds number, $Re_k = \frac{Uk}{\nu}$ [74, 75, 76].

Several studies were dedicated to imaging the flowfield to identify various features that could result in destabilization of the boundary layer. Whitehead[77] used surface oil flow to visualize

the flow features around isolated roughness elements in supersonic flow. He found a similar vortex structure composed of horseshoe vortices would form around various shapes of elements. He also found that these vortices persisted well downstream of the element. Another interesting aspect of Whitehead's study was the effect of spacing on a fence of roughness elements. He determined ranges of influence of other elements as well as the spacing away from the element the vortex structures would have based on inter-element spacing. Baker[7] studied these horseshoe vortex systems in subsonic flows and describes their features in great detail. As shown in Figure 2.5, vortex systems were found to form in 2, 4, and 6 steady vortex patterns as well as unsteady vortex systems depending on the roughness element diameter, over the boundary layer displacement thickness versus the Reynolds number based on element diameter, $Re_D = \frac{UD}{\nu}$.

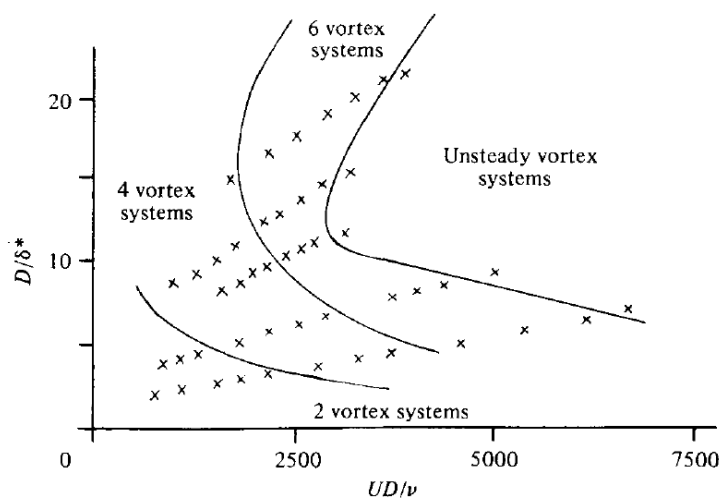


Figure 2.5: This plot shows the classes of horseshoe vortex systems that develop in front of isolated roughness elements. The results are plotted based on element diameter over boundary layer displacement thickness versus Reynolds number based on the element diameter. This figure was taken from Baker[7].

Another common feature of roughness elements is the formation of a wake flow consisting of vortices. The character of these vortices depends on the flow environment. In a crossflow environment the wake vortices can be co-rotating[78], while a direct flow will usually result in counter-rotating vortices[79, 8, 10]. These wake vortices are similar to the horseshoe vortex system in that they are a steady feature if the element has a small impact on the flow, assuming no freestream disturbances. An excellent visual image of the vortex system that forms both in front and behind a roughness element is reproduced in Fig. 2.6 from Fig. 4a in Bartkiewicz et al.[8]. Visible in the figure are the three vortices of the six vortex pattern in front of the element with iso-surfaces. These vortices wrap

around the element and convect downstream, leaving a higher wall heat flux than the surrounding areas. The two trailing, counter-rotating vortices behind the element are also visible in the plot with iso-surfaces. These iso-surfaces persist further down the domain, indicating the increased vortical strength of the trailing vortices as compared to the horseshoe vortices.

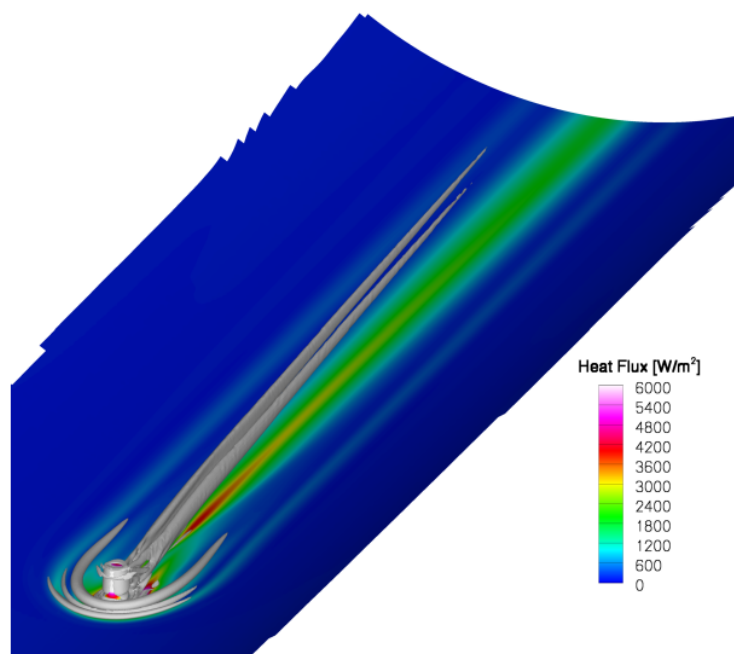


Figure 2.6: A reproduction of Fig. 4a from Bartkowicz et al.[8] that demonstrates the vortex system that forms around an isolated roughness element. The iso-surfaces are of the Q criterion and indicate the presence of a vortex. The contours are the wall heat flux. The flow is from the lower left to upper right of the figure.

The vortex system around the roughness element can become unsteady as the elements disrupts the flow more and more[80, 79, 8]. In the computational study by Bartkowicz et al., both the horseshoe vortices as well as the trailing vortices show unsteady behavior caused by the unstable nature of the leading vortex system. As they show in their study, the horseshoe vortices begin to breakdown further upstream of the trailing vortices. Acarlar and Smith[81] studied the formation of hairpin vortices over hemispherical roughness elements. In contrast to the work of Bartkowicz et al., their experiments indicated that, while the wake of the element was unsteady, the horseshoe vortices originating in the front of the element were steady. They also noticed that the hairpin vortices tilted and concentrated their vorticity as a result of the shear flow in the boundary layer, a hallmark of transient growth disturbances. Klebanoff[82] performed a similar study and included cylindrical elements as well as an sinusoidal disturbance to the freestream.

As stated in the previous chapter, it is these trailing vortices that have caused several researchers to investigate transient growth disturbances, or Klebanoff modes, and how the streaky structures that result from these disturbances lead to turbulence. An interesting set of experiments have been performed by Dr. Ed White and his students[80, 83, 17, 84, 10]. Using an array of cylindrical roughness elements, White and Ergin[10] and Ergin and White[80] measured the disturbance field behind the roughness array in order to determine the presence of optimal transient growth disturbances. They were able to measure transient growth of certain spanwise disturbance wavelengths, as shown in Figure 2.7a. White and Ergin also determined that the energy put into the disturbances was quadratic with roughness height. Numerical simulations confirming the experimental results were performed by Fischer and Choudhari[9], as seen in Figure 2.7b, as well as Rizzeta and Visbal[79]. Tumin and Reshotko[85] later showed that the receptivity of the disturbances generated by the roughness elements was non-linear. They also determined the transient growth that occurs well downstream of the elements is governed by linear theory. However, in all of these studies it was noted that the transient growth that occurred showed less growth than optimal disturbances. This result has called into question the realizability of optimal transient growth due to roughness elements.

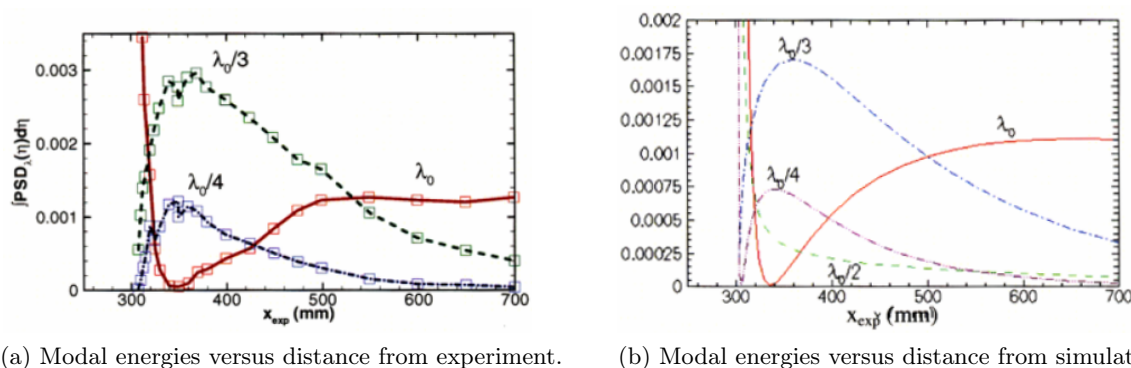


Figure 2.7: Comparison of the numerical simulation performed by Fischer and Choudhari[9] and the experimental data from White and Ergin[10]. Both studies show similar trends, however, the magnitude of disturbances is not equal.

As discussed in Schneider[11] and Choudhari et al.[86, 87, 88, 89] the mechanisms thought to affect transition in roughness cases depends on the roughness parameters. It is known that three dimensional roughness elements cause the transition location to rapidly move forward from the natural transition location, as demonstrated in Figure 2.8. The natural transition location would be defined by one of the modes governed by eigenvalue growth. An increase in roughness height

causes the transition location to depart from the natural location, which is thought to be due to the roughness amplifying the existing modal disturbances. A further increase in roughness height results in the formation of velocity and temperature streaks caused by the many vortices present in the flowfield around roughness elements. Transition in these cases is thought to be due instabilities that develop on the trailing streaks. When the roughness becomes of sufficient size, the vortex structure that forms in front of the element begins to breakdown, causing transition to occur in the near-wake region behind the element. Further research in this area is required to strengthen these conclusions.

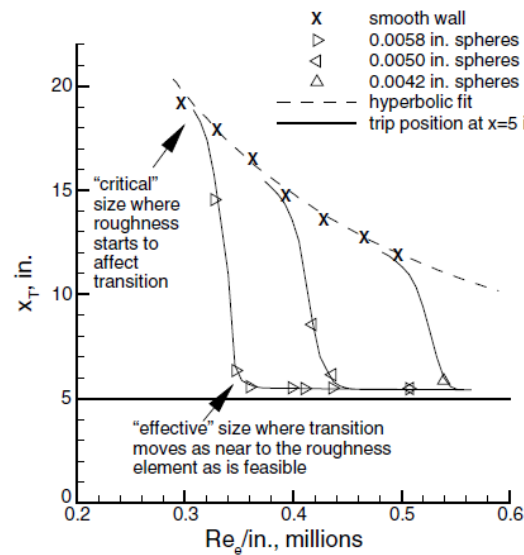


Figure 2.8: This plot demonstrates the progression of the transition location due to three dimensional roughness elements. This image was taken from Schneider[11].

2.2.2 Theoretical Basis of Transient Growth

Before discussing the transient growth on a mathematical level, it is instructive to first obtain a concrete understanding of the transient growth process by visualizing a boundary layer disturbance undergoing transient growth. Using the technique given in Chapter 8, a pair of streamwise vortices are introduced over a flat plate flow with a freestream Mach number of approximately three, shown in Fig. 2.9. In the plot, the iso-surface indicates the presence of one of the vortices. The contours on five spanwise slices as well as one streamwise slice depict a normalized temperature. The flat plate is indicated by the gray surface below and the flow velocity is indicated with the black arrow. The transient growth process in this case is caused by the streamwise vortex displacing high temperature,

low velocity fluid from low in the boundary layer and moving it to higher in the boundary layer, as seen along the centerline of the plot in Fig. 2.9. The vortex motion also causes low temperature, high velocity fluid to be displaced from high in the boundary layer and moving it to lower in the boundary layer (along the outer spanwise edges of the domain). After comparing the undisturbed flat plate flow (a spanwise invariant flow) from the flow in Fig. 2.9, one can see how the spanwise variation results is a disturbance that evolves as the flow develops in the streamwise direction.

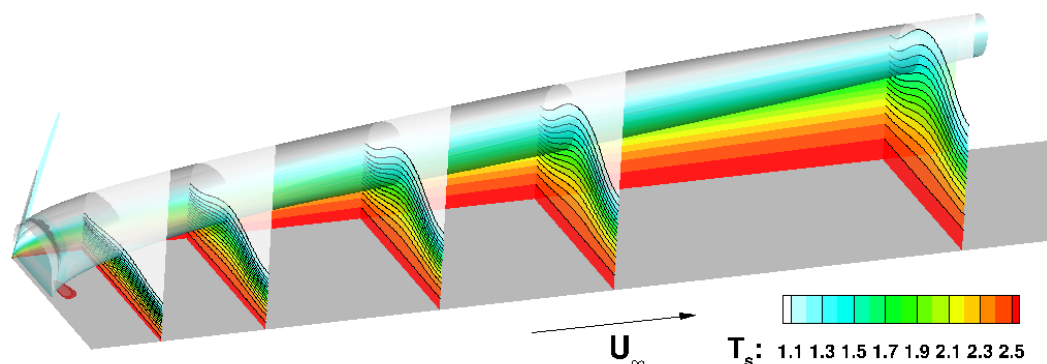


Figure 2.9: A pair of streamwise vortices undergoing transient growth in a flat plate boundary layer with a freestream Mach number of approximately three. The iso-surface indicates the presence of one of the vortices. The contours are on five spanwise slices as well as one streamwise slice and depict a normalized temperature. The flat plate is indicated by the gray surface below and the flow velocity is indicated with the black arrow.

For a more thorough understanding of how transient growth arises on a basic level, we follow the explanation of Butler and Farrell[31]. Transient growth results from the non-self-adjoint nature of the linearized Navier-Stokes operator. The term transient growth refers to temporary growth in time or space (and eventual decay) of some measure of disturbances in a particular flow. In a majority of transient growth analyses, the quantity measured is the disturbance energy, which is defined by an inner product of all disturbance quantities. This would imply that some or all of the disturbance quantities themselves may undergo a period of transient growth.

The self-adjointness of a linear operator depends on the inner product defined in the space in which it operates. For viscous shear flows, the linear Navier-Stokes operator is non-self-adjoint in several inner products, including the one that defines disturbance energy.[31] One property of a non-self-adjoint linear operator is that the eigenmodes of the operator are not orthogonal and thus do not evolve independently in time or space. It is this interaction of modes that results in a period of transient growth even though a traditional, single mode analysis may show that these modes

only decay as time or distance goes to infinity. Large growth can occur if several modes initially destructively interfere, resulting in a small amount of initial disturbance energy. As the individual modes decay at different rates, the leading order term governing the growth in amplitude of certain disturbance quantities becomes linear with time or space, resulting in the total disturbance energy increasing algebraically. Because a modal disturbance's growth must be exponential, transient growth and the disturbances that cause it are considered to be non-modal. Given a sufficient length of time or distance, the decay of each mode will begin to dominate, resulting in an exponential decay of disturbance energy.

To see how transient growth arises in fluid flows, we look to the governing equations of viscous shear flow in the incompressible regime. In this case, the Navier-Stokes equations, when linearized about a small three-dimensional disturbance, can be reformulated into an equation for disturbance velocity, v , and an equation for disturbance vorticity, ω , parallel with the mean velocity gradient

$$\left(\frac{\partial}{\partial t} + U\frac{\partial}{\partial x}\right)\Delta v - \frac{\partial^2 U}{\partial y^2}\frac{\partial v}{\partial x} - \frac{1}{\text{Re}}\Delta(\Delta v) = 0, \quad (2.1)$$

$$\left(\frac{\partial}{\partial t} + U\frac{\partial}{\partial x}\right)\omega - \frac{1}{\text{Re}}\Delta\omega = -\frac{\partial U}{\partial y}\frac{\partial v}{\partial z}, \quad (2.2)$$

where $\Delta = \nabla^2$, U is the mean flow velocity in the direction x , y is the direction of the mean velocity gradient, z is the spanwise direction, and Re is the Reynolds number. Due to the common application of these equations to wall-bounded flows, the components parallel with the mean velocity gradient will be referred to as wall-normal. Assuming the disturbance has a standard modal form, i.e.

$$\begin{aligned} v(x, y, z, t) &= \tilde{v}(y) \exp[i(\alpha x + \beta z) + \sigma t], \\ \omega(x, y, z, t) &= \tilde{\omega}(y) \exp[i(\alpha x + \beta z) + \sigma t], \end{aligned}$$

these equations can be written as

$$\left(-i\alpha U\Delta + i\alpha\frac{d^2 U}{dy^2} + \left[\frac{\Delta(\Delta)}{\text{Re}}\right]\right)\tilde{v} = \Delta\tilde{v}, \quad (2.3)$$

$$\left(-i\alpha U + \frac{\Delta}{\text{Re}}\right)\tilde{\omega} - i\beta\frac{dU}{dy}\tilde{v} = \sigma\tilde{\omega}, \quad (2.4)$$

where $\Delta = d^2/dy^2 - k^2$ and $k^2 = \alpha^2 + \beta^2$. In operator form, these equations can be viewed as the system

$$\begin{bmatrix} \mathcal{L} & 0 \\ \mathcal{C} & \mathcal{S} \end{bmatrix} \begin{bmatrix} \tilde{v} \\ \tilde{\omega} \end{bmatrix} = \sigma \begin{bmatrix} \tilde{v} \\ \tilde{\omega} \end{bmatrix}, \quad (2.5)$$

$$\mathcal{L} = \Delta^{-1} \left(-i\alpha U \Delta + i\alpha \frac{d^2 U}{dy^2} + \left[\frac{\Delta(\Delta)}{\text{Re}} \right] \right), \quad (2.6)$$

$$\mathcal{S} = \left(-i\alpha U + \frac{\Delta}{\text{Re}} \right), \quad (2.7)$$

$$\mathcal{C} = -i\beta \frac{dU}{dy}. \quad (2.8)$$

This system is composed of the Orr-Sommerfeld operator \mathcal{L} , the Squire operator \mathcal{S} , and a coupling operator \mathcal{C} . Thus, the Navier-Stokes operator is non-self-adjoint whenever the coupling operator is non-zero, the Orr-Sommerfeld operator is non-self-adjoint, or the Squire operator is non-self-adjoint. The Orr-Sommerfeld and Squire operators only become self-adjoint when α equals zero and the coupling operator is zero.[31]

The eigenmodes of this system consist of two types: Squire modes and Orr-Sommerfeld modes. A Squire mode is a solution to the homogeneous normal vorticity equation, while an Orr-Sommerfeld mode is a solution to the system of Orr-Sommerfeld and normal vorticity equations. An example of an Orr-Sommerfeld mode is a Tollmein-Schlichting wave when the system is restricted to two dimensions. In cases where a set of initial disturbances have a non-zero α and/or β , we see that multiple disturbances may interact because of the non-self-adjoint property of the linearized Navier-Stokes operator, which may also result in transient disturbance growth. It has been shown by Gustavsson[90], that even a single Orr-Sommerfeld mode with only a spanwise variation in normal velocity is capable of causing transient growth. The three-dimensional implications of an Orr-Sommerfeld mode were previously overlooked due to Squire's theorem.[91] This theorem states that for a given unstable, three-dimensional, modal disturbance, there exists a more unstable two-dimensional disturbance at a lower Reynolds number.

One could also look at the basis of transient growth in viscous shear flows from the following perspective. The coupling term in Eq. 2.5 shows that the normal vorticity equation is driven by the normal velocity. Because the generation of normal vorticity is proportional to the mean shear gradient, a large disturbance in normal vorticity can be caused by a small disturbance in normal velocity given a sufficiently large gradient in the mean flow velocity. In the case where the normal

velocity only decays, it will pull energy from the velocity gradient for a period of time or distance before viscosity damps all disturbances and the flow returns to its basic state. For a more thorough explanation of transient growth in different flows, the reader is referred to the book by Schmid and Henningson.[34]

2.2.3 Optimal Disturbances

As seen from the equations above, a vast array of disturbances is capable of causing transient growth of disturbance energy. It is therefore of great interest to determine which initial conditions provide the largest growth in a flow over a specified domain. This optimal disturbance provides an upper bound on growth due to realistic disturbances. Also, the shape of the optimal disturbance can provide guidance for understanding which class of disturbances will cause the largest growth for a specific flow. The definition of optimal depends heavily on the inner product used to evaluate the property being maximized. A change in the inner product can affect the shape and wavenumbers of the initial and output disturbances as well as the profile and maximum of the growth factor.[30, 92] In spatial transient growth analyses, the optimal initial condition is solved for using the method of Lagrange multipliers, which utilizes a set of adjoint governing equations and adjoint disturbance variables. These adjoint equations can be obtained in a continuous manner[30, 15] or a discretized manner.[30, 92]

2.2.4 Theoretical development

Although the mathematical implications of transient growth theory have been known for some time[93], the application of the theory to fluid mechanics began with Ellingsen and Palm[94]. In their paper, they used an inviscid analysis to show that an initial disturbance without a streamwise component introduced into a shear layer will cause the streamwise disturbance velocity to increase linearly with time. Landahl[95] proved that any parallel shear flow has the potential for linear growth of the disturbance kinetic energy for any three dimensional disturbance with a non-zero disturbance velocity parallel to the mean velocity gradient. The first viscous analysis of transient growth was performed by Hultgren and Gustavsson[96], in which they found that the addition of viscosity caused the initial linear growth to decay over time. The first optimizations were carried out by Farrell[97] and Boberg and Brosa.[32] The theory was further developed in viscous shear flows by a number of studies that highlighted the potential for large growth in Couette, Poiseuille,

and incompressible and compressible boundary layer flows[31, 98, 90, 99].

The first general spatial transient growth analysis was performed for parallel shear flows by Schmid et al.[100] This spatial theory was later refined by Tumin and Reshotko[101] and Reshotko and Tumin[102] for both incompressible and compressible flows. In these two studies, a number of trends were discovered including the variation of the growth factor with wall temperature and radius of curvature for blunt body geometries. These trends compared very well with the trends of the "blunt body paradox." Because of this, Reshotko and Tumin were able to make the first correlation for transition due roughness on blunt geometries based on theory.

Non-parallel effects present in incompressible boundary layer flows were first considered by Luchini[103] and Andersson et al.[30]. Luchini showed, for sufficiently large Reynolds numbers, the scaling of disturbance velocities leads to the conclusion that the maximum disturbance energy growth is attained when the initial disturbance has no streamwise velocity component. Andersson et al. did not limit their study in the way Luchini had and found that their results converged to Luchini's results as they increased the Reynolds number. Luchini also discovered that for a given set of spatial disturbances, the maximum disturbance growth occurs when these disturbances are steady. These theoretical results are in agreement with the physical cause for optimal transient growth in shear flows, which has been shown by previous studies[31, 103, 30] to be steady, streamwise vortices. Transient growth occurs due to these vortices causing the lift-up effect[104], in which the streamwise mean flow momentum is displaced along the mean flow velocity gradient. This displacement causes low momentum fluid to move up the velocity gradient and high momentum fluid to move down the velocity gradient, resulting in an increase in streamwise disturbance velocity. For compressible boundary layer flows, the lift-up effect also results in an increase in the temperature disturbance. Andersson et al.[30] were able to make a correlation for the transition of a flat plate boundary layer subjected to moderate levels of freestream turbulence and found it to agree well with experimental data. Tumin and Reshotko[15] developed a compressible extension to the model used by Luchini[103] and Andersson et al.[30] In their study they found similar trends as in their previous work[102, 101] with the parallel flow approximation.

2.3 Modern Developments of Transient Growth and Roughness Transition

Since the development of linear, optimal transient growth theory, a number of studies have been made investigating the effects of secondary instabilities for the incompressible regime. Andersson et al.[16] studied the stability of the optimal disturbances to a secondary disturbance using a linear Floquet expansion for a various range of input energies. Although the stability analysis was inviscid, the results of their analysis compared well to DNS. They found that when the streamwise streak amplitude reached 26% of the freestream velocity the streaks became unstable to sinuous instability modes. Brandt et al.[105] improved on these results by showing that the secondary instability is convective in nature, implying that the streaks tend to amplify external noise. Although questions arose about the breakdown process of the streamwise streaks, Schlatter et al.[33] provided further confirmation that this sinuous type of secondary instability was in fact the dominant mode of streak breakdown. Additionally, Denissen and White[17] found that a wall-normal scaling of the optimal disturbances results in much larger growth potential of the secondary disturbance. This larger growth potential required a distinction to be made between optimal disturbances of linear theory and “most dangerous” disturbances with respect to transition.

The increase in computing power coupled with low dissipation numerical schemes has allowed for increasingly accurate simulations of both isolated and distributed roughness elements. These simulations provide great insight into the transition process seen in experiment and flight. Bartkowicz et al.[8] performed a DNS of a Purdue experiment[106] of a cylindrical, isolated roughness element. In their study, they were able to match qualitatively well to flow features and unsteadiness observed in the experiment. Additionally, they were able to match the driving frequency of the unsteadiness and determine the cause to be the unsteady horseshoe vortex system in front of the element. This was later verified in further experimental testing described in[107]. Iyer et al.[108, 109] has performed DNS of several different roughness cases and found good qualitative agreement with the experiments of Danehy et al.[110] Lastly, Choudhari et al.[88], Chang et al.[87], and Li et al.[111] have reformulated the PSE to assess the secondary instabilities associated with three-dimensional flows perturbed by streamwise vortices, such as flows behind roughness elements. Using these equations, they are able to use the e^N method to predict the stability characteristics of the roughness wake. They have found similar instabilities as those described in the analyses of transient growth disturbances described above. Along with these stability calculations, they have also perform several DNS of

different roughness cases including the effect of roughness height and shape.

Chapter 3

Mathematical Models

3.1 Governing Equations

An extended set of Navier-Stokes equations is required to sufficiently model the physical processes that occur in the high-enthalpy flows of interest to this work. These processes include chemical reactions and vibrational excitation, for which this extended set allows. Because of the addition of chemical reactions, each species requires its own conservation equation. Although other forms of the species conservation equations can be written (for example the equations could be based on mass fractions, moles, or extent of reaction for a particular reaction set), the current set are based on the mass density of each species. Also, the summation notation (or Einstein notation) has been employed in order to simplify the equation set, in which a repeated sub-index indicates a vector contraction unless otherwise stated. In Cartesian coordinates, x_i , these equations are as follows

$$\frac{\partial \rho_s}{\partial t} + \frac{\partial}{\partial x_i} (\rho_s u_i) = - \frac{\partial}{\partial x_i} (\rho_s v_{si}) + w_s, \quad (3.1)$$

where ρ_s is the mass density of species s , which is not a contracted index, u_i is the fluid velocity in the x_i direction, v_{si} is the diffusion velocity of species s in the x_i direction, and w_s is the chemical source term to be discussed later. By summing over the species mass densities, we obtain the mixture mass density, ρ . The sum of the species mass density equations should still preserve the original conservation of mass equation, which is

$$\frac{\partial \rho}{\partial t} + \frac{\partial}{\partial x_i} (\rho u_i) = 0. \quad (3.2)$$

Therefore, we have that the sum over all species of the viscous diffusion term and the chemical source terms on the right hand side of Eq. 3.1 are individually equal to zero.

Next, we have the conservation of linear momentum, which in Cartesian coordinates is

$$\frac{\partial}{\partial t}(\rho u_i) + \frac{\partial}{\partial x_j}(\rho u_i u_j) = -\frac{\partial P}{\partial x_i} + \frac{\partial \tau_{ij}}{\partial x_j}, \quad (3.3)$$

where P is the fluid pressure and τ_{ij} is the viscous stress tensor. This equation represents momentum in each of the x_i directions. For the current work, all body forces on the fluid are assumed to negligible and have been omitted from the momentum equations.

In modeling the molecular vibration, we assume energy exchanges between vibrational modes occur sufficiently fast for all vibrational modes to be in equilibrium. This assumption allows the multiple conservations equation for each vibrational mode to be reduced to a single equation for the total vibrational energy. Additionally, this assumption eliminates the need to supply rates for vibrational energy exchanges. Therefore, the conservation of total vibrational energy per unit volume is

$$\frac{\partial E_v}{\partial t} + \frac{\partial}{\partial x_j}(u_j E_v) = -\frac{\partial q_{vi}}{\partial x_i} - \frac{\partial}{\partial x_i} \left(\sum_s \rho_s e_{vs} v_{si} \right) + Q_{t-v} + \sum_s e_{vs} w_s, \quad (3.4)$$

where q_{vi} is the vibrational heat transfer in the i direction, e_{vs} is the vibrational energy per unit mass of species s , and Q_{t-v} represents the translational-vibrational energy exchange.

Finally, we have the conservation of total energy equation

$$\frac{\partial E}{\partial t} + \frac{\partial}{\partial x_j}(u_j (E + P)) = \frac{\partial}{\partial x_j}(u_i \tau_{ij}) - \frac{\partial q_i}{\partial x_i} - \frac{\partial q_{vi}}{\partial x_i} - \frac{\partial}{\partial x_i} \left(\sum_s \rho_s h_s v_{si} \right), \quad (3.5)$$

where q_i represents the heat transfer of translational and rotational energy in the i direction, and h_s is the enthalpy contained in species s .

3.1.1 State Equations

The fluid pressure, P , is found using the ideal gas law,

$$P = \rho \bar{R} T = \sum_s \frac{\rho_s}{M_s} R T, \quad (3.6)$$

where R is the universal gas constant, M_s is the molecular weight of the species considered, \bar{R} is the gas constant specific to the mixture considered, and T is the translational-rotational temperature.

These two degrees of freedom are assumed to be in equilibrium. For the flows considered, the rotational state of the gas generally equilibrates with the translational state within a few molecular collisions, making the assumption of a single temperature valid. Other internal modes, such as electronic, etc. are omitted from the equation set.

The total energy per unit volume of the fluid, E , is defined as

$$E = \frac{1}{2}\rho u_i u_i + \sum_s \rho_s c_{vs} T + \sum_s \rho_s e_{vs} + \sum_s \rho_s h_s^\circ,$$

where

$$c_{vs} = c_{vs}^{tr} + c_{vs}^{rot}$$

and is the specific heat at constant volume of the species. Each component of the specific heat is calculated using

$$c_{vs}^{tr} = \frac{3}{2} \frac{R}{M_s}$$

and

$$c_{vs}^{rot} = \frac{R}{M_s}$$

assuming linear polyatomic species. The vibrational energy per unit mass of species s is defined by the harmonic oscillator model of molecular motion and assumes a Boltzmann distribution of vibrational states. The formula for this energy is

$$e_{vs} = \frac{R}{M_s} \sum_{m=1}^{nms} \frac{\theta_{v,m}}{\exp(\theta_{v,m}/T_v) - 1},$$

where $\theta_{v,m}$ is the characteristic vibrational temperature for mode m and nms is the number of vibrational modes of species s . Using this formula, a degeneracy is simply counted as another vibrational mode. The formation enthalpy of the species s , h_s° , represents the stored chemical energy of the gas. Because of this, the value of formation enthalpy depends on the molecule and also on the reference enthalpy used. In general, the formation enthalpy reference is based on the state of a pure substance that exists naturally at a standard temperature and pressure, for example 100 *kPa* and 298.15 *K*. An example of a reference substance is diatomic nitrogen or diatomic oxygen, which have an enthalpy of formation of zero.

The species enthalpy is defined as

$$h_s = c_{vs}T + \frac{P_s}{\rho_s} + e_{vs} + h_s^\circ = c_{ps}T + e_{vs} + h_s^\circ,$$

where c_{ps} is the specific heat at constant pressure of species s .

3.1.2 Diffusive Relations

The shear stress tensor is expressed by τ_{ij} and is defined as

$$\tau_{ij} = \mu \left(\frac{\partial u_i}{\partial x_j} + \frac{\partial u_j}{\partial x_i} - \frac{2}{3} \frac{\partial u_k}{\partial x_k} \delta_{ij} \right),$$

where μ is the dynamic viscosity of the mixture. In the shear stress equation, Stokes hypothesis has been used to determine the bulk viscosity of the gas, which is

$$2\mu + 3\lambda = 0.$$

The heat flux vector, q_i , is defined using Fourier's Law, which is

$$q_i = -\kappa \frac{\partial T}{\partial x_i} = -(\kappa_{tr} + \kappa_{rot}) \frac{\partial T}{\partial x_i},$$

$$q_{v,i} = -\kappa_v \frac{\partial T}{\partial x_i}$$

where κ is the translational-rotational heat conductivity of the gas mixture considered and κ_v is the vibrational heat conductivity. We define the mixture diffusive relations using Wilke's mixing rule

$$\mu = \sum_s \frac{\mu_s X_s}{\phi_{w,s}} ; \kappa_r = \sum_s \frac{\kappa_{r,s} X_s}{\phi_{w,s}}$$

$$c_s = \frac{\rho_s}{\rho} ; X_s = \frac{c_s M}{M_s} ; M = \left(\sum_s \frac{c_s}{M_s} \right)^{-1}$$

$$\phi_{w,s} = \sum_r X_r \left[1 + \sqrt{\frac{\mu_s}{\mu_r}} \left(\frac{M_r}{M_s} \right)^{1/4} \right]^2 \left(8 \left(1 + \frac{M_s}{M_r} \right) \right)^{-1/2},$$

where the species viscosity is given by Blottner's formula

$$\mu_s = 0.1 \exp((A_s \ln T + B_s) \ln T + C_s).$$

The species conductivity, $\kappa_{r,s}$, is specified using Eucken's relation for translation, rotation, and vibration which is

$$\kappa_{tr,s} = \frac{5}{2} \mu_s c_{vs}, \quad \kappa_{rot,s} = \mu_s c_{vs}, \quad \kappa_{v,s} = \mu_s c_{vvs},$$

respectively. The vibrational specific heat at constant volume is determined by

$$c_{vvs} = \frac{\partial e_{vs}}{\partial T_v}.$$

The species diffusion velocity, v_{si} , is determined by Fick's law which is

$$\rho_s v_{si} = -\rho D_{sr} \frac{\partial}{\partial x_i} \left(\frac{\rho_s}{\rho} \right),$$

where D_{sr} is the binary diffusion constant. In general, the binary diffusion constant depends on both the species diffusing, s , and the species through which it is diffusing, r . However, for the current study, we assume that the binary diffusion coefficients for each species are equal for a given gas mixture. This coefficient, D , is derived from the Lewis number, which is

$$Le = \frac{\kappa}{\rho c_p D},$$

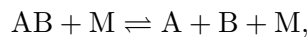
where c_p and κ are based on the gas mixture. The mixture value of c_p is determined using a mass-weighted average

$$\phi = \sum_s^{ns} \phi_s \frac{\rho_s}{\rho}.$$

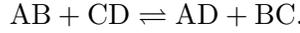
Mixture properties such as c_v , h° , and e_v are also calculated using a mass-weighted average.

3.1.3 Chemical Source Terms

For this work we only consider dissociation reactions and exchange reactions. A dissociation reaction has the form



where M is an arbitrary collision partner that facilitates the chemical reaction. The exchange reaction has the form



To determine the rate at which each reaction progress given the state of a gas mixture, we use the Arrhenius form governed by the forward and backward rate coefficients, k_f and k_b , respectively. For a dissociation reaction, the rate is defined as

$$R_{diss} = \sum_m k_{fm} [\text{AB}][\text{M}] - k_{bm} [\text{A}][\text{B}][\text{M}] = \sum_m k_{fm} \frac{\rho_{\text{AB}}}{M_{\text{AB}}} \frac{\rho_m}{M_m} - k_{bm} \frac{\rho_{\text{A}}}{M_{\text{A}}} \frac{\rho_{\text{B}}}{M_{\text{B}}} \frac{\rho_m}{M_m}. \quad (3.7)$$

For an exchange reaction, the rate is defined as

$$R_{exch} = k_f [\text{AB}][\text{CD}] - k_b [\text{AD}][\text{BC}] = k_f \frac{\rho_{\text{AB}}}{M_{\text{AB}}} \frac{\rho_{\text{CD}}}{M_{\text{CD}}} - k_b \frac{\rho_{\text{AD}}}{M_{\text{AD}}} \frac{\rho_{\text{BC}}}{M_{\text{BC}}}. \quad (3.8)$$

The source terms, w_s , are determined by summing the reaction rates multiplied by the signed stoichiometric coefficient of species s , ν_{sr} , over all reactions, which is written as

$$w_s = M_s \sum_r \nu_{sr} R_r,$$

If a species is a reactant in the reaction, the sign of ν_{sr} is negative, whereas ν_{sr} for a product species is positive. For example, in the dissociation of N_2 ,



the signed stoichiometric coefficient of N_2 would be -1 and the coefficient of N would be 2 .

The chemical rate coefficients, k_f and k_b , are determined based on Park's model[112, 113] for vibration-dissociation coupling, which has become known as the T-Tv model. Using this model, the forward rate coefficients are based on the modified Arrhenius form:

$$k_f(T) = C_f T^\eta \exp\left(-\frac{\theta}{T}\right),$$

where C_f is the collision coefficient, η is simply an exponential coefficient for a varying temperature dependence, and θ is related to the activation energy of the reaction through Boltzmann's constant. These coefficients are determined empirically and are obtained from several different sources

[112, 114, 115, 116]. For dissociation reactions, the forward rates are dependent on an effective temperature, T_{eff} , which is the geometric mean of the translational-rotational temperature and the vibrational temperature, or

$$T_{eff} = \sqrt{T \cdot T_v},$$

while exchange and ionization reactions, the rates are dependent only on the translational-rotational temperature. Additionally, the collision coefficient depends both on the reacting species and the collision partner. Because of this, the dissociation reactions may have a different collision coefficient for each collision partner.

The backward rates are determined through the equilibrium constant, K_{eq} , which is

$$K_{eq} = \frac{k_f}{k_b}.$$

In all reactions, the equilibrium constant is calculated using only the translational-rotational temperature. Park's 1990[112] empirical fit equation is used to determine the value of the equilibrium constant,

$$K_{eq} = C \exp(A_1 z^{-1} + A_2 + A_3 \ln z + A_4 z + A_5 z^2),$$

where $z = 10000/T$, C is a pre-exponential factor used for unit conversions, and A_i are empirical fit coefficients. For most reactions used in this work, these fit coefficients are taken from Park[112], however, some are created by matching the equilibrium constants generated using data from McBride et al.[117].

3.1.4 Vibrational Source Terms

The translational-vibrational energy exchange rate for a vibrational mode m is calculated using the Landau-Teller model, which is given by the formula

$$Q_{t-v,m} = \rho_m \frac{e_{vm}^*(T) - e_{vm}(T_v)}{\langle \tau_m \rangle},$$

where $e_{vm}^*(T)$ is the local equilibrium vibration energy, while $e_{vm}(T_v)$ is the current vibrational energy. The species averaged relaxation time is

$$\langle \tau_m \rangle = \frac{\sum_s [S]}{\sum_s [S]/\tau_{ms}} = \frac{1}{\sum_s X_s/\tau_{ms}},$$

where $[S]$ is the molar concentration of species s , X is the mole fraction of species s , and τ_{ms} is the inter-species relaxation times, which are based on Millikan and White's semi-empirical curve first, which are

$$\tau_{ms}P = \exp\left(A_{ms}\left(T^{-1/3} - 0.015\mu_{ms}^{1/4}\right) - 18.42\right),$$

$$A_{ms} = 1.16 \times 10^{-3} \mu_{ms}^{1/2} \theta_{v,m}^{4/3},$$

$$\mu_{ms} = \frac{M_m M_s}{M_m + M_s}.$$

In this equation, P is the gas pressure and has units of atmospheres and μ_{ms} is the reduced mass of the collision partners. In general, these formulas are used, however, some species interactions have empirical corrections to the relaxation times[118, 119].

3.2 Review of Parabolized Stability Equations

For the current work, the stability analyses are performed using PSE-Chem solver contained in the software suite called STABL (Stability and Transition Analysis for hypersonic Boundary Layers) written by Dr. Heath Johnson. PSE-Chem solves the two-dimensional Cartesian and axi-symmetric linear parabolized stability equations and includes the effects of chemical reactions and translational-vibrational energy exchange. The parabolized stability equation set is derived by representing the state variables of a flow by a steady mean flow and a disturbance,

$$\phi = \phi_0 + \phi',$$

where ϕ is a state variable of the gas, $()_0$ represents the mean flow component, and $()'$ represents the disturbance component. After substituting this decomposition into the Navier-Stokes equations, the components describing the evolution of the mean flow are subtracted from the equation set and the equations governing the disturbance evolution are left. At this point, the linear and non-linear disturbance components are separated. Although these equations can be solved when retaining the non-linear disturbance components, PSE-Chem solver eliminates the non-linear terms. The rationale and consequences for modeling only the linear disturbance terms are discussed in Section 2.1.1.

The disturbance variables are modeled by a oscillatory wave component and a slowly varying shape function as in

$$\phi' = \chi(x_1, x_2) \exp(i(\beta x_3 - \omega t)),$$

where the shape function is χ , the frequency is ω , and the spanwise wavenumber is β . Because PSE-Chem performs spatial stability analysis, both the frequency and spanwise wavenumbers are real. The growth of disturbances is modeled in the shape function, which is

$$\chi(x_1, x_2) = \psi(x_1, x_2) \exp(i\theta(x_1)),$$

where ψ is a normalized shape function and θ is the wave potential. The complex streamwise wave number, α , is related to the wave potential by

$$\frac{\partial \theta}{\partial x_1} = \alpha.$$

The downstream evolution of the disturbance amplitude is governed by the complex component of the streamwise wave number.

The equation set is parabolized by retaining only first-order derivatives in the streamwise direction of the shape function, ψ , and assuming higher-order streamwise derivatives are approximately zero. This step yields a nearly parabolic system, however, it still allows for an upstream-traveling characteristic in the subsonic region of the boundary layer. To suppress this characteristic and allow for stable downstream marching, the streamwise pressure gradient is damped depending on the local mach number. By only damping the streamwise direction the elliptic nature of the wave in the wall-normal direction is preserved. Further details discussing the pressure gradient suppression are available in Herbert[52] and Johnson[120].

The governing equations used for a quasi-parallel linear stability analysis are obtained by eliminating the dependence of the shape function, ψ , on the streamwise direction entirely. The analysis is considered quasi-parallel because the mean flow contains non-parallel flow, while the stability analysis assumes parallel flow, allowing for the estimation of the disturbance growth at a single streamwise location. Obtaining a disturbance growth estimation is useful because it quickly provides a map of amplification versus frequency along the streamwise direction (called a linear stability diagram) as well as the initial guess used in the PSE marching scheme.

As previously stated, the transition prediction using PSE-Chem is based on the semi-empirical e^N method, which uses experimentally measured transition locations to estimate where the calculated disturbance growth rate will cause transition. The N factor is calculated for a certain frequency at

a distance along the vehicle using the formula

$$N = \int_{s_0}^s \sigma d\zeta,$$

where s_0 is the first neutral location for the disturbance, s is the current surface distance, and σ is the disturbance growth. The disturbance growth is calculated using the following formula

$$\sigma = -Im(\alpha) + \frac{1}{2E} \frac{dE}{d\zeta},$$

where E is the disturbance kinetic energy and is calculated as

$$E = \int_n \rho_0 \left(|u'|^2 + |v'|^2 + |w'|^2 \right) d\eta.$$

The inclusion of the integrated disturbance kinetic energy is included to account for changes in the shape function as the disturbance evolves downstream. This discussed in better detail in Johnson[120]. For a more detail explanation of the stability analysis, the reader is referred to the works by Herbert[52], Johnson[120], Johnson and Candler[121] and Johnson et al.[122].

The viscosity for each species is calculated using a composition of various models, each appropriate for a different temperature range. The models are unified using blending functions to maintain continuity for both the value and derivative value of viscosity. The conductivity is calculated using Eucken's relation. The mixture quantities are then calculated using Wilke's semi-empirical mixing law. It is assumed that vibrational-vibrational energy exchanges happen on a relatively short time scale and thus are in equilibrium and governed by a single temperature, T_v . It is also assumed that rotation and translation are coupled and are governed by the translational temperature. The translational-vibrational energy exchanges are governed by the Laudau-Teller model. The characteristic relaxation times are based on the Millikan and White model.

3.3 General Procedure for Acoustic Wave Equations

The method to determine the acoustic wave formulation through a gas in equilibrium is to linearize the reacting Euler equations to a disturbance of all the properties that define the gas. Traditionally, an acoustic analysis is performed without viscous effects because the perturbations caused by the acoustic wave are sufficiently small that viscous damping is usually minimal. A test case of using

carbon dioxide with a temperature of 1000 K , a density of 0.1 kg/m^3 , and a frequency of 100 kHz was performed and found that the effect of viscosity was to cause a damping rate of 0.5 percent per wavelength, which is relatively small relative to the potential damping caused by an internal molecular process. Additionally, eliminating viscous effects allows for a more focused study of the acoustic interaction with an internal molecular process.

The properties that define the gas in the current study include density (ρ), pressure (p), velocity (u), enthalpy (h), and non-equilibrium variables (\vec{q}). The non-equilibrium variables include vibrational energy (e_v) and/or the extent of reaction for a dissociating gas (α). Temperature is solved for by using the ideal gas law. The momentum equations are used for generating a relationship between velocity disturbances and pressure disturbances. Then the mass conservation equation is used to determine the relationship between total density and velocity, which leads to the relationship between density and pressure. The relationship effectively defines the speed of the acoustic wave. Using the state equation for enthalpy, the enthalpy disturbance is rewritten in terms of pressure, density, and non-equilibrium variables. With this, the wave number is solved for using the conservation of enthalpy equation. Disturbance quantities are denoted with a prime ((\prime)) and mean properties are denoted with a subscript zero ($(\prime)_0$). All variables are assumed to be complex, while the physical form of the wave is the real value of the solution. The disturbance equations are

$$\frac{\partial \rho'}{\partial t} + U_{0,i} \frac{\partial \rho'}{\partial x_i} + \rho_0 \frac{\partial u'_i}{\partial x_i} = 0, \quad (3.9)$$

$$\rho_0 \frac{\partial u'_i}{\partial t} + \rho_0 U_{0,j} \frac{\partial u'_i}{\partial x_j} + \frac{\partial p'}{\partial x_i} = 0, \quad (3.10)$$

$$\rho_0 \frac{\partial h'}{\partial t} + \rho_0 U_{0,j} \frac{\partial h'}{\partial x_j} - \frac{\partial p'}{\partial t} - U_{0,j} \frac{\partial p'}{\partial x_j} = 0, \quad (3.11)$$

where h' is defined as

$$h' = \left. \frac{\partial h}{\partial p} \right|_{p_0} p' + \left. \frac{\partial h}{\partial \rho} \right|_{\rho_0} \rho' + \left. \frac{\partial h}{\partial q_i} \right|_{q_{i,0}} q'_i. \quad (3.12)$$

A general non-equilibrium relaxation process obeys

$$\frac{\partial q'_j}{\partial t} + U_{0,k} \frac{\partial q'_j}{\partial x_k} = \mathbf{A} (q_i^{*'} - q'_i), \quad (3.13)$$

where

$$q_i^{*'} = \left. \frac{\partial q_i^*}{\partial p} \right|_{p_0} p' + \left. \frac{\partial q_i^*}{\partial \rho} \right|_{\rho_0} \rho'. \quad (3.14)$$

In Equation 3.13, the mean density coefficient on the material derivative seen in Equation 3.10 and Equation 3.11 cancels due to the equilibrium state of the mean flow. In Equation 3.14, the superscript * denotes the equilibrium value under the current pressure and density. The \mathbf{A} is a matrix related to the inverse of relaxation time, defined as

$$\mathbf{A} \equiv -\frac{\partial}{\partial q_j} \left(\frac{\partial q_i}{\partial t} \right) = A_{ij} \quad \sim \frac{1}{\tau}. \quad (3.15)$$

The perturbation in the relaxation time of a non-equilibrium process is assumed to be negligible. The disturbance equation of state is given by

$$\frac{dT}{T} = \frac{dp}{p} - \frac{d\rho}{\rho} - M_{mix} \sum_i \sum_j \nu_{ij} d\alpha_i. \quad (3.16)$$

3.3.1 Fujii's method : Streamfunction Approach

Following Vincenti and Kruger[62], Fujii[5] solved the acoustic disturbance equations using a streamfunction. A derivation using Fujii's method has been included below.

We restrict the equation set to one-dimensional planar sound propagation through a static gas ($U_{0,j} = 0$). In order to eliminate p' and u' , we introduce a function ψ and make the following relationships

$$p' = -\rho_0 \frac{\partial \psi}{\partial t}, \quad u' = \frac{\partial \psi}{\partial x}. \quad (3.17)$$

Using these relationships, Equation 3.10 becomes

$$\rho_0 \frac{\partial^2 \psi}{\partial t \partial x} - \rho_0 \frac{\partial^2 \psi}{\partial t \partial x} = 0.$$

Equation 3.9 becomes

$$\frac{\partial \rho'}{\partial t} = -\rho_0 \frac{\partial^2 \psi}{\partial x^2}.$$

Differentiating Equation 3.12 with respect to time, we obtain

$$\frac{\partial h'}{\partial t} = \frac{\partial h}{\partial p} \Big|_{p_0} \frac{\partial p'}{\partial t} + \frac{\partial h}{\partial \rho} \Big|_{\rho_0} \frac{\partial \rho'}{\partial t} + \frac{\partial h}{\partial q_i} \Big|_{q_{i,0}} \frac{\partial q'_i}{\partial t}.$$

After substituting for the pressure disturbance in Equation 3.11,

$$\frac{\partial h'}{\partial t} = \frac{1}{\rho_0} \frac{\partial p'}{\partial t} = -\frac{\partial^2 \psi}{\partial t^2},$$

we have

$$-\frac{\partial^2 \psi}{\partial t^2} = -\rho_0 \frac{\partial h}{\partial p} \Big|_{p_0} \frac{\partial^2 \psi}{\partial t^2} - \rho_0 \frac{\partial h}{\partial \rho} \Big|_{\rho_0} \frac{\partial^2 \psi}{\partial x^2} + \frac{\partial h}{\partial q_i} \Big|_{q_{i,0}} \frac{\partial q'_i}{\partial t}. \quad (3.18)$$

Differentiating Equation 3.13 with respect to time, we obtain

$$\frac{\partial}{\partial t} \left(\frac{\partial q'_j}{\partial t} \right) = \mathbf{A} \left(\frac{\partial q_{i,0}^*}{\partial t} - \frac{\partial q'_i}{\partial t} \right),$$

and substituting in Equation 3.14

$$\frac{\partial}{\partial t} \left(\frac{\partial q'_j}{\partial t} \right) = \mathbf{A} \left(-\rho_0 \frac{\partial q_{i,0}^*}{\partial p} \Big|_{p_0} \frac{\partial^2 \psi}{\partial t^2} - \rho_0 \frac{\partial q_{i,0}^*}{\partial \rho} \Big|_{\rho_0} \frac{\partial^2 \psi}{\partial x^2} - \frac{\partial q'_i}{\partial t} \right). \quad (3.19)$$

After rearranging Equation 3.18, we have

$$\frac{1 - \rho_0 \frac{\partial h}{\partial p} \Big|_{p_0}}{\rho_0 \frac{\partial h}{\partial \rho} \Big|_{\rho_0}} \frac{\partial^2 \psi}{\partial t^2} - \frac{\partial^2 \psi}{\partial x^2} + \frac{1}{\rho_0 \frac{\partial h}{\partial \rho} \Big|_{\rho_0}} \frac{\partial h}{\partial q_i} \Big|_{q_{i,0}} \frac{\partial q'_i}{\partial t} = 0. \quad (3.20)$$

Assuming the frequencies for the fluctuation q'_i and ψ to be identical, we can make the following relationships

$$\frac{\partial \vec{q}'}{\partial t} = \tilde{\mathbf{f}}(x) \exp(i\omega t), \quad (3.21)$$

$$\psi = g(x) \exp(i\omega t). \quad (3.22)$$

Substituting these relationships into Equations 3.18 and 3.19, we have

$$(i\omega I_{ji} + A_{ji}) \mathbf{f}_i = A_{ji} \left(\rho_0 \omega^2 g \frac{\partial q_{i,0}^*}{\partial p} \Big|_{p_0} - \rho_0 \frac{\partial^2 g}{\partial x^2} \frac{\partial q_{i,0}^*}{\partial \rho} \Big|_{\rho_0} \right) \quad (3.23)$$

and

$$-\left(\frac{1 - \rho_0 \frac{\partial h}{\partial p} \Big|_{p_0}}{\rho_0 \frac{\partial h}{\partial \rho} \Big|_{\rho_0}}\right) \omega^2 g - \frac{\partial^2 g}{\partial x^2} + \frac{1}{\rho_0 \frac{\partial h}{\partial \rho} \Big|_{\rho_0}} \frac{\partial h}{\partial q_i} \Big|_{q_{0,i}} f_i = 0. \quad (3.24)$$

We now make the assumption that

$$g = C \exp(Dx), \quad (3.25)$$

$$\psi = C \exp\left(-\frac{2\pi \operatorname{Re}(D)x}{\operatorname{Im}(D)\lambda}\right) \exp\left(i\omega\left(t + \frac{\operatorname{Im}(D)x}{\omega}\right)\right), \quad (3.26)$$

where

$$\lambda = \frac{a}{f} = -\frac{2\pi(\omega/\operatorname{Im}(D))}{\omega}.$$

Solving for f_i in Equation 3.23,

$$f_i = (i\omega I_{ji} + A_{ji})^{-1} A_{ji} \left(\rho_0 \omega^2 g \frac{\partial q_i^*}{\partial p} \Big|_{p_0} - \rho_0 g'' \frac{\partial q_i^*}{\partial \rho} \Big|_{\rho_0} \right),$$

and substituting this into Equation 3.24, we obtain

$$-\left(\frac{\frac{1}{\rho_0} - \frac{\partial h}{\partial p} \Big|_{p_0}}{\frac{\partial h}{\partial \rho} \Big|_{\rho_0}}\right) \omega^2 - D^2 + \frac{1}{\frac{\partial h}{\partial \rho} \Big|_{\rho_0}} \frac{\partial h}{\partial q_i} \Big|_{q_{i,0}} (i\omega I_{ji} + A_{ji})^{-1} A_{ji} \left(\omega^2 \frac{\partial q_i^*}{\partial p} \Big|_{p_0} - D^2 \frac{\partial q_i^*}{\partial \rho} \Big|_{\rho_0} \right) = 0.$$

From this version of the conservation of enthalpy equation, we can solve for the wave number and determine the dispersion relation for the acoustic wave. This is

$$D^2 = \frac{-\omega^2 \left(\frac{1}{a_f^2} - \frac{1}{\frac{\partial h}{\partial \rho} \Big|_{\rho_0}} \frac{\partial h}{\partial q_i} \Big|_{q_{i,0}} (i\omega I_{ji} + A_{ji})^{-1} A_{ji} \frac{\partial q_i^*}{\partial p} \Big|_{p_0} \right)}{1 + \frac{1}{\frac{\partial h}{\partial \rho} \Big|_{\rho_0}} \frac{\partial h}{\partial q_i} \Big|_{q_{i,0}} (i\omega I_{ji} + A_{ji})^{-1} A_{ji} \frac{\partial q_i^*}{\partial \rho} \Big|_{\rho_0}}. \quad (3.27)$$

We have simplified this equation using the relationship for the frozen speed of sound,

$$a_f^2 = \frac{\left. \frac{\partial h}{\partial \rho} \right|_{p_0}}{\left. \frac{1}{\rho_0} - \frac{\partial h}{\partial p} \right|_{p_0}}, \quad (3.28)$$

given in Vincenti and Kruger on page 256. Fujii notes that Equation 3.27 reduces to

$$D^2 = \frac{-\omega^2 (\omega\tau^+ + 1)}{i\omega\tau^+ a_f^2 + a_e^2} = \frac{-\omega^2}{a_e^2} \left[\frac{1 + X (\omega\tau^+)}{1 + X^2 (\omega\tau^+)^2} + i \frac{(1 - X) \omega\tau^+}{1 + X^2 (\omega\tau^+)^2} \right], \quad (3.29)$$

for a single relaxation mode, where

$$\tau^+ = \frac{\tau \left(\frac{\partial h}{\partial p} - \frac{1}{\rho} \right)}{\frac{\partial h}{\partial p} + \frac{\partial h}{\partial q_i} \frac{\partial q_i^*}{\partial p} - \frac{1}{\rho}}$$

and a_e is the equilibrium speed of sound, which is defined as

$$a_e^2 = - \frac{\frac{\partial h}{\partial p} + \frac{\partial h}{\partial q_i} \frac{\partial q_i^*}{\partial p}}{\frac{\partial h}{\partial p} + \frac{\partial h}{\partial q_i} \frac{\partial q_i^*}{\partial p} - \frac{1}{\rho}}, \quad (3.30)$$

and X is defined as the square of the ratio of the frozen to the equilibrium speed of sound,

$$X \equiv \left(\frac{a_f}{a_e} \right)^2.$$

Fujii also notes that the sign of $\frac{\text{Re}(D)}{\text{Im}(D)}$, which determines whether the relaxation mode acts as a damping or amplifying force, depends on the sign of $1 - X$, or $a_e - a_f$. Fujii also shows that

$$\frac{\text{Re}(D)}{\text{Im}(D)} \begin{cases} > 0 & (a_f > a_e) \Rightarrow \text{damping} \\ < 0 & (a_f < a_e) \Rightarrow \text{amplifying} \end{cases}.$$

3.3.2 Balakumar's Formulation : Frozen Acoustic Wave

Rather than use a streamfunction, ψ , as Fujii did, Balakumar[68] formulated his acoustic wave as being driven by a pressure disturbance, which results in changes to all of the other flow variables. Balakumar includes a mean flow velocity and assumes the wave is frozen with respect to chemical and vibrational modes. Thus, we only use Eqs. 3.9-3.12 due to the non-equilibrium variables, q'_i ,

being equal to zero. In this analysis, the pressure disturbance takes the form

$$p' = \tilde{p}_{ac} \exp(\iota(k_i x_i - \omega t)), \quad (3.31)$$

where p' is the pressure disturbance amplitude, ι is the unit imaginary number, k_i is the wave number vector, x_i is the vector of spatial dimensions, ω is the corresponding angular frequency.[68, 69] The value of \tilde{p}_{ac} is a specified fraction of the freestream pressure. Since the gas is frozen, this disturbance has an instant effect on the other variables, as in

$$\begin{pmatrix} \rho' \\ u'_j \\ T' \end{pmatrix} = \begin{pmatrix} \frac{\partial \rho}{\partial p} \\ \frac{\partial u_j}{\partial p} \\ \frac{\partial T}{\partial p} \end{pmatrix} p' = \begin{pmatrix} \frac{\partial \rho}{\partial p} \\ \frac{\partial u_j}{\partial p} \\ \frac{\partial T}{\partial p} \end{pmatrix} p_{ac} \exp(\iota(k_i x_i - \omega t)), \quad (3.32)$$

implying that all disturbance properties are dependent on the same radian frequency, ω . No internal modes are present to cause a phase shift in the wave. Starting with Equation 3.9, we obtain

$$\rho' = -u'_i \left(\frac{k_i}{(U_{0,j} k_j - \omega)} \right). \quad (3.33)$$

Moving to Equation 3.10, we can solve for u'_i in terms of p' as

$$u'_i = -\frac{k_i}{\rho_0 (U_{0,j} k_j - \omega)} p'. \quad (3.34)$$

After substituting this into Equation 3.33, we obtain

$$\rho' = \frac{k_i k_i}{(U_{0,j} k_j - \omega)^2} p'. \quad (3.35)$$

In this case, the enthalpy is defined by

$$h = c_v T + \frac{p}{\rho},$$

which implies

$$dh = c_p dT.$$

Using a reduced form Equation 3.16, this equation becomes

$$dh = c_p T \left(\frac{dP}{P} - \frac{d\rho}{\rho} \right) = \frac{a_f^2}{(\gamma - 1)} \left(\frac{dP}{P} - \frac{d\rho}{\rho} \right). \quad (3.36)$$

From this we have

$$h' = \frac{a_f^2}{(\gamma - 1)} \left(\frac{1}{p_0} - \frac{k_i k_i}{(U_{0,j} k_j - \omega)^2 \rho_0} \right) p'.$$

After substituting this into Equation 3.11, we obtain

$$(U_{0,j} k_j - \omega)^2 = k_i k_i a_f^2. \quad (3.37)$$

The equation constitutes the dispersion relation between the frequency ω and the wavenumber magnitude $|k_i|$. The individual components of the wave, k_i , are determined by the direction of the planar wave given as a set of direction cosines, fcs_i , which is

$$k_i = |k_i| fcs_i.$$

Lastly, the temperature relation is solved for by using the ideal gas law, given by Eq. 3.16. For a frozen wave this equation reduces to

$$\frac{dT}{T} = \frac{dp}{p} - \frac{d\rho}{\rho}, \quad (3.38)$$

making a disturbance in temperature related to a disturbance in pressure and density

$$\frac{T'}{T_0} = \frac{p'}{p_0} - \frac{\rho'}{\rho_0}. \quad (3.39)$$

Substituting in the Eq. 3.35, we can derive the relationship between a disturbance in pressure and temperature as

$$T' = \frac{T_0 (\gamma - 1)}{\rho_0 a_f^2} p' \quad (3.40)$$

Now that we have solved for all of the values in Eqs.3.32, we can write out the functional form

of the frozen acoustic wave

$$\begin{pmatrix} \rho' \\ u' \\ v' \\ w' \\ T' \end{pmatrix} = \begin{pmatrix} \frac{1}{a_f^2} \\ \frac{-k_1}{\rho_0(U_{0,j}k_j - \omega)} \\ \frac{-k_2}{\rho_0(U_{0,j}k_j - \omega)} \\ \frac{-k_3}{\rho_0(U_{0,j}k_j - \omega)} \\ \frac{(\gamma-1)T_0}{\rho_0 a_f^2} \end{pmatrix} p'. \quad (3.41)$$

3.4 Generalization of Balakumar's Formulation

We can now use Fujii's analysis with the full reacting Euler equations for an acoustic disturbance using Balakumar's pressure disturbance as the driver of the system's disturbances. Starting with Eq. 3.31, our disturbance system becomes the following:

$$\begin{pmatrix} \rho' \\ u'_j \\ T' \\ q'_i \end{pmatrix} = \begin{pmatrix} \frac{\partial \rho}{\partial p} \\ \frac{\partial u_j}{\partial p} \\ \frac{\partial T}{\partial p} \\ \frac{\partial q_i}{\partial p} \end{pmatrix} p' = \begin{pmatrix} \frac{\partial \rho}{\partial p} \\ \frac{\partial u_j}{\partial p} \\ \frac{\partial T}{\partial p} \\ \frac{\partial q_i}{\partial p} \end{pmatrix} p_{ac} \exp(i(k_i x_i - \omega t)) \quad (3.42)$$

Because the conservation of mass and momentum equations do not change, the relationships in Eqs. 3.33, 3.34, and 3.35 remain the same. Following the order of Fujii's analysis, we first apply the pressure disturbance to the non-equilibrium process equation, Eq. 3.13, which looks as

$$q'_i = ((U_{0,j}k_j - \omega) \mathbf{iI} + \mathbf{A})^{-1} \mathbf{A} \left(\frac{\partial q_i^*}{\partial p} \Big|_{p_0} + \frac{\partial q_i^*}{\partial \rho} \Big|_{\rho_0} \frac{k_i k_i}{(U_{0,j}k_j - \omega)^2} \right) p'. \quad (3.43)$$

The imaginary component of these equations describes the phase shift that occurs when a non-equilibrium process lags the pressure wave.

With the addition of the non-equilibrium processes and after substituting the equation for the

frozen speed of sound, Eq. 3.28, the enthalpy equation, Eq. 3.11, becomes

$$\frac{\partial \rho}{\partial p} = \frac{\frac{1}{a_f^2} - \frac{\partial h}{\partial q_i} \Big|_{q_{i,0}} \left(\frac{\partial h}{\partial \rho} \Big|_{\rho_0} \right)^{-1} ((U_{0,j} k_j - \omega) \mathbf{I} + \mathbf{A})^{-1} \mathbf{A} \frac{\partial q_i^*}{\partial p} \Big|_{p_0}}{1 + \frac{\partial h}{\partial q_i} \Big|_{q_{i,0}} \left(\frac{\partial h}{\partial \rho} \Big|_{\rho_0} \right)^{-1} ((U_{0,j} k_j - \omega) \mathbf{I} + \mathbf{A})^{-1} \mathbf{A} \frac{\partial q_i^*}{\partial p} \Big|_{p_0}}. \quad (3.44)$$

Equation 3.44 describes the wave speed of an acoustic wave through a gas in the familiar form of $\frac{\partial p}{\partial \rho} \Big|_s$. To solve for the wavenumber, we substitute in the known relationship for $\frac{\partial \rho}{\partial p}$, derived in Eq. 3.35, which is

$$\frac{k_i k_i}{(U_{0,j} k_j - \omega)^2} = \frac{\frac{1}{a_f^2} - \frac{\partial h}{\partial q_i} \Big|_{q_{i,0}} \left(\frac{\partial h}{\partial \rho} \Big|_{\rho_0} \right)^{-1} ((U_{0,j} k_j - \omega) \mathbf{I} + \mathbf{A})^{-1} \mathbf{A} \frac{\partial q_i^*}{\partial p} \Big|_{p_0}}{1 + \frac{\partial h}{\partial q_i} \Big|_{q_{i,0}} \left(\frac{\partial h}{\partial \rho} \Big|_{\rho_0} \right)^{-1} ((U_{0,j} k_j - \omega) \mathbf{I} + \mathbf{A})^{-1} \mathbf{A} \frac{\partial q_i^*}{\partial p} \Big|_{p_0}}. \quad (3.45)$$

Now we have an equation to solve for the dispersion relation between the frequency ω and the wave number k_i . Because this equation is cubic in k_i , three solutions exist to this dispersion relation. These solutions include a slow wave, with a propagation speed of $c_{slow} = |U_0| - a$, a fast wave, $c_{fast} = |U_0| + a$, and an unknown third solution. Further research is required to identify the physical nature of this third solution.

As in the frozen case, we summarize the relationship of acoustic wave in reacting flow with a mean flow velocity in Equations 3.46. A full description of the terms and dependencies used in the acoustic wave formulation is contained in the appendix.

$$\left\{ \begin{array}{c} \rho' \\ u' \\ v' \\ w' \\ T' \\ q' \end{array} \right\} = \left\{ \begin{array}{c} \frac{k_i k_i}{(U_{0,j} k_j - \omega)^2} \\ \frac{-k_1}{\rho_0 (U_{0,j} k_j - \omega)} \\ \frac{-k_2}{\rho_0 (U_{0,j} k_j - \omega)} \\ \frac{-k_3}{\rho_0 (U_{0,j} k_j - \omega)} \\ \frac{T}{p} - \frac{T}{\rho} \frac{\partial \rho}{\partial p} - T M_{mix} \sum_i \sum_j \nu_{ij} \frac{\partial \alpha_i}{\partial p} \\ ((U_{0,j} k_j - \omega) \mathbf{I} + \mathbf{A})^{-1} \mathbf{A} \left(\frac{\partial q_i^*}{\partial p} \Big|_{p_0} + \frac{\partial q_i^*}{\partial \rho} \Big|_{\rho_0} \frac{k_i k_i}{(U_{0,j} k_j - \omega)^2} \right) \end{array} \right\} p'. \quad (3.46)$$

3.5 Transient Growth Formulation

3.5.1 Disturbance Equations

The equations of the transient growth disturbance are derived from the Navier-Stokes equations by separating the instantaneous flow into a mean component and a fluctuating or disturbance component and then linearizing the equations. For the following derivation mean properties are represented by $()_0$ and the disturbance properties are represented by $()'$. These properties which define the flow are as follows

$$\phi' = (\rho'_s, u'_i, T', T'_v)^T$$

The conservation of mass equation becomes

$$\frac{\partial}{\partial t} \left(\frac{\partial \rho}{\partial \phi} \phi' \right) + \frac{\partial}{\partial x_i} (\rho_0 u'_i) + \frac{\partial}{\partial x_i} \left(u_{0,i} \frac{\partial \rho}{\partial \phi} \phi' \right) = 0 \quad (3.47)$$

In this equation, the mean flow properties must still satisfy the Navier-Stokes equations, thus, the terms consisting solely mean flow properties are eliminated. As stated above, this is a linear analysis, therefore disturbance terms of order $()^2$ are approximately zero and are omitted from the derivation. One important aspect of the current notation is that all partial derivatives with respect to ϕ are applied to the mean flow property in the numerator.

After utilizing the Schmidt number, which relates the binary diffusion constant to the molecular viscosity or

$$Sc = -\frac{\mu}{\rho D},$$

and collecting the terms based on the derivatives of the set of disturbance variables, the conservation of species densities becomes

$$\begin{aligned} \frac{\partial \rho'_s}{\partial t} + \frac{\partial}{\partial x_i} (\rho'_s u_{0,i}) + \frac{\partial}{\partial x_i} (\rho_{s,0} u'_i) &= \left(\frac{1}{Sc} \frac{\partial}{\partial x_i} \left(\frac{\partial \mu}{\partial \phi} \frac{\partial c_{s,0}}{\partial x_i} + \mu_0 \frac{\partial}{\partial x_i} \left(\frac{\partial c_s}{\partial \phi} \right) \right) + M_s \sum_r v_{sr} \frac{\partial R_r}{\partial \phi} \right) \phi' \\ &+ \frac{1}{Sc} \left(2\mu_0 \frac{\partial}{\partial x_i} \left(\frac{\partial c_s}{\partial \phi} \right) + \frac{\partial \mu_0}{\partial x_i} \frac{\partial c_s}{\partial \phi} + \frac{\partial \mu}{\partial \phi} \frac{\partial c_{s,0}}{\partial x_i} \right) \frac{\partial \phi'}{\partial x_i} + \frac{1}{Sc} \mu_0 \frac{\partial c_s}{\partial \phi} \frac{\partial^2 \phi'}{\partial x_i^2} \end{aligned} \quad (3.48)$$

To complete this equation we need to expand the three terms that are dependent on multiple disturbance quantities. However, for the sake of brevity, these expansions have been written in the appendix.

The conservation of disturbance momentum equation is

$$\begin{aligned} \frac{\partial}{\partial t} \left(u_{0,i} \frac{\partial \rho}{\partial \phi} \phi' \right) + \frac{\partial}{\partial t} (\rho_0 u'_i) + \frac{\partial}{\partial x_j} \left(u_{0,i} u_{0,j} \frac{\partial \rho}{\partial \phi} \phi' \right) + \frac{\partial}{\partial x_j} (\rho_0 u'_i u_{0,j}) + \frac{\partial}{\partial x_j} (\rho_0 u_{0,i} u'_j) \\ = -\frac{\partial}{\partial x_i} \left(\frac{\partial P}{\partial \phi} \phi' \right) + \frac{\partial}{\partial x_j} \left(\mu_0 \left(\frac{\partial u'_i}{\partial x_j} + \frac{\partial u'_j}{\partial x_i} - \frac{2}{3} \frac{\partial u'_k}{\partial x_k} \delta_{ij} \right) \right) \\ + \frac{\partial}{\partial x_j} \left(\frac{\partial \mu}{\partial \phi} \phi' \left(\frac{\partial u_{0,i}}{\partial x_j} + \frac{\partial u_{0,j}}{\partial x_i} - \frac{2}{3} \frac{\partial u_{0,k}}{\partial x_k} \delta_{ij} \right) \right). \end{aligned} \quad (3.49)$$

To complete this equation, we only need to define the partial derivatives of pressure with respect to the set of disturbance variables. Using the ideal gas law in Eq. 3.6, we have

$$\frac{\partial P}{\partial \phi} = \begin{cases} \frac{R}{M_r} T & \phi = \rho_r; r = 1 \rightarrow ns \\ \sum_s \frac{\rho_s}{M_s} R = \rho \bar{R} & \phi = T \\ 0 & \phi = u_i, T_v \end{cases}.$$

Because the disturbance energy is dependent on ρ'_s , u'_i , T' , and T'_v , a conservation equation of a disturbance in total energy would not be as useful as an equation for a single disturbance property. Since the disturbance temperatures play a minor role in the above equations, it would be beneficial to use the internal enthalpy, which is a function of the translational-rotational temperature and the

vibrational temperature. To obtain this equation, we perform the following steps. First, we derive the conservation of kinetic energy equation by dotting velocity vector with Equation 3.3,

$$\frac{\partial}{\partial t} \left(\frac{1}{2} \rho u_i u_i \right) + \frac{\partial}{\partial x_j} \left(\frac{1}{2} \rho u_i u_i u_j \right) = -u_i \frac{\partial P}{\partial x_i} + \frac{\partial (u_i \tau_{ij})}{\partial x_j} - \tau_{ij} \frac{\partial u_i}{\partial x_j}. \quad (3.50)$$

We then subtract this equation from the conservation of total energy equation, Eq. 3.5 to obtain the conservation of internal enthalpy equation,

$$\begin{aligned} & \frac{\partial}{\partial t} \left(\sum_s \rho_s h_s - P \right) + \frac{\partial}{\partial x_j} \left(u_j \sum_s \rho_s h_s \right) = \\ & u_i \frac{\partial P}{\partial x_i} + \tau_{ij} \frac{\partial u_i}{\partial x_j} - \frac{\partial q_i}{\partial x_i} - \frac{\partial q_{vi}}{\partial x_i} - \frac{\partial}{\partial x_i} \left(\sum_s \rho_s h_s v_{si} \right). \end{aligned} \quad (3.51)$$

From this form of the equation, we can derive the equation for disturbance temperature, which is

$$\begin{aligned} & \frac{\partial}{\partial t} \left(\sum_s \rho'_s h_{s,0} \right) + \frac{\partial}{\partial t} \left(\sum_s \rho_{s,0} \frac{\partial h_s}{\partial \phi} \phi' \right) - \frac{\partial}{\partial t} \left(\frac{\partial P}{\partial \phi} \phi' \right) + \frac{\partial}{\partial x_j} \left(\sum_s (u'_j \rho_{s,0} + u_{0,j} \rho'_s) h_{s,0} \right) \\ & + \frac{\partial}{\partial x_j} \left(u_{0,j} \sum_s \rho_{s,0} \frac{\partial h_s}{\partial \phi} \phi' \right) = u'_j \frac{\partial P_0}{\partial x_i} + u_{0,j} \frac{\partial}{\partial x_i} \left(\frac{\partial P}{\partial \phi} \phi' \right) \\ & + \left(\frac{\partial \mu}{\partial \phi} \phi' \left(\frac{\partial u_{0,i}}{\partial x_j} + \frac{\partial u_{0,j}}{\partial x_i} - \frac{2}{3} \frac{\partial u_{0,k}}{\partial x_k} \delta_{ij} \right) + \mu_0 \left(\frac{\partial u'_i}{\partial x_j} + \frac{\partial u'_j}{\partial x_i} - \frac{2}{3} \frac{\partial u'_k}{\partial x_k} \delta_{ij} \right) \right) \frac{\partial u_{0,i}}{\partial x_j} \\ & - \frac{\partial}{\partial x_i} \left(\frac{\partial \kappa}{\partial \phi} \phi' \frac{\partial T_0}{\partial x_i} \right) - \frac{\partial}{\partial x_i} \left(\kappa_0 \frac{\partial T'}{\partial x_i} \right) - \frac{\partial}{\partial x_i} \left(\frac{\partial \kappa_v}{\partial \phi} \phi' \frac{\partial T_{v,0}}{\partial x_i} \right) - \frac{\partial}{\partial x_i} \left(\kappa_{v,0} \frac{\partial T'_v}{\partial x_i} \right) \\ & + \mu_0 \left(\frac{\partial u_{0,i}}{\partial x_j} + \frac{\partial u_{0,j}}{\partial x_i} - \frac{2}{3} \frac{\partial u_{0,k}}{\partial x_k} \delta_{ij} \right) \frac{\partial u'_i}{\partial x_j} + \frac{\partial}{\partial x_i} \left(\sum_s \frac{1}{S_c} \frac{\partial \mu}{\partial \phi} \phi' \frac{\partial c_{s,0}}{\partial x_i} h_{s,0} \right) \\ & + \frac{\partial}{\partial x_i} \left(\sum_s \frac{1}{S_c} \mu_0 \frac{\partial}{\partial x_i} \left(\frac{\partial c_s}{\partial \phi} \phi' \right) h_{s,0} \right) + \frac{\partial}{\partial x_i} \left(\sum_s \frac{1}{S_c} \mu_0 \frac{\partial c_{s,0}}{\partial x_i} \frac{\partial h_s}{\partial \phi} \phi' \right). \end{aligned} \quad (3.52)$$

As before, the partial derivatives needed to complete this equation are contained in the appendix.

We now apply a linear disturbance to all gas quantities in the conservation of vibrational energy equation and obtain

$$\frac{\partial}{\partial t} \left(\sum_s \rho'_s e_{vs,0} \right) + \frac{\partial}{\partial t} \left(\sum_s \rho_{s,0} c_{vvs} T'_v \right) + \frac{\partial}{\partial x_j} \left(u'_j \sum_s \rho_{s,0} e_{vs,0} \right) + \frac{\partial}{\partial x_j} \left(u_{0,j} \sum_s \rho'_s e_{vs,0} \right)$$

$$\begin{aligned}
& + \frac{\partial}{\partial x_j} \left(u_{0,j} \sum_s \rho_{s,0} c_{vvs} T'_v \right) = - \frac{\partial}{\partial x_i} \left(\frac{\partial \kappa_v}{\partial \phi} \phi' \frac{\partial T_{v,0}}{\partial x_i} \right) - \frac{\partial}{\partial x_i} \left(\kappa_{v,0} \frac{\partial T'_v}{\partial x_i} \right) + \frac{\partial Q_{t-v}}{\partial \phi} \phi' \\
& + \sum_s c_{vvs} T'_v w_{s,0} + \sum_s e_{vs,0} \frac{\partial w_s}{\partial \phi} \phi' + \frac{\partial}{\partial x_i} \left(\sum_s \frac{1}{Sc} \frac{\partial \mu}{\partial \phi} \phi' \frac{\partial c_{s,0}}{\partial x_i} e_{vs,0} \right) \\
& + \frac{\partial}{\partial x_i} \left(\sum_s \frac{1}{Sc} \mu_0 \frac{\partial}{\partial x_i} \left(\frac{\partial c_s}{\partial \phi} \phi' \right) e_{vs,0} \right) + \frac{\partial}{\partial x_i} \left(\sum_s \frac{1}{Sc} \mu_0 \frac{\partial c_{s,0}}{\partial x_i} c_{vvs} T'_v \right). \tag{3.53}
\end{aligned}$$

Finally, we can reduce the disturbance variable set by deriving the disturbance form of the ideal gas law. Starting from Equation 3.6, we have

$$P' = \sum_s \frac{\rho'_s}{M_s} RT_0 + \rho_0 \bar{R} T'. \tag{3.54}$$

3.5.2 Non-Dimensionalization

For this analysis, we are considering compressible flow over a flat plate. This allows us to eliminate several terms from the disturbance equations above. We must non-dimensionalize the equation set to determine which of these terms can be omitted. For a compressible, flat plate boundary layer, it is common[30, 103, 15] to non-dimensionalize the governing equations using a characteristic length along the plate, L , and a characteristic boundary layer height, ε , for spatial dimensions and freestream values for other properties. The boundary layer height is determined by the following relation

$$\varepsilon = \text{Re}^{-1/2} = \sqrt{\frac{\mu_\infty}{\rho_\infty u_\infty L}},$$

where the subscript ∞ denotes a freestream property and Re is the Reynolds number. The freestream velocity does not have a direction index because it is assume that the freestream flow velocity is in only the x_1 direction. The disturbance and mean flow parameters are scaled as

$$\begin{aligned}
& x_i \sim L, \quad i = 1; \quad x_i \sim \varepsilon L, \quad i = 2, 3 \\
& u_{i,0}, u'_i \sim u_\infty, \quad i = 1; \quad u_{i,0}, u'_i \sim \varepsilon u_\infty, \quad i = 2, 3 \\
& \rho_0, \rho', \rho_{s,0}, \rho'_s \sim \rho_\infty; \quad P_0 \sim \rho_\infty u_\infty^2; \quad P' \sim \varepsilon^2 \rho_\infty u_\infty^2 \\
& T_s, T' \sim T_\infty; \quad T_{vs}, T'_v \sim T_{v\infty}; \quad \mu_s, \mu' \sim \mu_\infty.
\end{aligned} \tag{3.55}$$

We assume that the freestream Reynolds number is much larger than one, $\text{Re} \gg 1$, which implies that all terms proportional to $\frac{1}{\text{Re}}$, or ε^2 , are much less than one and can be eliminated from the

disturbance equations. It is also important to note two properties of a flat-plate boundary layer. First, all mean flow properties are constant with respect the spanwise, or z , direction, which means all spanwise derivatives of mean flow properties are zero, including the partial derivatives with respect to ϕ . Second, the mean flow spanwise velocity, w_0 , is equal to zero.

Previous studies[31, 30, 103, 101] have shown the largest gain in disturbance energy is due to disturbances that are periodic in the spanwise direction and do not vary in time or the streamwise direction. Therefore, we assume the disturbances are of the form $a(x, y, z) = \hat{a}(x, y) \exp(\iota\beta z)$, where a is a disturbance variable, \hat{a} is the amplitude function corresponding to a , β is the spanwise wave number, and $\iota = \sqrt{-1}$.

3.5.3 Optimization Method

In order to determine the input disturbance that obtains the largest gain over a specified domain, Andersson et. al[30] rearranged the incompressible governing equations into a form that is easily recognizable as a parabolic system. The form they use is

$$(Af)_x = B_0f + B_1f_y + B_2f_{yy},$$

where f is the vector of disturbance variables, $f = (\hat{u}', \hat{v}', \hat{w}', \hat{P}')^T$ (with the superscript T denoting the transpose), and A , B_0 , B_1 , and B_2 are 4x4 matrices with only real entries. The subscript x and y denote derives in their respective directions. Tumin and Reshotko[15] use a similar form for the compressible governing equations, however, the compressible equations require an extra term, D , and looks like

$$(Af)_x = (Df_y)_x + B_0f + B_1f_y + B_2f_{yy} \quad (3.56)$$

where f is now $f = (\hat{u}', \hat{v}', \hat{w}', \hat{T}', \hat{P}')^T$ and A , B_0 , B_1 , B_2 , and D are 5x5 matrices with only real entries. In both incompressible and compressible cases, the spanwise velocity needs to be redefined as $\hat{w} = \hat{w}\iota$ and the spanwise momentum equation must be multiplied by ι in order to obtain coefficient matrices with only real entries. Redefining the spanwise velocity causes a ninety-degree phase shift on the disturbance wave as compared to other disturbance variables as in

$$\begin{aligned} u' &= \text{Re}(\hat{u}' \exp(\iota\beta z)) = \hat{u}' \cos(\beta z) \\ w' &= \text{Re}(\iota\hat{w}' \exp(\iota\beta z)) \rightarrow \text{Re}(\hat{w}' \exp(\iota\beta z)) = -\hat{w}' \sin(\beta z) \end{aligned} \quad (3.57)$$

We now rearrange the equation set in order to determine the entries of the coefficient matrices. This step is written in detail in the appendix and the our final form of the transient growth disturbance equations is

$$\left(A\hat{\phi}'\right)_x = \left(D\hat{\phi}'_y\right)_x + B_0\hat{\phi}' + B_1\hat{\phi}'_y + B_2\hat{\phi}'_{yy}. \quad (3.58)$$

The optimization procedure is a maximization of the disturbance energy at the output of a specified domain. In previous compressible transient growth studies[15, 101, 98, 102], the Mack energy norm[20]

$$E = \int_0^\infty \left[\rho_0 (\hat{u}'^2 + \hat{v}'^2 + \hat{w}'^2) + \frac{\hat{\rho}'^2 T_0}{\gamma \rho_0 Ma^2} + \frac{\hat{T}'^2 \rho_0}{\gamma (\gamma - 1) T_0 Ma^2} \right] dy \quad (3.59)$$

was used to quantify this energy. To extend the optimization reacting flows, we need to define an energy that accounts for species density changes and vibrational energy. We can gain some insight into a proper disturbance energy by rewriting the Mack energy norm in dimensional quantities, which is

$$E = \frac{1}{\rho_\infty U_\infty^2} \int_0^\infty \left[\rho_0 (\tilde{u}'^2 + \tilde{v}'^2 + \tilde{w}'^2) + \frac{P_0}{\rho_0^2} \tilde{\rho}'^2 + \frac{\rho_0 c_v}{T_0} \tilde{T}'^2 \right] dy.$$

In this form, the disturbance energy is similar to the total energy of the flow. Following this form, the addition of a vibrational temperature for a single species of gas would make the disturbance energy

$$E = \frac{1}{\rho_\infty U_\infty^2} \int_0^\infty \left[\rho_0 (\tilde{u}'^2 + \tilde{v}'^2 + \tilde{w}'^2) + \frac{P_0}{\rho_0^2} \tilde{\rho}'^2 + \frac{\rho_0 c_v}{T_0} \tilde{T}'^2 + \frac{\rho_0 c_{vv}}{T_{v0}} \tilde{T}_v'^2 \right] dy. \quad (3.60)$$

However, until a proper definition for disturbance energy is derived, we must restrict the optimization to a compressible, perfect gas flow. Thus, to define the inner product on the space of disturbances, we use the Mack energy norm, which is rewritten as

$$E(q) = (q, q) = \int_0^\infty q^H \mathbf{M} q dy$$

$$q = \left(\hat{u}', \hat{v}', \hat{w}', \hat{\rho}', \hat{T}' \right)^T \quad (3.61)$$

$$\mathbf{M} = \text{diag} \left[\rho_0, \rho_0, \rho_0, \frac{T_0}{(\gamma \rho_0 Ma^2)}, \frac{\rho_0}{\gamma (\gamma - 1) T_0 Ma^2} \right]$$

where the superscript H denotes the complex conjugate transpose. The amount of disturbance growth over the plate is characterized by the growth factor, G , which is the ratio of energy input at $x = x_{in}$ to the energy output at $x = x_{out}$,

$$G = E_{out}/E_{in} \quad (3.62)$$

. Following Luchini's method[103] described above, only wall-normal and spanwise disturbances are input to the system at $x = x_{in}$, with the expectation that these components will be zero at $x = x_{out}$. This reduces the energy of disturbances to

$$E_{in} = \int_0^{\infty} [\rho_0 (\hat{v}'^2 + \hat{w}'^2)] dy \quad (3.63)$$

$$E_{out} = \int_0^{\infty} \left[\rho_0 \hat{u}'^2 + \frac{\hat{\rho}'^2 T_0}{\gamma \rho_0 Ma^2} + \frac{\hat{T}'^2 \rho_0}{\gamma (\gamma - 1) T_0 Ma^2} \right] dy \quad (3.64)$$

The output energy can be simplified using a relationship derived from the non-dimensionalized ideal gas law, which is

$$P_0 \gamma Ma = \rho_0 T_0.$$

Using the relation of $P_0 = 1/\gamma Ma^2$ for boundary layers[22], we have

$$\rho_0 T_0 = 1,$$

thus the disturbance equation of state becomes

$$\hat{\rho}' = \frac{-\hat{T}'}{T_0} = -\rho_0 \hat{T}'. \quad (3.65)$$

Using this equation, the output energy expression is further reduced to

$$E_{out} = \int_0^{\infty} \left[\rho_0 \hat{u}'^2 + \frac{\hat{T}'^2}{(\gamma - 1) T_0 Ma^2} \right] dy. \quad (3.66)$$

Power iterations using the real and adjoint equations are performed to determine the input disturbance functions for a given wave number, β , that maximizes the output. The adjoint equations are

defined by the adjoint relation

$$(g, \mathcal{A}f) = (\mathcal{A}^*g, f) \quad (3.67)$$

where \mathcal{A} is the real operator, \mathcal{A}^* is the adjoint operator, f is defined above, and g is the vector of adjoint variables, $g = (g_1, g_2, g_3, g_4, g_5)^T$. After applying appropriate boundary conditions on f and g (defined below), the vector g must satisfy

$$-A^T g_x = (D^T g_x)_y + B_0^T g - (B_1^T g)_y + (B_2^T g)_{yy} \quad (3.68)$$

which also define the adjoint equations.

The optimization algorithm solves parabolic system of equations, Eqs. 3.56 by propagating the initial conditions at $x = x_{in}$

$$\begin{aligned} \hat{v}'(x_{in}, y), \hat{w}'(x_{in}, y) &\neq 0 \\ \hat{u}'(x_{in}, y), \hat{T}'(x_{in}, y), \hat{P}'(x_{in}, y) &= 0 \end{aligned} \quad (3.69)$$

downstream with boundary conditions on f as

$$\begin{aligned} y = 0 : \hat{u}', \hat{v}', \hat{w}', \hat{P}'_y &= 0; \quad y = y_{max} : \hat{u}', \hat{v}'_y, \hat{w}', \hat{T}', \hat{P}' = 0 \\ y = 0 : \begin{cases} \hat{T}' = 0 & \text{isothermal wall} \\ \hat{T}'_y = 0 & \text{adiabatic wall} \end{cases} \end{aligned} \quad (3.70)$$

The initial conditions on the adjoint variables, at $x = x_{out}$, are derived in the process of satisfying the adjoint relation above and are given by

$$\begin{aligned} A^{11}(x_{out}, y) g_1(x_{out}, y) + A^{21}(x_{out}, y) g_2(x_{out}, y) + A^{51}(x_{out}, y) g_5(x_{out}, y) &= \rho_0(x_{out}, y) \hat{u}'(x_{out}, y) \\ g_3(x_{out}, y), g_4(x_{out}, y) &= 0 \\ A^{11}(x_{out}, y) g_1(x_{out}, y) + A^{21}(x_{out}, y) g_2(x_{out}, y) &= \frac{\hat{T}'(x_{out}, y)}{(\gamma-1)[T_0(x_{out}, y)Ma]^2} \end{aligned} \quad (3.71)$$

where the superscript numbers indicate the row and column of the matrix. This set of initial conditions does not define the $g_2(x_{out}, y)$ term, allowing the term to be arbitrary. As in Tumin and Reshotko[15], $g_2(x_{out}, y)$ is set to zero. The adjoint equations are also parabolic and are solved by propagating the initial conditions, Eq. 3.71, upstream and applying the following boundary conditions on g

$$\begin{aligned}
y = 0 : g_2, g_3, g_4 = 0; y = y_{max} : B_1^{12} g_1 + B_1^{22} g_2 + B_1^{32} g_3 - (B_2^{32} g_3)_y + B_1^{52} g_5 = 0 \\
y = 0 : \begin{cases} g_5 = 0 & \text{isothermal wall} \\ \frac{1}{2} B_1^{54} g_5 - B_2^{54} g_{5,y} = 0 & \text{adiabatic wall} \end{cases} \quad (3.72)
\end{aligned}$$

as required to satisfy the adjoint relation. To fully constrain the numerical discretization, these boundary conditions are supplemented by

$$y = 0 : g_{1y} = 0; y = y_{max} : g_{(\cdot)y} = 0 \quad (3.73)$$

The next power iteration is started by setting $f(x_{in}, y)$ to initial data given by

$$\begin{aligned}
\rho_0(x_{in}, y) \hat{v}'(x_{in}, y) &= A^{32}(x_{in}, y) g_3(x_{in}, y) \\
\rho_0(x_{in}, y) \hat{w}'(x_{in}, y) &= A^{43}(x_{in}, y) g_4(x_{in}, y) \\
\hat{u}'(x_{in}, y), \hat{T}'(x_{in}, y), \hat{P}' &= 0
\end{aligned} \quad (3.74)$$

which are also derived in the process of satisfying the adjoint relation.

Chapter 4

Numerical Methods

4.1 Flow Solver : The Finite Volume Method

The flow solver used in the current study is US3D[123], which solves the three-dimensional (3D), reacting Navier-Stokes equation using a finite volume approach. A brief overview of the fundamentals of the finite volume approach are provided below.

We begin by rewriting the conservation laws of the previous chapter in terms of a set of conserved variables, U , fluxes, \vec{F} , and source terms, W , which is

$$\frac{\partial U}{\partial t} + \nabla \cdot \vec{F} = W, \quad (4.1)$$

where conserved variable set is

$$U = (\rho_s, \rho u_i, E_v, E)^T$$

and the source terms are

$$W = \left(w_s, 0, \left(Q_{t-v} + \sum_s e_{vs} w_s \right), 0 \right)^T.$$

The fluxes are separated into inviscid components and viscous components,

$$\vec{F} = \vec{F}_I + \vec{F}_V,$$

due to the difference in their nature; inviscid fluxes become hyperbolic at supersonic mach numbers while the viscous fluxes remain elliptic. The inviscid components of the fluxes in Cartesian

coordinates are

$$F_I = \begin{Bmatrix} \rho_1 u \\ \vdots \\ \rho_{ns} u \\ \rho u u + P \\ \rho u v \\ \rho u w \\ E_v u \\ (E + P) u \end{Bmatrix}, \quad G_I = \begin{Bmatrix} \rho_1 v \\ \vdots \\ \rho_{ns} v \\ \rho u v \\ \rho v v + P \\ \rho v w \\ E_v v \\ (E + P) v \end{Bmatrix}, \quad H_I = \begin{Bmatrix} \rho_1 w \\ \vdots \\ \rho_{ns} w \\ \rho u w \\ \rho v w \\ \rho w w + P \\ E_v w \\ (E + P) w \end{Bmatrix}. \quad (4.2)$$

The viscous flux components are

$$F_V = \begin{Bmatrix} \rho_1 v_{1,x} \\ \vdots \\ \rho_{ns} v_{ns,x} \\ -\tau_{xx} \\ -\tau_{xy} \\ -\tau_{xz} \\ q_{v,x} + \sum_{s=1}^{ns} \rho_s e_v v_{s,x} \\ q_x + q_{v,x} - u_i \tau_{i,x} + \sum_{s=1}^{ns} \rho_s e_v v_{s,x} \end{Bmatrix}, \quad G_V = \begin{Bmatrix} \rho_1 v_{1,y} \\ \vdots \\ \rho_{ns} v_{ns,y} \\ -\tau_{xy} \\ -\tau_{yy} \\ -\tau_{yz} \\ q_{v,y} + \sum_{s=1}^{ns} \rho_s e_v v_{s,y} \\ q_y + q_{v,y} - u_i \tau_{i,y} + \sum_{s=1}^{ns} \rho_s e_v v_{s,y} \end{Bmatrix},$$

$$H_V = \begin{Bmatrix} \rho_1 v_{1,z} \\ \vdots \\ \rho_{ns} v_{ns,z} \\ -\tau_{xz} \\ -\tau_{yz} \\ -\tau_{zz} \\ q_{v,z} + \sum_{s=1}^{ns} \rho_s e_v v_{s,z} \\ q_z + q_{v,z} - u_i \tau_{i,z} + \sum_{s=1}^{ns} \rho_s e_v v_{s,z} \end{Bmatrix}. \quad (4.3)$$

Next, we integrate the conservation equations, Equations 4.1, over an arbitrary, constant volume,

Ω . Applying the Divergence Theorem to the flux term, we have

$$\frac{\partial \bar{U}}{\partial t} + \frac{1}{V} \int_{\partial\Omega} (\vec{F} \cdot \vec{n}) dS = \bar{W},$$

where \bar{U} and \bar{W} are now the average quantities of the volume and $\partial\Omega$ is the external surface of the volume with the outward surface normal \vec{n} . The arbitrary volume, Ω , can now be approximated as a polygon consisting of several planar faces, allowing the surface integral to be rewritten as a sum of fluxes over the faces of the volume, which is

$$\frac{\partial \bar{U}}{\partial t} + \frac{1}{V} \sum_{faces} (\vec{F} \cdot \vec{n}) S = \bar{W}. \quad (4.4)$$

This equation can be applied to solve the fluid flow over an arbitrary shape by discretizing the flow domain with a series of polygons, which are typically hexahedrals (rectangular prisms), tetrahedrals, pyramids, or triangular prisms. The conserved variable vector is stored at the center of each polygon (cell) since the quantity is the average over the volume. Therefore, the flux at each face is calculated by reconstructing the continuous (or approximately continuous in the case of shocks) flowfield variables at the face centroid. This reconstructed variable set at the face is considered to be the average value across the face.

4.1.1 Inviscid Fluxes

As previously stated, the inviscid fluxes are hyperbolic in nature for flows where the Mach number is greater than one. For hyperbolic equations, information travels along characteristics. Therefore, we use a modified form of the characteristic-based inviscid flux scheme called Steger-Warming flux-vector splitting, named after the authors Steger and Warming, who proposed the method[124]. The Steger-Warming method utilizes the fact that the inviscid fluxes are linear and homogenous with respect to the conserved variable vector, meaning

$$\vec{F}(\lambda U) = \lambda \vec{F}(U),$$

where λ is an arbitrary scalar. The homogeneity of the flux allows it to be exactly represented by a jacobian, which is

$$\vec{F}(U) = \frac{\partial \vec{F}}{\partial U} U = AU,$$

where A is the flux jacobian. The flux jacobian is then split into left- and right-moving components in order to use an upwind-biased flux evaluation as required for stability of hyperbolic systems. The direction of the flux components are determined by the direction of the characteristics in the flow, which define the eigenvalues of the jacobian. Thus, a characteristic's velocity can be determined by diagonalizing the flux jacobian. Because the diagonalization of $\frac{\partial \vec{F}}{\partial U}$ is difficult, a primitive variable set is introduced in order to simplify the process of diagonalization. This variable set is defined by

$$V = (\rho_s, u_i, e_v, p)^T.$$

Additionally, the flux is evaluated in a local coordinate system based on the face's normal surface vector, which is

$$\vec{F}_I \cdot \vec{n} = F'_I = \left\{ \begin{array}{c} \rho_1 u' \\ \vdots \\ \rho_{ns} u' \\ \rho u u' + P s'_x \\ \rho v u' + P s'_y \\ \rho w u' + P s'_z \\ E_v u' \\ (E + P) u' \end{array} \right\},$$

where s'_x , s'_y , and s'_z are the components of the unit normal vector of the face and u' is the flow velocity normal to the face defined by

$$u' = u s'_x + v s'_y + w s'_z.$$

Using the primitive set, the flux jacobian is rewritten as

$$A' = \frac{\partial U}{\partial V} \frac{\partial V}{\partial U} \frac{\partial F'_I}{\partial V} \frac{\partial V}{\partial U}.$$

The matrix $\frac{\partial V}{\partial U} \frac{\partial F'_I}{\partial V}$ can be diagonalized as

$$\frac{\partial V}{\partial U} \frac{\partial F'_I}{\partial V} = C^{-1} \Lambda' C,$$

where Λ' is the diagonal eigenvalue matrix and C is the matrix composed of eigenvectors. The eigenvalue matrix has three different components:

$$\left\{ \begin{array}{l} \lambda_{E,V} = u' \\ \lambda_{FA} = u' + a \\ \lambda_{SA} = u' - a \end{array} \right\},$$

where a is the speed of sound and the subscript indicates the type of characteristic. The first eigenvalue is related to an entropy or vorticity disturbance, which travel at the flow velocity u' . The next two eigenvalues are related to fast, λ_{FA} , and slow, λ_{SA} , acoustic waves, which travel at the speed of sound with and against the flow velocity. As seen from the eigenvalues, the characteristics are all moving in the positive direction if u' is positive and greater than a . In the case where u' is less than a , the slow acoustic wave will be traveling against the flow. Based on this behavior, the flux can be split into positive and negative moving characteristics by isolating all positive eigenvalues into the matrix Λ_+ and the negative eigenvalues into the matrix Λ_- . Additionally, a rotation is applied to transform the momentum components from the local coordinate system to the Cartesian system in order to avoid singularities. The inviscid flux is now written as

$$\begin{aligned} F'_+ &= S^{-1}R^{-1}C^{-1}\Lambda'_+CRSU = A'_+U \\ F'_- &= S^{-1}R^{-1}C^{-1}\Lambda'_-CRSU = A'_-U \end{aligned},$$

where S is the primitive to conservative transformation matrix $\frac{\partial V}{\partial U}$ and R is the rotation matrix. The total inviscid flux is the combination of the flux in each direction,

$$F'_I = F'_+ + F'_-.$$

In order to demonstrate the upwind nature of the flux scheme, we use the arbitrary mesh shown in Figure 4.1 as a reference. In the figure, the cell centroids are shown in blue circles, the faces in black lines, and the nodes as the black circles. The flux being calculated is across the face between cells i and $i + 1$. For simplicity, we refer to this face as $i + 1/2$. The positive-moving and negative-moving flux component directions are indicated by the arrows. Using this stencil, an upwind method would be

$$\begin{aligned} F'_{+,i+1/2} &= A'_{+,i}U_i \\ F'_{-,i+1/2} &= A'_{-,i+1}U_{i+1} \end{aligned}.$$

This is the first-order accurate Steger-Warming (SW) method. For the current work, this method is modified to have the properties of the jacobian calculated at the face by a simple average of the neighboring cell values, thus is called Modified Steger-Warming (MSW)[125] and is written

$$\begin{aligned} F'_{+,i+1/2} &= A'_{+,i+1/2} U_i \\ F'_{-,i+1/2} &= A'_{-,i+1/2} U_{i+1} \end{aligned} \quad (4.5)$$

The modification provides a central-differencing influence that results in less numerical dissipation than the original Steger-Warming method. However, near large discontinuities, such as shocks, this method may not provide a sufficient amount of dissipation to maintain numerical stability. To address this issue, a pressure switch has been added to smoothly transition the jacobian calculation from MSW to the original SW in the presence of pressure gradients that occur at shocks.

A sample flux evaluation would consist of the following evaluations. For a general control volume in continuum flow, all face surface normals of the cell point outwards. Thus, a flux is defined as positive if it leaves the cell and vice versa based on the dot product of the flux with a face's surface normal. In a structured formulation, a one-dimensional flux evaluation on the cells in Figure 4.1 would look as

$$\begin{aligned} \frac{\partial U_i}{\partial t} &= \frac{-1}{V_i} [F_{i+1/2} \cdot n_{i+1/2} + F_{i-1/2} \cdot n_{i-1/2}] = \frac{-1}{V_i} [F'_{i+1/2} - F'_{i-1/2}], \\ \frac{\partial U_i}{\partial t} &= \frac{-1}{V_i} \left[A'_{+,i+1/2} S_{i+1/2} U_i - A'_{+,i-1/2} S_{i-1/2} U_{i-1} \right. \\ &\quad \left. - \left(A'_{-,i-1/2} S_{i-1/2} U_i - A'_{-,i+1/2} S_{i+1/2} U_{i+1} \right) \right]. \end{aligned}$$

In an unstructured mesh, the flux evaluation is based on the face surface normal, which points from the cell on the face's left, cell-left, toward the cell on the face's right, cell-right. In Figure 4.1, we will define cell-left as cell i and cell-right as cell $i + 1$. The positive-moving component of the flux travels from cell-left to cell-right, while the negative-moving component of the flux travels from cell-right to cell-left as indicated in the figure as well as the origin of information Equations 4.5. Therefore, the same one dimension flux evaluation for the structured formulation would become

$$\frac{\partial U_{CL}}{\partial t} = \frac{-1}{V_{CL}} \sum_{faces} F'_{i+1/2},$$

$$\frac{\partial U_{CR}}{\partial t} = \frac{1}{V_{CR}} \sum_{faces} F'_{i+1/2}.$$

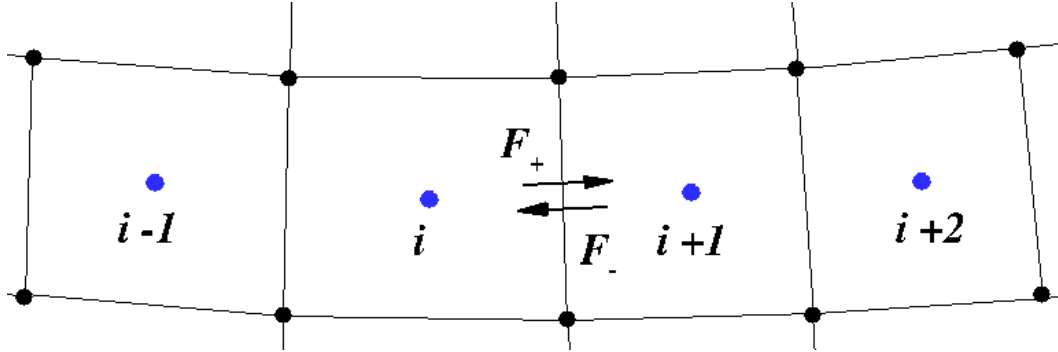


Figure 4.1: The plot shows an arbitrary mesh that discretizes a flow domain.

4.1.2 Viscous Fluxes

The viscous fluxes are elliptic in nature and are calculated using a central-based scheme. As seen in Equations 4.3, the flux terms are composed of flow variables and derivative quantities that must be evaluated at the face. The flow variables are calculated using a simple average of the neighboring cell values. The derivative quantities are calculated using the deferred correction method, which projects the gradient in the neighboring cells onto the face's surface normal vector. In order to provide the derivatives needed, the gradients of flow variable must be calculated for each cell. In US3D, gradients are calculated using one of three methods. The first method uses a least-squares approximation that weights the data based on the distance from the cell's centroid. This method is essentially fitting a plane through the local domain of flow variables from which a derivative is obtained. This method is the default because it provides a consistent means for determining gradients for various cell types encountered in unstructured grids. Another benefit to this method is that it limits to the correct Taylor series approximation for the derivative across the face in a uniform mesh. The second method using the divergence theorem to construct a gradient, which is essentially the reverse of the finite volume method. Although this method works, it proves to be less accurate than the first method. The last method available in US3D calculates the derivatives normal and tangential to a face by means of constructing finite differences on a local stencil. This method works well for hexahedral meshes, however, it is limited to only hexahedrals, thus is not used in general.

4.1.3 Time Advancement

After solving for the fluxes, we can move this term to the right hand side of Equation 4.4 and we are left with

$$\frac{\partial \bar{U}}{\partial t} = -\frac{1}{V} \sum_{faces} \left(\vec{F} \cdot \vec{n} \right) S + \bar{W}, \quad (4.6)$$

which only leaves the time advancement to be solved. A basic method is to approximate the time derivative by a simple, first-order, backward finite difference, which is called the Explicit Euler method and is written

$$\frac{\bar{U}^{n+1} - \bar{U}^n}{\Delta t} = -\frac{1}{V} \sum_{faces} \left(\vec{F}^n \cdot \vec{n} \right) S + \bar{W}^n,$$

where the superscript n denotes the current time step. The method is called explicit because right hand side is directly calculated and the next time step, $n + 1$, is solved for explicitly. Higher-order explicit methods are possible using multiple evaluations of the spatial fluxes in one of two ways. Multiple time steps can be stored and higher-order finite differences applied. Another method is to evaluate subiterations within the same time step using the explicit Runge-Kutta (RK) schemes.

A disadvantage of the explicit methods is the stable time step of an explicit method is limited and can be debilitating for some numerical simulations. An implicit method overcomes this obstacle by evaluating the right hand side of Equation 4.6 at the next time step, which allows the simulation to be theoretically stable at any time step. To do this, we first separate the inviscid and viscous fluxes. The inviscid fluxes at $n + 1$ can be approximated by a linearization of the flux calculation with respect to the conserved variables, which is

$$\begin{aligned} F_I^{n+1} &= F_I^n + \left. \frac{\partial F_I}{\partial U} \right|^n (\bar{U}^{n+1} + \bar{U}^n) + O(\Delta t^2) \\ F_I^{n+1} &\approx F_I^n + A_I^n \delta \bar{U}^n \end{aligned}$$

The source terms are treated in a similar fashion as

$$\begin{aligned} \bar{W}^{n+1} &= \bar{W}^n + \left. \frac{\partial \bar{W}}{\partial U} \right|^n (\bar{U}^{n+1} + \bar{U}^n) + O(\Delta t^2) \\ \bar{W}^{n+1} &\approx \bar{W}^n + D^n \delta \bar{U}^n \end{aligned},$$

where D^n is the source term jacobian. In both cases, the jacobians are evaluated at the current time step implying that their variation is frozen with respect to time. A first-order implicit method

for solving the Euler Equations would appear as

$$\delta\bar{U}_i^n + \frac{\Delta t}{V_i} \sum_{faces} (A^n S \delta\bar{U}_f^n) - \Delta t D_i^n \delta\bar{U}_i^n = -\frac{\Delta t}{V_i} \sum_{faces} F_I^n S + \Delta t \bar{W}_i^n, \quad (4.7)$$

where $\delta\bar{U}_f^n$ is the change in the conserved variable vector of the cell from which the flux originates as discussed in Section 4.1.1. In Equation 4.7 the right-hand side is composed of the explicit fluxes and source terms and the left-hand side is the implicit operator.

Solving Equations 4.7 as is would require the inversion of a potentially very large matrix. Rather than perform this computationally intensive process, a series of approximations can be made to the implicit operator to reduce the operation involved in solving for $\delta\bar{U}$. Before we discuss these approximations, we must first analyze the terms involved in the summation of fluxes in the implicit operator. The summation can be broken into fluxes originating in cell i and those of cell i 's neighbors, which is

$$\frac{\Delta t}{V_i} \sum_{faces} (A^n S \delta\bar{U}_f^n) = \frac{\Delta t}{V_i} \sum_{faces} (A^n S \delta\bar{U}_i^n) + \frac{\Delta t}{V_i} \sum_{faces} (A^n S \delta\bar{U}_{nbr}^n).$$

The first approximation is known as the full-matrix, point relaxation method[126]. This is accomplished by using a series of pseudo advancement steps known as *kmax* iterations. This method uses information from the previous *kmax* iteration for neighboring cells, allowing these terms to be moved to the right hand side. The first *kmax* iteration is computed using the following initial guess

$$\left(\frac{V_i}{\Delta t} I + \sum_{faces} (A^n S) + V_i D_i^n \right) \delta\bar{U}_i^{(0)} = - \sum_{faces} F_I^n S + V_i \bar{W}_i^n.$$

After solving this matrix system once at every cell, δU in neighboring cells is populated and can be incorporated into successive *kmax* iterations, which are now

$$\left(\frac{V_i}{\Delta t} I + \sum_{faces} (A^n S) + V_i D_i^n \right) \delta\bar{U}_i^{(k)} = \sum_{faces} (A^n S \delta\bar{U}_{nbr}^{(k-1)}) - \sum_{faces} F_I^n S + V_i \bar{W}_i^n.$$

Arriving at $k = kmax$, the solution for the next time step is set by

$$\delta\bar{U}_i^n = \delta\bar{U}_i^{(kmax)}.$$

The second approximation made to the implicit matrix system is known as the Gauss-Seidel, line

relaxation method[127]. This method utilizes the structure of the grid, primarily near the wall in the boundary layer clustering, to directly solve the implicit, conserved variable vector for multiple cells in a line. Typically, lines are made from the wall through the boundary layer. Using the cell diagram in Fig. 4.1 to describe the structure of a line of cells and the same *kmax* relaxation iterations of the point relaxation method, the line relaxation solve is started with the following initial guess

$$\tilde{A}\delta\bar{U}_i^{(0)} + \tilde{B}\delta\bar{U}_{i+1}^{(0)} + \tilde{C}\delta\bar{U}_{i-1}^{(0)} = - \sum_{faces} F'_I{}^n S + V_i \bar{W}_i^n,$$

where

$$\begin{aligned} \tilde{A} &= \frac{V_i}{\Delta t} I + \sum_{faces} (A^n S) + V_i D_i^n, \\ \tilde{B} &= A'_{-,i+1/2} S_{i+1/2}, \\ \tilde{C} &= -A'_{+,i-1/2} S_{i-1/2}. \end{aligned}$$

The δU vector in neighboring cells of the data line is again populated after the first *kmax* iteration and can be incorporated into successive iterations, which looks as

$$\tilde{A}\delta\bar{U}_i^{(k)} + \tilde{B}\delta\bar{U}_{i+1}^{(k)} + \tilde{C}\delta\bar{U}_{i-1}^{(k)} = \sum_{faces} (A^n S \delta\bar{U}_{nbr}^{(k-1)}) - \sum_{faces} F'_I{}^n S + V_i \bar{W}_i^n.$$

The solution for the next time step is again set by

$$\delta\bar{U}_i^n = \delta\bar{U}_i^{(kmax)}.$$

This implicit method allows for greater stability and a faster rate of convergence than the point relaxation method because it solves along the high gradients in the boundary layer. However, this method will result in biasing the flow along the direction of the line solves. Thus, line relaxation should not be used in the simulation of fluid flows involving unsteadiness and vortical structures, which require an equal numerical treatment in all directions. For more information about the time advancement methods, the reader is referred to Wright et al.[126], Wright et al.[127], and Nompelis[42].

The viscous fluxes undergo a similar treatment as the inviscid fluxes with an additional simplification. A large number of the gradient terms are eliminated by making a “thin-layer” approximation. This approximation assumes that when the flux through the face is calculated, gradients that are

tangential to the face will be approximately zero after taking the dot product with the face's surface normal. For more information about this approximation, the reader is referred to Nompelis[42].

4.1.4 Higher-order Inviscid Flux Methods

Higher-order spatial flux evaluation methods involve obtaining a more accurate approximation of the flow properties at the face. The modified Steger-Warming flux can be rewritten as

$$F'_{I,i+1/2} = A'_{i+1/2}(\Lambda) \frac{(U_{i+1} + U_i)}{2} + A'_{i+1/2}(|\Lambda|) \frac{(U_{i+1} - U_i)}{2},$$

which consists of a central-average based symmetric portion of the fluxes and a dissipative portion of the fluxes,

$$D_{i+1/2} = A'_{i+1/2}(|\Lambda|) \frac{(U_{i+1} - U_i)}{2},$$

where $A'_{i+1/2}(X)$ implies the flux jacobian evaluated with the vector X for the eigenvalues. In the low dissipation flux evaluation, the dissipative flux is multiplied by a numerical switch, α_{diss} , that varies from 0 to 1, which looks as

$$F'_{I,diss} = \alpha_{diss} D_{i+1/2}$$

The numerical switch is intended to apply dissipation where necessary to maintain numerical stability, such as in the presence of shock waves, and remove dissipation elsewhere in the domain where dissipation is unnecessary. One possible switch is the Ducros switch[128], which is

$$\alpha_{diss,ducros} = \min \left(\left(\frac{\theta^2}{\theta^2 + \omega^2 + \epsilon} \right), 1 \right),$$

where θ is the divergence of the velocity, ω is the vorticity, and ϵ is a small factor to avoid a division by zero. This switch turns on ($\alpha_{diss} \rightarrow 1$) in the presence of large flow divergence (i. e. shocks) and limits to zero in the presence of large vorticity, which occurs in the boundary layer as well as vortical structure in the flow. However, one drawback to this switch is that it is active in the freestream, causing a large amount of dissipation to be applied. Therefore, this switch does a very good job when simulating boundary layer phenomena like turbulence and flow around roughness elements. In the case of freestream acoustic waves, this switch tends to artificially reduce the amplitude of the wave before it reaches the boundary layer.

The symmetric portion of the fluxes can be replaced with high-order approximations to the

conserved variables at the face. When these approximations are made, they utilize the neighboring cells conserved variables and gradients as well as the gradients in the second set of neighboring cells. All of these components are summed in a way that recovers a high-order approximation of the gradient of the flux in cell rather than just the flux at the face, which is done for the following reason. The one dimensional finite volume method evaluates the flux at two faces across the cell. These fluxes are then combined to create an approximation to the gradient of the flux which is seen in the conservation equations, Equations 4.1. Therefore, regardless of the accuracy of the fluxes at each face, the gradient of the flux is at best second-order accurate. If the fluxes are calculated with the gradient of the flux in mind, a higher degree of accuracy is achieved. For more information about high-order inviscid fluxes, the reader is referred to the works of Subbareddy and Candler[129] and Bartkowicz et al.[8].

4.2 Optimal Disturbance Solver

As discussed in Section 3.5.3, the determination of the optimal initial disturbance for a given set of flow conditions and geometry requires the propagation of an initial guess forward through the real mean flow solution and then backward through the adjoint mean flow. All mean flow derivatives are calculated and stored. Next, finite differences are applied in both the streamwise and wall-normal directions in order to propagate the real and adjoint disturbance variables. The streamwise derivatives in the real equations are discretized using a second-order-backward finite difference, while those in the adjoint equations are discretized using a second-order-forward finite difference. At each of the boundaries, where a second order stencil is not possible, a first-order finite difference is used in place of the second-order finite difference. The wall-normal derivatives in both sets of equations are discretized using a second-order-central finite difference and are formulated implicitly. For the current implementation, all optimization grids have constant spacing in both the wall-normal and streamwise directions. Although this method is not ideal for computational cost, the problem is small enough to make this method sufficient. Applying the finite difference approximations first to the real equations, given in Eq. 3.56, we have

$$\frac{3}{2}A^i f^i - 2A^{i-1} f^{i-1} + \frac{1}{2}A^{i-2} f^{i-2} = \frac{3}{2}D^i \frac{\partial f^i}{\partial y} - 2D^{i-1} \frac{\partial f^{i-1}}{\partial y} + \frac{1}{2}D^{i-2} \frac{\partial f^{i-2}}{\partial y}$$

$$+ \Delta x \left[B_0^i f^i + B_1^i \frac{\partial f^i}{\partial y} + B_2^i \frac{\partial^2 f^i}{\partial y^2} \right], \quad (4.8)$$

where the superscript i indicates the an arbitrary streamwise location and Δx is the spacing in the streamwise direction. Applying the finite difference approximations to the adjoint equations, given in Eq. 3.68, we have

$$\begin{aligned} \frac{3}{2} (A^{T,i} g^i) - 2 (A^{T,i} g^{i+1}) + \frac{1}{2} (A^{T,i} g^{i+2}) &= -\frac{3}{2} \frac{\partial}{\partial y} (D^{T,i} g^i) + 2 \frac{\partial}{\partial y} (D^{T,i} g^{i+1}) \\ &- \frac{1}{2} \frac{\partial}{\partial y} (D^{T,i} g^{i+2}) + \Delta x \left[B_0^i g^i - \frac{\partial}{\partial y} (B_1^i g^i) + \frac{\partial^2}{\partial y^2} (B_2^i g^i) \right]. \end{aligned} \quad (4.9)$$

At each i location the disturbance variables are solved for by building a block-tridiagonal system and solving it using LU decomposition. After applying the second-order-central finite differences, the real governing equations are rewritten into three block matrices at an arbitrary wall-normal location, j , as

$$\begin{aligned} \tilde{A}_j &= \frac{3}{4\Delta y} D^{i,j} - \frac{\Delta x}{\Delta y^2} B_2^{i,j} + \frac{1\Delta x}{2\Delta y} B_1^{i,j}, \\ \tilde{B}_j &= \frac{2\Delta x}{\Delta y^2} B_2^{i,j} - \Delta x B_0^{i,j} + \frac{3}{2} A^{i,j}, \\ \tilde{C}_j &= -\frac{3}{4\Delta y} D^{i,j} - \frac{\Delta x}{\Delta y^2} B_2^{i,j} - \frac{1\Delta x}{2\Delta y} B_1^{i,j}. \end{aligned}$$

The disturbance variables that are already known are stored in the vector on the right-hand-side, which is written

$$\begin{aligned} RHS_j &= 2A^{i-1,j} f^{i-1,j} - \frac{1}{2} A^{i-2,j} f^{i-2,j} - \frac{1}{\Delta y} D^{i-1,j} (f^{i-1,j+1} - f^{i-1,j-1}) \\ &+ \frac{1}{4\Delta y} D^{i-2,j} (f^{i-2,j+1} - f^{i-2,j-1}). \end{aligned}$$

It is important to note that the order of equations stored in the block matrices is the streamwise, wall-normal, and spanwise conservation of momentum equations, the conservation of energy equation, and then the conservation of mass equation. This equation order maintains the diagonal dominance that is required for the LU decomposition. This is due to the order of the variables stored in the real disturbance vector f . The adjoint equations do not need such treatment and are stored as the adjoint mass equation, adjoint streamwise, wall-normal, and spanwise momentum equations, and then the adjoint energy equation. Applying a similar reorganization to the discretized adjoint

equations, it is possible to build the block-tridiagonal system to solve for the disturbance variables at each location i . This block system looks as

$$\begin{bmatrix} I & BC_1 & 0 & \cdots & & & \\ \tilde{A}_2 & \tilde{B}_2 & \tilde{C}_2 & \ddots & & & \\ 0 & \ddots & \ddots & \ddots & & & \\ \vdots & \ddots & \tilde{A}_{N_y-1} & \tilde{B}_{N_y-1} & \tilde{C}_{N_y-1} & & \\ & & & BC_{N_y} & I & & \end{bmatrix} \begin{bmatrix} f^{i,1} \\ f^{i,2} \\ \vdots \\ f^{i,N_y-1} \\ f^{i,N_y} \end{bmatrix} = \begin{bmatrix} 0 \\ RHS_1 \\ \vdots \\ RHS_{N_y-1} \\ 0 \end{bmatrix},$$

where I is the identity matrix, N_y is the number of wall-normal j locations, BC_1 enforces the wall boundary conditions, and BC_{N_y} enforces the freestream boundary conditions. The boundary conditions on the real disturbance variables are given in Eqs. 3.70 and the boundary conditions on the adjoint disturbance variables are given in Eqs. 3.72 and 3.73

Using these implicit steps, an initial guess of the real disturbance variables based on Eqs. 3.69, at $i = 1$, is propagated downstream from $i = 2$ until $i = Nx$, where Nx is the number of streamwise i locations. The initial conditions on the adjoint equations, given in Eqs. 3.71, are applied at $i = Nx$. The adjoint disturbance variables are then propagated upstream from $i = Nx - 1$ until $i = 1$. At this point, the real disturbance variables are reset according to Eqs. 3.74. This is done for several power iterations until the real disturbance variables have reached an acceptable level of convergence. Generally, a residual on the order of 10^{-14} takes five power iterations, indicating the optimal solution is well separated from other possible solutions as discussed in Anderson et al.[30]. Additionally, between each iteration the input energy is normalized to unity, $E_{in} = 1$.

Chapter 5

Properties of Acoustic Damping

5.1 Theoretical Results of Acoustic Damping

5.1.1 Properties of Acoustic Damping

Although it is important to consider all of the internal relaxation modes of a particular gas composition as Fujii and Hornung[6, 5] have done, we can still gain insight into an acoustic disturbance's interaction with the gas by studying the properties of a single relaxation mode. For a single relaxation mode, the relaxation matrix in Eq. 3.15 becomes the mode's inverse relaxation time, $1/\tau$. With this simplification, we can solve for the optimum angular frequency of acoustic damping for a given relaxation mode, which is

$$\omega_{opt}\tau_0 = \sqrt{(1 + h_{q,\rho}) (1 - a_f^2 h_{q,p})}, \quad (5.1)$$

$$h_{q,p} = \frac{\left. \frac{\partial h}{\partial q_i} \right|_{q_{i,0}} \left. \frac{\partial q_i^*}{\partial p} \right|_{p_0}}{\left. \frac{\partial h}{\partial \rho} \right|_{\rho_0}}; \quad h_{q,\rho} = \frac{\left. \frac{\partial h}{\partial q_i} \right|_{q_{i,0}} \left. \frac{\partial q_i^*}{\partial \rho} \right|_{\rho_0}}{\left. \frac{\partial h}{\partial \rho} \right|_{\rho_0}},$$

$$a_f^2 = \frac{\left. \frac{\partial h}{\partial \rho} \right|_{\rho_0}}{\frac{1}{\rho_0} - \left. \frac{\partial h}{\partial p} \right|_{p_0}},$$

where ω_{opt} is the optimum angular frequency, h is the enthalpy of the gas, ρ is the density, p is the pressure, $q_{()}$ is the governing parameter of the internal molecular process, a_f is the frozen speed

of sound, and the subscript 0 indicates an evaluation at the equilibrium gas state. As stated in Vincenti and Kruger,[62] a good approximation to Eq. 5.1 is simply

$$f_{opt} \approx \tau_0^{-1}, \quad (5.2)$$

where f_{opt} is the optimum frequency.

In addition to solving for the optimum frequency, we can also solve for the damping per wavelength at the optimum frequency, $\varepsilon_{\lambda,max}(f)$, which is

$$\varepsilon_{\lambda,max}(f) = 2\pi \frac{a_f - a_e}{a_f + a_e}, \quad (5.3)$$

where a_e is the equilibrium speed of sound, which has the form

$$a_e^2 = -\frac{\frac{\partial h}{\partial \rho} + \frac{\partial h}{\partial q_i} \frac{\partial q_i^*}{\partial \rho}}{\frac{\partial h}{\partial p} + \frac{\partial h}{\partial q_i} \frac{\partial q_i^*}{\partial p} - \frac{1}{\rho}}.$$

As seen in the formula, the equilibrium speed of sound is similar to the frozen speed of sound, however, it depends on the equilibrium properties of the relaxation mode, q_i^* .

In order to gain a better understanding of the meaning of Eqs. 5.1 and 5.3, it is instructive to use a concrete example for a relaxation mode. For this, we use a fictitious diatomic molecule with a single vibrational mode that is incapable of dissociating. The optimum frequency of acoustic damping for a vibrational mode becomes

$$f_{opt} = \frac{\sqrt{\left(1 + \frac{c_{vv}^*}{c_p}\right) \left(1 + \frac{c_{vv}^*}{c_v}\right)}}{2\pi\tau_0},$$

where c_p and c_v are the translational-rotational specific heats at constant pressure and volume, respectively and c_{vv}^* is the vibrational specific heat evaluated at the translation temperature. The formula for c_{vv}^* is given by

$$c_{vv}^* = \frac{R_u}{M_s} \left(\frac{\theta_{vs}}{T}\right)^2 \frac{\exp(\theta_{vs}/T)}{\exp(\theta_{vs}/T) - 1},$$

where R_u is the universal gas constant, M_s is the molecular weight of the gas, T is the translational temperature, and θ_{vs} is the characteristic vibrational temperature of the vibrational mode. Thus, the optimum frequency has a weak dependence on the energy contained in a vibrational mode.

However, the approximation made in Eq. 5.2 still holds, resulting in a strong dependence of the optimum frequency on the vibrational relaxation time. Therefore, a gas's ability to damp an acoustic wave relies heavily on the rate at which energy is transferred to and from the gas's internal molecular processes.

The damping per wavelength at the optimum frequency for a vibrational mode becomes

$$\varepsilon_{\lambda, max(f)} = 2\pi \frac{\sqrt{1 + \frac{c_{vv}^*}{c_v}} - \sqrt{1 + \frac{c_{vv}^*}{c_p}}}{\sqrt{1 + \frac{c_{vv}^*}{c_v}} + \sqrt{1 + \frac{c_{vv}^*}{c_p}}},$$

which has a strong dependence on the vibrational specific heat. The vibrational specific heat is a gauge for the amount of energy contained in a vibrational mode. Therefore, the gas's ability to damp an acoustic wave also depends on the amount of energy that can be transferred to an internal molecular process.

An interesting result of these formulas is that for all diatomic gases the maximum damping rate is the same and limited to approximately 13.4 percent. When $T \gg \theta_v$ and T is large, c_{vv}^* limits to R_s , therefore we have

$$\lim_{T \rightarrow \infty} \left(1 + \frac{c_{vv}^*}{c_v}\right) = \frac{7}{5},$$

$$\lim_{T \rightarrow \infty} \left(1 + \frac{c_{vv}^*}{c_p}\right) = \frac{9}{7}.$$

Substituting these values into the equation for the maximum damping frequency, we have

$$f_{max} = \frac{\sqrt{\frac{9}{7} \frac{7}{5}}}{2\pi\tau_0} = \frac{3}{2\sqrt{5}\pi\tau_0} \simeq \frac{0.2135}{\tau_0}.$$

The maximum absorption rate limits to

$$\max(\varepsilon_\lambda) = 2\pi \frac{\sqrt{\frac{7}{5} \frac{7}{9}} - 1}{\sqrt{\frac{7}{5} \frac{7}{9}} + 1} = 2\pi \frac{7 - 3\sqrt{5}}{7 + 3\sqrt{5}} \simeq 0.133745.$$

In order to demonstrate the dependence of the damping per wavelength of a vibrational mode on the relaxation time and the vibrational specific heat, we use Fujii's code[5] to solve for the damping per wavelength over a wide range of frequencies and temperatures, shown in Fig. 5.1. In the figure, each curve represents the damping per wavelength at a fixed translational temperature with the arrow in the diagram indicating an increasing temperature. The peaks of all of the curves

directly follow the evolution of the vibrational specific heat, with the curve where the temperature is approximately equal to the characteristic vibrational temperature indicated in the plot. From gas dynamics, we know the vibrational relaxation time decreases with increasing temperature, thus the maximum of each peak shifts to higher frequency as the temperature increases.

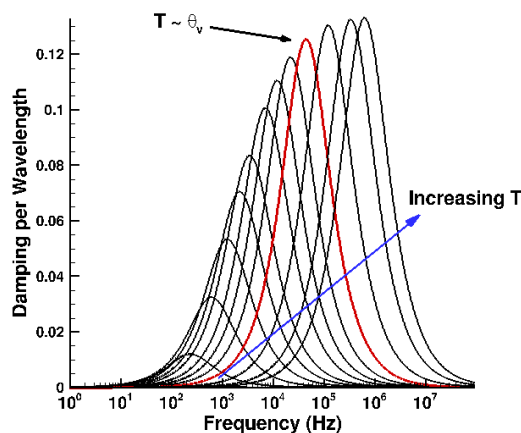


Figure 5.1: Damping per wavelength versus frequency over a range of temperatures for a fictitious diatomic molecule.

Finally, the last aspect of vibrational damping is the effect of degeneracy. We explore this effect by increasing the number of degeneracies of a linear molecule without modifying the molecules other properties. Although a degeneracy of two doubles the vibrational energy of a single vibrational mode, a degeneracy of two does not double the damping rate per wavelength. This is illustrated in Fig. 5.2, where the bottom curve is the damping for a single vibrational mode and the arrow indicates an increase of the degeneracy by one until a degeneracy of eight. A doubling of the damping rate requires a degeneracy of three and another doubling requires a degeneracy of seven. This indicates when multiple damping modes interact, the modes do not interact in a linear fashion.

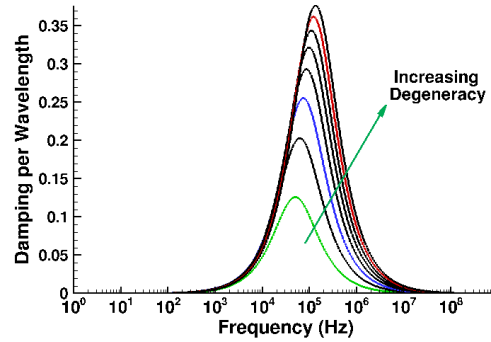


Figure 5.2: A plot showing the damping rate per wavelength at a constant temperature with an increasing number of degeneracies (indicated in the plot by the arrow) starting with a degeneracy of one. A doubling in damping rate per wavelength from a single vibrational mode (green) requires a degeneracy of three (blue) and another doubling of damping rate per wavelength require a degeneracy of seven (red).

A similar analysis can be performed for a chemical dissociation process. From the vibrational relaxation process, we can gain an intuition for the important factors for acoustic damping in a chemical process. The optimum frequency of damping for the vibrational case was strongly dependent on the vibrational relaxation time. The equivalent relaxation time for a chemical process is dependent on the forward rate of reaction. The formula for the optimum frequency of damping for a ideal diatomic dissociation is as follows

$$f_{opt} = \frac{k_f}{2\pi} \left(\frac{4N_1 + N_2}{N_2} \right) \sqrt{\left(1 + \frac{\left(1 + \left(\frac{d(\ln K)}{dT} \right)^{-1} \frac{1}{T} \right) c_{chem}}{c_{p,t+r,mix}} \right) \left(1 + \frac{c_{chem}}{c_{v,t+r,mix}} \right)},$$

$$c_{chem} = \frac{\Delta H_r}{TM_{mix} + \left(\frac{d(\ln K)}{dT} \right)^{-1} \left(\frac{1}{N_1} + \frac{4}{N_2} \right)},$$

$$k_f = C_f T^{\eta_f} \exp \left(\frac{-E_a}{kT} \right),$$

where ΔH_r is the heat of the reaction, N_1 refers to the dissociating species, and N_2 refers to the product species. Thus, by modifying the activation energy, E_a , of the reaction, the optimum frequency of damping can be modified. A simple example case is oxygen dissociation. The acoustic damping rate per wavelength is calculated for several different activation energies by modifying the

characteristic temperature of the reaction, shown in Fig. 5.3a, which is

$$\theta_r = \frac{E_a}{k}.$$

As the activation energy increases the speed of the relaxation decreases, thus causes the optimum damping frequency to decrease. An interesting aspect of this equation is the dependence of the damping process on the product species. If the product species does not exist in the mean state, the chemical damping process does not occur.

The analog for the energy capacity of the chemical process is the heat of reaction, ΔH_r . Evaluating the formula for maximum damping, Eq. 5.3, the damping due to a chemical process is

$$\varepsilon_{\lambda, max(f)} = 2\pi \frac{\sqrt{1 + \frac{c_{chem}}{c_{v,t+r,mix}}} - \sqrt{1 + \frac{\left(1 + \left(\frac{d(\ln K)}{dT}\right)^{-1} \frac{1}{T}\right) c_{chem}}{c_{p,t+r,mix}}}}{\sqrt{1 + \frac{c_{chem}}{c_{v,t+r,mix}}} + \sqrt{1 + \frac{\left(1 + \left(\frac{d(\ln K)}{dT}\right)^{-1} \frac{1}{T}\right) c_{chem}}{c_{p,t+r,mix}}}}.$$

This equation has roughly the same dependence on the heat of reaction as the specific heat of vibration in the vibrational damping case. Using the oxygen dissociation case, the formation enthalpy of monatomic oxygen can be modified to change the total heat of reaction of the dissociation process, which is done for several case shown in Fig. 5.3b. For this test, we hold the equilibrium constant fixed. Although this is not physically realistic because van't Hoff's law shows that the equilibrium constant depends on the heat of reaction, however, for the purpose of demonstration this assumption will be acceptable. As the heat of reaction increases, the damping rate per wavelength increases. Just as in the vibrational damping case, the energy capacity does have an impact on the optimum frequency.

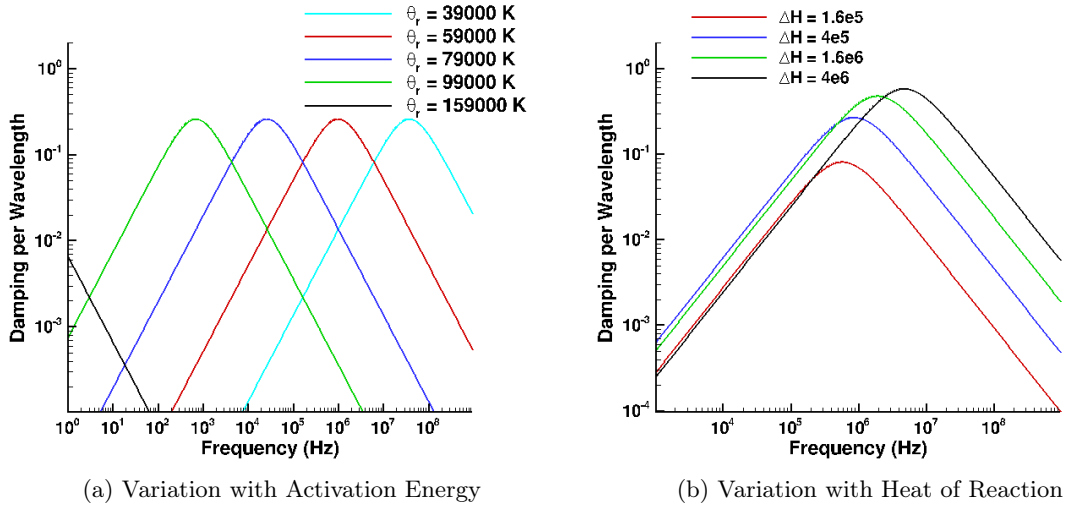
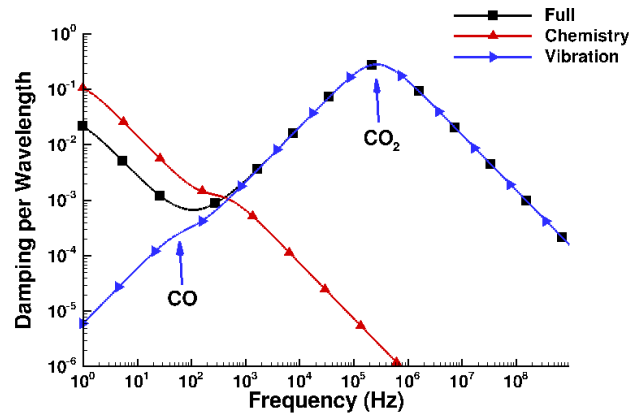


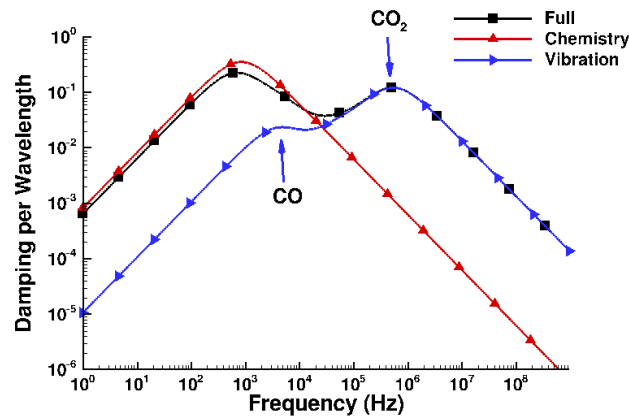
Figure 5.3: Chemical damping processes examples

Knowing the strong dependence of an internal molecular process's relaxation time on the effectiveness of acoustic damping, we can determine which relaxation modes are responsible for damping second mode disturbances given a set of boundary layer conditions. In the case of the sharp cones being tested in the T5 tunnel, the boundary layer temperatures range from 1000 K to 2500 K with a density of approximately 0.1 kg/m^3 . By selectively freezing chemical dissociation and molecular vibration, we can determine the frequency domain for which each of these relaxation modes are capable of damping acoustic waves. We do this for an equilibrium mixture of gas starting from CO_2 with a final density of 0.1 kg/m^3 for two different temperatures. As shown in Fig. 5.4, the molecular vibration has a shorter relaxation time than the chemical dissociation, thus the damping that occurs at higher frequencies is due to the molecular vibration. Because the second mode frequencies that cause transition are in the $1 - 10\text{ MHz}$ range, this serves as further validation that the vibrational modes of CO_2 , particularly the two bending modes due to their low characteristic vibrational temperature, are responsible for the delays in transition seen in the T5 experiments and computations.[58, 6, 71, 13, 56] Another interesting aspect of separating the two types of relaxation modes is that these modes do not necessarily combine in a constructive manner. This is due to the manner with which the acoustic waves pass through the gas. If the frequency of the wave is significantly higher than the optimum frequency, energy does not have time to transfer to the internal mode and the wave sees the gas as a frozen gas. If the frequency of the wave is significantly lower than the optimum, then the energy of the wave transfers sufficiently fast for the internal modes to equilibrate as the wave passes, thus the wave sees the gas in equilibrium. Therefore, the

peak in vibrational damping is unaffected by chemical damping because the chemical processes are essentially frozen at the higher frequencies. The peak in chemical damping is lowered because the presence of a vibrational mode in equilibrium reduces the energy available for chemical dissociation at lower frequencies.



(a) Damping rate at $T = 1750 K$.



(b) Damping rate at $T = 3000 K$.

Figure 5.4: Damping per wavelength versus frequency for an equilibrium mixture of gas starting from CO_2 with a final density of 0.1 kg/m^3 and at two different temperatures. The vibrational mode responsible for each peak in vibrational damping is noted on each plot.

5.1.2 Acoustic Damping for Mixtures of Air and CO_2

Although Fujii and Hornung[6, 5] tested both equilibrium air and carbon dioxide separately, it is important, in this study, to understand the damping properties of various mixtures of these two gas compositions because of their use in Chapter 6. We begin by using Fujii's code to calculate the damping properties of initial mixtures of air and carbon dioxide for increments of ten percent

mass fraction of carbon dioxide starting with zero and ending at pure CO_2 . This is done for a temperature range of $500 - 4000 K$ and density of $0.1 kg/m^3$. The broadband effect of increasing the mass fraction of carbon dioxide is to reduce the damping rate specific to air, while increasing the damping rate of carbon dioxide, as shown in Fig. 5.5 for four mass fractions of carbon dioxide at two different temperatures.

Although the broadband effect is important to understand, it is more relevant to focus on a particular frequency that is present in a hypervelocity boundary layer. As shown in Chapter 6 a good frequency for this analysis is $1 MHz$. Another important metric is the amplification rate of a second mode disturbance in order to gauge relative effect of damping. Based on the acoustic DNS in Chapter 7, the amplification rate per wavelength is approximately 25 percent per wavelength. Thus, a damping rate of five percent per wavelength can be used to determine an effective damping condition. Looking at the damping per wavelength for different temperatures and mass fractions of carbon dioxide, shown in Fig. 5.6a, five percent per wavelength is only reached for temperatures higher than $1500 K$, occurring at a mass fraction of carbon dioxide of approximately 45 percent. This temperature represents the maximum boundary layer temperature of a $5 MJ/kg$ flow of carbon dioxide in the T5 tunnel. Both $2000 K$ and $2500 K$ reach five percent per wavelength at a mass fraction of carbon dioxide of approximately 25 and 20 percent, respectively. These temperatures represent the maximum boundary layer temperature reached in a $10 MJ/kg$ flow of carbon dioxide and air, respectively. Thus, for effective damping in a flow of air with carbon dioxide injection, this analysis suggests that the optimum flow enthalpy be near $10 MJ/kg$ for a practical amount of mass injection into the boundary layer. Reformatting these data to be dependent on temperature, shown in Fig. 5.6b for select mass fractions of carbon dioxide, the optimum temperature for all mass fractions above zero lies between $2000 K$ and $2500 K$. The data show that a reasonable mass fraction of carbon dioxide obtained by injection, ~ 30 percent, requires a temperature of at least $1800 K$ to reach five percent damping per wavelength.

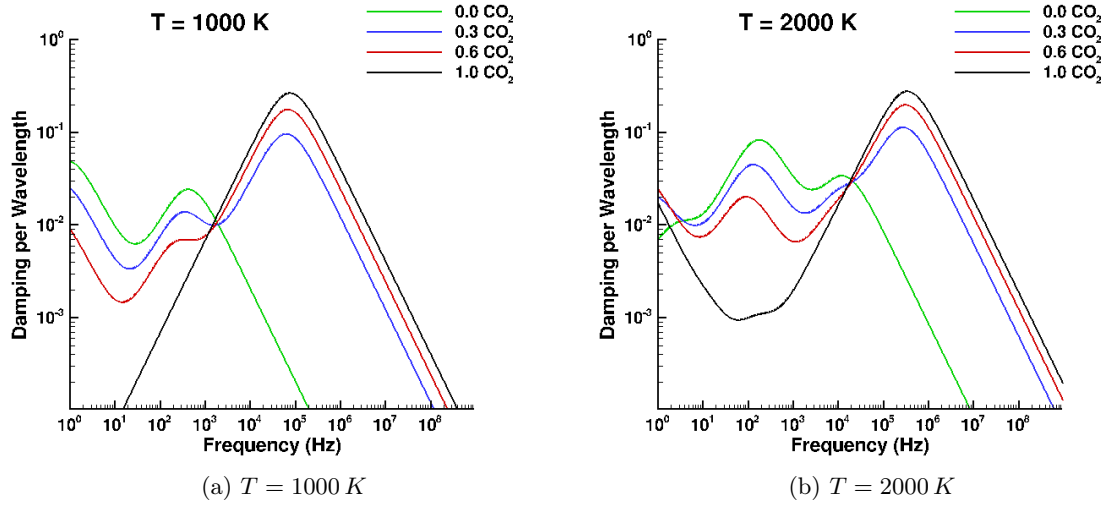


Figure 5.5: Damping per wavelength for various mixtures of air and carbon dioxide at two different temperatures (indicated in the sub-figure caption). As the mass fraction of carbon dioxide increases, the damping per wavelength profile shifts toward the pure carbon dioxide case.

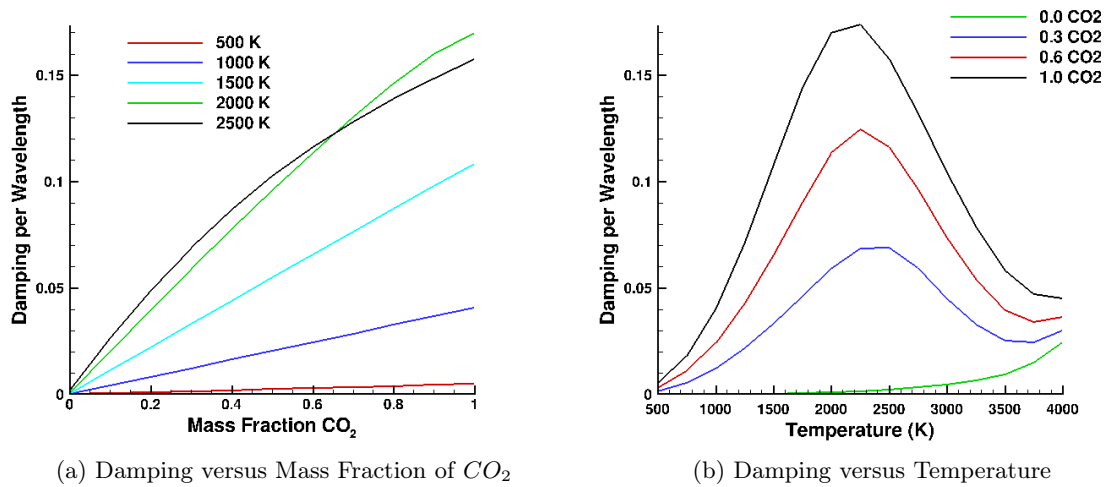


Figure 5.6: Damping per wavelength for various mixtures of air and carbon dioxide at a frequency of 1.0 MHz . The temperature ranges from 500 K to 4000 K with a density of 0.1 kg/m^3 .

5.1.3 Acoustic Damping in a Flow with a Mean Velocity

One aspect of acoustic damping that is not contained in Fujii and Hornung's[5] analysis is the effect of a mean flow velocity. Including a mean flow allows for the estimation of acoustic damping of frequencies in the lab frame, rather than those moving with the gas. Additionally, the new formulation can calculate the differences in damping between acoustic waves moving with the flow,

fast waves, and those moving against the flow, slow waves. Following the analysis in Section 3.3, the wavenumber formula has a similar form to that of Fujii's analysis. Therefore, we can infer how the optimum damping frequency will vary with the mean flow, which is

$$\omega_{opt}\tau_o \propto \text{abs}(M \pm 1), \quad (5.4)$$

where the addition refers to fast waves and the subtraction refers to slow waves. It should be noted that this is an approximation because, as stated in Section 3.3, the wavenumber equation is cubic with the wavenumber and an analytical solution was not found. To confirm this behavior of the optimum damping frequency as well as understand the behavior of acoustic damping from the lab frame, we use a modified version of Fujii's code to test the acoustic damping of carbon dioxide at a temperature of 1000 *K* and a density of 0.1 *kg/m*³ for various Mach numbers. The results of this test are shown in Fig. 5.7. The analysis shows the approximation in Eq. 5.4 to be hold true. As the mean flow velocity increases towards Mach 1, the optimum damping frequency of a slow wave shifts to lower frequency and limits toward zero frequency. Interestingly, the maximum damping rate per wavelength increases as the optimum frequency moves left. The damping rate follows the slope of the frozen wave damping limit on the right, which is inversely proportional to the frequency. This shows that near Mach 1, a slow wave will lose its energy in a relatively small number of wavelengths. This analysis would also seem to say that a slow wave at Mach 1 would have an infinite damping rate and therefore could not exist, however, the equation set used to generate this analysis assumes that the acoustic wave is moving in space and can be described with a spatial wavenumber, which is not the case for a slow wave in Mach 1 flow. As the flow mach number increases from Mach 1 the optimum damping frequency shifts back to the right and at higher mach numbers the optimum occurs at higher frequencies than in a static gas. As shown in Eq. 5.4, a mean flow velocity can only cause the optimum damping frequency to increase for a fast acoustic wave. As in the slow wave case, the frozen damping limit to the right of the peak is maintained. Thus, as the Mach number increases, the flow becomes less effective at damping acoustic waves.

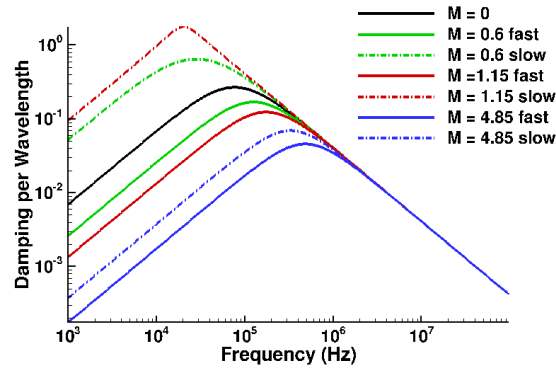


Figure 5.7: Damping per wavelength of the vibrational modes of carbon dioxide at $T = 1000 K$ for various Mach numbers. The behavior of the optimum damping frequency is described by Eq. 5.4. Interestingly, the damping rate on the right of the optimum is not affected by the mean flow.

5.2 Acoustic Wave Simulations

5.2.1 Static Gas Simulations

5.2.1.1 Problem Setup

To recreate the conditions considered by Fujii and Hornung[5], we introduce an acoustic wave into a one-dimensional domain that is 50 cm long and consists of 30050 cells. This domain has two sections, the first of which is 30 cm long and has 30000 equally spaced cells. The second section has cells that quickly increase their length, in order to minimize wave reflection. The domain is filled with an inviscid, static gas in thermal and chemical equilibrium for temperatures ranging from 300 K to 5000 K at a density of 0.1 kg/m^3 . The gas mixtures tested start from a composition nitrogen, air, and carbon dioxide at room temperature. The vibrational relaxation parameters are calculated as suggested by Millikan and White[130], except for all interactions with carbon dioxide, which are calculate based on Camac's rates[119], in accordance with Fujii's code. The wave is passed through the domain at a constant time step determined by having a CFL number of approximately 0.1. The spatial fluxes are calculated using the non-dissipative, sixth-order-central scheme describe above. The time advancement used is the explicit third order Runge-Kutta method. We specify the acoustic wave at the inflow boundary using the formulation given by solving the non-reacting Euler equations. The form of the acoustic wave is given by the frozen wave formula in Eq. 3.31. This serves as an approximation to the fully reacting case, however, this proves to be a sufficient initial condition in several test cases. After the wave has passed through a majority of the equally

spaced section of the domain, the spatial decay of the wave can be calculated. Fujii and Hornung show that this decay should be exponential with distance. Therefore, we determine the maximum amplitude at each half-wavelength and take the natural logarithm of these data. This results in a straight line and has a slope of the damping rate per wavelength.

5.2.1.2 Results

Before we compare the acoustic damping in US3D to the theoretical results of Fujii's code,[5] we first need to determine the dissipation due to the numerical method. We do this by freezing the vibrational mode of the gas being simulated, in this case carbon dioxide, and calculate the acoustic absorption rate. The frozen absorption rate, as indicated by the wave amplitude in Fig. 5.8, was calculated to be essentially zero over the domain. This shows that the numerical method is not adding artificial dissipation to the wave. Next, we allow for both chemical and vibrational processes. For this temperature range, nitrogen is essentially non-reacting, thus is dominated by a single vibrational mode of damping. The results show that US3D matches the damping rates calculated by Fujii's code almost exactly, seen in Fig. 5.9. Oxygen begins appreciably dissociating around 3000 K , adding one degree of complexity to the damping calculation by including damping due to chemical dissociation. As shown in Fig. 5.10a, the temperature range dominated by vibration shows excellent agreement, while the agreement in the region dominated by chemical damping is good until a temperature of 4500 K . Increasing the complexity further, the multiple modes of vibration and dissociation of the carbon dioxide are tested. As with the two previous cases, the damping rates from the two codes show excellent agreement over the range of temperatures dominated by vibrational relaxation, seen in Fig. 5.10b. The range of chemical damping again shows disagreement, however, the overall agreement between the two codes is much better for the carbon dioxide system than the oxygen system. Further investigation is required to determine the cause for the differing behavior between the two damping rate calculations for the regions dominated by chemical dissociation. A possible reason for the discrepancies lies in the method with which the reaction set is handled by each code. As Fujii states, the chemical reaction set is determined by a linearly independent set of reactions and a conservation of atomic species. In his code, the damping rate does include the effects of the linearly dependent reactions, however, this is still different than calculating the forward and backward rates individually. Therefore, the difference in damping rates could be due to differences in the two models.

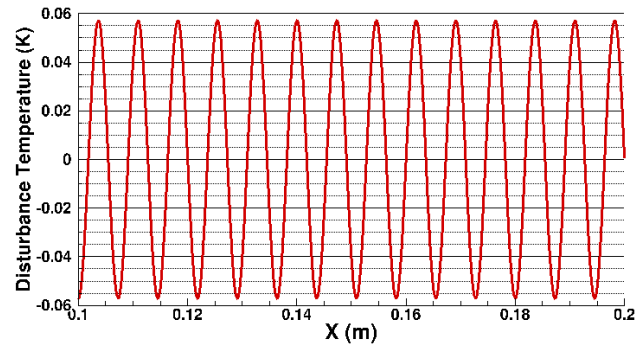


Figure 5.8: A frozen acoustic wave at $T = 1000\text{ K}$ and a frequency of 100 kHz in carbon dioxide. The amplitude of the wave is essentially constant throughout the domain.

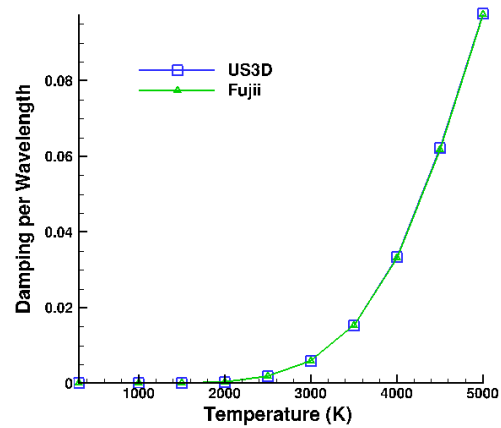


Figure 5.9: A comparison of the damping rate per wavelength for a range of temperatures in nitrogen. US3D matches Fujii's calculation almost exactly.

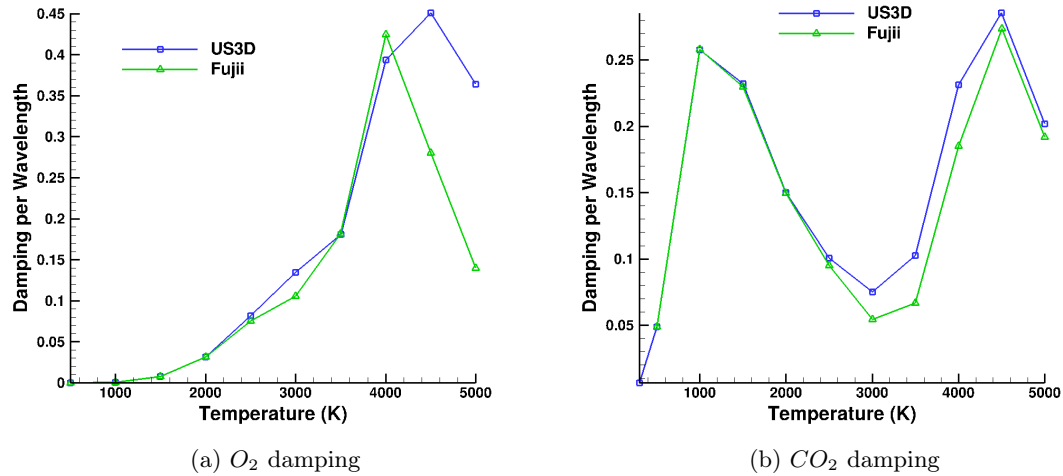


Figure 5.10: A comparison of the damping rate per wavelength for a range of temperatures in oxygen (a) and carbon dioxide (b). The temperature range dominated by vibration show excellent agreement, while the agreement in the region dominated by chemical damping is moderate for oxygen and decent for carbon dioxide.

Now that we have confidence in the ability of US3D to capture the acoustic damping process, we can investigate the behavior of the gas properties as the wave propagates. We begin with the vibrational damping process because US3D shows better agreement with Fujii's code and for its relevance in the following chapters. In the vibrational relaxation case, the internal energy is vibrational energy, characterized by the vibrational temperature, and the driving force is the translational-rotational energy, characterized by the translational temperature. As described in Section 2.1.2, the acoustic damping process has an equilibrium limit at lower frequencies, a frozen limit at higher frequencies, and an optimum damping frequency in between. To see characteristics of the damping process at each of these three stations, we show the use the same frequency through carbon dioxide at different temperatures, indicated in Fig. 5.11. In each of the following cases, the wave is propagating from left to right. Starting with the case of $T_0 = 2500 K$, which demonstrates the equilibrium wave, shown in Fig. 5.12, the transfer of energy to vibration is sufficiently fast that the vibrational temperature is essentially the same as translational temperature. This implies that there exists only a slight phase shift between the translational and vibrational temperatures. The next case has a mean temperature of $1000 K$, which demonstrates a wave with near optimal damping and is shown in Fig. 5.13. In this case, the phase shift between the translation and vibrational temperatures has increased to approximately 55° . The energy transfer rate has slowed such that vibrational mode can no longer equilibrate as the wave disturbs the mean properties,

however, it still not too slow to engage a response from the vibrational mode. Finally, the last case has a mean temperature of 300 K . In this case, the energy transfer rate between the translational and vibrational energies has slowed to the point that the acoustic wave elicits virtually no response from the vibrational mode, as demonstrated by the small vibrational temperature disturbance. The phase shift between the vibrational and translational temperatures has almost reached its theoretical maximum of 90° . In each of these cases, the peak in the vibrational temperature occurs as the vibrational disturbance wave crosses the translation temperature wave, indicating the underlying physics that the driven wave cannot overcome the magnitude of the driver wave.

From these example cases, we can see that starting from zero frequency, where the internal relaxation process is fully equilibrated with the gas, an increase in frequency results in an increase in the phase shift between in the internal process and the properties driving the internal process. This is reflected in the theory describing this process, shown in Eq. 3.43. The optimal damping occurs where the effective frequency, $U_{0,j}k_j - \omega$, is on the same scale as the relaxation time, τ_0 . The evidence for this lies in the denominator of Eq. 3.43 and the equation for the optimum frequency of damping, Eq. 5.1. As the frequency continues to increase, the phase shift grows and the effectiveness of the damping decreases.

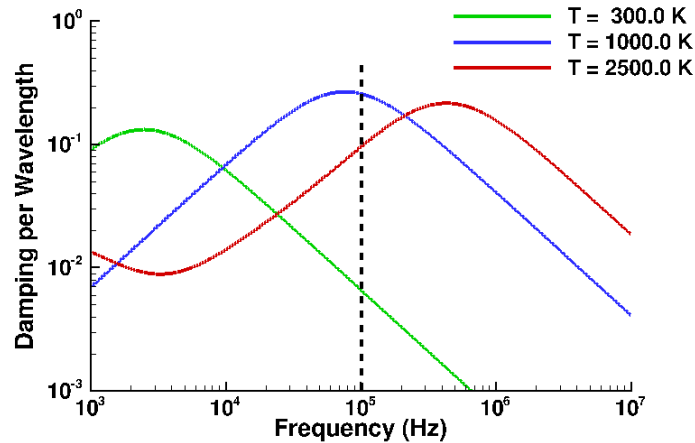


Figure 5.11: The damping rate per wavelength for three different temperatures of carbon dioxide. The black dashed line indicates the frequency used in the simulation, 100 kHz . The three temperatures indicated are chosen to demonstrate the properties of an equilibrium wave, a frozen wave, and a wave with near optimal damping.

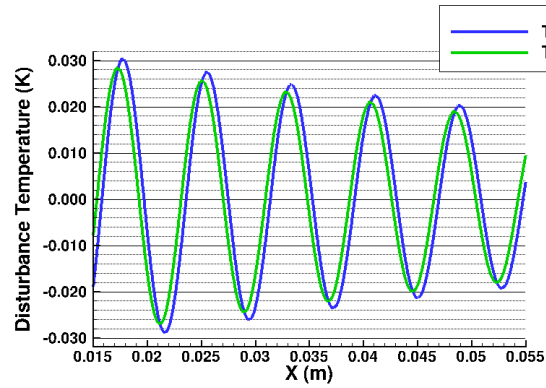


Figure 5.12: An Acoustic wave traveling through carbon dioxide with a frequency of 100 kHz and a temperature of 2500 K . This case demonstrates an equilibrium wave.

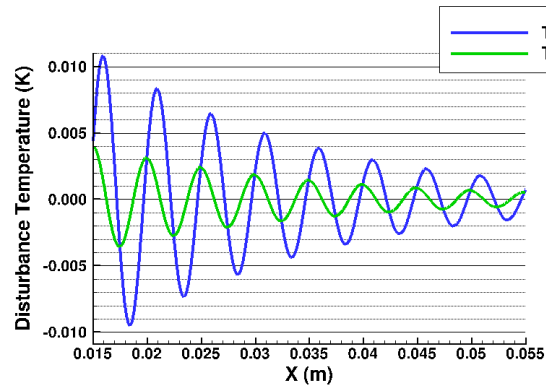


Figure 5.13: An acoustic wave traveling through carbon dioxide in equilibrium with a frequency of 100 kHz and a temperature of 1000 K . This case demonstrates a wave with near optimal damping.

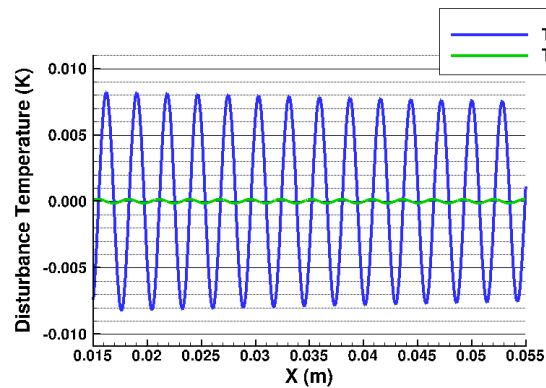


Figure 5.14: Acoustic wave traveling through carbon dioxide in equilibrium with a frequency of 100 kHz and a temperature of 300 K .

Another effect of the damping process is the phase shift that occurs between the pressure wave and the density wave. In the equilibrium limit ($\omega \rightarrow 0$), the compression caused by the pressure

wave instantly affects the density of the gas, thus the density and pressure waves are in phase and travel at the equilibrium speed of sound. As the frequency increases towards the optimal frequency, the gas's internal processes delay the effect of the compression, causing a phase shift between the pressure and density waves. As the frequency reaches the frozen limit ($\omega \rightarrow \infty$), energy can no longer be absorbed into the gas's internal modes. Thus, the pressure wave again instantly affects the density and the two waves are again in phase and travel at the frozen sound speed. This variation in the phase shift of the density disturbance is shown in Eq. 3.44, by the same coefficient that leads the internal mode's variation in Eq. 3.43 in both the numerator and the denominator. However, a better way to see this relationship lies in the imaginary component of Eq. 3.29, which can be rewritten as

$$\frac{(1 - X)}{(\omega\tau^+)^{-1} + X^2(\omega\tau^+)}.$$

At a frequency of zero, the density disturbance lacks the complex component that results in a phase shift of the density wave because the inverse $\omega\tau^+$ in the denominator tends to infinity. At infinite frequency, the density disturbance again lacks a complex component because the $\omega\tau^+$ in the denominator tends to infinity. In simulation, the lag of the density wave is seen in all cases that undergo acoustic damping.

The internal mode for chemistry in Fujii's equation set is the extent of reaction, α , and it follows the same trend as the vibrational temperature in the previous cases. Using data from Fig. 5.10a, three cases with different mean temperatures are chosen to demonstrate the phase shift of the extent of reaction, shown in Fig. 5.15. Starting with a mean temperature of 2500 K, the dissociation process begins and the extent of reaction disturbance wave is essentially zero and has a phase shift of approximately 90°. At 4500 K, the extent of reaction disturbance has a phase shift of approximately 45° for the pressure disturbance, indicating that it is near the peak damping for damping due to oxygen dissociation. Finally, at 5000 K, the phase shift is approximately 35°, which is reflected in the gas's lessened ability to damp the wave. To demonstrate the effect of damping on the pressure, temperature, and species density disturbances in the chemical dissociation process, two cases are chosen from a temperature and frequency regime where the damping is dominated by chemical relaxation. The first case is an equilibrium mixture of oxygen at a temperature of 3500 K and a density of 0.1 kg/m³, shown in Fig. 5.16. In order to compare the different disturbance components, each has been normalized based on the disturbance equation of state, Eq. 3.39, which

is now

$$\frac{p'}{P_0} = \frac{\rho'}{\rho_0} + \frac{T'}{T_0} = \sum_s^{n_s} \frac{\rho'_s}{\rho_0} + \frac{T'}{T_0}.$$

The two species densities lag the pressure disturbance indicating that the gas is damping the wave through chemical relaxation. Because of the dissociation reaction, the density of monatomic oxygen lags the density of diatomic oxygen. The peak in the total density disturbance, which has been omitted from Fig. 5.16 for clarity, lies at a weighted average location of the two species densities. The phase shift between the pressure and density waves results in the temperature disturbance leading pressure wave. The complexity of the chemical relaxation damping process is increased in the second case which consists of an equilibrium mixture of carbon dioxide at a temperature of 4500 K and a density of 0.1 kg/m³. In this case, the density disturbance of the polyatomic molecules, O₂ and CO₂, lead the entire system. The dissociation products of these two polyatomics, CO and O, which have the largest mass fractions at this temperature, lag the pressure disturbance. This figure is included to demonstrate the complexity the chemical system can have on the gas properties caused by the acoustic wave. The phase shift of the total density disturbance for the oxygen and carbon dioxide cases presented is 3.8° and 5.0°, respectively. Based on these phase shifts, we can infer that the carbon dioxide case exhibits a stronger damping effect, which proves true upon calculating the damping rate per wavelength.

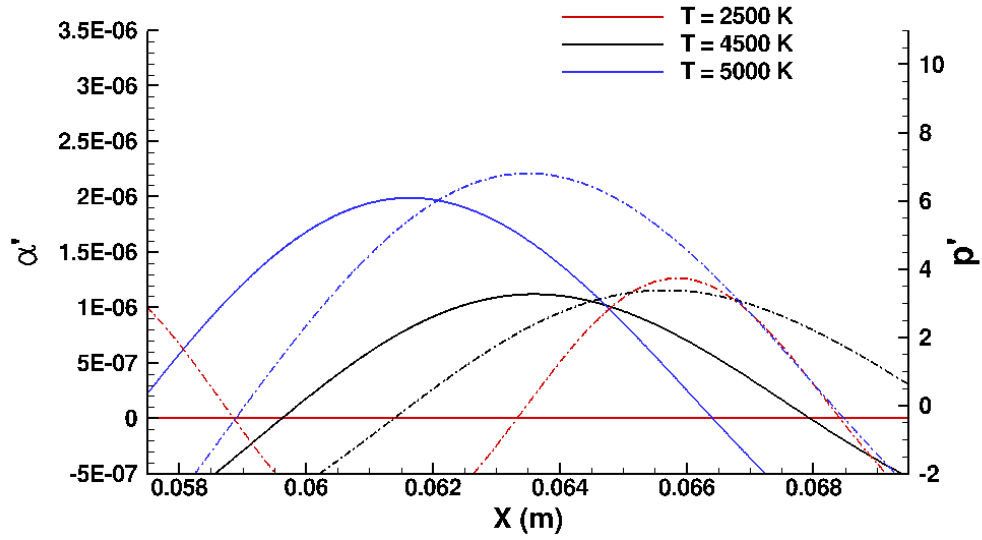


Figure 5.15: The extent of reaction and pressure disturbance waves versus distance. The approximate equilibrium temperature is of each curve is given in the legend. The extent of reaction is plotted using solid lines with the ordinate on the left. The pressure disturbance is plotted using dash-dot lines with the ordinate on the right.

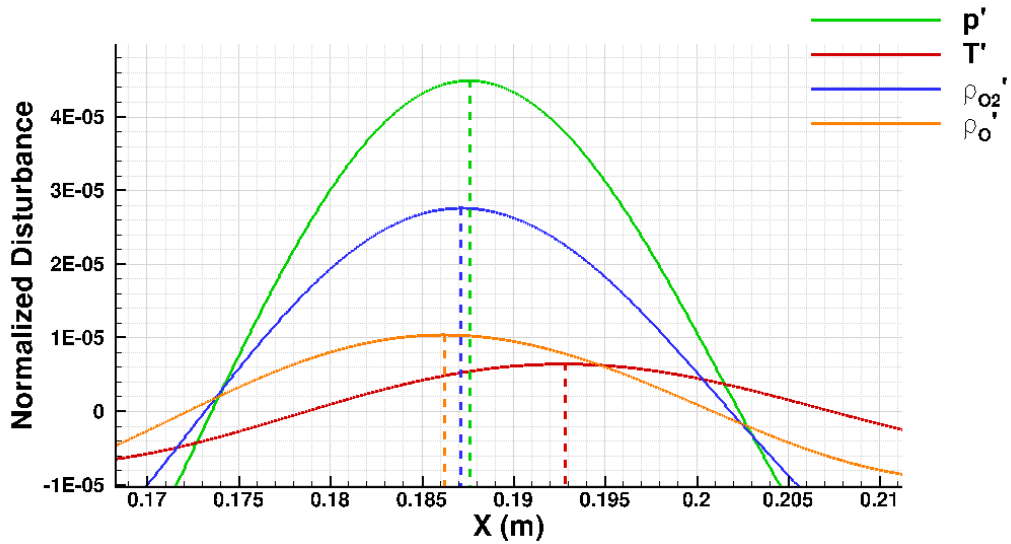


Figure 5.16: Normalized disturbance quantities from an acoustic wave of 20 kHz traveling through an equilibrium mixture of oxygen at a temperature of 3500 K and a density of 0.1 kg/m^3 . In order to clarify the phase shift between each of the components, a dashed line with the same color as the disturbance quantity has been drawn from the peak amplitude to the abscissa axis.

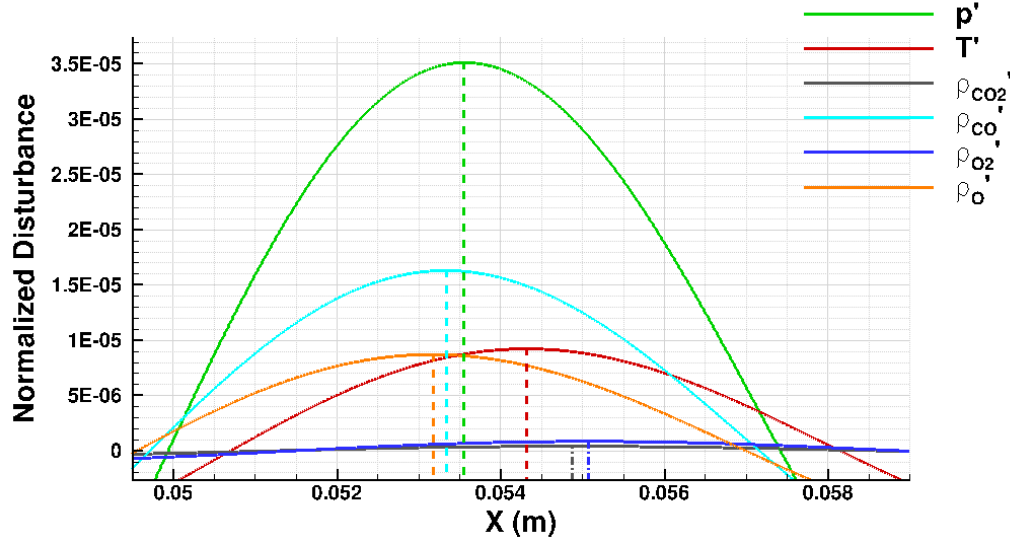


Figure 5.17: Normalized disturbance quantities from an acoustic wave of 100 kHz traveling through an equilibrium mixture of carbon dioxide at a temperature of 4500 K and a density of 0.1 kg/m^3 . In order to clarify the phase shift between each of the components, a dashed line with the same color as the disturbance quantity has been drawn from the peak amplitude to the abscissa axis.

5.2.2 Mean Flow Simulations

5.2.2.1 Problem Setup

In order to verify the equilibrium damping rate, the frozen damping rate, and the optimum damping rate of a slow and fast waves, several different frequencies are tested in the mean flow simulations. Because this implies a varying wavelength, several different grids are made in order to approximately maintain the number of cells per wavelength as well as the grid structure that consists of a constant spacing section and a buffer region. The varying wavelength also requires that the domain length vary in order to capture a sufficient number of wavelengths for evaluation of the damping rate per wavelength. In each case, the domain is filled with an inviscid gas composed of carbon dioxide in thermal and chemical equilibrium with a temperature of 1000 K that has a constant mean flow Mach number of 1.15.

5.2.2.2 Results

A summary of the frequencies tested and their damping rates are shown with the symbols in Fig. 5.18. As seen in the figure, the simulations agree very well with the theoretical calculations at all points. This verifies that the theory of acoustic damping in a gas with a mean flow accurately

describes the physics. Two cases, one a fast wave and the other a slow wave, are chosen to investigate the waveforms of each wave type. In both cases, the mean flow and wave are moving from left to right. We first look at the temperature disturbances of a fast wave, shown in Fig. 5.19. As seen in the figure, a fast acoustic wave appears to propagate in a similar fashion as the static case. The vibrational temperature disturbance lags the translational temperature disturbance in the upstream direction as the gas respond to the driver wave. In the slow wave case, shown in Fig. 5.20, the vibrational temperature disturbance appears to lead the translational temperature disturbance. However, the wavefront of the slow wave is propagating upstream, from right to left, and the mean flow is convecting the disturbances downstream. Thus, knowing that the vibrational response must always lag the temperature disturbance in the upstream direction relative to the waves motion, we should expect to see the peak of the vibrational temperature disturbance to appear downstream of the peak of the translational temperature disturbance relative to the mean flow.

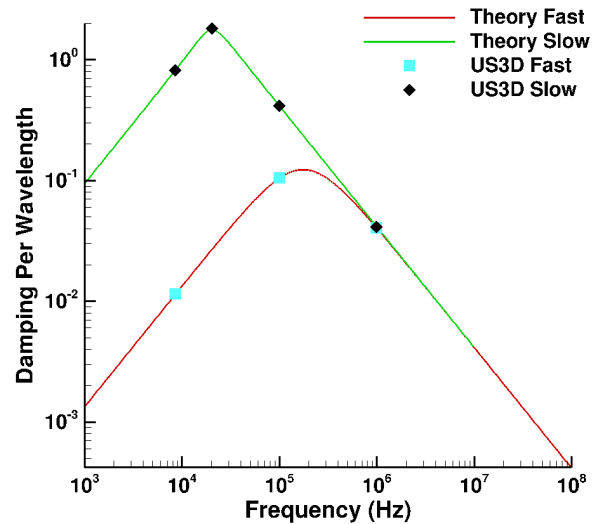


Figure 5.18: Damping rate per wavelength in carbon dioxide with a temperature of 1000 K , a density of 0.1 kg/m^3 , and a mean flow Mach number of 1.15 for both slow and fast acoustic waves. The excellent agreement between the theoretical and computational codes indicate that the theory accurately describes the physics behind acoustic damping. The two data points at 1 MHz overlay each other at the scale of the plot, however, they each lie on top of the corresponding theoretical curve.

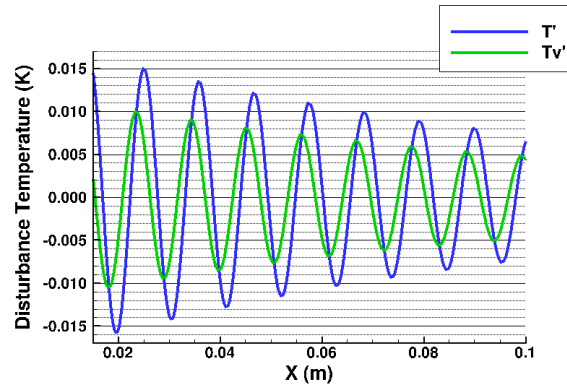


Figure 5.19: A fast acoustic wave traveling through carbon dioxide in equilibrium with a frequency of 100 kHz and a temperature of 1000 K , a density of 0.1 kg/m^3 , and a mean flow Mach number of 1.15. The wave propagates in a similar fashion as in the static cases with the vibrational temperature disturbance lagging the translational temperature disturbance in the upstream direction.

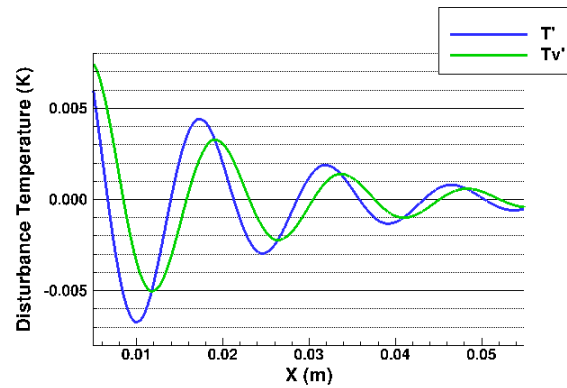


Figure 5.20: A slow acoustic wave traveling through carbon dioxide in equilibrium with a frequency of 8.6 kHz and a temperature of 1000 K , a density of 0.1 kg/m^3 , and a mean flow Mach number of 1.15.

5.3 Conclusion

In this chapter, the parameters for determining the optimal damping frequency for a general internal molecular process is given and applied to molecular vibration and chemical dissociation. The theory shows the interesting result of a maximum damping per wavelength caused by single mode of molecular vibration being approximately 13.4 percent. Using Fujii's code, various mixtures of air and carbon dioxide were tested in order to gain an understanding of the mass fractions of carbon dioxide to cause significant damping in a static gas in equilibrium. Next, that addition of a mean flow velocity was tested and the damping properties of slow and fast acoustic waves was determined.

Using these theoretical data, highly resolved simulations of acoustics are performed. Results showed good agreement between the theory and computations, giving confidence to both the theoretical models and the ability of the simulations to accurately capture the physics of acoustic waves. Using these simulations, various aspect of the acoustic waves undergoing the damping process are examined. Lastly, the theory of acoustic damping with a mean flow velocity is verify through the use of simulation. As in the case of a static gas, the properties of slow and fast acoustic waves undergoing damping are also examined.

Chapter 6

2nd Mode Transition Delay

6.1 T5 Smooth Cone Simulations

6.1.1 Problem Setup

The test body used for all of the acoustic damping cases is based on the model that is used in the T5 tunnel, which is a 5° half-angle cone. This test body is used because a cone is a fundamentally simple, yet important vehicle shape for hypersonics and because of the wealth of test data from previous experiments in the T5 Tunnel[12, 58, 57, 131, 67, 132]. The nose radius of the cone is sufficiently small, $0.06 - 0.15 \text{ mm}$ [57], to allow it to be treated as sharp. Although such a sharp nose is not physically possible under the high-enthalpy conditions common in the T5 tunnel flow, Germain and Hornung found that as a new cone tip (0.06 mm) melted to its stable nose radius (0.15 mm), no measurable change in transition location was detected[57].

For the smooth cone cases, three different chemistry sets were used in the computations in order to reduce the number of species involved with each case. For pure air simulations, a five species air model containing N_2 , O_2 , NO , N , and O is used with three dissociation reactions and two exchange reactions. For carbon dioxide simulations, a five species model containing CO_2 , CO , O_2 , C , and O is used with three dissociation reactions and three exchange reactions. For simulations mixtures of air and carbon dioxide, a seven species model containing CO_2 , CO , N_2 , O_2 , NO , N , and O . The chemistry files used for each of the chemistry sets are contained in the appendix. The vibrational relaxation parameters are those suggested by Millikan and White[130], except for those given in the appendix. A summary of these test cases is provided in Table C.2 in the appendix.

6.1.2 Derivation of Freestream Conditions for T5 Cone Simulations

6.1.2.1 The T5 Tunnel and Assumptions

In order to determine the freestream conditions present in the T5 tunnel, we need to simulate the process that occurs to generate the fluid flow through the nozzle. The T5 tunnel is a free-piston, reflected shock tunnel and a diagram is shown in Fig. 6.1. High pressure air is stored in the secondary reservoir and is released into the compression tube, driving the free piston down the tube. As the piston travels down the compression tube, it compresses the driver gas held inside this section, which is typically pure helium or a mixture of argon and helium depending on the flow total enthalpy. When the driver gas reaches a sufficient pressure, it causes the primary, steel diaphragm to burst. The high pressure driver gas, which is now in contact with the test gas in the shock tube, causes the initial shock to travel down the shock tube. The shock is reflected off of the end of the shock tube which consists of the end wall and a secondary, mylar diaphragm blocking flow through the nozzle. This secondary diaphragm bursts after the shock reflects and is essentially vaporized. The two shocks heat and compress the gas, which then expands and accelerates down the nozzle. The test time for the T5 tunnel is limited to approximately $1 - 2\text{ ms}$. Although this may seem short, this test time translates to several flow times, allowing for a roughly steady state of flow to be obtained over the test article.

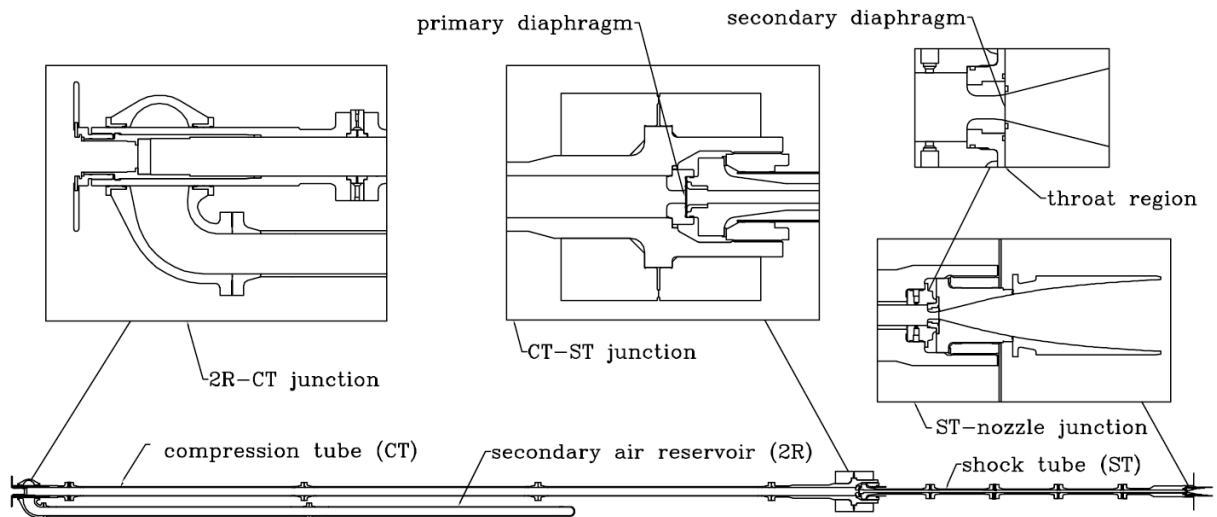


Figure 6.1: A diagram of the T5 tunnel taken from Fujii[4].

Ideally, the reservoir conditions for the nozzle would be calculated based on the initial pressure, initial temperature, gas mixture in the shock tube and the speed of the shock. However, the T5 tunnel experiments typically only report a flow total enthalpy and reservoir pressure, which is based on their own code that calculates the post-reflected-shock conditions. Therefore, we must estimate the reservoir conditions based on these two parameters alone. We first assume that the gas is essentially static after the reflected shock passes and has a sufficient time to reach chemical and thermal equilibrium. Using the code Chemical Equilibrium with Applications (CEA) from McBride et al.[117], we can calculate the gas mixture composition, density, and temperature at equilibrium and specify these conditions at the inflow for a nozzle simulation. Realistically, the reservoir conditions of a reflected shock tunnel at high-enthalpy ($> 5 MJ/kg$) are much more difficult to determine and are still an unsolved problem in fluid flow[41, 133, 42]. The flow through the nozzle may not be fully equilibrated, may contain leaked driver gas[134], particles from one or both of the diaphragms, and carbon molecules from oil used on the mechanical parts. We also assume, for shots involving “air”, the gas composition of air is $0.767 N_2$ and $0.233 O_2$, which ignores the less prevalent components such as argon and CO_2 . Finally, we restrict the reservoir composition to the chemistry sets listed above for their respective test gases. This eliminates some trace species, however, the change to the mixture temperature and density is less than one percent.

6.1.2.2 Nozzle Simulation

We perform this simulation with one of two methods. The first is to use a structured, two-dimensional, axi-symmetric CFD code similar to US3D that was tailored to running nozzle flow simulations and will be referred to as the “Nozzle code”. This CFD code is capable of simulating the flow through the nozzle, however, it has difficulty simulating the nozzle flow over the cone. Thus, the second method is to use an axi-symmetric grid with US3D to simulate the cone in the nozzle. The second method is more computationally intensive, thus is used as a validation of the first method. For each method, a one-dimensional nozzle flow solution is applied as the initial condition in order to aid in starting the supersonic nozzle flow. The inflow boundary condition is subsonic and enforces a constant total enthalpy and total mass flux as well as equal flow properties along all inlet faces.

The first method of obtaining a nozzle flow solution is run on a grid that is 490×217 cells in the streamwise and wall-normal directions, respectively. The wall clustering is such that the first cell

spacing is 10^{-6} times the throat diameter, a good rule of thumb for high-enthalpy nozzles. The Mach contours of shot 2540 are shown in Fig. 6.2 and serve as a sample calculation for all of the smooth cone cases. As seen in Fig. 6.2, a reasonably constant core flow is maintained until approximately 0.2 m down from the nozzle throat. After this location, the flow departs from the one-dimensional nozzle flow approximation and takes on a much more three-dimensional character. An assumption made in the calculation of the smooth cone mean flows below using STABL is a constant inflow condition. Thus, this inflow condition must be specified. In the T5 tunnel, the test cone protrudes a distance of up to approximately 0.5 m into the nozzle itself (personal communication with Joe Jewell). Additionally, as the flow expands through the nozzle, the entire T5 tunnel shifts due to the recoil of firing the piston and again as the piston stops at the end of the compression tube. The shifting of the tunnel causes the test cone's position relative to the nozzle change throughout the experiment. These considerations make it difficult to extract a single set of gas conditions that accurately capture the real nozzle flow. However, a center-line average at the end of the nozzle is chosen to represent the flow conditions for the smooth cone calculations. In order to gauge the consistency of the chosen conditions, a line of data points in the streamwise direction are extracted near the end of the nozzle and are shown in Fig. 6.3. As seen in the figure, the presence of a compression wave at $\sim 0.6\text{ m}$ causes the pressure to vary approximately 24 percent and density to vary approximately 17 percent. However, after the compression wave, the static pressure varies by approximately 7 percent. The mean flow velocity varies by approximately 0.5 percent during the compression wave and approximately 0.2 percent after the compression wave. The presence of the compression wave will be discussed below.

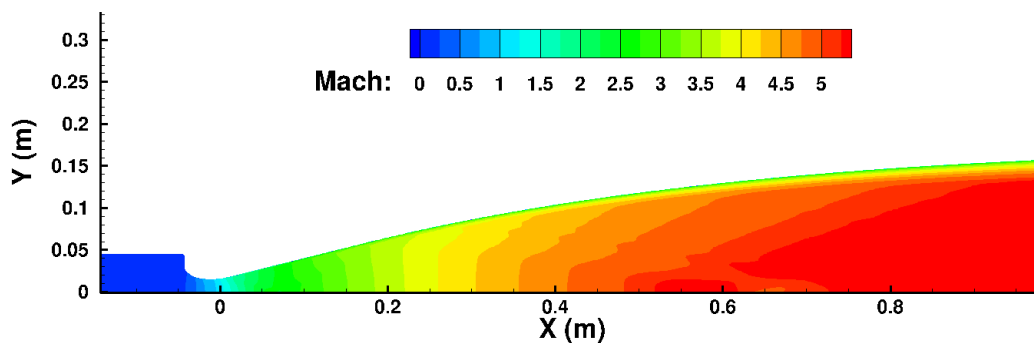


Figure 6.2: Mach contours of shot 2540 in the T5 tunnel based on a Nozzle code simulation.

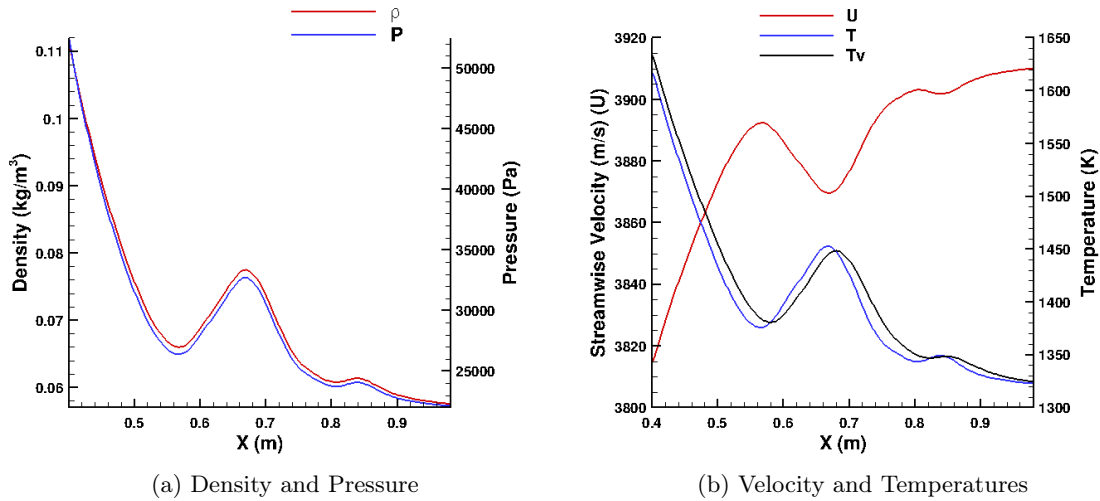


Figure 6.3: Variations in the gas properties near the end of the nozzle based on the Nozzle code simulation.

The second method of obtaining a nozzle flow solution is run on a grid that is 789×291 cells in the streamwise and wall-normal directions, respectively. A sample calculation using this method is shown in Fig. 6.4 with contours of Mach number. The grid structure of these simulations is different than the previous method to accommodate the full length of the cone. As seen in Fig. 6.4, the cone protrudes approximately 0.48 m into the nozzle and the shock that results from the presence of the cone is visible. Also, the T5 nozzle joins with another chamber that has a larger cross-sectional area, which results in a rapid expansion of the flow. Rather than conforming the grid to this complex geometry, an approximation of the change in cross-sectional area is made using a spline and results in a smooth (of class C^2) expansion of the geometry. This effect of the expansion does not interfere with the flow over the cone until 0.1 m from the end of the cone. The effect the expansion has on the wall heat flux is discussed below and verified by Germain[131] and Adam[12].

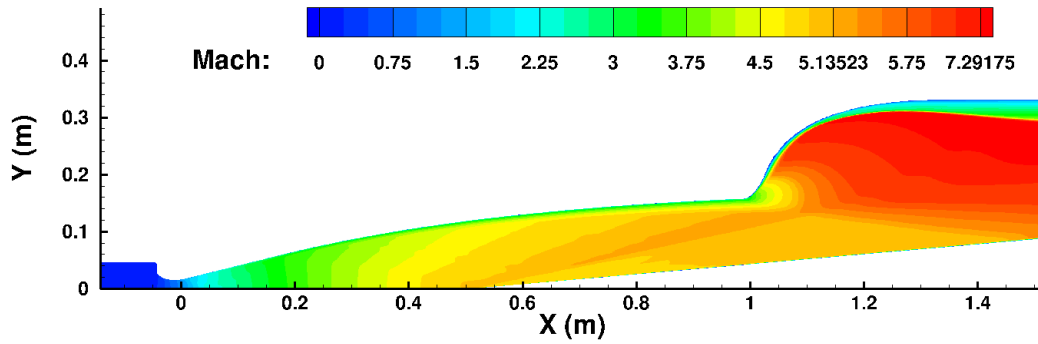


Figure 6.4: Mach contours of shot 2540 in the T5 tunnel based on a US3D simulation.

In order to compare the flow properties calculated by the two codes, a line of sample data is extracted in the radial direction at a streamwise location of approximately 0.45 m , shown in Fig. 6.5. The freestream pressure, Fig. 6.5a, is essentially the same across the nozzle and differ at the wall by 1.5 percent. The streamwise velocity, Fig. 6.5b, compares very well across the entire nozzle. The density, Fig. 6.5c, follows a similar trend as the pressure until the boundary layer, where significant disagreement between the two codes occurs. A similar difference exists for the translational temperature, Fig. 6.5d. Additionally, US3D predicts a larger separation in the vibrational and translational temperatures, approximately 20 K , compared to the Nozzle code, approximately 5 K . Despite the differences in the tunnel wall boundary layer, the two codes show very similar conditions in front of the test cone.

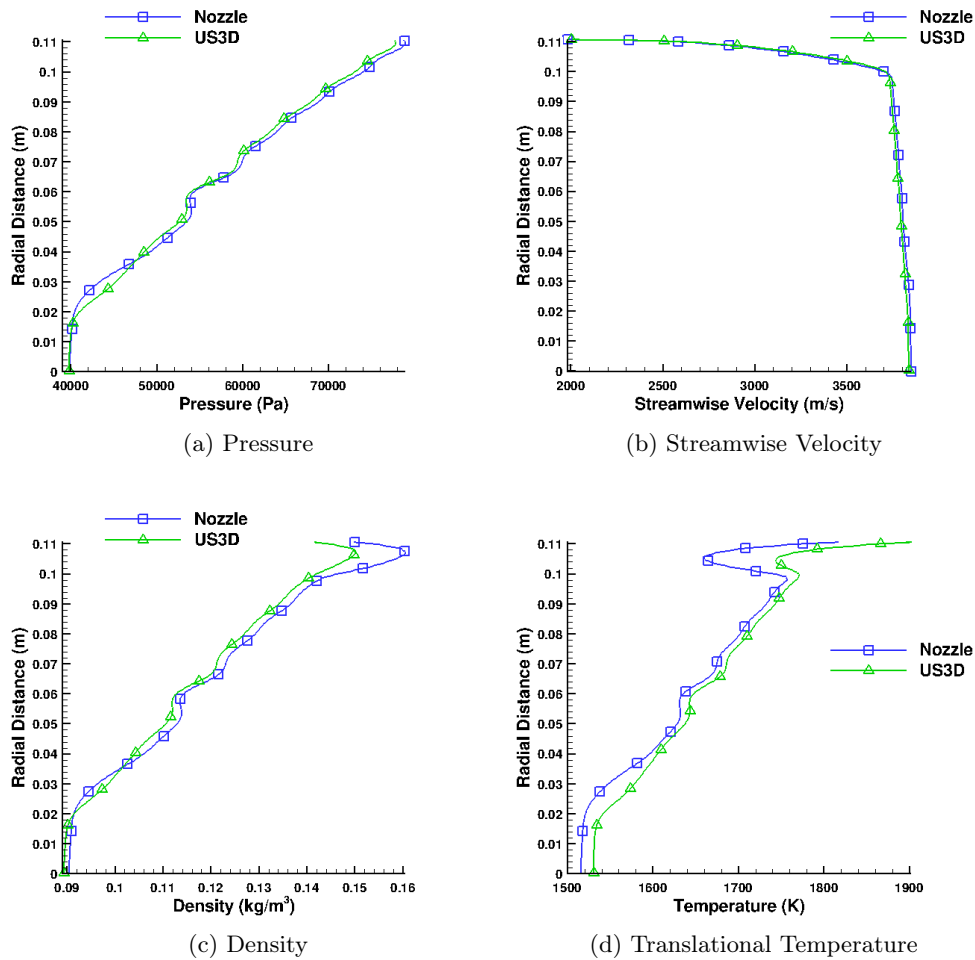


Figure 6.5: Comparisons of various gas properties in the radial direction across the nozzle at a streamwise location of 0.45 m .

As seen in previous figures, a compression wave exists in the nozzle that results in a relatively large variation in the flow properties, especially the pressure. To understand where this wave originates and what its consequences are, contours of the density gradient magnitude are used to follow the evolution of the wave throughout the nozzle, shown in Fig. 6.6. In the sub-figure of Fig. 6.6, the compression wave is shown originating shortly after the throat of the nozzle. This is likely due to one of two reasons. The first is a discontinuous change in the second derivative of the nozzle geometry (personal communication with Hans Hornung and Stuart Laurence). However, this nozzle geometry was designed specifically to avoid this problem and was confirmed using an inviscid computation (personal communication with Hans Hornung). The second reason is that the nozzle geometry causes a bunching of the flow characteristics. This results in a compression wave that reduces the rate of expansion through the nozzle. After being generated near the throat, the

compression wave travels along characteristics crossing the nozzle center-line and reflecting off of the wall at approximately 0.2 m . At this location, the presence of the compression wave causes an oscillation of the boundary layer evident in the density gradient magnitude of Fig. 6.6. The result of this oscillation is several more waves that are emitted from the boundary layer and travel toward the cone. These waves are of sufficient strength to disrupt the shock off of the cone and the boundary layer on the cone, especially the wave that reflects off of the cone wall at approximately 0.7 m .

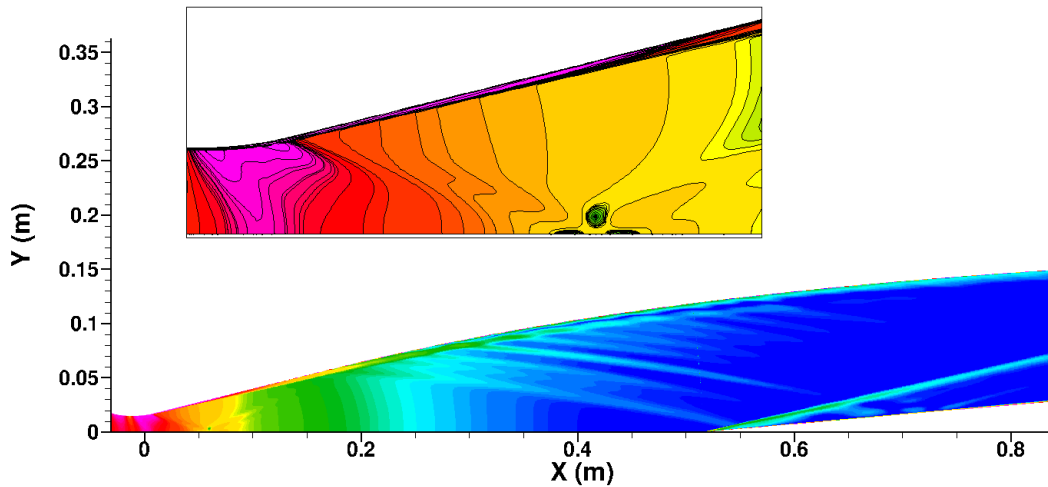


Figure 6.6: Contours of the density gradient magnitude for shot 2540.

6.1.2.3 Heat Flux Comparisons

Applying the approximate freestream conditions calculated using the Nozzle code for a simulation of the mean flow over the cone with STABL, the laminar wall heat flux can be extracted and compared to that which is calculated using US3D, shown in Fig. 6.7. Additionally, the time-averaged heat flux measurements from the thermocouples mounted on the cone are included in the comparison for validation purposes. The two computational methods show very similar heat flux values, with the exception of the increase in wall heating in the US3D simulations that is due to the compression waves reflecting off of the cone surface. The experiment shows higher heating near the nose of the cone relative to the computations. The increased heating in the US3D heating estimate due to the compression wave may be a contributor to these measured heating values. However, more detailed instrumentation would be required to verify that this is correct. Due to the difference in heating magnitudes, it is likely not the only reason for increased heating on the cone in the experiment.

Using US3D, the Spalart-Allmaras[135] turbulence model can be modified such that the entire cone is treated with a turbulent boundary layer to obtain a turbulent heating estimate. Comparing this calculation with the experimental data, shown in Fig. 6.8, reveals that US3D under-estimates the turbulent heating relative to the experiment. Interestingly, the sharp drop-off in heat flux seen in the US3D profile, which is due to the expansion fan from the end of the nozzle impacting the cone, is reflected in the experimental heat flux measurements. This indicates that the cone's position in the nozzle is approximately correct. Extracting the boundary layer edge conditions from the US3D calculation, contained in Table 6.1, the three theoretical heating estimates shown in Fig. 6.8 can be used for additional validation. These heating estimates are calculated following the methods described by Adam[12]. The theoretical turbulent estimates include the van Driest II model and the White and Christoph model. In his thesis, Adam notes that the White and Christoph model offers better results for cold wall experiments. Based on the agreement between these estimates and the experimental heating, it appears that the Spalart-Allmaras model is insufficient for capturing the turbulent heating over the test cone. However, several assumptions and compressibility factors are made in order to calculate the theoretical heating estimates. Additionally, this assertion makes the assumption that the US3D simulation has accurately modeled the flow through the nozzle, which would require a better characterization of the experimental flowfield to prove.

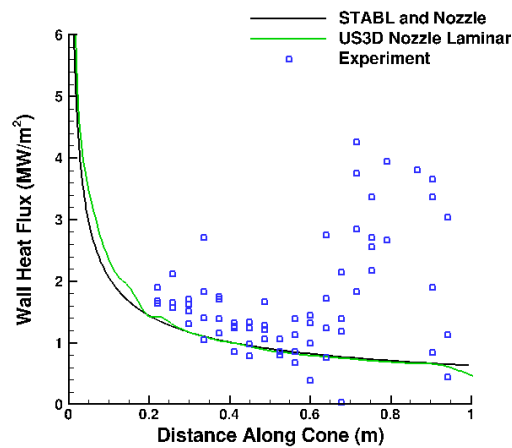


Figure 6.7: Comparison of laminar heat flux between the US3D nozzle simulation, the STABL mean flow calculation, and the experiment

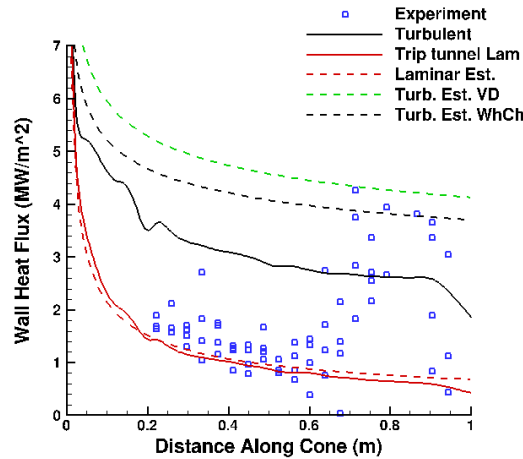


Figure 6.8: Comparison of the laminar and turbulent wall heating from the US3D nozzle simulation, experiment, and theoretical estimates. The theoretical turbulent estimates include the van Driest II (VD) model and the White and Christoph (WhCh) model.

Table 6.1: Edge and Stagnation conditions for shot 2540 extracted from a US3D simulation.

Reservoir Temperature (K)	5953.2	Edge Temperature (K)	1481.4
Reservoir Pressure (MPa)	51.6	Edge Pressure (Pa)	33332
Total Enthalpy (MJ/kg)	9.47	Edge Density (kg/m^3)	0.0774
Wall Temperature (K)	293	Edge Velocity (m/s)	3844.7
Approximate γ	1.4	Edge Mach	4.95

6.1.3 Simulation and Stability Analyses

6.1.3.1 Transition N Factor

With a reasonable estimate of the freestream conditions flowing over the test cone in the T5 tunnel, we can simulate the flow over the cone using the CFD solver contained in the STABL software suite. After reaching steady state, the mean flow provide the base flowfield on which to calculate the boundary layer stability analysis using the PSE-chem solver in STABL. As discussed in Section 3.2, a PSE analysis is performed by guessing a particular frequency at a particular starting location and tracking the downstream evolution of the disturbance at the guessed frequency. Using a linear stability analysis, referred to as an LST analysis, an LST diagram can be generated to guide the placement of the guesses for the PSE analysis by analyzing the amplification of disturbances at a single location in the boundary layer. Additionally, an LST diagram can provide insight in the type of disturbance present in the boundary layer by comparing the amplification at different frequencies to frequency estimates of the various modes. The LST diagram for shot 2540, contained

in Fig. 6.9a, shows amplification, denoted by $-ai$ for the negative of the imaginary component of the wavenumber, α , near to the second mode disturbance estimate. This indicates the boundary layer instability for this flow is caused by second mode disturbances. Once an effective set of guess matrices are generated, the PSE analysis calculates the amplification of each frequency, which is usually plotted as the exponential N factor. Based on this analysis, the boundary layer is expected to transition when any frequency reaches a critical N factors. Therefore, it is common to plot the maximum envelope of N factor across all frequencies. To demonstrate this, the maximum N factor calculated for shot 2540 is shown in Fig. 6.9b. In addition to the maximum N factor, five frequencies are chosen to show how the maximum N factor envelope is determined. The frequency responsible for the maximum N factor at each location can be compared to the amplification determined by the LST analysis, shown in Fig. 6.9a by the curve labeled 'Max N factor'. The curve of most amplified frequency follows the downstream side of the amplification determined by the LST analysis because a given frequencies amplitude is expected to be at a maximum where the boundary layer begins to damp the disturbance after having amplified it. The location of the most amplified frequency also illustrates how a rough estimate of the PSE-based N factor can be calculated by integrating the amplification at a constant frequency from left to right in the LST diagram.

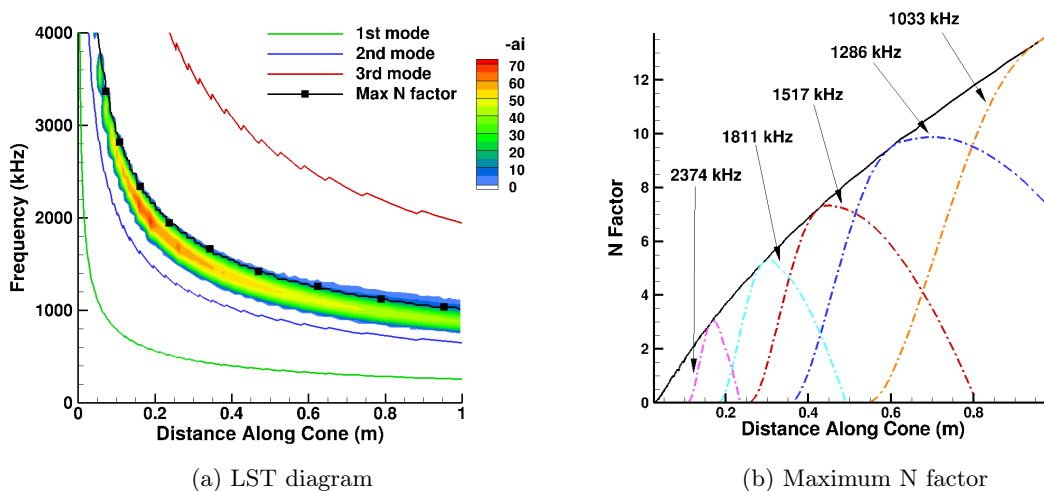


Figure 6.9: Linear stability diagram and maximum N factors from the stability analysis of shot 2540.

Next, the experimental transition location must be estimated. For the current study, two methods for determining this location are used. The first is a qualitative method based on estimating

the location at which the thermocouples on the test cone first depart from the laminar heating estimate. This process is depicted in Fig. 6.10 for shot 2540. Based on the thermocouple data, labeled 'Experiment', the first departure from laminar heating occurs at approximately at 60 *cm* down the cone from the nose. The maximum N factor at this location is approximately 9.5. In this case, the laminar heating estimate is based on the mean flow from STABL. In general, the laminar heating estimate is calculated at the T5 tunnel. Using this method based on simulations from the Nozzle code and STABL for determining the transition N factor, several shots are analyzed and their transition N factors compiled in Fig. 6.11a. The data are based on shots with a test gas of CO_2 from the work of Adam[12] and shots with a test gas of air from Jewell (personal communication with Joe Jewell). Because the thermocouple data from Adam's work were not available, the transition locations are those which Adam estimated. In addition to the transition N factor, error bars are added to each datum and reflect the maximum change in N factor when shifting the transition location by ± 4 *cm*. This is done in attempt to account for some uncertainty in the transition location, that may actually occur at a thermocouple either upstream or downstream of the estimated location (each thermocouple is separated by approximately 4 *cm* [13]. This is motivated in part due to the time-averaged thermocouple data that may potentially mask the variation of the transition location during the tunnel test time (personal communication with Stuart Laurence). The variation in N factor with enthalpy for both gases is unexpected because the T5 tunnel is not classified as a quiet tunnel. Thus, an experimental boundary layer in the T5 tunnel is expected to transition at an N factor of approximately 5.5. Despite this, the current analysis shows the T5 tunnel is capable of quiet tunnel or free flight performance for enthalpies less than 6 *MJ/kg* in carbon dioxide flows and enthalpies greater than 7.5 *MJ/kg* in air flows. Because this conclusion seems erroneous, several different approaches at reanalyzing these data are taken. The first is to evaluate the transition location based on the intermittancy method used and described by Jewell[13] and obtained from Jewell (personal communication with Joe Jewell). This method analyzes the variation in the instantaneous thermocouple measurements throughout the test time. The transition location is determined to occur in the area of the first thermocouple that meets a specified criteria of variation. The transition N factors based on these new transition location are compiled for comparison to the previous data for the air cases in Fig. 6.11b. These new data show slight differences than the previous data, however, the same trend seen in Fig. 6.11a occurs.

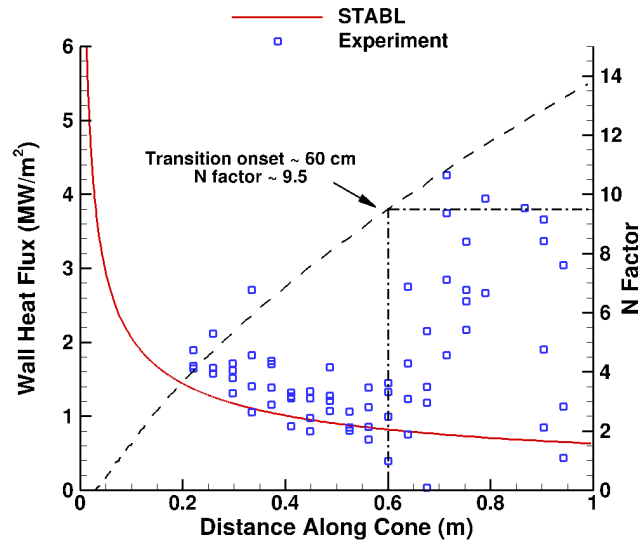


Figure 6.10: Figure depicting the qualitative method for determining the transition location.

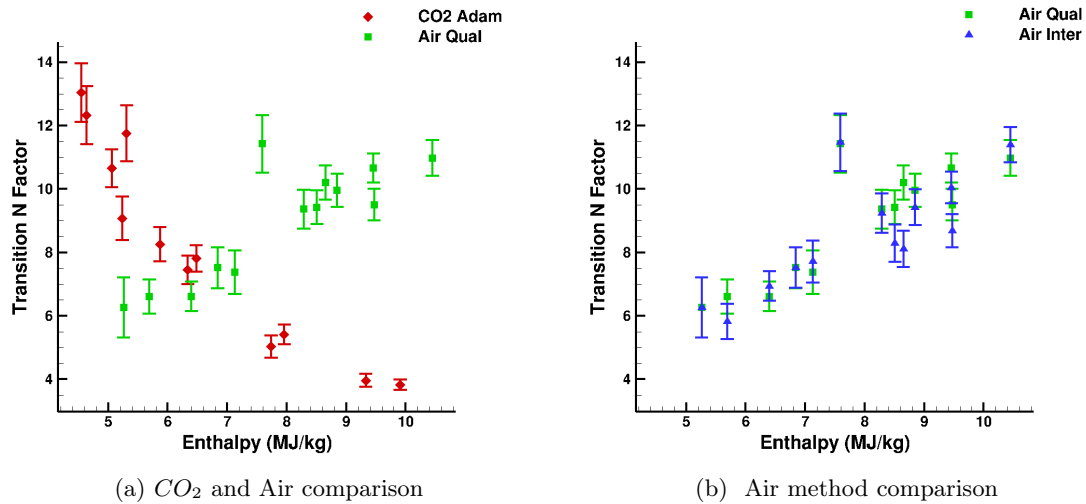


Figure 6.11: Transition N factor versus the flow total enthalpy for flows of Air and CO_2 . The transition location is determined based on the method given in the legend of each plot. “Adam” implies that the transition location was determined from Adam’s data[12]. “Qual” implies the qualitative method of determining the transition location. “Inter” implies the intermittancy method for determining the transition location described by Jewell et. al[13]. The error bars on each datum are calculated as the maximum change in N factor when shifting the transition location by ± 4 cm.

6.1.3.2 Transition Reynolds Number

In order to compare the transition data for the carbon dioxide cases, the transition Reynolds number based on Eckert’s reference temperature, Re_{tr}^* , is calculated from the mean flow obtained from

STABL. In Germain and Hornung[57] and Adam[12], it is shown that high-enthalpy transition due to second mode disturbances can be correlated using this metric. The formula for Re_{tr}^* is the following

$$\text{Re}_{tr}^* = \frac{\rho^* U_e x_{tr}}{\mu^*},$$

where U_e is the boundary layer edge velocity and ρ^* and μ^* are evaluated at the reference temperature assuming that the pressure and mass fractions at the boundary layer edge are held constant. The reference temperature is calculated using the following

$$\frac{T^*}{T_e} = 0.5 + \frac{\gamma - 1}{12} r \cdot M_e^2 + 0.5 \left(\frac{T_w}{T_e} \right),$$

where r is the recovery factor, T_w is the wall temperature, M_e is the boundary layer edge Mach number, and T_e is the boundary layer edge temperature. In this case, the recovery factor is approximate as the square root of the Prandtl number, $\sqrt{\text{Pr}}$. These data are compiled for comparison to Adam's data[12] in Fig. 6.12a. Both the current data and data from Adam show significant scatter, however, the trend of the current data show a decreasing transition Reynolds number with increasing enthalpy while Adam's data show the opposite trend. The same comparison is performed for the air cases and is shown in Fig. 6.12b. Because the shots simulated are not the same as those in Adam[12], shots with similar total flow enthalpies are taken from Adam[12]. The current data set are of the similar magnitude and show the same trend with enthalpy as those of Adam, however, the slope at which the transition Reynolds number increases is greater for the current data. In order to understand the similarities and differences in the transition Reynolds number, some sample data from these calculations are contained in Tables 6.2 and 6.3. The carbon dioxide flows show similar edge densities, however, the Adam's edge temperature shows a greater variation than the current set of data. More importantly, the reference temperature lies below the edge temperature in Adam's data, while it is greater than the edge temperature for the current data. This indicates that the conditions and gas composition calculated at the boundary layer edge differ significantly. This difference could be due to the differences in the method that the nozzle flow is calculated as well as differences between the chemical reaction and vibrational relaxation rates. For the air cases, the edge densities are not expected to be similar because the comparison shots do not have identical reservoir pressures. Both the edge temperatures and the reference temperatures are similar. This indicates that, for the air cases, the conditions and gas composition between the current data and

Adam's data are similar.

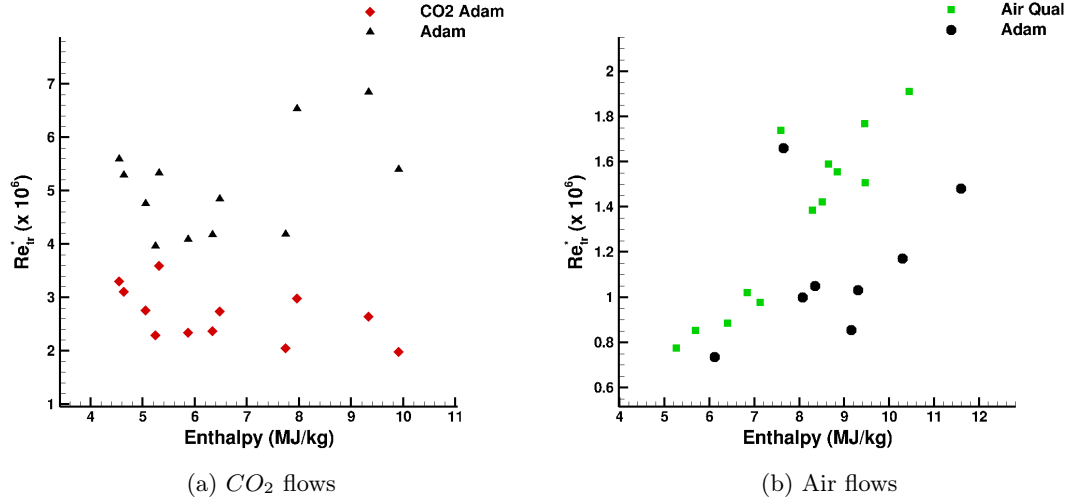


Figure 6.12: Comparisons of Re_{tr}^* versus the flow total enthalpy for flows of air and CO_2 . The data for the CO_2 cases are based on the same shots, while the air cases are based on two different shot series.

Table 6.2: Comparison of conditions for the CO_2 cases.

Shot	T_e (K)	T^* (K)	ρ_e (kg/m^3)	T_e (K)	T^* (K)	ρ_e (kg/m^3)
1121	2402	1559	0.0812	1992.40	2463.55	0.08315
1123	1760	1535	0.1527	1594.33	2012.19	0.15733
1126	1196	1174	0.2290	1251.59	1632.16	0.23268

Table 6.3: Comparison of conditions for the air cases.

Shot	T_e (K)	T^* (K)	ρ_e (kg/m^3)	Shot	T_e (K)	T^* (K)	ρ_e (kg/m^3)
1152	1472	2371	0.0661	2614	1551.21	2367.61	0.074080
1156	1255	2104	0.0797	2616	1330.31	2108.81	0.083807
1157	881	1602	0.1032	2537	1054.78	1769.58	0.081922

6.1.3.3 The Effect of Internal Processes

As demonstrated in Chapter 5, the rate of relaxation for an internal process can have a significant effect on the growth and decay of acoustic and second mode disturbances. One assumption made in simulating these flows is that the chemical reaction and vibrational relaxation rates are representative of the gas in the experimental flow. If these rates are incorrect, then the damping due to the gas's internal process would be misrepresented, leading to an incorrect transition N factor.

In order to gauge the potential for change in transition N factor, we can use a unique feature of the computational stability analysis, which is to freeze both the chemical and vibrational modes in the mean flow and stability analysis. For the current analysis, these internal modes are only frozen during the stability analysis in order to obtain an estimate of the disturbance energy absorbed by the modes. The transition N factor from select cases is compiled in Fig. 6.13. For both gases, the vibrational relaxation is responsible for disturbance damping. In the carbon dioxide, a greater amount of disturbance damping occurs as compared to the air cases. Based on data from Chapter 5, this is expected. If the relaxation parameters of carbon dioxide were different, it might allow for more damping at lower enthalpies and less damping at higher enthalpies, bringing the transition N factor closer to that of conventional wind tunnels. Also, if the vibrational relaxation properties of the oxygen and *NO* in air were different, it may result in larger disturbance damping at high enthalpies.

Another aspect that may be present in high enthalpy facilities is a variation of the tunnel noise radiated from the turbulent boundary layer on the tunnel walls due to acoustic damping. Because the linear PSE does not take into account the freestream noise levels, the trends in the data in Fig. 6.11a could indicate a varying level of freestream noise. At lower enthalpies of carbon dioxide flows, the flow through the nozzle maintains a higher mass fraction of carbon dioxide at temperatures and pressures favorable for acoustic damping. At higher enthalpies of air flow, the gas composition, temperature, and pressure is more favorable for acoustic damping. Sample data of the gas properties for select cases has been extracted and analyzed for acoustic damping, shown in Fig. 6.14. These data are taken at a location obtained by following the characteristic lines from the approximate location of the cone nose to the tunnel boundary layer edge. Because this is only an estimate, damping properties based on a static gas, shown in Fig. 6.14a, and those based on a gas with a mean velocity, shown Fig. 6.14b, are used. At first glance the static gas damping exactly reflects the trend in transition N factor seen in Fig. 6.11a. However, the magnitude of damping between the air cases and carbon dioxide cases are sufficiently different that one would expect a larger difference in transition N factor between the two gas compositions. Adding a mean flow, maintains the trend seen in the static gas analysis, while lowering the damping that occurs in the carbon dioxide cases. However, the problem of the magnitude disparity still exists between the two gas composition, making acoustic damping of the tunnel noise unlikely to have a dominant role in the transition N factor variations.

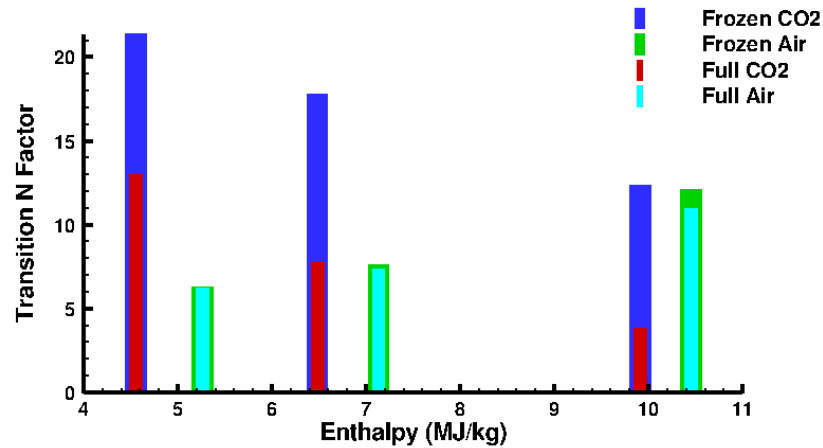


Figure 6.13: Transition N factor versus total enthalpy based on a stability analysis with chemical reactions and vibrational relaxation ('Full') and a stability analysis without any internal processes ('Frozen') for two cases of air and two cases of carbon dioxide.

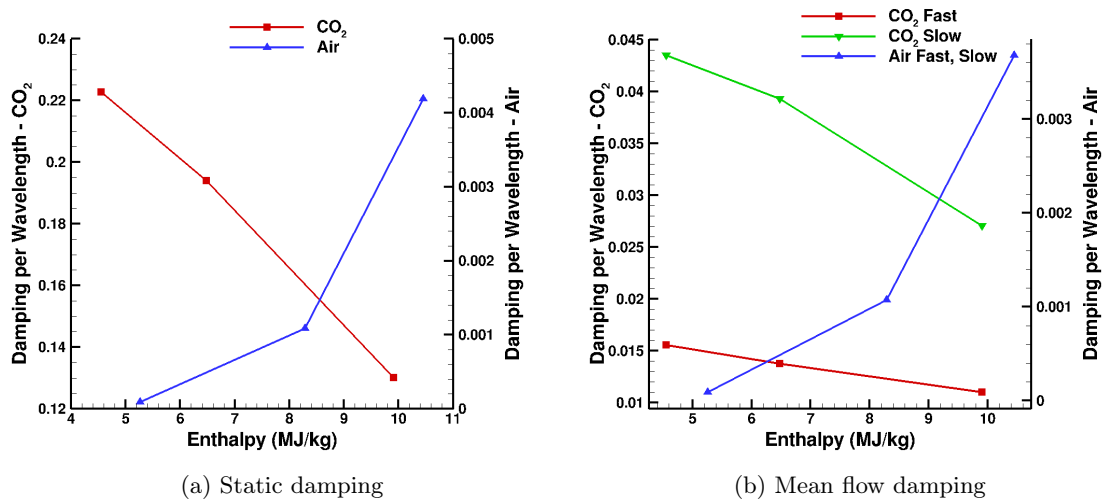


Figure 6.14: Damping per wavelength versus total enthalpy for three cases of air and three cases of carbon dioxide with and without a freestream velocity. The flow properties for these cases are taken from a location based on following the acoustic characteristics from the cone nose to the boundary layer edge on the tunnel wall.

6.1.3.4 Realistic Nozzle Flow Effects

Lastly, we consider the effect of a varying freestream over the test cone shown in Figs. 6.4 and 6.5 based the US3D nozzle simulations. The mean flow data over the cone are extracted and a stability analysis is performed for select cases of the air flows. A comparison of the maximum N factors calculated based on simulations from the Nozzle code and US3D, shown in Fig. 6.15, shows the

two methods produce a similar disturbance amplification near the nose, however, the overall effect is to reduce disturbance amplification. The compression waves seen in Fig. 6.6 impact the cone at approximately $0.2m$ from the nose, which results in the large variation in the N factor at this location. Based on the transition locations obtained using the qualitative method, the effect of the varying freestream is to lower the transition N factor, as shown in Fig. 6.16a. Although the transition N factor is lower in the US3D cases, it still remains much higher than the conventional tunnel level of 5.5. The effect of the transition Reynolds number, shown in Fig. 6.16b is similar and moves the current data set closer to Adam's data. However, the current data still show a larger increase in transition Reynolds number with an increase in total enthalpy. This analysis does highlight the potential importance of the cone location on the transition N factor

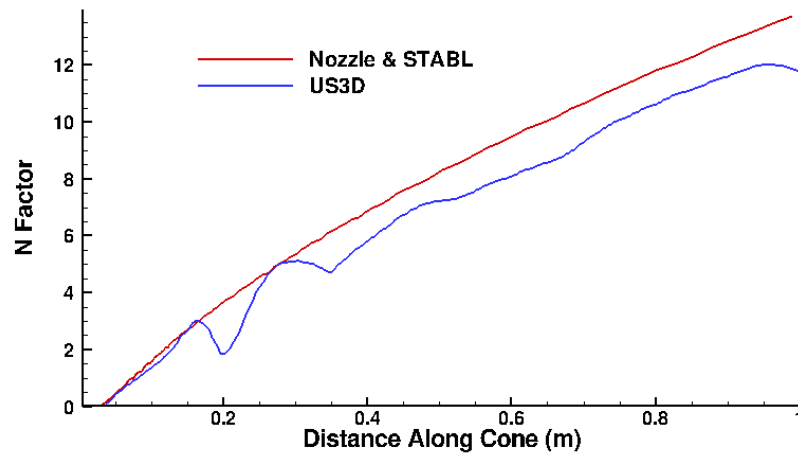


Figure 6.15: Comparison of the maximum N factor versus distance along the cone between the stability analysis based on the Nozzle code simulation ('Nozzle & STABL') and the stability analysis based on the US3D simulation ('US3D').

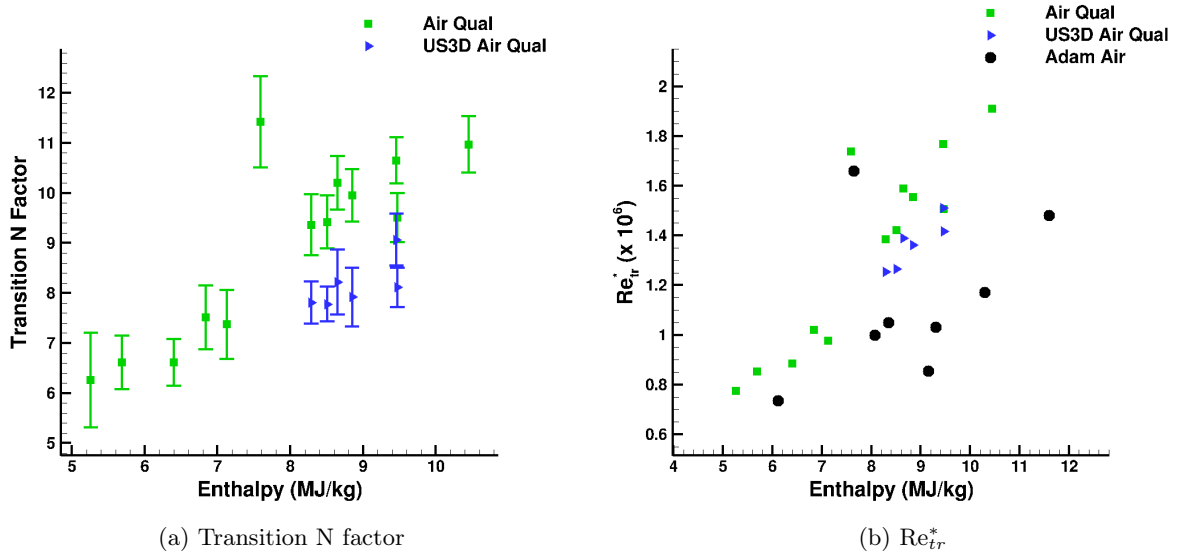


Figure 6.16: Comparison of the transition N factor and Re_{tr}^* versus total enthalpy between the stability analysis based on the Nozzle code simulation and the stability analysis based on the US3D simulation.

6.1.4 Conclusion

Although a successful comparison of data obtained by computational analyses to data from smooth cone experiments was not obtained, several factors present in high-enthalpy flow experiments were identified. This analysis displays to some degree the difficulty and complexity of producing and understanding the high enthalpy flow environment. In order to obtain better agreement between computations and experiments, the flow in reflected shock tunnels like T5 must be better characterized to verify the accuracy of simulation. Additionally, the models and rates used to model non-equilibrium process must be reanalyzed in order to guarantee an accurate representation of the flow in high enthalpy facilities.

6.2 Theoretical Injection

6.2.1 Nitrogen Freestream

We now move onto gas injection, by first considering a purely theoretical test body in order to gain a basic understanding of the injection process, create an expectation for the simulation of the T5 cone below, and also isolate the effects of non-equilibrium processes. For the first set of cases, the free-stream is composed of only nitrogen in an attempt to reduce the influence of the free-stream

gas. Based on the work by Fujii and Hornung[6], nitrogen has a lower absorption rate of acoustic energy as compared to air, which will further reduce the free-stream gas's ability to damp second mode disturbances. These theoretical injection cases have mass transpired over a interval starting at 10 cm and ending at 90 cm from the nose of the cone. The injection profile is gradual and is based on a wall-suction model suggested by Malik[46] and further investigated by Johnson et al.[136]. The mass flux through the wall is specified by edge properties and a dimensionless wall blowing parameter, f_w , seen in Eq. 6.1.

$$f_w = \frac{\sqrt{2Re_x}\rho_w v_w}{\rho_e v_e} \quad (6.1)$$

In this equation, Re_x is the Reynolds number based on the surface distance along the cone, ρ is the fluid density, v is the fluid velocity, the subscript e denotes boundary layer edge properties, and the subscript w denotes wall properties. For these cases the parameter f_w is held constant, making the mass flux vary along the length of the cone. Using this model, it should be possible to see the effects of non-equilibrium processes that support previous work[58, 56, 6]. The grid for these simulations is composed of a structured set of quadrilaterals. The wall-normal direction has 300 cells with the spacing at the wall set such that the y^+ value is less than one and the maximum geometric growth rate is 2.7 percent. The wall-tangential direction has 1000 cells, which are clustered to the nose of the cone and have a maximum growth rate of 4.4 percent. The conditions for the following simulations are chosen to be similar to shot 548 performed in the T5 tunnel, with the properties contained in Table 6.4. The free-stream total enthalpy is such that the flow should achieve a temperature range in the boundary layer where carbon dioxide is capable of acoustic damping. As previously stated, the free-stream consists of a partially dissociated mixture of nitrogen. The chemistry sets used for these simulations are combinations of those given above with the addition of Argon. The vibrational relaxation parameters for the nozzle flow are those suggested by Millikan and White[130], except for those given in the appendix. For the cone flow, the vibrational relaxation parameters are those suggested by Millikan and White[130]. The free-stream Mach number is 6.5 and the wall condition is isothermal with a temperature of 293 K. Several cases of cold gas injection are run with f_w ranging from 0.05 to 0.6. The effect of pre-heating the injection gas to a temperature of 1000 K is also tested in several cases with f_w ranging from 0.05 to 0.4. Finally, several cases are run without the presence of vibration with a f_w value of 0.1. A summary of these test cases, as well as total mass flux for each case, is included in the appendix in Table C.3.

Table 6.4: Freestream Conditions for the first set of theoretical injections cases.

Stagnation Conditions		Freestream Conditions		Edge Conditions	
Pressure (<i>MPa</i>)	55.0	Density (<i>kg/m³</i>)	0.51855	Unit Reynolds (<i>1/m</i>)	$6.0003 * 10^6$
Temperature (<i>K</i>)	6958	Temperature (<i>K</i>)	925.5	Density (<i>kg/m³</i>)	0.072
Enthalpy (<i>MJ/kg</i>)	9.39	Velocity (<i>m/s</i>)	4039.7	Velocity (<i>m/s</i>)	3975

6.2.2 Smooth Cone and Cold Carbon Dioxide Injection

A cone without injection is also tested to provide a baseline transition location from which to gauge transition delay, shown in Fig. 6.17a. Using the same critical N factor as in shot 2540, transition is expected to occur near 66 *cm* from the nose of the cone. Wall-blowing usually has a destabilizing effect on a boundary layer, so it is expected that increasing mass flow rate of blowing would cause a decrease in stability. However, we expect the stabilizing effect of carbon dioxide to reduce disturbance amplification. The stability results for the cold carbon dioxide injection are as expected and are contained in Fig. 6.17b. Initially, the injection of carbon dioxide increases the stability moving transition back to 75 *cm*. As the mass flux increases the amplification increases, indicating an optimum amount of injection. When f_w is 0.3, the stabilizing effect of the carbon dioxide is offset by the destabilizing effect of blowing. For the higher values of f_w this destabilizing trend continues.

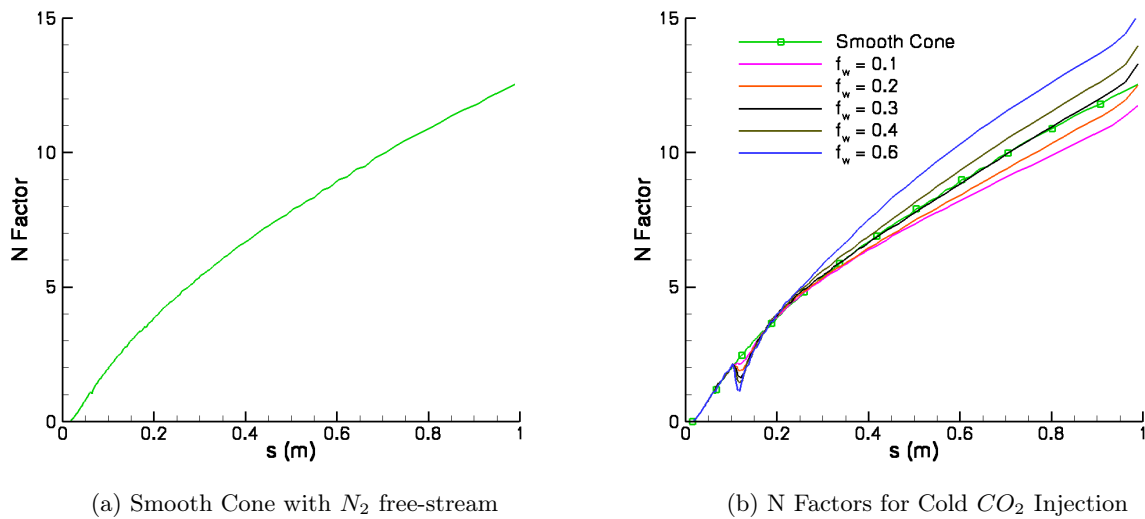


Figure 6.17: These plots show the stability analysis results for the smooth cone, a), and cold carbon dioxide injection, b), with a free-stream composed of nitrogen. The free-stream conditions for these cases are contained in Table 6.4. The case with f_w set to 0.1 shows the maximum transition delay. Cases with higher mass flux result in more amplification.

6.2.3 Alternate Injection Gases

The stability analyses of the alternate injection gas cases, seen in Fig. 6.18, show that only a small difference exists between the injection of air, nitrogen, and argon and that blowing for all three of these gases only destabilizes the boundary layer. These qualities suggest that the stagnation enthalpy of the free-stream is too low to take advantage of the non-equilibrium effects of oxygen and nitrogen and are in agreement with the previous experiments at T5 and the analysis performed by Fujii and Hornung[6, 5]. Argon is added to this set of cases because argon lacks a vibrational mode and has a similar molecular weight to carbon dioxide, which provides a similar impact of injection relative to carbon dioxide without the effects of vibration. As seen in Fig. 6.18, the injection of argon increases disturbance amplification to a similar level as that of air or nitrogen, verifying that it is the presence of vibration that causes the delay in transition location. The reason for this delay will be discussed below in Section 6.2.5.

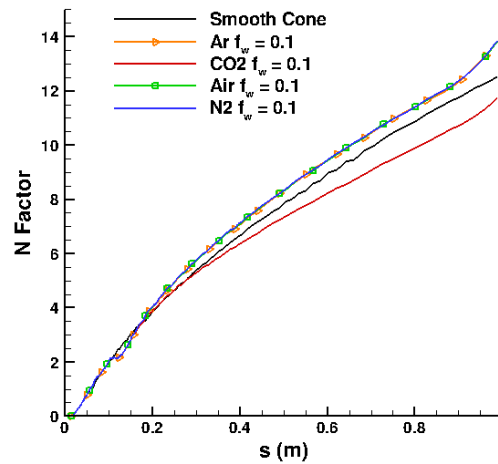


Figure 6.18: This plot shows the stability analysis results for select cases of alternate gas injection. The injection of the alternate gases results in larger disturbance amplification than in the smooth cone case.

6.2.4 Heated Gas Injection

One option to increase the effectiveness of the disturbance damping of carbon dioxide is to pre-heat the gas before injecting it. The goal of pre-heating is to reduce the distance required for the high temperatures in the boundary layer to heat the cold injection gas to temperatures ideal for acoustic damping. In the STABL CFD solver, pre-heating is accomplished by changing the wall temperature to be higher over the injection section versus the surrounding areas. The stability analyses, seen in Fig 6.19, show transition delay for all cases tested with heated carbon dioxide injection, as expected. However, as discussed in Section 2.1 and in Malik[46], wall heating tends to reduce second mode disturbance amplification. In order to isolate the effects of damping due to carbon dioxide and wall heating on the transition delay, we can run two addition cases: one with a higher temperature solid wall and one with injection of a heated gas that does not cause transition delay such as N_2 . The stability analysis results, shown in Fig. 6.20, show that the higher wall temperature smooth cone case does have a reduction in disturbance amplification as compared to the cold wall case. However, the reduction in disturbance amplification between the case of pre-heated carbon dioxide injection and of higher wall temperature is larger than the reduction between the cold carbon dioxide and smooth cone cases. This indicates that the contribution of vibration to disturbance damping is greater in the pre-heated injection case as expected from theory. Also, the injection of pre-heated N_2 , which has approximately the same disturbance amplification as compared to the cold smooth

cone case, results in promoting transition relative to the hot wall case, just as in the cold wall case

Using a critical N factor of 9.5, the estimated transition location can be measured. A summary of these locations for all of the theoretical cases tested is plotted in Fig 6.21.

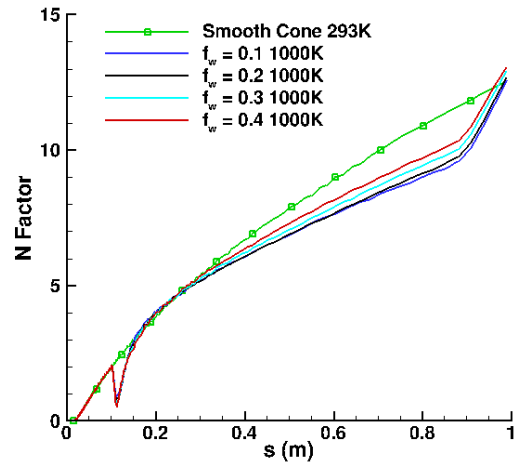


Figure 6.19: This plot shows the stability analysis results for select cases of heated CO_2 injection. The wall temperature in each case is indicated in the legend. The transition delay occurs for all cases tested.

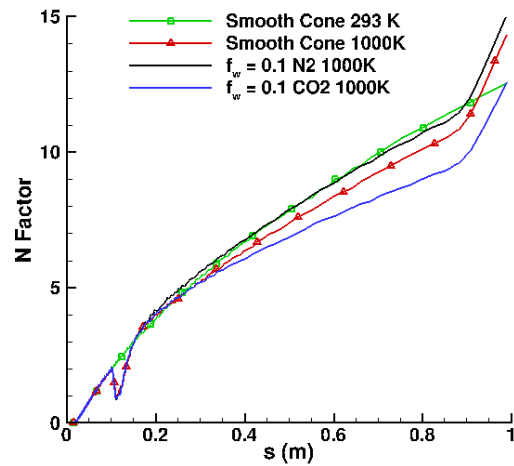


Figure 6.20: The show the stability analysis results for two smooth cone cases and two cases of injection with different gases. All wall temperatures are indicated in the legend.

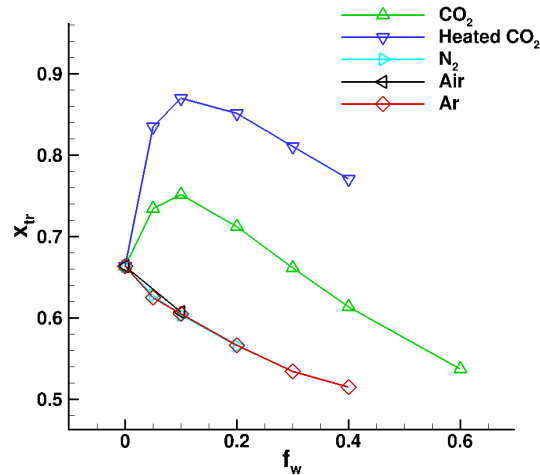


Figure 6.21: This plot is a summary of the transition locations for the theoretical injection cases based on the critical N factor of 9.2. The injection of carbon dioxide shows an optimum amount of mass injected.

6.2.5 Effect of Relaxation Processes

The effect on boundary layer transition delay of each of these modes is again assessed by freezing the chemical and vibrational modes of disturbance energy absorption. The freezing of each relaxation process is done with PSE-chem analysis, while the mean flow has both vibration and chemistry active. This test is performed for the injection of cold carbon dioxide, heated carbon dioxide and nitrogen all with f_w set to 0.1. As seen in Fig 6.22, both the full relaxation and vibrational relaxation from the injection of cold carbon dioxide follow the same curve, indicating that the vibrational relaxation is responsible for absorbing energy from disturbances. To verify this, a stability analysis with only chemical relaxation is compared to one with no relaxation processes active and is found to be identical. For this temperature range, the vibrational mode is expected to be the dominant mechanism for reducing the amplification of acoustic disturbances, as discussed in Fujii and Hornung[6]. However, the impact of the acoustic damping due to vibration is minimal in this simulation compared with the theoretical damping shown by Fujii and Hornung[6]. The mean flow simulation shows that the maximum mass fraction of CO_2 in the boundary layer is approximately four percent, which is commensurate for the amount of damping shown in the stability analysis. For the heated carbon dioxide case, a similar damping trend occurs with the only difference being the amplitude with which the N factors are increased without vibrational relaxation. The case with nitrogen shows no difference in amplification, verifying that the non-equilibrium in the disturbances

has no effect for nitrogen for this temperature range.

To understand the reason for the additional delay in carbon dioxide injection cases, we extract the boundary layer translational temperature and vibrational temperature profiles from all cases of gas injection at various locations on the cone, shown in Fig. 6.23. In the case of carbon dioxide injection, the presence of carbon dioxide causes an increase in the rate of energy transfer between the translational energy and the vibrational energy of the gas by reducing the mixtures relaxation time. The effect of this energy transfer is to heat the upper part of the boundary layer, causing the boundary layer to become thicker relative to the other injection gases. Thus, for these flow conditions, the presence of vibrational energy adds a source of heating making the mean flow more stable to second mode disturbances, which is a similar effect as that of wall heating. To further verify this delaying effect, the case with carbon dioxide injection is rerun with vibration frozen in the mean flow simulation. The stability analysis results, seen in Fig. 6.22 indicated in the legend with the title “MF w/o Vibration”, show this case causes a similar level of disturbance amplification as that of N_2 , air, and Argon injection. Freezing vibration in the mean flow of the N_2 , air, and Argon injection cases has essentially no effect on the disturbance amplification.

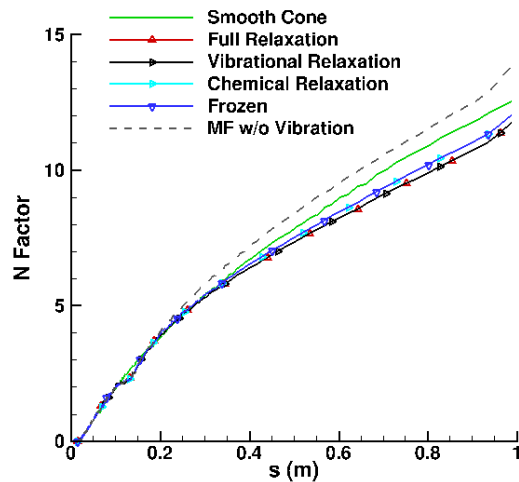


Figure 6.22: This plot shows the effect of non-equilibrium processes on the disturbances for cold carbon dioxide with f_w set to 0.1. The vibrational modes of carbon dioxide results in a transition delay relative to the smooth case due to boundary layer heating and acoustic damping.

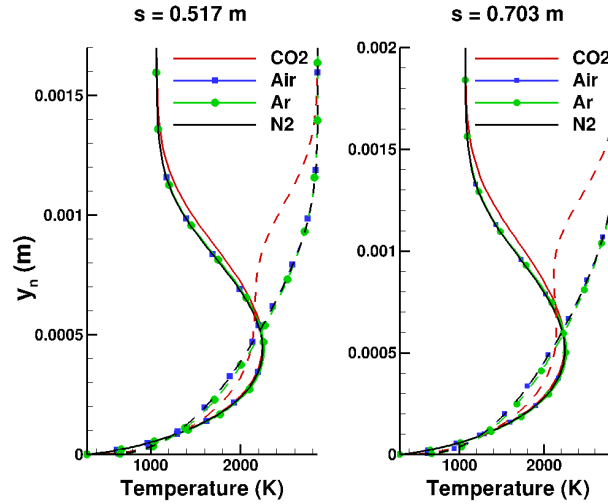


Figure 6.23: Boundary layer profiles of translational and vibrational temperature for the different injection cases. The location for the data extraction is indicated at the top of each plot. This comparison makes evident the heating of the boundary layer gas caused by the vibrational energy.

6.2.6 Air Freestream

The second set of cases with the theoretical injection scheme has a freestream that is composed of a mixture of partially dissociated air. This case is based on shot 2541 performed in the T5 Tunnel with the various flow conditions contained in Table 6.5. The key difference is between the two freestreams tested is that the air mixture contains O and NO , which results shorter mixture relaxation time than the $N_2 - N$ system. This difference is evident in the freestream vibrational temperature for each set of flow conditions. For the nitrogen freestream, the vibrational temperature is $2857.7 K$, while the vibrational temperature for the air freestream is $1369.4 K$. The chemistry sets used for these simulations are combinations of those given above with the addition of Argon. The vibrational relaxation parameters for the nozzle flow are those suggested by Millikan and White[130], except for those given in the appendix. For the cone flow, the vibrational relaxation parameters for the nozzle flow are those suggested by Millikan and White[130]. The free-stream Mach number is 5.29 and the wall condition is isothermal with a temperature of $293 K$. Several cases of cold gas injection are run with f_w ranging from 0.05 to 0.6. The effect of pre-heating the injection gas to a temperature of $1000 K$ is also tested in a case with f_w set to 0.1. A summary of these test cases, as well as total mass flux for each case, is also included in the appendix in Table C.4.

Table 6.5: Freestream Conditions for the second set of theoretical injections cases.

Stagnation Conditions		Freestream Conditions		Edge Conditions	
Pressure (<i>MPa</i>)	50.92	Density (<i>kg/m³</i>)	0.05572	Unit Reynolds (<i>1/m</i>)	$4.884 * 10^6$
Temperature (<i>K</i>)	5968	Temperature (<i>K</i>)	1369.4	Density (<i>kg/m³</i>)	0.0698
Enthalpy (<i>MJ/kg</i>)	9.51	Velocity (<i>m/s</i>)	3957.9	Velocity (<i>m/s</i>)	3892

6.2.7 Smooth Cone and Cold Carbon Dioxide Injection

Using a smooth cone simulation without injection again serves as the baseline for gauging transition delay. The stability analysis results, shown in Fig. 6.24, show that transition will occur at approximately 65 cm for a critical N factor of 9.5, essentially the same location as the previous set of freestream conditions. The introduction of cold carbon dioxide results in larger disturbance amplification with increasing mass flux, also shown in Fig. 6.24. This indicates that the acoustic damping caused by carbon dioxide's vibrational modes is unable to compete with the destabilizing influence of the injection. Investigating

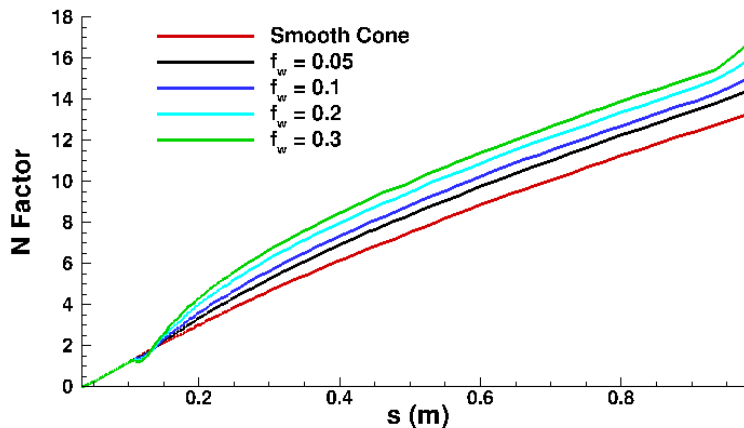


Figure 6.24: This plots shows the stability analysis results for the smooth cone and cold carbon dioxide injection cases. For these freestream conditions, injection of carbon dioxide only results in transition promotion.

6.2.8 Alternate Injection Gases

Interestingly, carbon dioxide injection results in a greater disturbance amplification than the injection of other gases, as inferred in stability analysis results shown in Fig. 6.25. This indicates that the presence of the vibrational modes of carbon dioxide result in a reduction of the boundary

layer's stability. To understand this effect, we again extract translational and vibrational temperature profiles from the boundary layer of different injection cases, shown in Fig. 6.26. The boundary layer profiles show that the vibrational temperature lags the translational temperature as the gas slows near the wall. The reduced vibrational relaxation times caused by the presence of carbon dioxide allow a greater amount of energy to flow from translation to vibration than in the other injection cases. Thus, for these freestream conditions, the vibration energy acts as a heat sink for the translational energy, cooling the boundary layer in the case of carbon dioxide injection. The effect of boundary layer cooling is to reduce the stability of mean flow with respect to second mode disturbances, which is a similar effect as that of wall cooling. Also, the acoustic damping caused the accessibility of carbon dioxide's vibrational modes is in competition with the reduced vibrational relaxation rate in the mean flow, whereas in the previous set of freestream conditions, these two effects were additive.

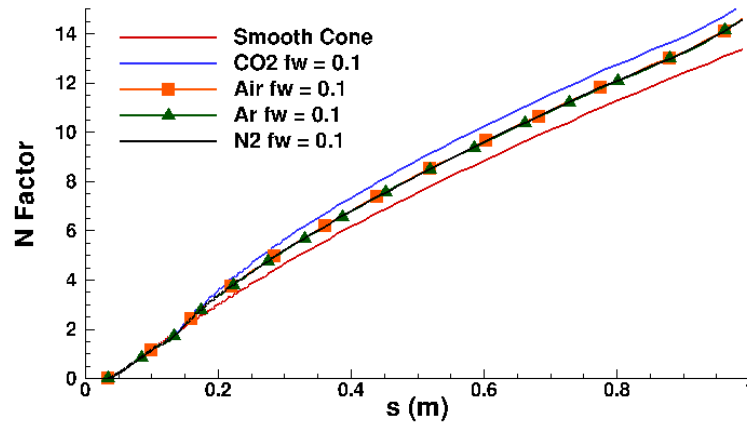


Figure 6.25: The plot shows the stability analysis results for select cases of gas injection. For these freestream conditions, gas injection for all gases decreases the stability of the boundary layer. The injection of carbon dioxide results in greater amplification of second mode disturbances than other gases.

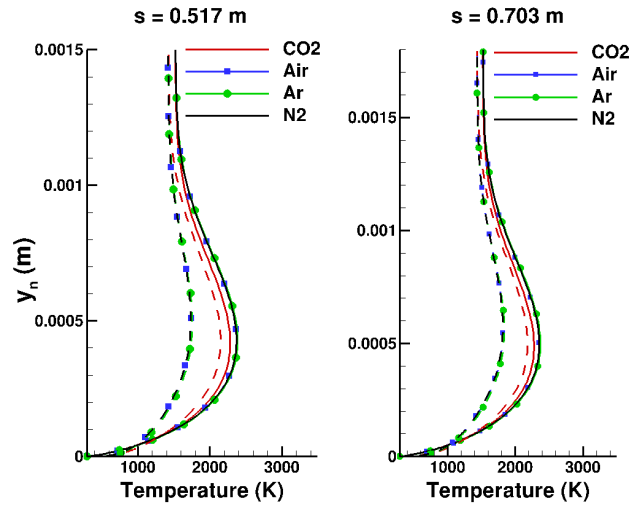


Figure 6.26: Boundary layer profiles of translational and vibrational temperature for the different injection cases. The location for the data extraction is indicated at the top of each plot. This comparison makes evident the heating of the boundary layer gas caused by the vibrational energy.

6.2.9 Heated Gas Injection

In attempt to achieve some delay in the transition location, the injected carbon dioxide is pre-heated to 1000 K and f_w is set to 0.1. The stability analysis results for this case, seen in Fig. 6.27, show that even pre-heating the carbon dioxide causes a greater amplification of disturbances than the smooth cone case. The heated gas adds higher translational and vibrational energy at the wall. Thus, less boundary layer cooling occurs, which reduces the impact of faster translational-vibrational equilibration.

Assuming a critical N factor of 9.5, we again can collect the transition locations into a summary, shown in Fig. 6.28. These data show for these freestream conditions, gas injection of any kind results in a promotion of transition.

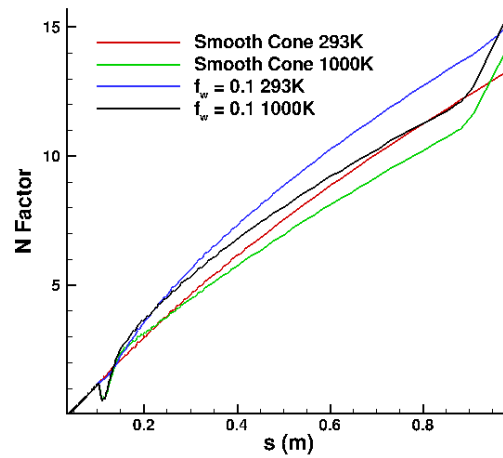


Figure 6.27: This plot shows the stability analysis results for select cases of heated CO_2 injection. The wall temperature in each case is indicated in the legend. The injection of heated carbon dioxide results in transition promotion.

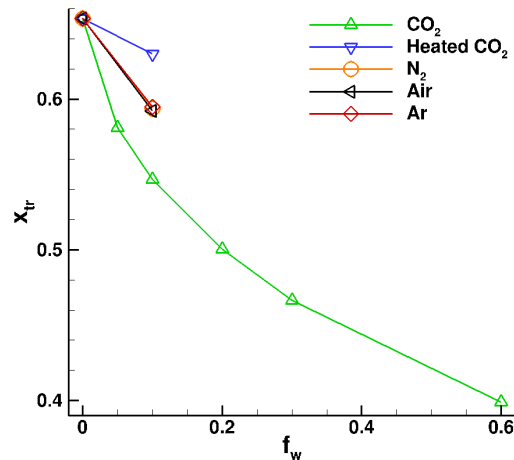


Figure 6.28: This plot is a summary of the transition locations for the theoretical injection cases based on the critical N factor of 9.5. These data show for these freestream conditions, gas injection of any kind results in a promotion of transition.

6.2.10 Conclusion

These two sets of freestream conditions illustrate three problem dimensions of injecting gas into a boundary layer. The injection process, in general, reduces the boundary layer stability. The presence of vibrational energy modes, in general an internal molecular process, has two potential effects. The first is to affect the mean flow boundary layer profile by heating or cooling the flow depending on

the state of the gas as it enters the boundary layer. The second is to affect the disturbances by either damping or amplifying the acoustic waves that cause second mode disturbances. Whether an internal process damps or amplifies depends on the state of the gas, namely the temperatures and densities, as well as the relaxation rate and energy capacity of the internal modes. Thus, a successful transition delay experiment for a given set of freestream conditions would require managing these three properties of gas injection in high-enthalpy flows. For the current flow and injection parameters an small degree of disturbance damping due to the presence of carbon dioxide in the boundary layer. Based on the previous chapters results, this is expected due to the relatively small mass fraction of carbon dioxide in these injection cases. However, the various trends of caused by internal molecular processes on boundary layer transition determined in this section are in good agreement with those investigate in the work by Johnson[120] and Johnson et al.[136].

6.3 Porous Injection

6.3.1 Model and Simulation Parameters

The T5 tunnel test body is a sharp, five-degree-half-angle cone. The surface of the cone is smooth with the exception of a porous material between 12.8 cm and 16.9 cm from the nose of the cone. This material has pores with a diameter of approximately $10\ \mu\text{m}$. In the numerical simulations, the porous wall transpiration is modeled through the use of the wall-blowing condition contained in the CFD solver. It is assumed that mass flow rate through the porous material is a constant over a given area. In an axi-symmetric simulation, this results in a top hat distribution of mass flux per meter across the length of the injection region. To maintain continuity of the mass flux of injection gas through the wall between the solid and porous surfaces, a function based on hyperbolic tangent is generated to approximate the top hat distribution. The grid used in these simulations is generated by a module included in STABL. Due to the structured nature of the CFD solver, all cells of the grid are quadrilateral. The wall-normal direction has 300 cells and the cells are clustered near the wall to guarantee that the y^+ values are all less than one and have a maximum geometric growth rate of 2.7 percent in order to properly resolve the boundary layer gradients. The wall-tangential direction has 1249 total cells. A majority of these cells are clustered near the nose and have a maximum geometric growth rate of 5.8 percent until the injection region. At this location, 100 cells are distributed across the porous wall surface. From the end of the injection region until the end

of the cone the cell sizes have a maximum geometric growth rate of 2.4 percent. The conditions for this set of injection simulations are also chosen to be similar to shot 2541 performed in the T5 tunnel and consist of a partially dissociated mixture of air with the physical properties listed in Table 6.5. The wall condition for this experiment is considered to be isothermal with a temperature of 293 K . The chemistry sets used for these simulations are combinations of those given above with the addition of Argon. The vibrational relaxation parameters for the nozzle flow are those suggested by Millikan and White[130], except for those given in the appendix. For the cone flow, the vibrational relaxation parameters are those suggested by Millikan and White[130].

A number of cases are run using carbon dioxide as the injection gas with a total mass flow rate ranging from 0.5 grams per second (g/s) to 13.5 g/s . Air and nitrogen are also injected to determine the effectiveness of injection gases with different vibrational and chemical parameters. For these cases the injection gas temperature is assumed to be equal to the wall temperature. To gauge the effect of heating the carbon dioxide before injection, four cases are run with injection temperatures of 1000, 1500, 2000, and 2500 K . These last six cases all have different mass flow rates in order to match the penetration height of transpiration for the cold carbon dioxide case with a total mass flow rate of 13.5 g/s . A summary of these test cases is provided in Table C.5 in the appendix.

6.3.2 Cold Carbon Dioxide Injection

The stability analyses of cases with injection of 3 g/s through 7.5 g/s follow this trend, seen in Fig. 6.29a. Transition is predicted in the post-injection region for the 3 g/s case; however, it may not be due to the variability in the amplification required for transition. All other cases show sufficient amplification to transition immediately following the injection region. The N factor plots for cases of 6 g/s and 7.5 g/s are truncated toward the nose of the vehicle due to the presence of a recirculation zone at the front of the transpiration. It is unknown if this recirculation exists in the experimental flow field and also the effect the recirculation has on the boundary layer stability. Some conditions in the PSE analysis were not calculated in order to avoid integrating through a recirculation zone and therefore the data in this region have been omitted from the results. All of the N factor profiles are similar in the region immediately following injection, indicating that the flow features such as the penetration height of the injection and distance of the boundary layer recovery are also similar, with their amplitudes dependent on the total mass injected. For the cases with injection of 10 g/s to 12 g/s , the stability analyses show a further increase in amplification with injection rate, seen in

Fig. 6.29b. The cases with injection of 13 g/s and 13.5 g/s show an increase in stability, however, all cases in this range have sufficient amplification after the injection to transition. One feature common to all injection cases simulated is the growth of N factor is more rapid than in the smooth cone case on the later part of the cone. The reason for this is best demonstrated by the stability diagram from the case with injection of 6 g/s , seen in Fig. 6.30. The second mode disturbances continue to experience the largest amplification; therefore it is expected that the most-amplified frequencies will follow the boundary layer thickness. During the injection, the boundary layer thickness increases from the injection gas, thus resulting in a drop in the frequencies being amplified. After the injection, the boundary layer thickness decreases until resuming its natural growth. The distance where this growth begins represents a recovery distance for the boundary layer. The change in slope of the boundary layer thickness allows for a band of frequencies to be continuously amplified for a greater length than in the smooth cone case. Due to this flow feature, the recovery distance is a factor that could cause transition for all simulations after the flow has absorbed the disturbance the injection. Also visible on the stability diagram is the amplification of several higher modes of disturbances.

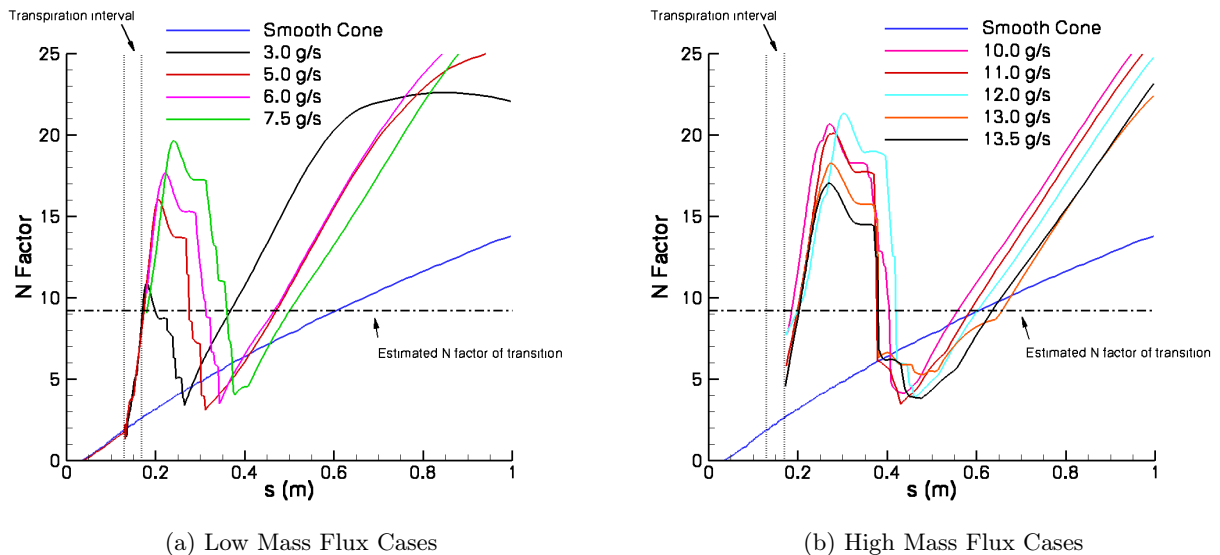


Figure 6.29: These plots show the results from the stability analyses of cold carbon dioxide injection. The free-stream conditions for these cases are contained in Table 6.5. The low mass flux cases are shown in a). The high mass flux cases are shown in b). The 3 g/s case is in a borderline state of transition, while all other cases reach an N factor sufficient to cause transition immediately following the injection region.

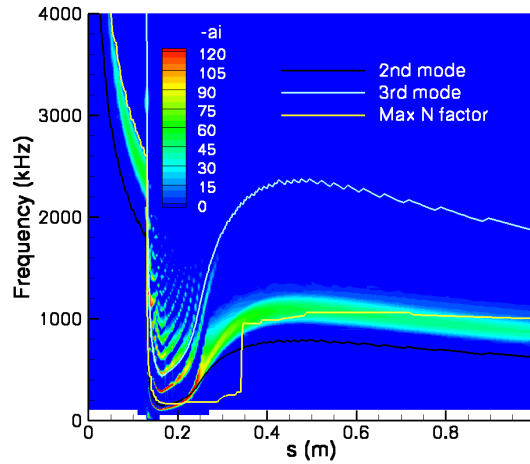


Figure 6.30: This plot shows the LST stability diagram for the case of cold carbon dioxide injection at a rate of 6 g/s . The sharp drop in amplified frequencies is due to the rapid increase in boundary layer thickness. The frequencies rise as the boundary layer recovers from the injection until resuming its natural growth. Also visible is the amplification of higher modes of disturbances.

6.3.3 Alternate Injection Gases

From previous experiments at the T5 tunnel, it is known that flows involving air and pure nitrogen will transition at a lower Reynolds number for stagnation enthalpies ranging from 4 MJ/kg to 10 MJ/kg than flows involving carbon dioxide. Due to this knowledge, it is expected that injection of carbon dioxide would result in a more stable boundary layer relative to a boundary layer of air or nitrogen, if carbon dioxide has a high enough temperature to be vibrationally excited. For the alternate injection gas cases the momentum of injection is matched to the carbon dioxide injection with a total mass flow rate of 13.5 g/s , requiring a different total mass flow rate for each case. The similarity of amplification, seen in Fig. 6.31a, suggests that the momentum of injection is more important in determining the stability when the injection gases are cold. It is easiest to understand a possible reason for these similarities by inspecting the boundary layer profiles of the case with carbon dioxide injection, seen in Fig. 6.31b. These profiles show that a majority of the injected carbon dioxide remains relatively cold. At these low temperatures, the carbon dioxide does not have the ability to absorb disturbance energy with the same capacity that it does at higher temperatures.

6.3.4 Heated Carbon Dioxide Injection

In order to ensure the effectiveness of the injected carbon dioxide to absorb energy from acoustic disturbances, the gas is heated before injection to a temperature range where the effects of non-equilibrium occur. The carbon dioxide is assumed to be in chemical and thermal equilibrium before injection. For the case of 2500 K this results in approximately twenty percent, by mass, of the carbon dioxide being dissociated. This implies that fewer molecules are present to absorb energy from disturbances, however, as shown in Fig. 17, the carbon dioxide is more efficient around 2000 K than it is below 1000 K . For these cases, the momentum of injection has been matched with the 13.5 g/s case of cold carbon dioxide injection. The effect of injecting less mass has not been separated from injecting heated gas. The stability analyses in Fig. 6.32 show a reduction in amplification with an increase in temperature of the injection gas in the post-injection region. For the case where the injection gas is 1000 K , the boundary layer is in a borderline state of transition following the injection. If this case does not transition at this distance on the cone, then transition is expected at approximately the same location as the smooth cone case. However, all other cases are expected to transition earlier than the smooth cone case due the amplification that occurs where the boundary layer recovers.

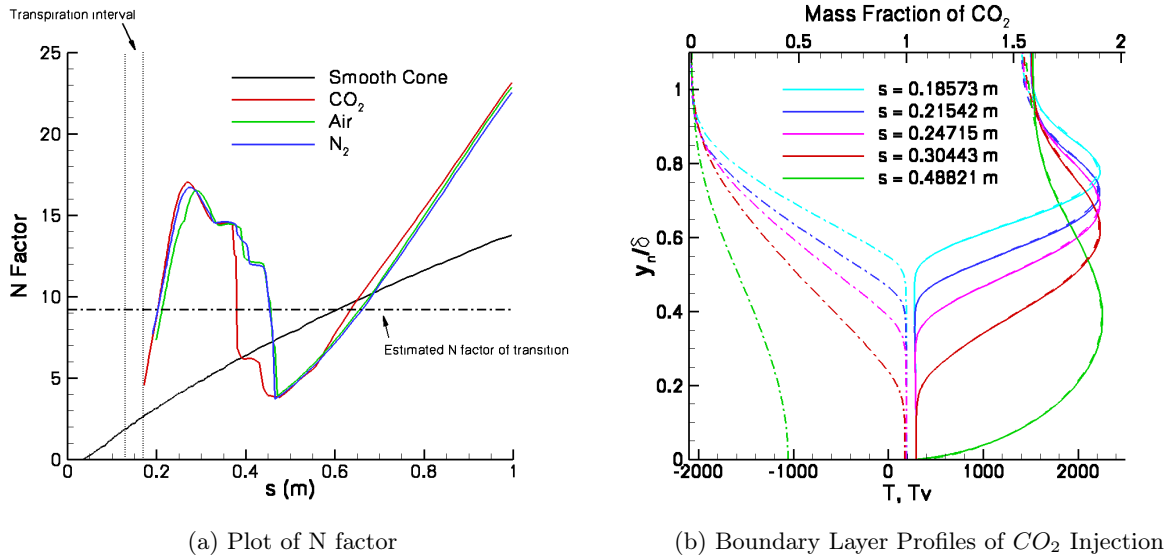


Figure 6.31: The plot on the left, a), shows the N factors that result from the injection of various gases while preserving the penetration height of transpiration. The plot on the right, b), shows the normalized boundary layer profiles of mass fraction of carbon dioxide (dashed dot), translational temperature (solid), and vibrational temperature (dashed). This plot shows a layer of cold carbon dioxide that is inefficient for absorbing energy from acoustic disturbances. The free-stream conditions for these cases are contained in Table 6.5. Each case has a different total mass flux in order to match the penetration height of the injection. The variable y_n indicates the wall-normal direction.

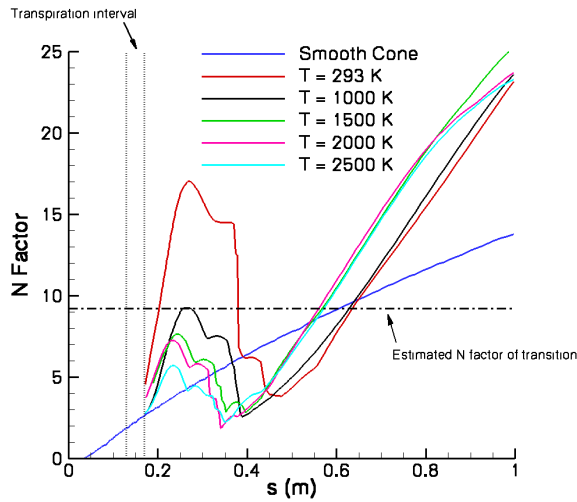


Figure 6.32: This plot shows the results from the stability analyses of heated carbon dioxide injection. The free-stream conditions for these cases are contained in Table 6.5. As expected, an increase in temperature of the injected gas further reduces the amplification experienced in the post-injection region.

6.3.5 Conclusion

The current modeling approach disagrees with the experiments of Jewell et al.[13], in that all cases of injection show transition to immediately following the injection. One important aspect of this problem is the level of mass flux through the injector results in a large bubble of nearly stagnant injection gas around the injector. An assumption made in the development of the linear stability analysis with LST and PSE is the boundary layer is essentially parallel with wall around which it forms. The stagnant fluid has a velocity vector near the wall that is essentially wall-normal, thus breaking the assumption made by the linear analysis. This fact calls into question the reliability of the analysis in the region around the injector. To address this, the applicability of a PSE analysis must be qualified through the use of acoustic direct numerical simulations (DNS). The groundwork for this type of simulation is laid out in Chapter 7.

Regardless of the amplification shown around the injector, all cases also show a large amount of disturbance amplification well downstream of injector section of the cone. This is due to the boundary layer recovering from the injection process, which results in a roughly constant boundary layer height for an extended period of time. The constant boundary layer height allows for a particular band of frequencies to more rapidly amplify than a case without injection. This type of injector demonstrates the need for the additional dimension of the recovery distance to the problem of transition delay by means of injection.

Chapter 7

Direct Simulation of Acoustic Waves Over a Cone

7.1 Introduction

The work in this chapter is motivated by two key points. As discussed in the previous chapter, recent experiments of Jewell et al.[13] demonstrate that injection of CO_2 can stabilize a hypervelocity boundary layer on a cone, thus providing a practical application of acoustic damping theory. Attempts using a linear PSE analysis proved inadequate for capturing the physics of the injection and transition process. By simulating the acoustic waves thought to be responsible for transition, the interaction of the injection process and the boundary layer disturbances will be accurately captured. With an accurate representation of the experimental flowfield it may be possible to obtain reasonable agreement between computations and experiment. Second, the success of the many cases of acoustic and vorticity wave simulations performed by Balakumar et al.[68, 14, 69] provide a motivation to extend these types of simulations into the hypervelocity regime in order to verify the results of stability analyses using the PSE. In the current chapter, we again use linear PSE stability analyses to determine the impact of molecular vibration on the particular flow conditions considered and to determine relevant acoustic frequencies for simulation. Next, we use the low-dissipation numerical flux scheme to perform direct numerical simulations of the receptivity process on a sharp cone in vibrationally active flow. This is done for two cases. The first case has only a single vibrational mode of CO_2 and the second case has all four of the vibrational modes of CO_2 active. We use these simulations to study the growth and decay process of a second mode disturbance as

well as investigate the vibrational response of the acoustic wave and the disturbance generated by the acoustic wave in a realistic hypersonic flow problem. These simulations also serve as a point of validation for the stability analyses of hypervelocity flow using the PSE.

7.2 Sharp Cone Model

The model for these simulations is a 7° half-angle, sharp tipped cone with a nose radius of 0.0125 mm , as used in Balakumar and Kegerise.[14] For the current simulations, we use a length of 0.5 m . Simulation parameters were chosen such that we were able to obtain results that we would expect to see the effects of acoustic damping while satisfying the constraints of our numerical method. This implies that the freestream temperature be low relative to all of the characteristic vibrational temperatures of CO_2 , of which the lowest is 959.66 K , to satisfy the frozen wave inflow condition discussed above. We also need to have a sufficiently large freestream total enthalpy to cause acoustic damping in the boundary layer. For guidance on the minimum enthalpy required, we look to Fig. 3 in Fujii and Hornung[6], reproduced here in Fig. 7.1, which shows a plateau in the acoustic absorption rate per wavelength beginning around $4 - 5\text{ MJ/kg}$. This enthalpy is calculated without the formation enthalpy of CO_2 . Thus for this initial study, we have chosen the freestream conditions contained in Table 7.1. The freestream total enthalpy results in temperatures ranging from the isothermal wall temperature of 297 K to 1430 K for the single vibrational mode case and 1170 K in the case with all vibrational modes active. Finally, for reasons explained below, we use frequencies of 1.05 MHz , 1.4 MHz , and 2.2 MHz for the single vibrational mode case and 1.2 MHz for the case with all vibrational modes active in the acoustic wave simulations.

Table 7.1: Table of freestream conditions for the sharp cone case.

Freestream		Stagnation	
$T\text{ (K)}$	215.0	$h_0\text{ (MJ/kg)}$	4.644
$\rho\text{ (kg/m}^3\text{)}$	0.100	Re (1/m)	$2.607 \cdot 10^7$
$U\text{ (m/s)}$	3000.00	Mach	12.58

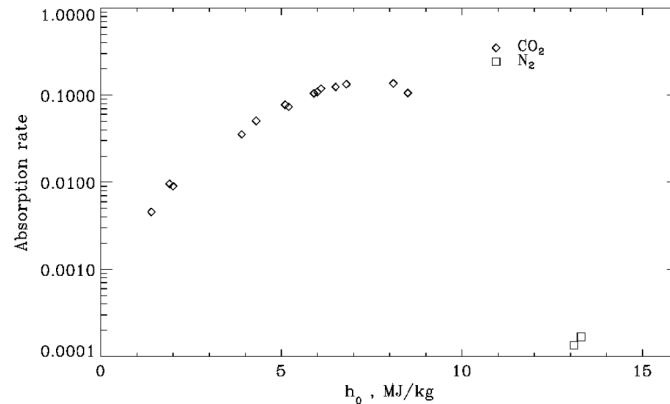


Figure 7.1: Acoustic absorption rate versus enthalpy for the approximated most amplified frequencies over a 5° half-angle cone in the T5 tunnel. This plot has been reproduced from Fig. 3 in Fujii and Hornung.[6]

We use a shock-fitted, single-block structured grid with dimensions of 9691 cells by 399 cells in the streamwise and wall-normal directions, respectively. The shock fitting allows a short distance for the acoustic wave to travel through the freestream before encountering the shock, thus taking full advantage of all cells in the domain. The grid is clustered to the wall such that the y^+ value is less than one. The solution is then obtained using the following steps. First, the mean flow is computed using the sixth-order accurate inviscid fluxes and first-order accurate, implicit DPLR. This allows for rapid convergence to the steady state solution. We then continue the simulation with the second-order Crank-Nicholson time advancement at a CFL of 250 to obtain a uniform base state, which requires several flow times. In addition to the mean flow, we run disturbance cases by introducing an acoustic wave at the inflow boundary of the domain. We run these simulations in a similar manner to the mean flow for several flow times, allowing the waves to propagate throughout the domain. The shock detection switch we use for these simulations is based on the arithmetic mean of the Ducros switch[128] and a switch based on the Mach number. Also, the vibrational relaxation coefficients are modified to the corrections for CO_2 given by Camac.[119]

7.3 Stability Analysis

The mean flow for the stability analysis is calculated using a structured, axi-symmetric CFD solver, which solves the reacting Navier-Stokes equations and is part of the STABL software suite written by Dr. Heath Johnson.[121] This flow solver is based on the finite-volume formulation. The inviscid fluxes are based on the modified Steger-Warming flux vector splitting method and are second-order

accurate with a MUSCL limiter as the TVD scheme. The viscous fluxes are second-order accurate. The time integration method is the implicit, first-order DPLR method. The mean flow is computed on a single-block, structured grid with dimensions of 999 cells by 299 cells in the streamwise and wall-normal directions, respectively, using the conditions in Table 7.1.

The stability analyses are performed using the PSE-Chem solver, which is also part of the STABL software suite. PSE-Chem solves the reacting, two-dimensional, linear parabolized stability equations to predict the amplification of disturbances as they interact with the boundary layer. The PSE-Chem solver includes finite-rate chemistry and translational-vibrational energy exchange. Traditionally, a boundary layer transition prediction using PSE-Chem is based on the semi-empirical e^N method to gauge the transition location, however, for the current work, we are mainly interested in the pressure fluctuation amplitude at the wall as a point of validation. Both the mean flow and stability analysis are capable of selectively freezing both chemical reactions and molecular vibration, allowing for the determination of internal molecular effects on boundary layer disturbances.

7.4 Stability Analysis of the Mean Flow

As demonstrated in the previous chapter, the stability analysis software PSE-Chem has the ability to selectively freeze chemical and vibrational processes. We can take advantage of this ability to determine if a given set of freestream conditions is sufficient to cause acoustic damping due to vibration relaxation. Using the same mean flow, we perform a stability analysis with vibrational relaxation turned on and another one with vibrational relaxation turned off. To gauge the effect of this relaxation mode, we can compare the predicted amplification of boundary layer disturbances for each of these cases. If the amplification is greater when vibrational relaxation is frozen, we know the relaxation process is damping the boundary layer disturbances and vice versa.

For the freestream conditions given in Table 7.1, we first simulate the flow over a sharp cone using with only one of the bending vibrational modes of CO_2 active using the flow solver in STABL. From this calculation, we obtain the boundary layer profiles of streamwise velocity, translational temperature, and vibrational temperature shown in Fig. 7.2. The accessibility of the low temperature vibrational mode causes the boundary layer to be near thermal equilibrium. We then use this mean flow to perform a stability analysis. As seen in Fig. 7.3, the case without vibrational relaxation results in larger N factors, implying more amplification, indicating that damping due to vibrational relaxation is occurring. Now that we are confident acoustic damping due to vibrational

relaxation will occur, we must choose a frequency to simulate. Based on this stability analysis, we have chosen to first simulate 1.4 MHz because it reaches a maximum amplification near the middle of the cone. This location allows the simulation to capture both the growth and decay of the disturbance. At this frequency, we test both slow and fast acoustic waves. Next, we simulate 1.05 MHz because the stability analysis shows a larger effect of vibrational relaxation than the previous case. Finally, we simulate 2.2 MHz in order to capture second mode amplification as well as third mode amplification. Although all of these frequencies shows a small amount of damping due to the presence of molecular vibration relative to the overall disturbance amplification, we still expect to see a phase shift in the vibrational temperature as described in the introduction.

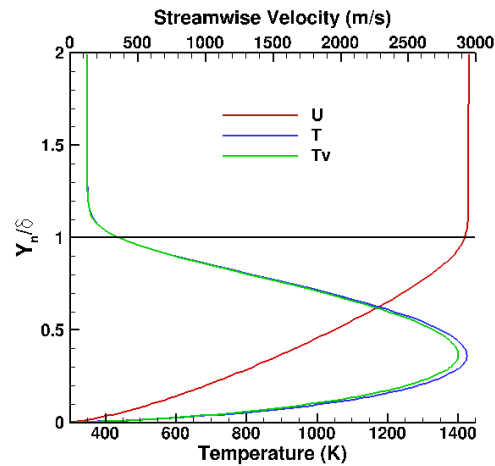


Figure 7.2: Boundary layer profiles of streamwise velocity (U), translational temperature (T), and vibrational temperature (Tv) versus wall-normal distance at length of 30 cm from the nose of the cone. The boundary layer is essentially in thermal equilibrium. The wall-normal distance has been normalized by the boundary layer thickness, δ .

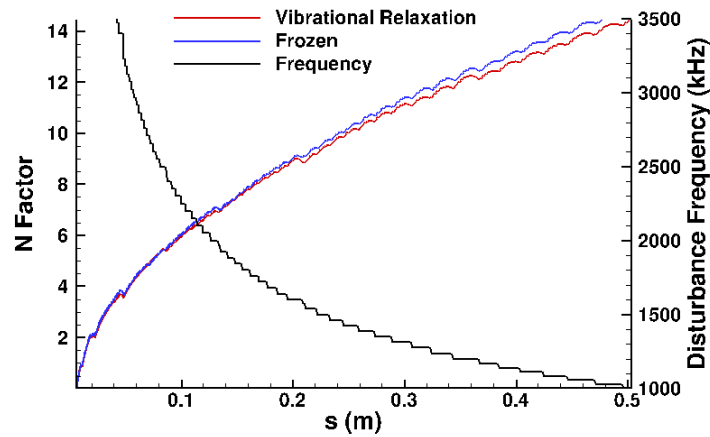


Figure 7.3: N factor and most amplified disturbance frequency versus distance along the cone for conditions in Table 7.1 using only the first bending vibrational mode of CO_2 .

Next, we simulate the same freestream conditions as before, contained in Table 7.1, with all of the vibrational modes of carbon dioxide active using flow solver in STABL. The boundary layer profiles of streamwise velocity, translational temperature, and vibrational temperature, shown in Fig. 7.4, are similar to previous case with smaller maximum translational and vibrational temperatures due to the increased energy capacity of the gas. The current flow also shows a larger degree of thermal non-equilibrium. Performing a stability analysis on this mean flow, we obtain a greater disturbance amplification as compared to the previous case, shown with N factor in Fig. 7.5. However, using STABL to inactivate the effect of molecular vibration in the disturbances, the current case shows a larger separation in disturbance amplification between vibrationally active and inactive stability analyses. This indicates that a greater degree of acoustic damping is occurring when all of the vibrational modes of CO_2 are active. For this case, we chose a frequency of 1.2 MHz because the effect of vibrational relaxation for frequencies that are most amplified near the end of the cone is shown to be greater for the current temperature range as demonstrated by Fujii and Hornung[5, 6] and also in Chapter 5.

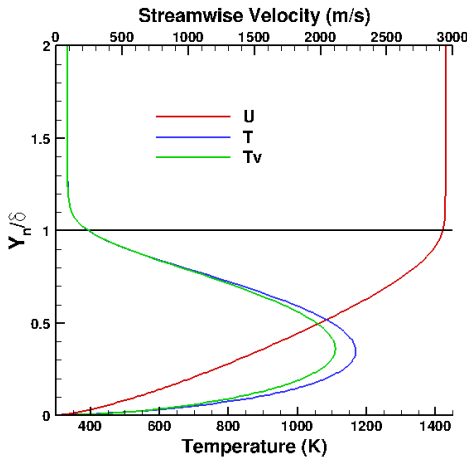


Figure 7.4: Boundary layer profiles of streamwise velocity (U), translational temperature (T), and vibrational temperature (Tv) versus wall-normal distance at length of 30 cm from the nose of the cone. With all vibrational modes of CO_2 present in the flow, the boundary layer has a larger degree of non-equilibrium. The wall-normal distance has been normalized by the boundary layer thickness, δ .

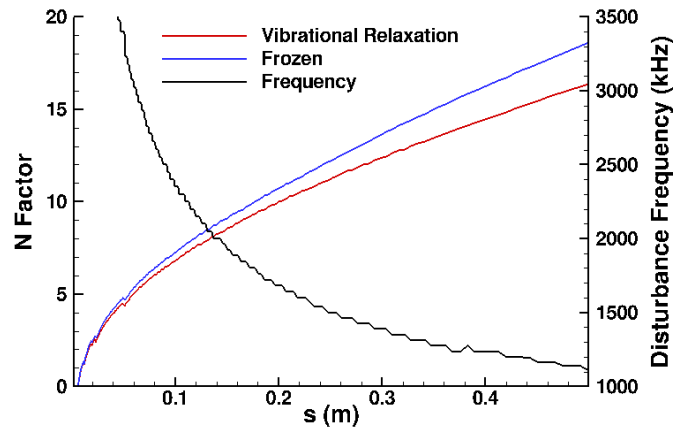


Figure 7.5: Comparison of N factor most amplified disturbance frequency versus distance along the cone for conditions in Table 7.1 using only the all of the vibrational mode of CO_2 .

Next we can gauge the contribution of each of the three unique vibrational modes of carbon dioxide by performing three stability analyses of the same mean flow, each with only one vibrational mode. Based on the analysis in Chapter 5 of a single vibrational mode above we expect to see a small change in the amplification from the anti-symmetric vibration mode with a characteristic vibrational temperature of 3382 K , a larger change from the symmetric vibrational mode with a characteristic vibrational temperature of 1918 K , and an even larger effect from the bending vibrational mode. As

seen in Fig 7.6, the stability analyses agree with our expectations and show that a lower characteristic vibrational temperature results in a greater impact on the predicted change in amplification.

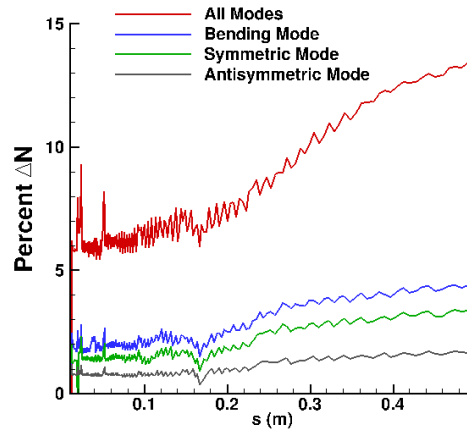


Figure 7.6: Comparison of the percent change in N factor versus distance along the cone due to the addition of various vibrational relaxation modes to the PSE stability analysis.

7.5 Sharp Cone Simulations

7.5.1 Validation

With an understanding of the different aspects of the flowfield and acoustic waves, we now apply the freestream conditions contained in Table 7.1 to the sharp cone grid described above. To ensure a good comparison between the DNS and PSE stability analysis, we have extracted the mean flow profiles in similar locations on the cone, as seen in Fig. 7.7. The agreement between the two flow solvers is very good for the streamwise velocity, Fig. 7.7a, and the translational temperature, Fig. 7.7b. A slight difference exists for the vibrational temperature, however, the difference represents a small percentage of the value of vibrational temperature. Performing a similar comparison between the flow solvers in the second case, we find that the boundary layer profiles are essentially identical.

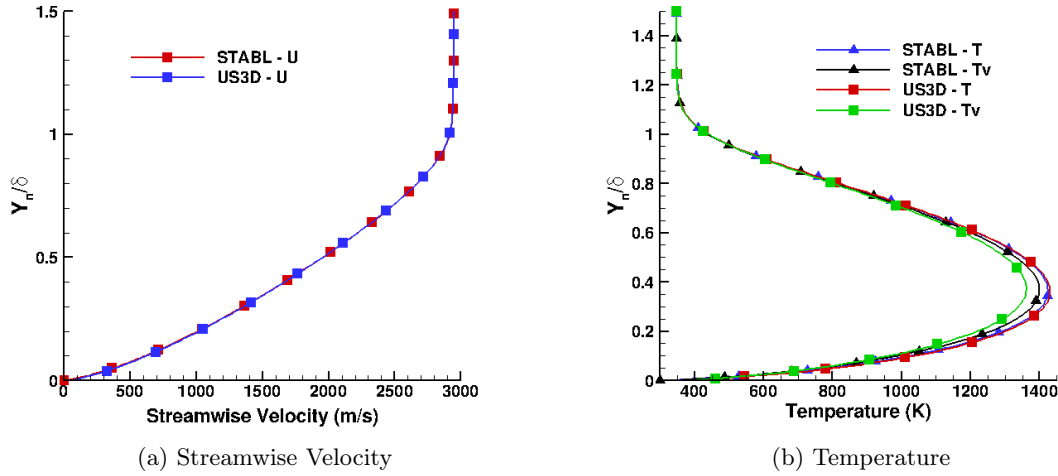


Figure 7.7: Comparison of the mean flow boundary layer profiles of streamwise velocity (Fig. 7.7a), translational temperature, and vibrational temperature (Fig. 7.7b). The boundary layer profiles between the two mean flows are nearly identical.

Next we add the presence of planar acoustic waves over the cone. We use a freestream acoustic wave amplitude of $\tilde{p}_{ac}/p_{\infty} = 1.0 * 10^{-5}$ for all frequencies tested in order ensure that the boundary layer disturbances maintain linear behavior over the length of the cone. As seen in Fig. 7.8, the disturbance field for the $1.4 MHz$, slow-wave case contains the same four regions described in Balakumar and Kegerise[14]: freestream, shock, shock layer, and boundary layer. In the freestream region, the wave simply propagates through the gas. In the shock region, the shock is displaced by the acoustic wave. Due to the large gradients in state variables, the small displacement of the shock results in a large disturbance magnitude relative to the freestream value. The shock layer consists of acoustic waves transmitted through the shock from the freestream as well as noise that has been radiated from the boundary layer. As in Balakumar and Kegerise's sharp cone case, the strength of the freestream disturbances in the shock layer is small relative to those in the boundary layer, suggesting that the boundary layer disturbance is generated near the nose of the cone. The final region is the boundary layer, where the amplification of the second mode disturbance can be seen by the increasing magnitude of the density disturbance in Fig. 7.8.

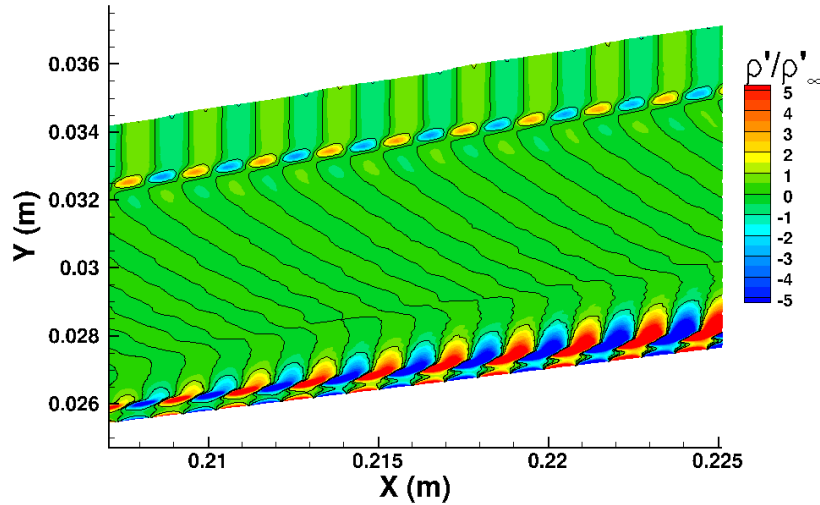


Figure 7.8: A view of the disturbance field using contours of normalized density disturbance at an approximate streamwise location of 21 *cm* from the nose of the cone for the 1.4 *MHz*, slow-wave case. The disturbance field contains the same four regions described in Balakumar and Kegerise[14]; freestream, shock, shock layer and boundary layer.

In order to validate our simulations, we extract the pressure disturbance at the wall for comparison to data from the linear PSE analysis. First, this is done for both slow and fast acoustic waves with a frequency of 1.4 *MHz* and is shown in Figs. 7.9a and 7.9b, respectively. In both cases, the observed second mode disturbance growth occurs in the same location with similar growth rates. Since the PSE analysis can only provide the relative growth of disturbances, the envelope of the PSE pressure disturbance has been scaled to correspond to the peak height in both slow and fast acoustic wave cases. The simulation and the PSE analysis agree reasonably well for the initial growth rate and initial peak location. The slow wave results in a larger reduction in disturbance amplitude over the front of the cone, however, it experiences a larger overall disturbance magnitude as compared to the disturbances generated by the fast wave. These results show the slow wave is more efficient at exciting the second mode disturbance on a sharp-nosed cone, which agrees well with the previous analyses of Balakumar[68] and Balakumar and Kegerise.[69]

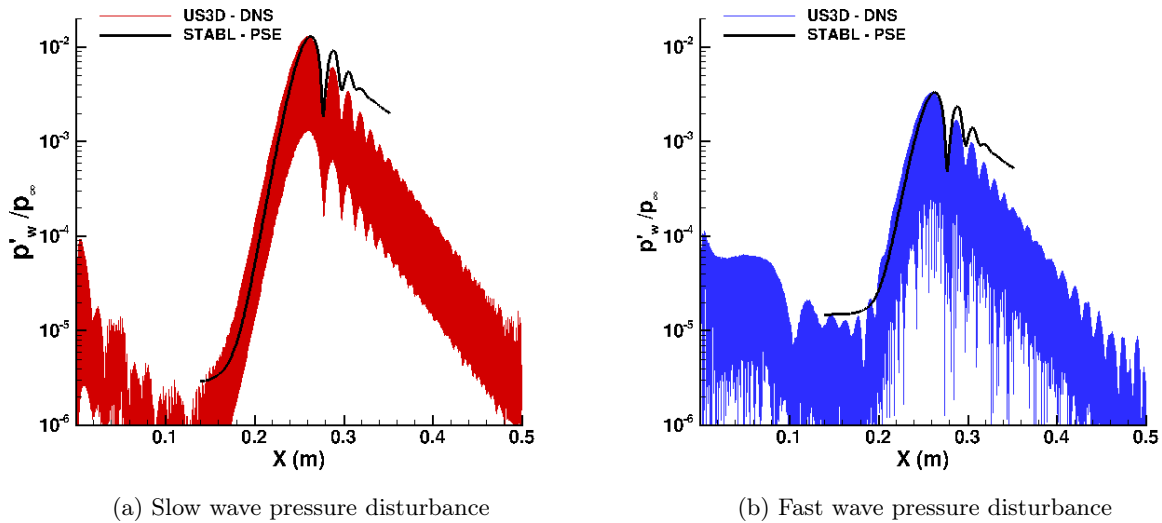


Figure 7.9: Comparison of the normalized wall pressure disturbance between the acoustic wave simulations and the linear PSE analysis for a frequency of 1.4 MHz . The type of acoustic wave used to generate the boundary layer disturbance is indicated in the sub-figure caption.

For the second frequency tested in the single vibrational mode case, 1.05 MHz , only the slow acoustic is simulated. As before, the disturbance initially decays after entering the boundary layer near the nose until exponentially amplifying when the boundary layer becomes tuned to this frequency. After performing similar manipulations of the PSE data, the wall pressure disturbance computed in the DNS shows similar agreement as before to the wall pressure disturbance calculated by the PSE, seen in Fig. 7.10a. In this case, the second mode disturbance amplifies roughly five orders of magnitude, whereas the previous frequency amplifies approximately three orders of magnitude.

The wall pressure disturbance of the last frequency simulated for the single vibrational mode case, 2.2 MHz , does not agree well with that of the PSE, as shown in Fig. 7.10b. For the second mode growth, the PSE analysis shows the disturbance amplifying upstream and peaking further downstream from the simulation using US3D. The grid has a higher cell density at this location, allowing for a similar points per wavelength as the 1.4 MHz case. However, the higher grid density also implies the local CFL is higher. The time advancement method, the second-order Crank-Nicholson method, allows for low dissipation only at low CFL numbers. Therefore, the lack of agreement in the second mode disturbance growth is attributed to the inadequacy of the numerical method at this location. Further down the cone, the same frequency experiences third mode disturbance growth as indicated by the PSE analysis shown in Fig. 7.10b. Arguably, the US3D simulation

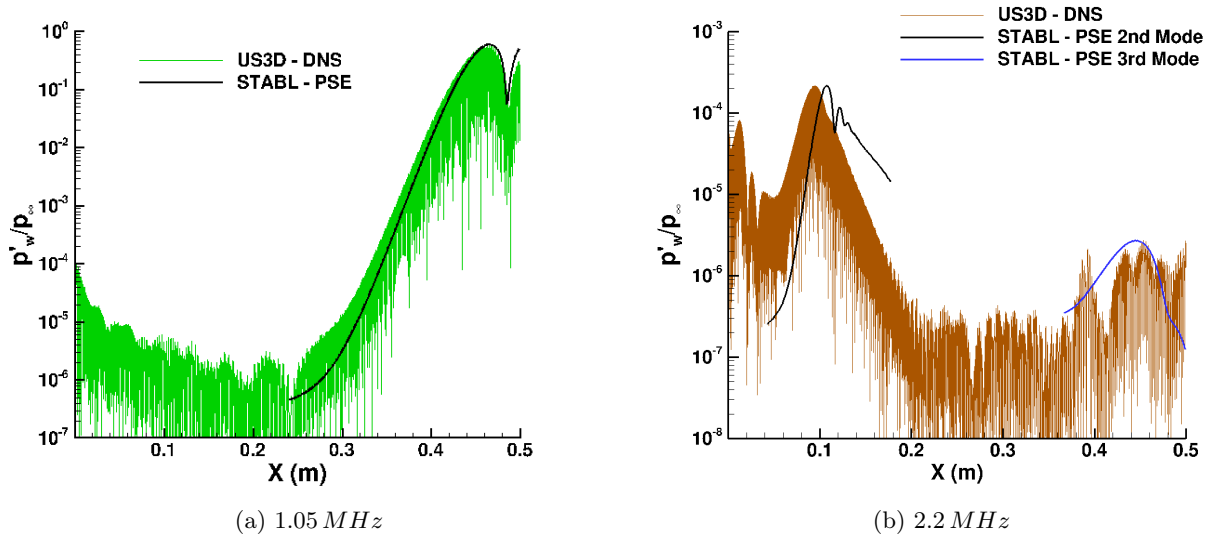


Figure 7.10: Comparison of the normalized wall pressure disturbance between the acoustic wave simulations and the linear PSE analysis for frequencies of 1.05 MHz and 2.2 MHz as indicated in the sub-figure caption. Both cases use a slow acoustic wave to generate the boundary layer disturbance.

also shows growth in this region, however, the grid is too sparse at this location to accurately capture disturbance evolution at this frequency.

The last case tested is a slow acoustic wave with a frequency of 1.2 MHz through CO_2 with all of the vibrational modes active. The DNS wall pressure disturbance data show an initial decay of the boundary layer disturbance until the frequency becomes tuned to boundary layer and begins exponential growth, seen in Figure 9b. However, the DNS and PSE differ on the evolution of the disturbance after the initial peak of disturbance growth. The DNS data show the disturbance beginning growth and decay cycles with a trend of damping, while the PSE data show the disturbance continues to amplify after beginning growth and decay cycles. Further investigation is required to identify the cause for the disagreement.

Another interesting feature observed in both the DNS simulations and PSE analyses is cyclical growth and decay of disturbance magnitude behind the initial peak of disturbance amplitude. To understand why this occurs, we have extracted several plots of the density disturbance at locations where growth or decay occur from the 1.4 MHz , slow-wave case, shown in Fig. 7.12. We have chosen the contour levels such that the shape of the boundary layer disturbance is easily visible. Additionally, the boundary layer edge is indicated by the solid white line and the approximate disturbance

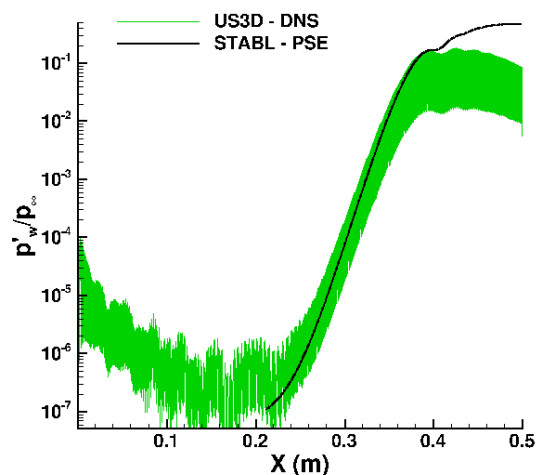


Figure 7.11: Comparison of the normalized wall pressure disturbance between the acoustic wave simulation and the linear PSE analysis for a frequency of 1.2 MHz .

sonic line is indicated by the dashed white line, both running roughly parallel with the wall. For this flow, the boundary layer edge is determined by the wall-normal height at which the total enthalpy is 99.5 percent of the freestream enthalpy. The disturbance sonic line is calculated as part of the linear PSE analysis. Starting in the initial growth region at approximately 25 cm , Fig. 7.12a, the disturbance takes a form that appears as an acoustic wave trapped and resonating in between the disturbance sonic line and the cone wall as described in the review paper by Fedorov.[2] During the first decay period, Fig. 7.12b, this structure begins to distort, which is the result of differing phase speeds of the disturbance across the boundary layer. The distortion of the disturbance results in a negative feedback effect that causes the disturbance amplitude to decay faster than exponentially. At approximately 28.5 cm , Fig. 7.12c, the wave takes a similar form to that of the initial growth region. This is again due to the phase speed difference across the boundary layer, however, at this location the disturbance now receives positive feedback and begins to amplify. Also visible in Fig. 7.12c is an interesting pattern in the wave form that lies at a height of approximately two boundary layer thicknesses. This pattern results from the interaction of the noise generated by the disturbance during the first amplification region and the current amplification region. Moving further downstream, Fig. 7.12d, the disturbance begins to decay, showing a similar pattern as in the previous decay section. The growth/decay cycles are essentially an acoustic beating process that occurs because of the varying phase speeds across the boundary layer height.

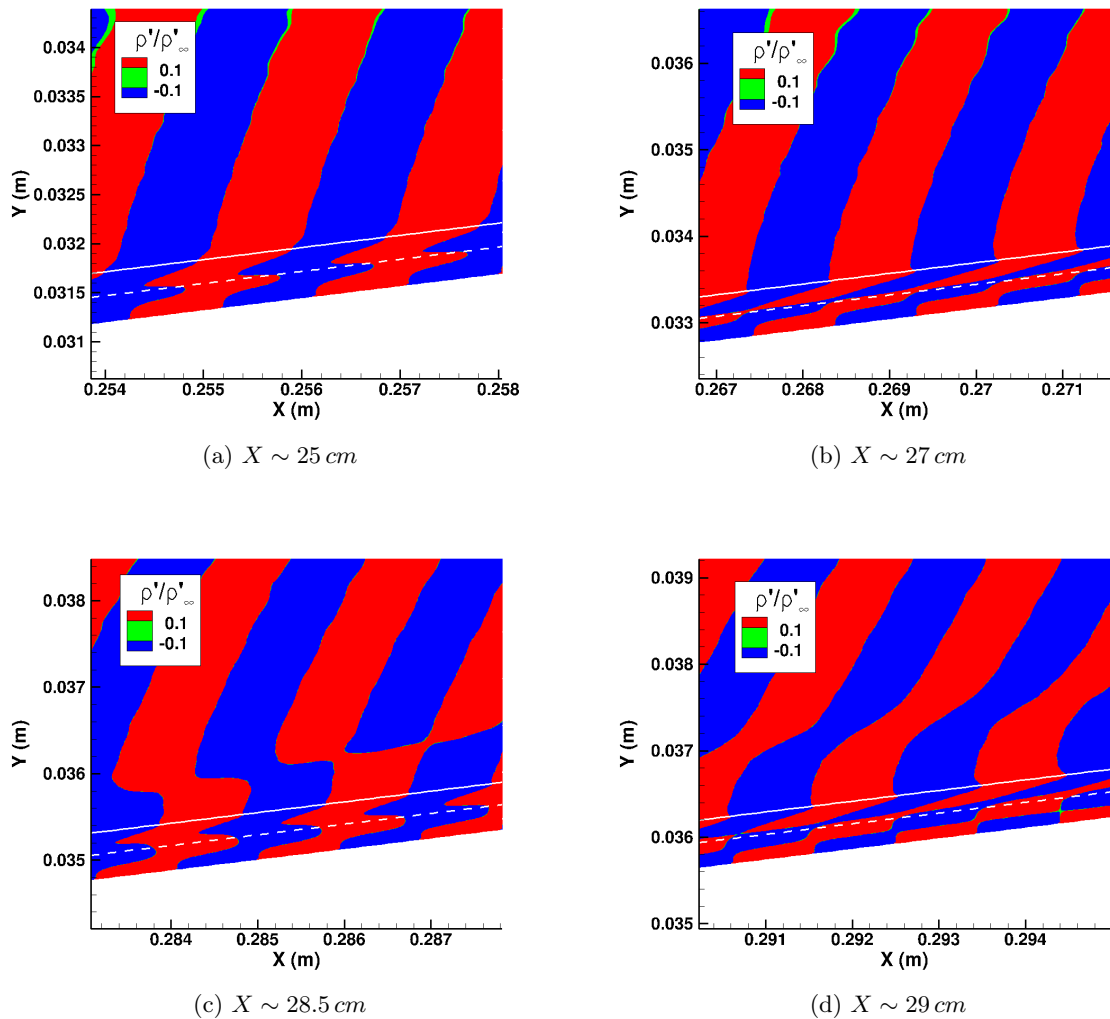


Figure 7.12: Plots of the normalized density disturbance at several locations on the cone from the 1.4 MHz , slow-wave case. The contours are chosen such that the shape of the boundary layer disturbance is easily visible. The boundary layer edge is indicated with the solid white line and the approximate disturbance sonic line is indicated by the dashed white line that run roughly parallel to the wall. For this flow, the boundary layer edge is determined by the location at which the total enthalpy is 99.5 percent of the freestream enthalpy. The disturbance sonic line is calculated as part of the linear PSE analysis

Several wall-normal locations throughout the boundary layer at different streamwise stations along the cone are sampled over time in order to determine the variation in frequency of the disturbance that may be caused by dispersion error for the 1.4 MHz , slow-wave case. These data are processed with a windowed Fast Fourier Transform (FFT) using Welch's method in Matlab. At each location sampled, the FFT data show a peak at 1.4 MHz as well as peaks at higher harmonic frequencies, a sample of these data is shown in Fig. 7.13. These results indicate that the numerical

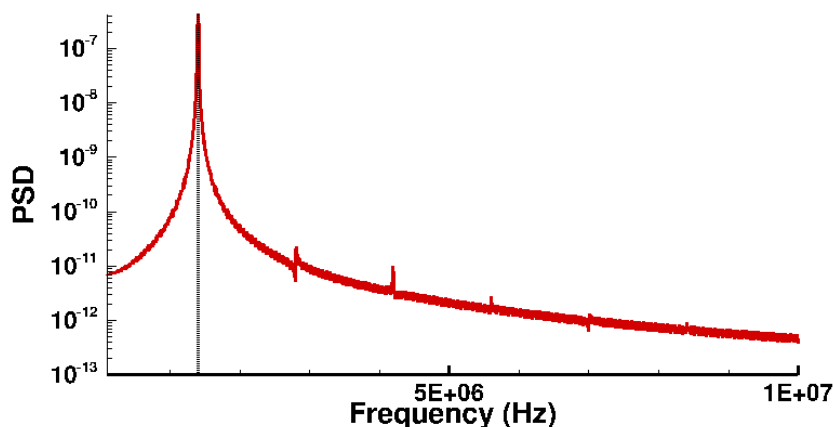


Figure 7.13: Power spectral density versus frequency for the 1.4 MHz , slow-wave case. The black line indicates the location of 1.4 MHz .

method is preserving the frequency of the disturbance for the length of the cone, indicating that the dispersion error is essentially zero. In each case where reasonable agreement was obtained, the disturbance amplification rate calculated by the PSE is larger than that of the DNS. This difference in growth rate could be due to a few causes, some physical and some artificial. One potential cause is the presence of dissipation in the numerical method that could be adding some artificial damping as the disturbance evolves. In these cases, an improvement in the dissipation switch could allow for an improvement in the agreement between US3D and the PSE stability analysis by reducing any potential numerical dissipation added in the boundary layer. In order to obtain better agreement in the 2.2 MHz case, the grid should be tailored to this frequency. In all cases tested, a more accurate time advancement method, such as RK3, could also result in better agreement between the PSE and DNS as seen in Balakumar et al.[68, 14, 69]. Further investigation is required to determine the cause for the discrepancy in amplification.

7.5.2 Vibrational Relaxation Effects

Before analyzing the flowfields of the acoustic simulations, it is instructive to determine the driving forces behind the evolution of the vibrational energy disturbance. In Fujii and Hornung's[5, 6] analysis, they assumed the acoustic wave was propagating through a gas in chemical and thermal equilibrium as well as having constant mean properties. While these assumptions allow us to gain insight into the acoustic interactions with gas, they are too restrictive when considering the spatially varying mean flow that may be in non-equilibrium, as in the current case. Maintaining

the assumption of linearity, we linearize the conservation of vibrational energy disturbance, Eq. 7.1, and translational energy disturbance, Eq. 7.2, which are

$$\frac{De'_v}{Dt} = -u'_i \frac{\partial e_{v,0}}{\partial x_i} + (e_v^{*'} - e'_v) \tau_{s,0}^{-1} + (e_{v,0}^* - e_{v,0}) \tau_{s,0}^{-2} \left(\frac{\partial \tau_s}{\partial T} T' + \frac{\partial \tau_s}{\partial P} p' \right), \quad (7.1)$$

$$\begin{aligned} \frac{De'}{Dt} = & - (e_{v,0}^* - e_{v,0}) \tau_{s,0}^{-2} \left(\frac{\rho'}{\rho_0} + \frac{\partial \tau_s}{\partial T} T' + \frac{\partial \tau_s}{\partial P} p' \right) - (e_v^{*'} - e'_v) \tau_{s,0}^{-1} \\ & - \left(\frac{\rho'}{\rho_0} U_{i,0} + u'_i \right) \frac{\partial e_0}{\partial x_i} - \frac{P_0}{\rho_0} \frac{\partial u'_i}{\partial x_i} - \frac{p'}{\rho_0} \frac{\partial U_{i,0}}{\partial x_i}. \end{aligned} \quad (7.2)$$

In Eq. 7.1, the vibrational energy disturbance is affected by three productions terms. The first relies on a mean gradient in the vibrational energy. For an acoustic wave, we have the additional relationship between the velocity disturbance and pressure disturbance, which is

$$u'_i = \frac{\partial u_i}{\partial P} p'.$$

For slow acoustic waves, the partial derivative is less than zero, or

$$\frac{\partial u_i}{\partial P} < 0$$

and for fast acoustic waves the partial derivative is greater than zero. Therefore, a positive mean gradient will result in positive production term for a slow wave and will result in a negative production term for a fast wave. A similar term is seen in Eq. 7.2, governing the evolution of the translational energy disturbance. The second production term is the one considered by Fujii and Hornung[5, 6] and results in a lag of the vibrational energy disturbance from the translational energy disturbance. The negative of this production term is seen in Eq. 7.2, indicating the interaction of these two disturbances. Finally, the third production term is proportional to the thermal non-equilibrium in the mean flow. If the mean vibrational temperature is less than the translational temperature the vibrational energy disturbance will amplify and vice versa. As in the last production term, the negative of this production term is also seen in Eq. 7.2, indicating another means for these disturbance quantities to interact.

To determine if acoustic damping is occurring, we extract several profiles parallel to the wall through the different regions of the flow from the 1.4 MHz, slow-wave case, which are indicated in Fig. 7.14. The first set of sample data, Fig. 7.15a, is taken from the freestream. These data show

a relatively weak response of the vibrational temperature to the oscillations in the translational temperature, indicating that our assumption of a frozen acoustic wave is valid. Also in the figure, the oscillations in vibrational temperature appear to lead those of the translational temperature. However, since the wave itself is traveling upstream, a lag in the vibrational temperature should appear as a phase shift in the downstream direction. In the second sampling location, Fig. 7.15b, the vibrational temperature disturbance amplitude is greater than the translational temperature disturbance. This interesting profile results from energy deposited into the disturbance by the shock and will be discussed later. At this location, the vibrational temperature disturbance has an almost indistinguishable lag from the translational temperature disturbance. The third sample data set, shown in Fig. 7.15c, is located in the noise radiated from the boundary layer at approximately two boundary layer heights. The vibrational temperature disturbance again shows a distinct lag from the translational temperature disturbance, suggesting the presence of acoustic damping. Despite this, both the translational temperature disturbance and the vibrational temperature disturbance appear to grow, however, this is simply an effect of the sampling location. As seen in Fig. 7.14, the line of data from third location runs parallel to the boundary layer. As the second mode disturbance amplifies, the amplitude of the noise radiated from the boundary layer edge also amplifies and travels out from the boundary layer along the acoustic characteristic. Therefore, a disturbance sampling that runs parallel with the boundary layer would show an increase in disturbance magnitude, as is reflected in Fig. 7.15c. The fourth set of sample data lies in between the boundary layer edge and the disturbance sonic line and is shown in Fig. 7.15d. At this location, the temperature disturbances are essentially in phase and are both growing due to the amplification of the second mode disturbance, as in the previous sample location. The fifth sampling location, Fig. 7.15e, lies within the disturbance sonic line and shows similar behavior to the fourth location. However, at this location the amplitude of the vibrational temperature disturbance is less than at the fourth location. This is due to the decrease in the mean flow temperatures near the wall which results in a reduction in the energy capacity of the vibrational mode as discussed in Section 5.1.1. A closer look at a single wavelength, shown in Fig. 7.16, reveals that the vibrational temperature disturbance now lags the translational temperature in the upstream direction, suggesting a change in the character of the acoustic disturbance.

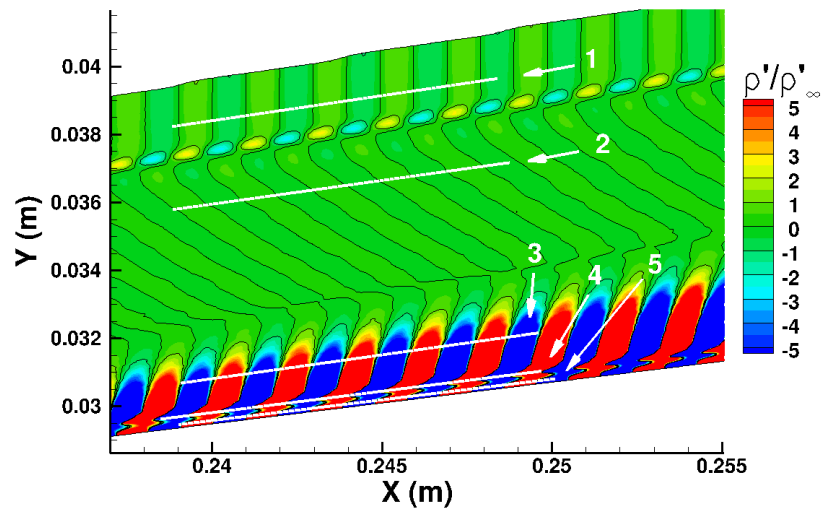


Figure 7.14: Contours of the density disturbance over the cone with the sampling locations to determine the presence of vibrational temperature lag. Each sampling line is indicated with a number in order to identify where the data are taken from in further figures.

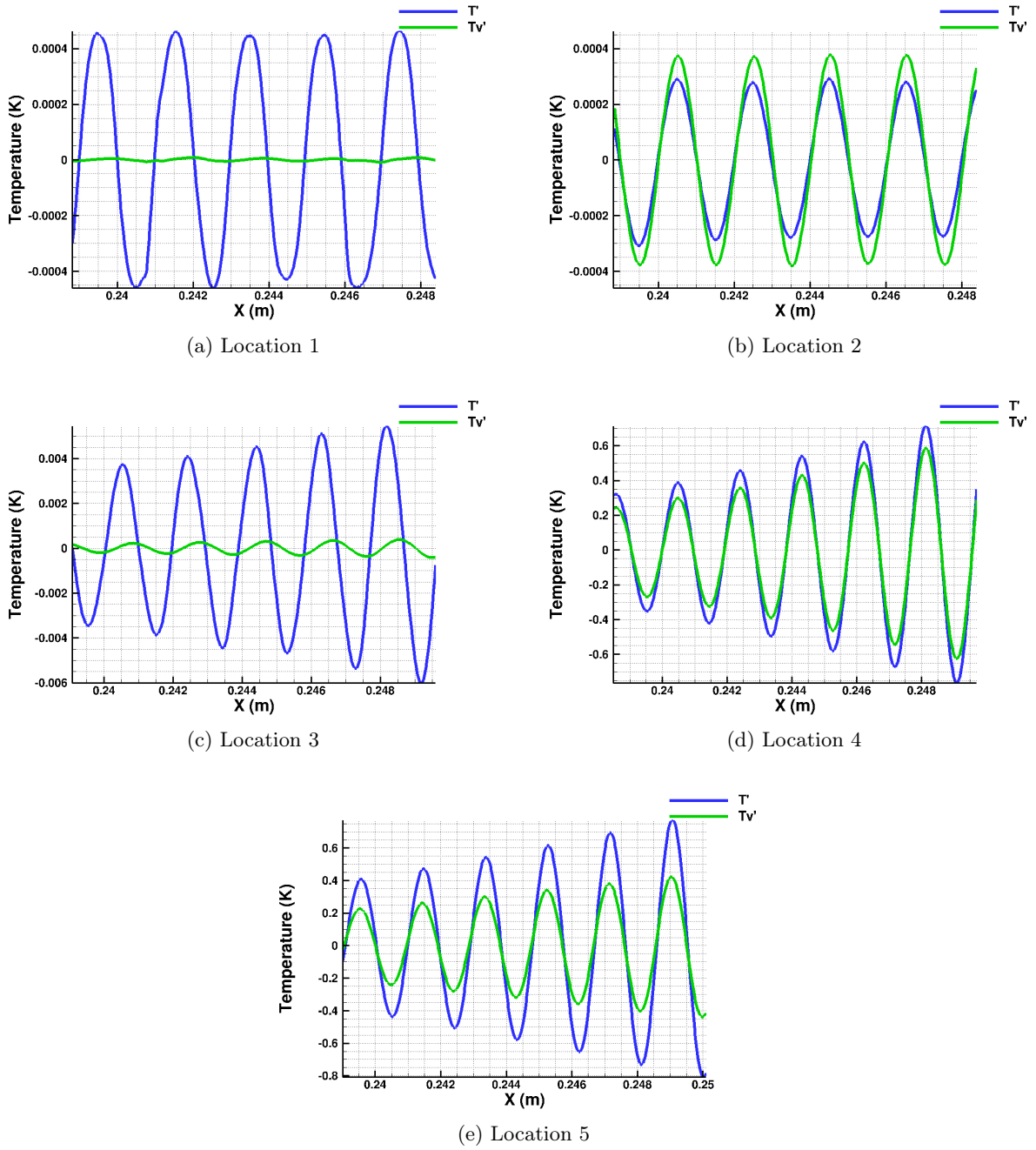


Figure 7.15: Translational and vibrational temperature disturbances versus streamwise distance. The number below each plot corresponds to the sample location indicated in Fig. 7.14.

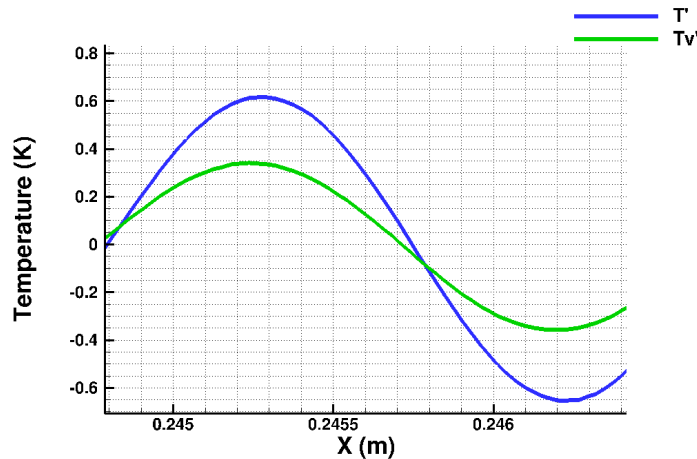


Figure 7.16: Close up view of one wavelength from sample location 5. The data show a slight lag of the vibrational temperature disturbance from the translational temperature disturbance in the upstream direction.

In order to make a comparison between the three different slow wave simulations, data are again extracted in lines parallel to the cone wall at wall-normal distance of 0.1, 0.2, 0.3, and 0.5 boundary layers thicknesses. A sample of the data extracted from a height of 0.3 boundary layer thicknesses from the 1.2 MHz case is shown in Figure 14. In order to compare the pressure disturbance, density disturbance, translational temperature disturbance, and the vibrational temperature disturbance in a meaningful way, these disturbances have been normalized based on the disturbance ideal gas law, Eq. 3.39, as was done in Section 5.2.1. The vibrational temperature disturbance has been scaled using the mean translational temperature in order to maintain the magnitude of the disturbance relative to the translational temperature disturbance. As seen in the figure, the density disturbance has phase shift in downstream direction relative to the pressure disturbance, while the translational temperature has a phase shift in the upstream direction. This is a similar trend seen in slow acoustic waves that experience damping due to an internal molecular process. However, in the current second mode disturbance, the vibrational temperature disturbance has a phase shift in the upstream direction from the translational temperature disturbance. A slow wave vibrational temperature disturbance would have a phase shift in the downstream direction as demonstrated in Fig. 5.20.

From each set of sample data the phase shift between the translational temperature disturbance and the vibrational temperature disturbance is calculated and compiled into Table 7.2. Comparing the 1.4 MHz and 1.05 MHz cases, the lower frequency experiences a larger phase shift indicating that more acoustic damping is occurring. This agrees with the results of the stability analysis

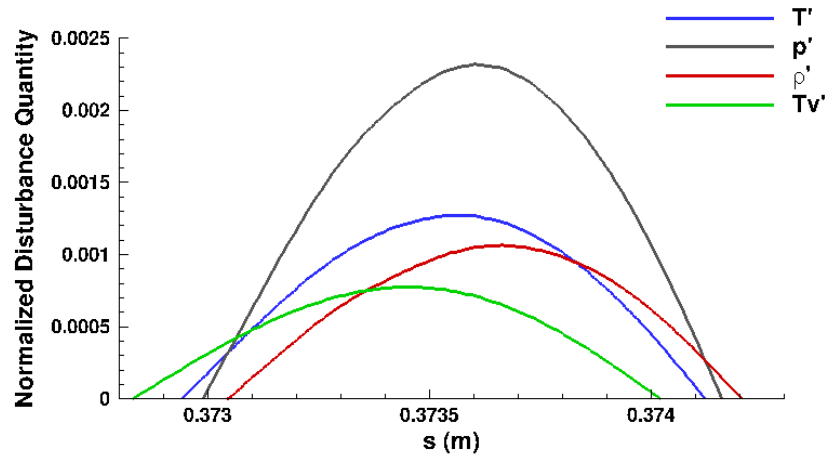


Figure 7.17: Normalized disturbance quantities versus distance along the cone for half of a disturbance wavelength at a wall-normal height of 0.3 boundary layer thicknesses. These data are sampled from a location where the disturbance is amplifying.

performed on the mean flow. A comparison between the 1.05 MHz case and the 1.2 MHz case shows similar values for the phase shift. However, because the 1.2 MHz case has all four vibrational modes of CO_2 present, it is expected that the effect of molecular vibration produce a greater amount of acoustic damping. This confirmed by the stability analysis results above. In each case, the phase shift increases as the height off of the cone wall increases for sample location 0.3 boundary layer thicknesses and down. Based on Fujii and Hornung's[6, 5] work, this trend is not expected because the increase in phase shift corresponds to an increase in mean translational temperature. In the equilibrium analysis performed by Fujii and Hornung, they show that the phase shift of a higher frequency wave would be larger than a lower frequency due to the vibrational relaxation rate at the temperatures in the boundary layer. Since the opposite trend is observed, it indicates that the other terms governing the vibrational energy disturbance are dominant in the boundary layer. At a height of 0.5 boundary layer thicknesses, the phase shift is now in the downstream direction, as indicated by the negative value given in Table 7.2, indicating that the disturbance has regained its slow wave character. For reference, the disturbance sonic line occurs at approximately 0.53 and 0.52 boundary layer thicknesses for the single vibrational mode case and the case with all vibrational modes present, respectively.

Lastly, we extract a set of sample data that is perpendicular with the wavefronts of the acoustic disturbance, the black line shown in Fig. 7.18, in order to explain the reason for the large vibrational temperature disturbance shown in Fig. 7.15b. As seen in the contour plot in Fig. 7.18, the

Table 7.2: Upstream phase shift in degrees versus the height above the wall in boundary layer thicknesses. A negative value indicates a downstream phase shift.

Height	1.4 <i>MHz</i>	1.05 <i>MHz</i>	1.2 <i>MHz</i>
0.1	2.94	4.92	4.74
0.2	7.28	9.45	7.74
0.3	12.67	15.93	16.09
0.5	-7.89	-3.36	-8.72

vibrational temperature disturbance amplifies behind the shock as well as in the boundary layer. The sample data, shown in Fig. 7.19, extend from the freestream to well within the shock layer. These data show a rapid increase in the translational temperature disturbance at the shock location due to the acoustic wave displacing the shock as indicated by the production term proportional the mean gradient in translational energy seen in Eq. 7.2. Interestingly, this sharp rise in disturbance magnitude does not occur in the fast wave case due to the phase alignment of the velocity disturbance with the pressure disturbance discussed above. After the shock, the translational temperature rapidly decays then slowly dissipates into the shock layer. The vibrational temperature disturbance is not immediately affected by the shock. However, as the mean temperatures begin to equilibrate, the vibrational temperature disturbance extracts energy from the mean translational-vibrational energy exchange as well as the mean gradient in vibrational energy. In this manner, the amplitude of the vibrational temperature disturbance is able to become larger than that of the translational temperature disturbance. Based on these sets of sample data, we can infer that the vibrational temperature disturbance is largely driven by energy exchanges in the mean flow, rather than the effects of acoustic damping.

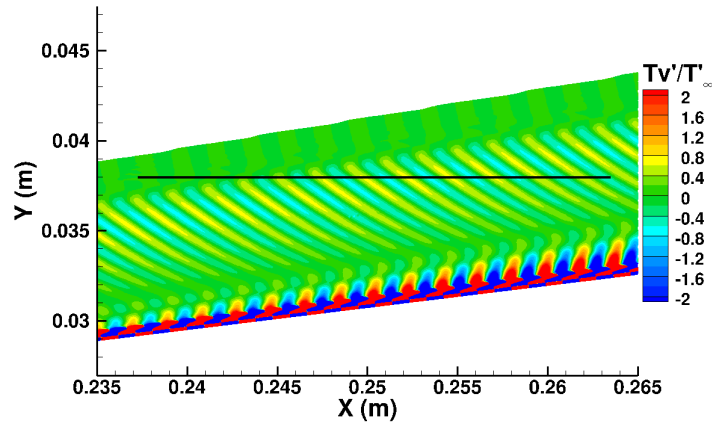


Figure 7.18: Contours of the normalized vibrational temperature disturbance field at an approximate streamwise location of 25 cm from the nose of the cone for the slow wave case. The vibrational temperature disturbance amplifies behind the shock due to the transfer of energy from molecular translation to molecular vibration. The line of sample data taken is indicated by the black line.

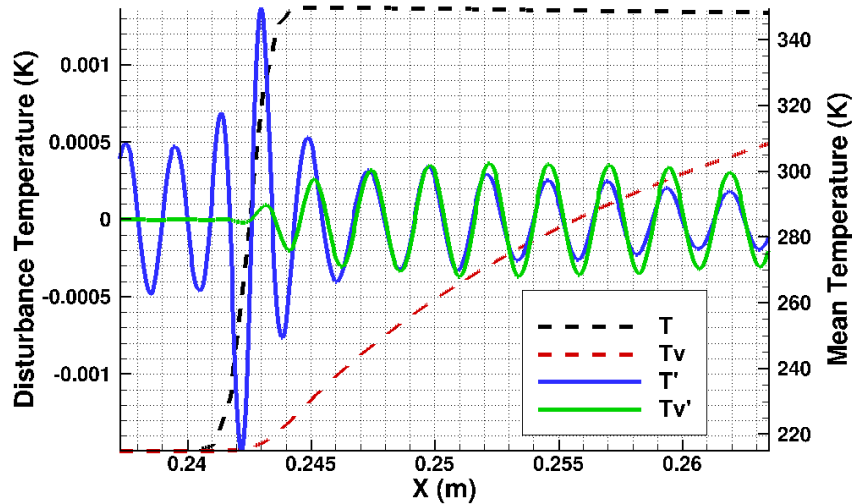


Figure 7.19: Mean (dashed lines) and disturbance (solid lines) temperatures versus streamwise distance sampled in a direction perpendicular to the wavefronts of the acoustic disturbance.

7.6 Conclusion

In the current chapter, the effect of the vibrational modes of carbon dioxide on acoustic disturbances has been studied through the use of DNS and linear PSE. Using the CFD solver US3D, acoustic waves were introduced into the freestream of a Mach 12 flow in order to study the receptivity of

a hypersonic boundary layer to acoustic disturbances as well as the interaction of boundary layer disturbances with molecular vibrational. Results show good agreement between DNS and PSE on the location and growth of boundary layer disturbances. In addition, the current DNS disturbance field shows similar features to previously published works. Evaluation of the frequency of the disturbance at several locations throughout the domain demonstrates that the numerical method has very little dispersion error. However, the difference in amplification rate between the DNS and PSE could be due the numerical method adding artificial dissipation. Further investigation is required to determine the discrepancy in amplification.

A review of the governing equations of the vibrational and translation disturbance energies show additional means of interaction between these two disturbances with each other and the mean flowfield than considered in previous analyses. Analyzing boundary layer disturbances reveals that the second mode disturbance has similar characteristics as the slow wave that generated the disturbance. However, the vibrational temperature disturbance shows a phase shift in the opposite direction compared to a slow acoustic wave. Based on these and other extracted disturbance profiles, the DNS data show that the vibrational temperature disturbance is largely driven by mean flow energy exchanges, rather than the effects of acoustic damping.

The level agreement achieved between the DNS and PSE indicate US3D is capable of simulating acoustic waves and second mode disturbances, given an appropriately tailored grid and numerical method. Thus, the results of this chapter lay the groundwork for simulating the porous injection experiments in the T5 tunnel. Such simulations should be capable of obtaining the agreement between computations and experiment.

Chapter 8

Transient Growth Disturbances

8.1 Optimal Compressible Disturbances

8.1.1 Base Flow

The base flow we use in the optimization is provided by one of two methods. In the first method, the base flow state for a given set of flow conditions is generated using the compressible similarity solution for a flat plate. We solve for the similarity solution numerically over a large number of points. We then interpolate the solution onto the optimization grid using linear interpolation. Because the similarity solution does not exist at $x = 0$, the base flow values at the first point are set to those of the freestream, as done by Andersson et al.[30]. We use this method for all validation cases of the optimization code against the published results of Tumin and Reshotko.[15] In the second method, the base flow solution is provided by US3D. The inviscid fluxes are evaluated using the sixth-order accurate in space, low-dissipation method. The time integration is a second-order accurate, full matrix point relaxation implicit method[137]. Once the CFD solution is obtained, we use the weighted least-squares method to accomplish the two-dimensional interpolation to the optimization grid.

We first validate our optimal disturbance solver using the published results of Tumin and Reshotko.[15] Due to the flow conditions chosen for the full simulations, we compare results of the Mach 3, adiabatic wall case although other validation cases were performed. The flow conditions used by Tumin and Reshotko are also used for the current validation. The gas has a specific heat ratio of 1.4 and a Prandtl number of 0.7. The viscosity is calculated using Sutherland's law

for air, with $a_s = 1.458 \cdot 10^{-6} \text{ kg/s}\cdot\text{m}$ and $b_s = 110.4 \text{ K}$, where

$$\mu(T) = a_s \frac{T^{1.5}}{T + b_s}.$$

The stagnation temperature of the flow is 333 K. In the current study, the Reynolds number is set to 10^6 , to ensure the applicability of the assumption made by Luchini[103] described in Section 2.2.4. Other gas properties of this flow are contained in Table 8.1. As used in Tumin and Reshotko's study, we use 100 equally spaced points to discretize the streamwise direction. In their code, Tumin and Reshotko use spectral collocation to calculate the wall-normal derivatives on a mesh of 100 points clustered to the wall and spread over a non-dimensional height of $y = 100$, as defined above. Since we use an equally spaced mesh, we use more points to ensure grid convergence and use 800 points spread over a non-dimensional height of $y = 45$. The optimization interval begins at $x = x_{in} = 0$ and ends at $x = x_{out} = 1$. Unless stated otherwise, the spanwise wavenumber, β , is set to 0.35. In addition to the scaling in Eqs. 3.55, all disturbance quantities presented, except for the growth factor, are normalized by the square root of the local value of disturbance energy, $\sqrt{E(x)}$.

Table 8.1: This table contains the freestream conditions used in the validation of the optimal disturbance solver.

Temperature	118.92 K	Pressure	858.65 Pa
Density	0.02515 kg/m^3	Mach	3.00
Velocity	655.8 m/s	Stagnation Enthalpy	0.334 MJ/kg

8.1.2 Validation

We begin our comparison to the published results of Tumin and Reshotko[15] with the growth factor, seen in Fig. 8.1. The two methods produce growth factor profiles that are nearly identical, proving that the current method is adequate to capture the growth of the optimal disturbance. This growth plot defines the transient growth behavior. Initially the disturbance growth rises in a linear or algebraic fashion as the streamwise vortices deform the flat plate boundary layer. This type of growth is due to the interaction of the wall-normal velocity and wall-normal vorticity disturbances, as discussed in Chapter 2.1.1. Eventually the viscous dissipation begins to overcome the vortices and the growth factor begins to decay. This decay is exponential because the two disturbances types, which are described by exponential growth and decay, no longer interact, also as discussed in Chapter 2.1.1. A similar agreement is observed when comparing the initial disturbance profiles, as

seen in Fig. 8.2a. Both of the input disturbance velocities, v and w , match very well to the published result of Tumin and Reshotko[15]. To demonstrate that these profiles represent a pair of streamwise vortices, the spanwise sinusoid variation has been applied to these profiles as defined in Eq. 3.57 and the resulting disturbance velocity vectors are plotted in Fig. 8.2b. A comparison of u and θ disturbances shows that these two methods are also in agreement at $x = x_{out}$, as seen in Fig. 8.3. The spanwise variation of these profiles results in the streamwise streaks of high temperature, low velocity streaks that are common behind roughness elements. Lastly, we performed a broad comparison of growth factor at $x = x_{out}$ over a range of β 's for three different wall temperatures in order to show that the current method is, in general, obtaining the same results as those published by Tumin and Reshotko.[15] As seen in Fig. 8.4, the two methods produce nearly identical results over the range of conditions.

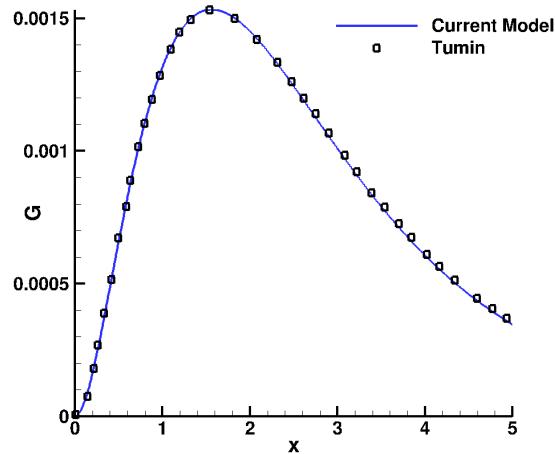


Figure 8.1: Comparison of the growth factor as calculated by the current method to the published result of Tumin and Reshotko[15] (indicated by Tumin in the plot legend). The two profiles are nearly identical, showing the agreement between the two methods. The growth factor is independent of Reynolds number and the x distance has been scaled by the length L .

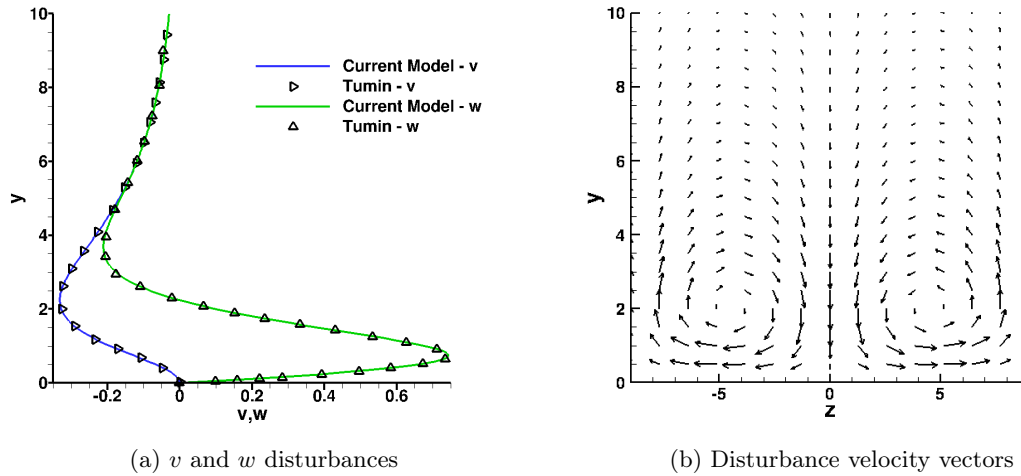


Figure 8.2: Comparison of the v and w disturbances at $x = x_{in}$ (a) as calculated by the current method to the published result of Tumin and Reshotko[15]. Both disturbance velocity components are nearly identical, showing the agreement between the two methods. The wall-normal distance has been scaled by εL and both velocity components have been scaled by εU_∞ . To demonstrate that these profiles represent a pair of streamwise vortices, the disturbance velocity vectors have been plotted at $x = x_{in}$ in sub-figure b.

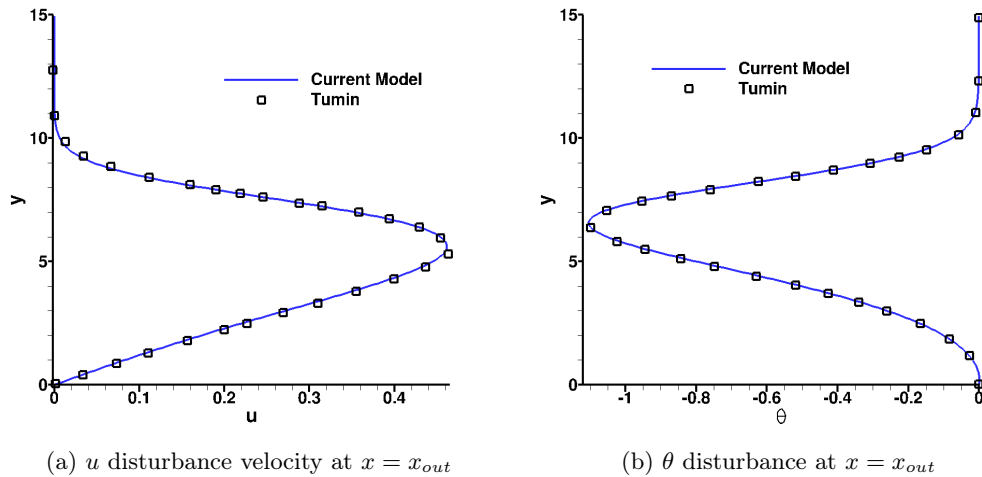


Figure 8.3: Comparison of the u and θ disturbances at $x = x_{out}$ as calculated by the current method to the published result of Tumin and Reshotko[15]. Both disturbance quantities are in good agreement between the two methods. The u disturbance has been scaled by U_∞ and the θ disturbance has been scaled by T_∞ .

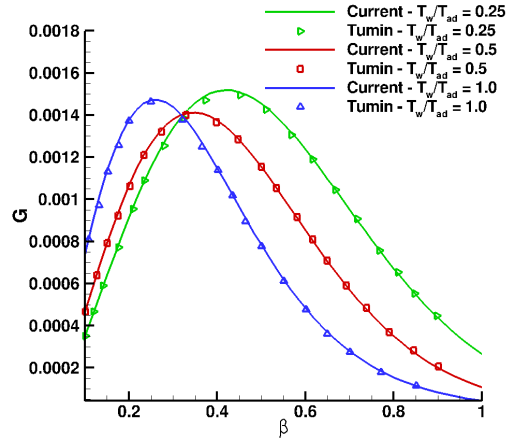


Figure 8.4: Comparison of the growth factor at $x = x_{out}$ over a range of β 's for three different wall temperatures. The two methods produce nearly identical results over the range of conditions.

Now that we have confidence that the method is functional, given sufficient grid density, we need to explore some additional properties of the method and of compressible optimal disturbances. First, we perform another grid convergence study focusing on the number of streamwise points used to discretize the optimization. The current method shows grid dependence in the initial disturbance quantities until approximately 3200 streamwise points, as seen in Fig. 8.5. This is most likely due to the large gradients in the mean flow properties at the front of the plate. Based on this conclusion, it would be better to have clustering in the streamwise direction. However, the effect of these changes in the input disturbance on the growth factor is most important in the search for the optimal disturbance. As seen in Fig. 8.6a, the growth factor shows no noticeable grid dependence past 200 streamwise points. The output disturbance quantities are the least sensitive to the grid, as seen in Fig. 8.6b. The insensitivity of the output disturbances to variations in the input disturbance is discussed by Luchini.[103]

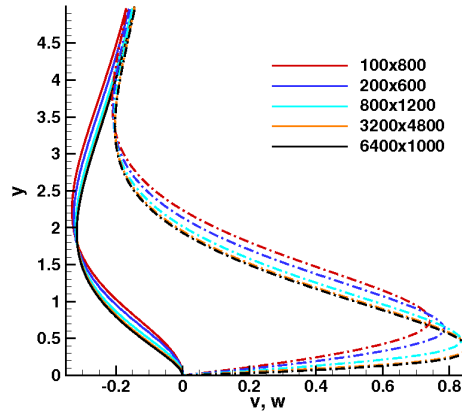


Figure 8.5: Grid convergence study on the shape of the initial disturbance quantities, v and w . Both quantities show grid dependence until approximately 3200 streamwise points. In the plot, the number of points used is given in the plot legend as the number of streamwise points by the number of wall-normal points. The v velocity disturbance is plotted with the solid line, while the w velocity disturbance is plotted with the dashed-dot line.

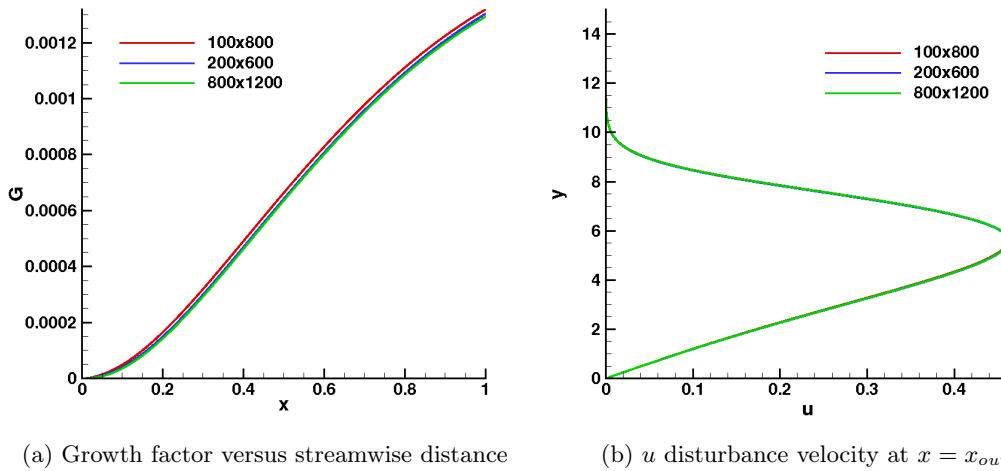


Figure 8.6: Results from the grid convergence study. The growth factor shows no noticeable grid dependence past 200 streamwise points. The output disturbance quantities are least sensitive to the grid.

Next, we explore the effects of the adiabatic wall condition for the temperature disturbance. Allowing the wall temperature to vary results in a non-zero temperature disturbance at the wall, as seen in Fig. 8.7. Physically, this is due to the vortical motion of the fluid causing alternating hot and cold spots on the wall. The adiabatic wall boundary condition also results in a larger growth factor over the domain, seen in Fig. 8.8a, and only a minor change in the input and output velocity disturbances as demonstrated with the u disturbance in Fig. 8.8b

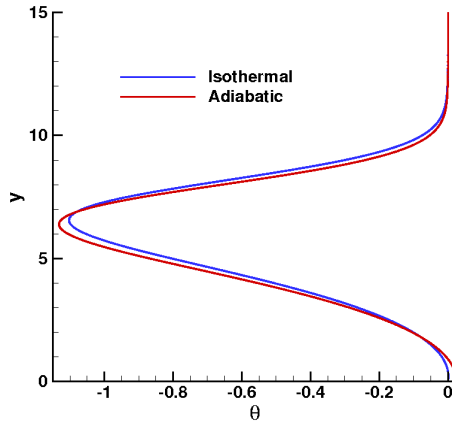
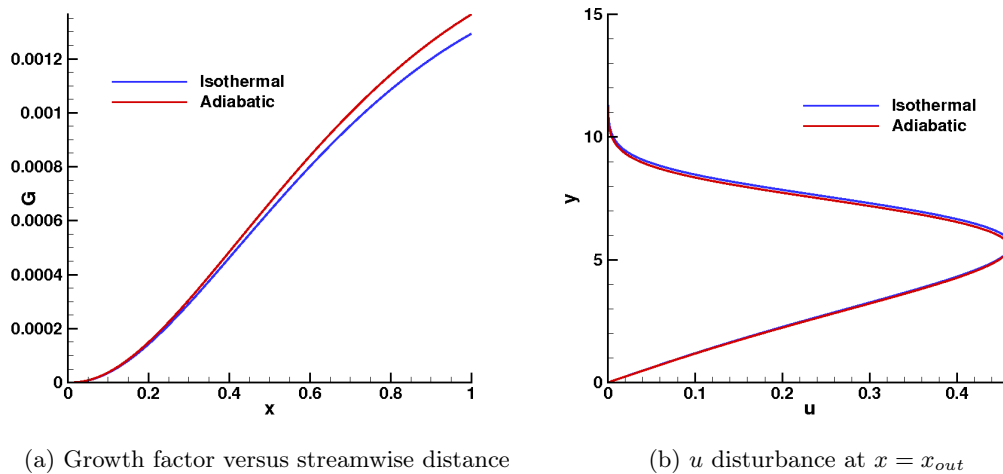


Figure 8.7: Comparison of θ disturbance at $x = x_{out}$ between the isothermal wall and adiabatic wall boundary conditions. The adiabatic wall case allows a non-zero value of θ at the wall.



(a) Growth factor versus streamwise distance

(b) u disturbance at $x = x_{out}$

Figure 8.8: Comparisons of growth factor over the domain and u disturbance at $x = x_{out}$ between the isothermal wall and adiabatic wall boundary conditions.

Lastly, we would like to highlight the effect of Prandtl number on the optimal disturbance. For the case of adiabatic wall, an increase in Prandtl number results in a higher wall temperature. Given the same boundary layer thickness, the increase in wall temperature results in a higher temperature gradient. This effect is similar to that of directly changing the wall temperature in an isothermal wall case and, given a suitably sized disturbance, results in a greater temperature disturbance as well as a larger growth factor over the domain, as demonstrated in Fig. 8.9. The wall temperature effect can also be seen in Figs. 7 and 8 in Tumin and Reshotko.[15] Despite the dependence of the growth factor on the Prandtl number, the input disturbance is minimally affected, as seen in Fig. 8.10. While the effect of Prandtl number may have implications for different gases, we only

want to emphasize its importance in validating the full simulations below.

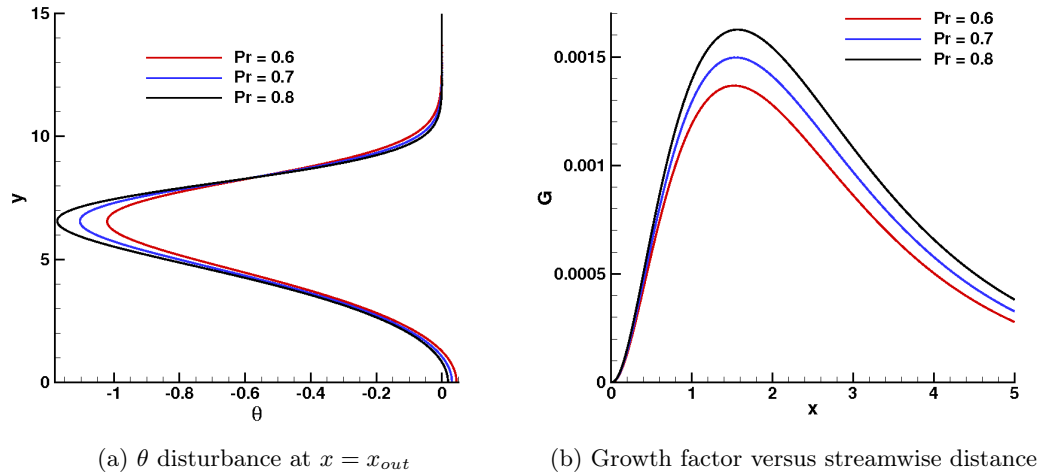


Figure 8.9: Effect of Prandtl number on the growth factor and θ disturbance. Increasing the Prandtl results in a greater temperature disturbance and a larger growth factor over the domain.

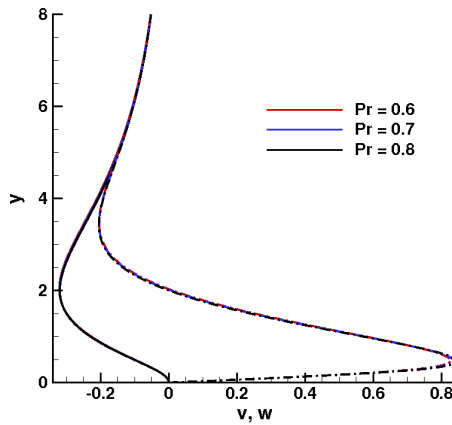


Figure 8.10: Effect of Prandtl number on v , solid line, and w , dash-dot line, disturbances at $x = x_{in}$. A change in the Prandtl number has a minimal effect on the input disturbance.

8.2 Full Simulations

Once the optimal disturbances are determined for the given flow conditions, the disturbances are enforced at the inflow of a full three-dimensional simulation using US3D. We do this in order to gauge the ability of the CFD solver to properly capture the linear evolution of the disturbances and

also to study the non-linear behavior of the streaks. The disturbances are calculated at each x, y point using a spanwise rms, which is given by

$$\phi_{rms}(x, y) = \sqrt{\frac{1}{N} \sum_{k=1}^N [\Phi(x, y, z_k) - \Phi_{bf}(x, y)]^2}, \quad (8.1)$$

where Φ is the full simulation quantity and $\Phi_{bf}(x, y)$ is the base flow quantity corresponding to the disturbance quantity ϕ_{rms} . The energy of disturbances at each x location, $E_{rms}(x)$, is calculated with spanwise rms quantities using the norm defined in Eq. 3.59. In the 3-D simulations, all quantities are normalized according to Eqs. 3.55, except for the spanwise rms disturbance velocities and the wall-normal velocity, V , which are normalized only by the freestream velocity. Therefore, the growth is calculated as defined in the optimization procedure and then normalized by Re_L . The 3-D disturbance values also differ from their 2-D optimization counterparts by an additional factor of $\sqrt{2}$, however, all presented results are normalized by the square root of the local value of disturbance energy, $\sqrt{E_{rms}(x)}$, thus eliminating the need to include this factor. This is a similar process to that used by Denissen et al.[83].

We use a single grid for all three-dimensional cases. The grid has a single-block, structured topology with a length of 0.3 meters and dimensions of 400x250x100 in the streamwise, wall-normal, and spanwise directions, respectively. The grid is clustered near the leading edge of the plate in the streamwise direction to capture the sharp gradients that occur at this location and also near the wall in the wall-normal direction in order to obtain an initial y^+ value of less than one. For the current study, the maximum amplitude of disturbances is located near the boundary layer edge, therefore, we apply additional clustering along the boundary layer edge. The base flow used to determine the optimal disturbance parameters is calculated on a grid with a single cell in the spanwise direction and identical in the streamwise and wall-normal directions. We performed a grid convergence study using a grid of similar structure with dimensions of 550x375x140. We found that the growth factor and the disturbance values at $x = x_{out}$ were identical. The characteristic length, L , is approximately 0.1 and the Reynolds number, Re , is approximately $6.65 \cdot 10^4$. The optimization interval starts at $x_{in} = 0$ and ends at $x_{out} = 1$. The freestream conditions for these cases are a perfect gas at Mach 2.95, with the full set of conditions given in Table 8.2. The plate boundary condition is adiabatic wall for all cases. The gas has a specific heat ratio of 1.4, a Prandtl number is 0.736, and a specific heat at constant pressure of $1004.51 J/Kg \cdot K$. For the viscosity, we use Sutherland's law with coefficients

Table 8.2: This table contains the freestream conditions used in the full simulations.

Temperature	150 K	Pressure	411.92 Pa
Density	0.00925 kg/m^3	Mach	2.95
Velocity	736.95 m/s	Stagnation Enthalpy	0.427 MJ/kg

for air defined above in Section 8.1.1.

Due to the differences between the compressible similarity solution and the supersonic, compressible flow solution (i.e. the presence of shocks), we use the base flow provided by US3D in the optimization process to solve for the optimal input disturbance using the linear theory code. Although the base flow solution now contains a weak shock, we use no additional numerical techniques to ensure stability of the method as the initial disturbance is propagated through the domain. The presence of the weak shock now implies a difference between the freestream conditions and the boundary layer edge conditions. For the current study, we use the freestream values for the normalization of disturbance properties. In the case of three dimensional disturbances, we calculate the non-dimensional input energy by integrating Eq. 3.63 over one wavelength, which is

$$E_{in} = \int_{-\frac{\pi}{\beta}}^{\frac{\pi}{\beta}} \int_0^{\infty} [\rho_s (v^2 + w^2)] dydz.$$

The discretized version of this integral is

$$E_{in} = 2\pi E_{rms}(x_{in}) = 2\pi \sum_{y=0}^{y_{max}} [\rho_s (v_{rms}^2 + w_{rms}^2)] \Delta y,$$

with the factor of two due to the spanwise rms values differing from the integrated values by a factor of $\sqrt{2}$ and the factor of π due to the integration of the spanwise wave over one wavelength. Using a non-dimensional input energy of $E_{in} = 4.725 \cdot 10^{-5}$, corresponding to unity in the linear theory code, we allow the optimal disturbances to propagate down the plate and obtain the growth profile shown in Fig. 8.11. The growth factor from US3D shows slightly larger growth than linear theory predicts, although the two profiles are similar. Unfortunately, a small amplitude, high-frequency disturbance exists in the solution domain as seen in the jagged curve in the US3D solution. This is most likely due to the shock detection switch causing the shock to oscillate between grid cells. We have also included the growth factor as calculated from the base flow generated using the compressible similarity solution. The differences in the two flowfields result in a significant difference in the growth

factor profile. Comparing the θ and u disturbances at $x = x_{out}$, in Fig. 8.12, the US3D results follow the linear theory results for a majority of the curve, differing at the maximum amplitude of the θ and u disturbances. Both methods show the non-zero θ disturbance at the wall resulting from the vortical motion of the disturbance, although US3D predicts a lower value of θ at the wall.

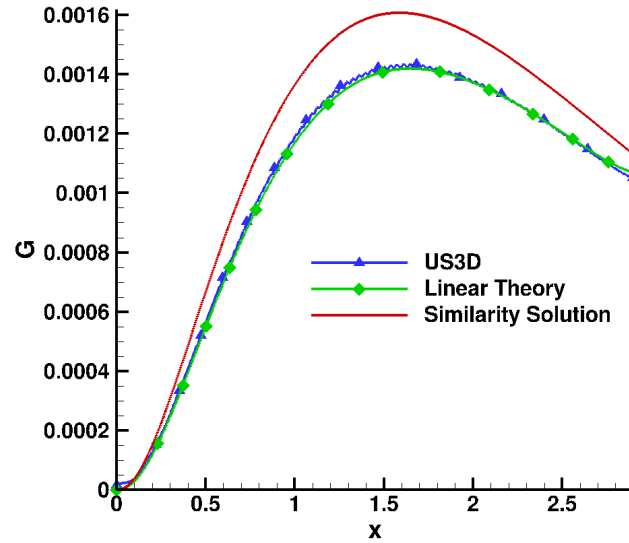


Figure 8.11: Comparison of growth factor between linear theoretical code and US3D. The growth factor curves are similar indicating reasonable agreement. The growth factor from the similarity solution is also plotted to show how the different base flowfields affect the optimal growth factor.

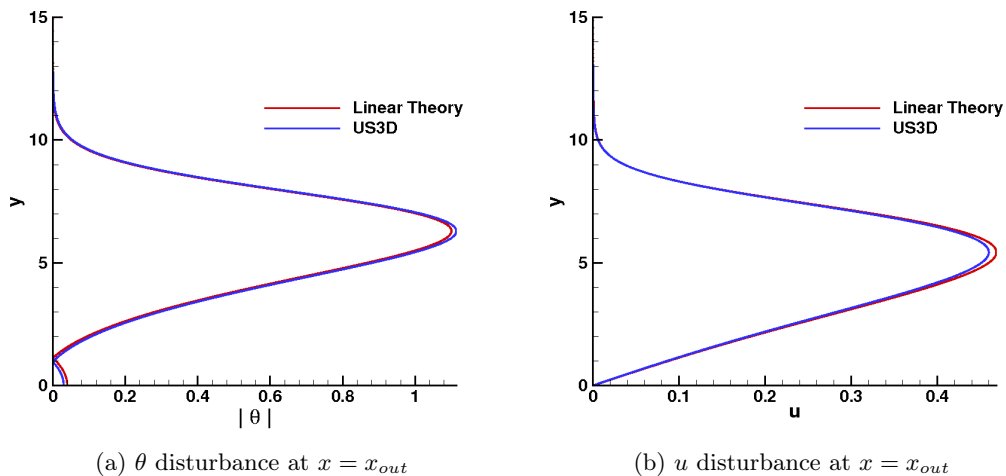


Figure 8.12: Comparison of θ and u disturbances at $x = x_{out}$ between US3D and linear theory. Although differences exist between the maximum amplitudes of both quantities, the curves are similar for a majority of the wall-normal distance. US3D also shows a smaller θ disturbance at the wall as compared to the linear theory.

With reasonable agreement between the results of US3D and the linear theory code, we now increase the input energy by factors of two to determine the approximate energy required for non-linear terms in the governing equations to begin affecting the solution. Previous studies[16, 92] have shown that the presence of non-linearities will result in a reduction in the growth factor over the domain. Therefore, non-linear effects are considered to begin when the input disturbance energy results in a departure from the linear growth factor. This growth factor makes its first noticeable departure when $E_{in} = 3.024 \cdot 10^{-3}$. As the input energy increases, the growth factor continues to lessen, plotted in Fig. 8.13a based on normalized disturbance energy, $E^{(x)}/E_{in}$, as was done in Andersson et al.[16]. This would indicate that non-linear terms cause the disturbance to dissipate at a higher rate than predicted by linear theory. Previous studies have shown the importance of the transient growth disturbance amplitude in determining when the streamwise streak becomes unstable to secondary disturbances. The amplitude function, A , is calculated based on Anderson et al.[16] as

$$A(x) = \frac{1}{2} \left[\max_{y,z} (U(x, y, z) - U_{bf}(x, y)) - \min_{y,z} (U(x, y, z) - U_{bf}(x, y)) \right], \quad (8.2)$$

where the subscript bf denotes base flow, remembering that the streamwise velocity, U , is normalized by the freestream value. As expected, the amplitude function increases with an increase in input disturbance energy, peaking at the same location as the disturbance energy. Input energies of $2.419 \cdot 10^{-2}$ and higher reach a value of 26%, making them susceptible to breakdown via sinuous-type secondary instabilities.

The output profiles also depart from the linear profile at $E_{in} = 3.024 \cdot 10^{-3}$, as seen in Figs. 8.14a and 8.14b. In these figures, the base flow profiles are plotted with an arbitrary amplitude scaling to show the height at which various features of the disturbances occur. At higher input energies, the disturbances increase their extent in the wall-normal direction and the non-linear terms begin to cause a reduction at the maximum amplitude, located near the edge of the boundary layer. This amplitude reduction results in a lobe forming at the boundary layer edge. Physically, this lobe is caused by the streamwise vortices having sufficient strength to move low momentum fluid up the mean velocity gradient and then away from the symmetry plane that lies between the vortices. Additional plots of the flow development can be viewed in Figs. 8.15 and 8.16.

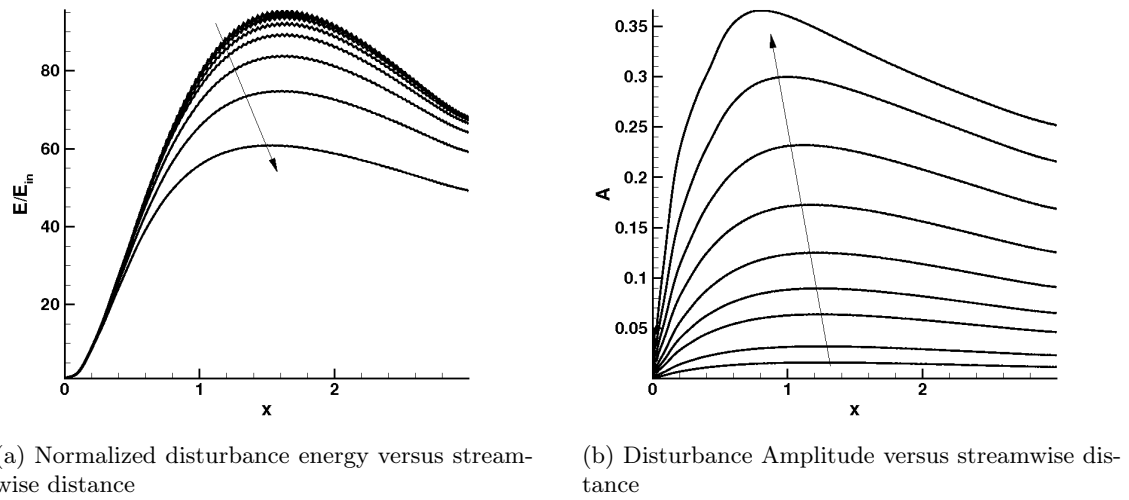


Figure 8.13: The effect of non-linearities on the normalized disturbance energy and transient growth disturbance amplitude. The input energies plotted are $E_{in} = 4.725 \cdot 10^{-5}$, $E_{in} = 1.890 \cdot 10^{-4}$, $E_{in} = 7.560 \cdot 10^{-4}$, $E_{in} = 1.512 \cdot 10^{-3}$, $E_{in} = 3.024 \cdot 10^{-3}$, $E_{in} = 6.048 \cdot 10^{-3}$, $E_{in} = 1.210 \cdot 10^{-2}$, $E_{in} = 2.419 \cdot 10^{-2}$, and $E_{in} = 4.839 \cdot 10^{-2}$. The arrow indicates the direction of increasing energy in both figures. The first noticeable departure from linear growth begins when $E_{in} = 3.024 \cdot 10^{-3}$. The amplitude function was found to be an important factor in streak breakdown due to secondary instabilities.[16]

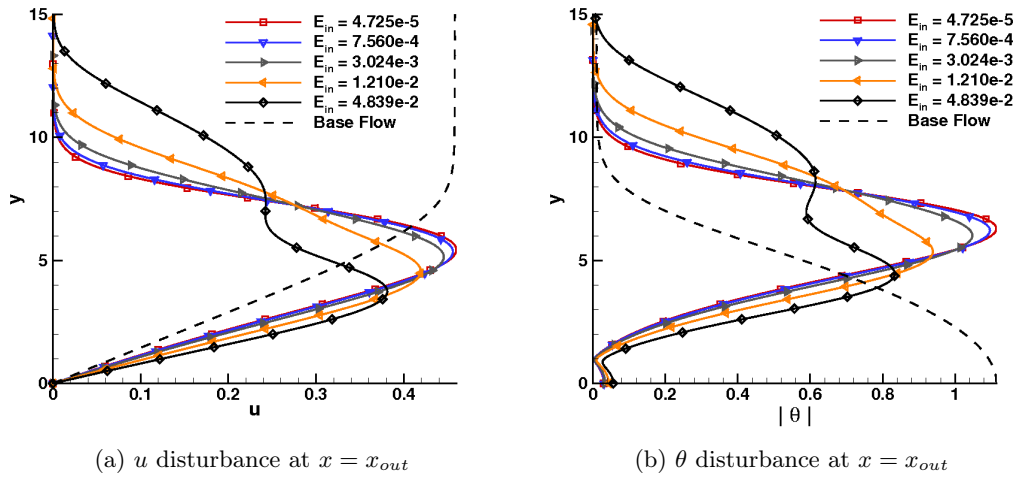


Figure 8.14: Comparison of θ and u disturbances at $x = x_{out}$ for the input energies indicated in each figure's legend. In addition to the disturbance values, the base flow quantity's amplitude has been scaled arbitrarily to show the height at which various features of the disturbances occur.

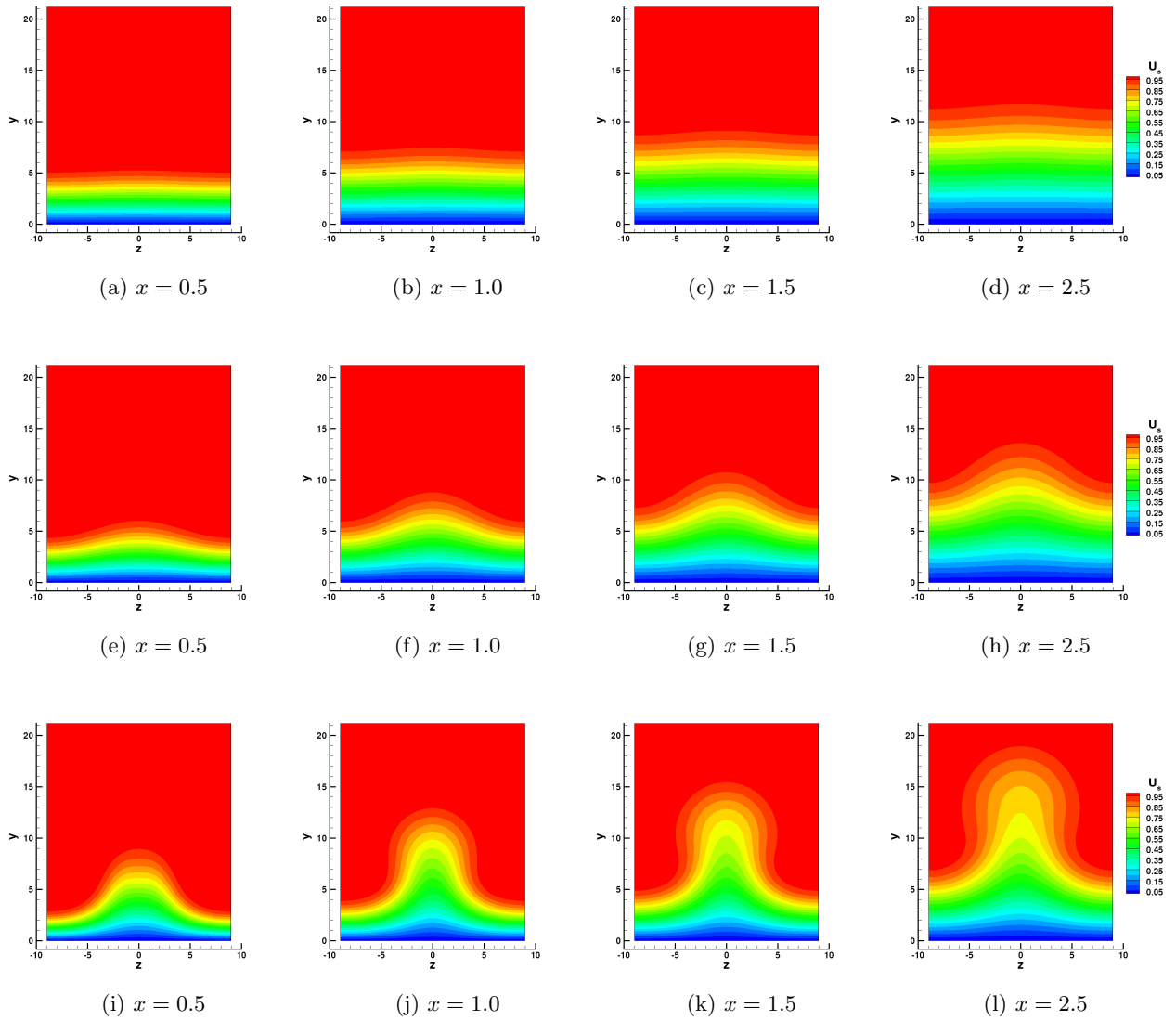


Figure 8.15: Evolution of the u disturbance for three different input energies. The top sequence of plots is $E_{in} = 4.725 \cdot 10^{-5}$, followed by $E_{in} = 3.024 \cdot 10^{-3}$ in the middle, and $E_{in} = 4.839 \cdot 10^{-2}$ at the bottom. The top sequence shows linear growth, the middle sequence shows growth that departs from linear theory, and the bottom sequence shows very non-linear behavior. In the bottom sequence, the vortices have sufficient strength to form a low momentum fluid lobe above the base flow boundary layer edge.

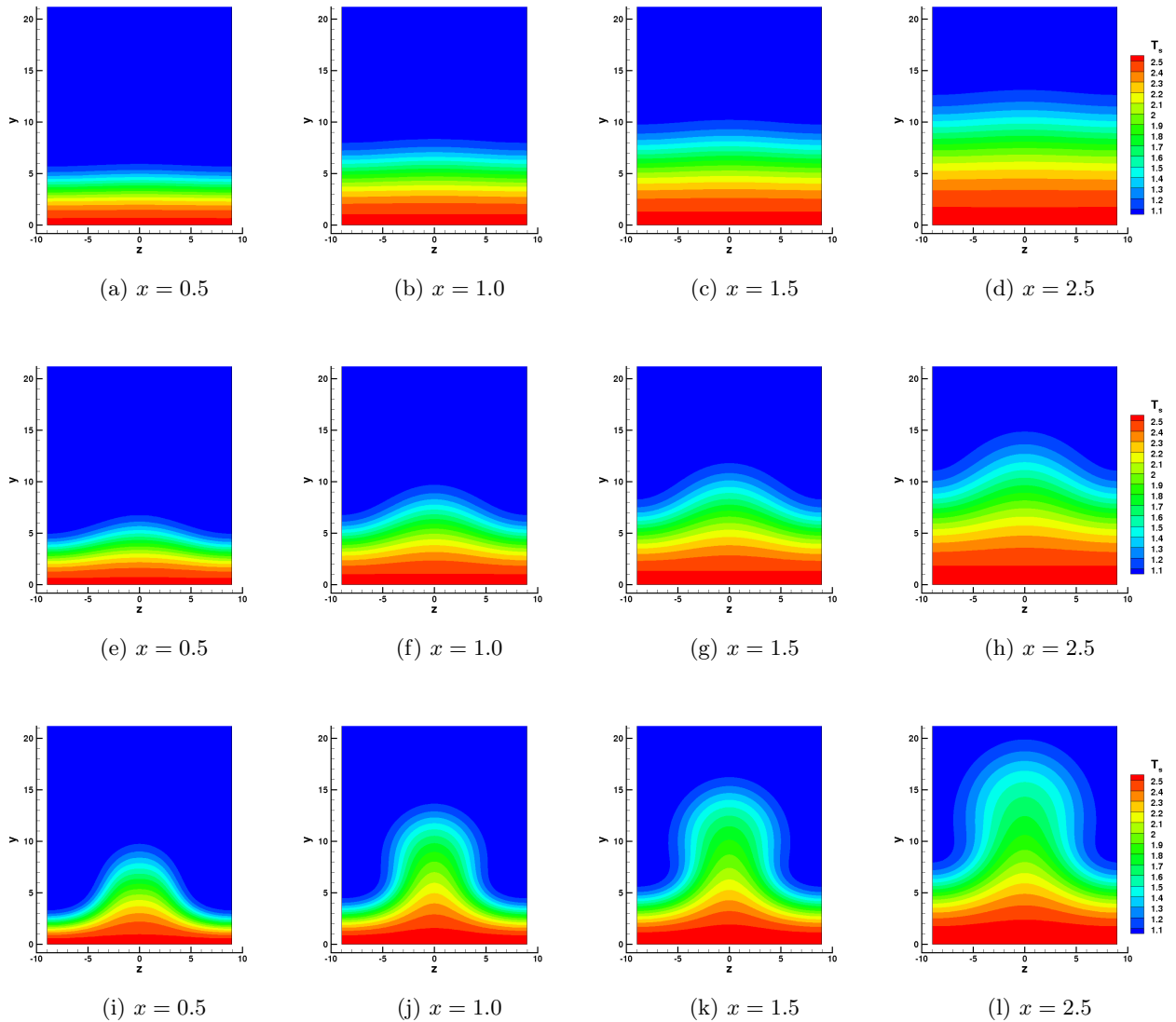
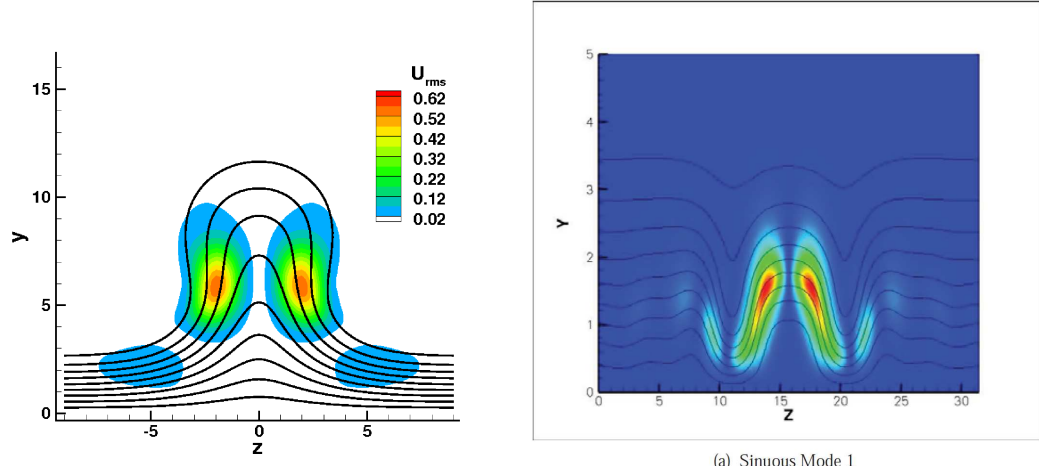


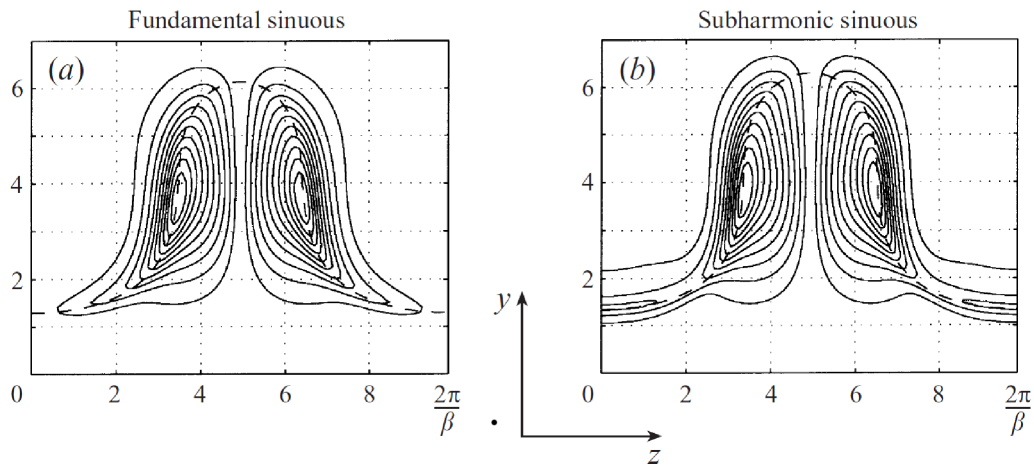
Figure 8.16: Evolution of the θ disturbance for three different input energies. The top sequence of plots is $E_{in} = 4.725 \cdot 10^{-5}$, followed by $E_{in} = 3.024 \cdot 10^{-3}$ in the middle, and $E_{in} = 4.839 \cdot 10^{-2}$ at the bottom. The top sequence shows linear growth, the middle sequence shows growth that departs from linear theory, and the bottom sequence shows very non-linear behavior. In the bottom sequence, the vortices have sufficient strength to form a high temperature fluid lobe above the base flow boundary layer edge. Each case reaches its maximum growth near $x = 1.5$.

Although higher input energies were simulated, the high frequency disturbance seen in Fig. 8.11 caused the flows to become unsteady. Because this disturbance is not controlled, not much can be determined from its resulting behavior. However, the temporal rms values of streamwise velocity are very similar in shape to that of the sinuous disturbance seen in Andersson et al.[16] and Denissen and White[17], as seen in Fig. 8.17.



(a) U_{rms} at $x = 0.7$ for the current study.

(b) Reproduction of Fig. 9a from Denissen and White[17]



(c) Reproduction of figures 12a and 12b from Andersson et al.[16]

Figure 8.17: Comparison of the temporal rms value of streamwise velocity for $E_{in} = 9.677 \cdot 10^{-2}$ to that of previous studies[16, 17]. Although the unsteadiness in the current study is due to an uncontrolled disturbance, the temporal rms values are very similar in shape to the sinuous disturbance seen in Andersson et al.[16] and Denissen and White.[17] For Fig. 8.17a and Fig. 8.17b, the color contours show streamwise velocity rms and each black line represents a 10% change in velocity relative to the freestream velocity. Denissen and White[17] are plotting the flowfield behind a roughness element. In Fig. 8.17c, Andersson et al.[16] are plotting contours of the sinuous disturbance amplitude in solid lines and the dashed line shows the shape of the streamwise streak resulting from an optimal disturbance.

8.2.1 Single Vortex Test

The counter-rotating streamwise vortices used in the optimal transient growth problem above are of primary interest due to their common presence behind roughness elements. However, they do not

represent the entire vortex system that forms around a roughness element nor a general vortex in a boundary layer. As demonstrated in Fig. 2.6, a roughness element causes a horseshoe vortex system that consists of multiple vortices that may not have a counter-rotating partner as they convect downstream. Theoretically, all of the horseshoe vortices should undergo a transient growth process because they represent a three-dimensional disturbance with a non-zero disturbance velocity parallel to the mean velocity gradient, as described by Landahl[95]. To test if this theory is true, a single vortex is simulated using the same parameters as the case with an input energy of $E_{in} = 4.725 \cdot 10^{-5}$, described above. The single vortex is generated by applying a Gaussian variation to the initial velocity disturbances from the optimal transient growth problem in the spanwise direction, rather than a single wavenumber as before. The resulting disturbance velocity vectors form a single vortex through the center of the domain, as shown in Fig. 8.18. As seen in Fig. 8.19, the single vortex results in a similar growth factor profile as the optimal disturbance shown in is shown in Fig. 8.11. The disturbance results in an initial period of linear growth that is followed by exponential decay. However, this disturbance does not reach the level of growth by $x = x_{out} = 1$ as the optimal disturbance above and the peak in growth occurs further down the plate. The interesting aspect of the test case is that Landahl's theory holds for this type of disturbance, which means that any single vortex with a component of velocity that is parallel to the mean velocity gradient should also undergo a transient growth process. Therefore, in the case of a roughness element, each of the horseshoe vortices from the element will undergo transient growth which results in a distortion of the mean flow.

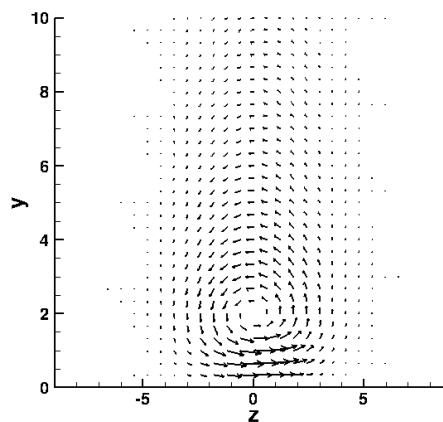


Figure 8.18: Disturbance velocity vectors at $x = x_{in}$ for the single vortex case. The vortex is generated by applying a Gaussian variation to the initial velocity disturbances from the optimal transient growth problem in the spanwise direction.

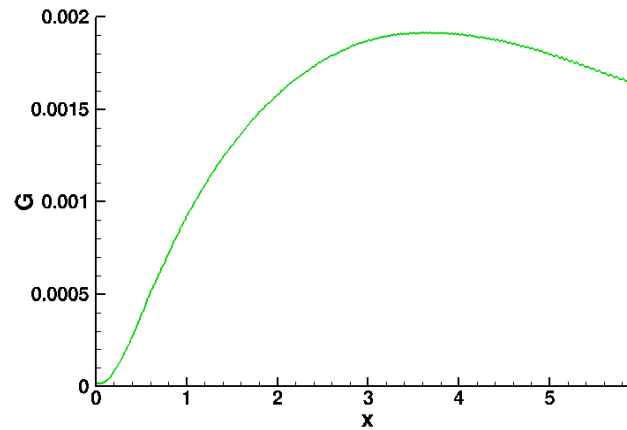


Figure 8.19: Growth factor versus streamwise distance for the single vortex problem.

8.3 Internal Relaxation Effects

8.3.1 Base Flow

With some confidence in the ability of US3D to capture the transient growth process, we can now add the presence of a vibrational mode to the flow to determine the general effect of an internal relaxation process on the disturbance growth. As discussed in Chapter 5, the effect of internal relaxation process was shown to be dependent on the rate of energy transfer and the energy capacity of the internal process. Therefore, to complete a general test of an internal process's effect on transient growth, we use an fictitious molecule for which we specify the characteristic vibrational temperature and the relaxation rate. Four different pairs of conditions are tested, which are listed in Table 8.3 and are labeled based on their origin of their parameters. The vibrational parameters are part of the Millikan and White relaxation time and are as follows

$$A = 1.16 \times 10^{-3} \mu_{ms}^{1/2} \theta_{v,m}^{4/3},$$

$$B = 0.015 \mu_{ms}^{1/4}.$$

For the case of 'O2-Air', the characteristic vibrational temperature is that of O_2 and the relaxation time is based on molecular weight of air, which is taken to be 28.97. The case of 'O2-O', the relaxation time is based on the experimentally corrected relaxation parameters used for $O_2 - O$ collisions. The case of 'CO2-CO2' uses Camac's rates[119] for CO_2 relaxation. The freestream is in

Table 8.3: Vibrational parameters for the vibrationally active simulations

Name	θ_v (K)	Vib. A	Vib. B	τ (s)	c_{vv} (J/(kg · K))
O2-Air	2239	129.317	0.0292	$2.933 \cdot 10^{-4}$	239.16
O2-O	2239	47.7	0.0590	$6.206 \cdot 10^{-7}$	239.16
CO2-CO2	959	36.5	-0.0193	$7.861 \cdot 10^{-6}$	277.41
N2-Air	3395	225.27	0.0292	$7.733 \cdot 10^{-2}$	190.46

Table 8.4: This table contains the freestream conditions used in the vibrationally active simulations.

Temperature	1500 K	Pressure	6328.41 Pa
Density	0.0147 kg/m^3	Mach	3.04
Velocity	2367 m/s	Stagnation Enthalpy	4.308 MJ/kg

thermal equilibrium with a temperature of 1500 K to ensure a varying energy capacity amongst the four test cases. The relaxation time, τ , and the specific heat of vibration, c_{vv} , in the freestream for each gas has also been compiled in Table. 8.3. A fifth case is run with the vibrational mode frozen to serve as direct comparison to the previous simulations. The Mach number and the freestream Reynolds number are approximately the same as the previous full simulation cases with values of 3.04 and $6.61 \cdot 10^4$. Other gas properties of this flow are contained in Table 8.4. The normalization distance, L , is again approximately 0.1. The grid is the same as before as well as the input disturbance profile prescribed at the inflow to the flat plate. The plate boundary condition is adiabatic wall for all cases. The gas has a specific heat ratio of 1.4, a Prandtl number is 0.736, and a specific heat at constant pressure of $1004.51 \text{ J/kg}\cdot\text{K}$. For the viscosity, we again use Sutherland's law with coefficients for air defined above in Section 8.1.1.

8.3.2 Simulation Results

Before comparing the overall energy growth and the growth, we begin with disturbance energies of quantities that remain consistent between the previous full simulations and the current, vibrationally active simulations. The streamwise velocity disturbance energy, shown in Fig. 8.20a, increases with and increase in the energy transferred into the vibrational mode. This is evident in the variation of the vibrational specific heat between the three difference characteristic temperatures, with the vibrational mode based on CO_2 having the largest disturbance energy. For the two cases with the vibrational mode based on O_2 , the case with a shorter relaxation time results in a larger streamwise velocity disturbance energy because the shorter relaxation time allows for more energy to transfer from the translational energy to the vibrational energy. The cause for this variation is due to vibrational mode cooling the boundary layer, which results in a lower viscosity and a thinner

boundary layer. This is evident in the mean flow streamwise velocity profiles shown in Fig. 8.20b. As the boundary layer thins, the vortices are distorting larger velocity gradients, which implies that the displacement of a given fluid element results in a larger change in the streamwise velocity. Additionally, the presence of a vibrational mode results in the peak of the energy disturbance to lie at different locations. The disturbance energy data show that the frozen case and the N_2 -Air case peak first, the CO_2-CO_2 and the O_2-O cases peak further downstream, and the O_2 -Air case peaks furthest downstream. The N_2 -Air case's vibrational relaxation time requires a streamwise distance several times larger than the vortical disturbances persist for the vibrational mode to act, leaving the velocity field of the flow essentially unmodified. Therefore, the N_2 -Air case and the frozen case are similar. In the CO_2-CO_2 and O_2-O cases, the vibrational modes extract energy at roughly the same rate, modifying the velocity field within the a similar, finite streamwise distance. This results in a slight delay of the peak of disturbance energy relative to the frozen case. The O_2 -Air case requires a longer streamwise distance for the vibrational mode modify the flow, however, it still is able to absorb a sufficient amount of energy to modify the flow field. Therefore, O_2 -Air case peaks furthest downstream.

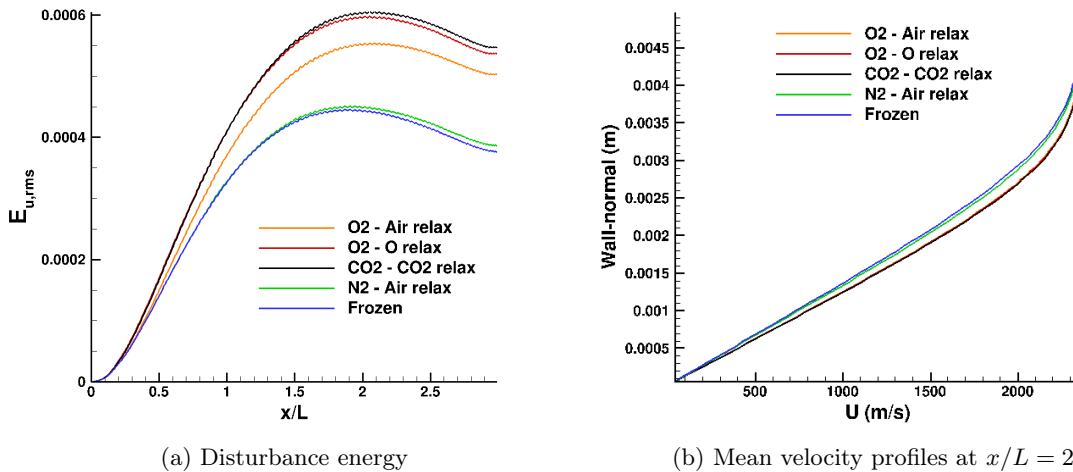


Figure 8.20: Disturbance energy of the streamwise velocity disturbance versus normalized streamwise distance and the mean streamwise velocity versus wall-normal distance at a normalized streamwise distance of 2.

The translational temperature disturbance shows a reduction in gain with the addition of vibrational disturbance, shown in Fig. 8.21a. However, unlike the streamwise velocity disturbance, the energy of the translational temperature disturbance is not simply dependent on the gradient in

the mean flow. If it were, the $CO_2 - CO_2$ case would show the least energy of disturbance due the smallest overall change of the translational temperature in the mean flow boundary layer, as shown in Fig. 8.21b, due to this vibrational mode absorbing the largest amount of translational energy. As shown in Fig. 8.21a, the minimum translation energy disturbance occurs for the O_2 -Air case, with the $CO_2 - CO_2$ case and then the $O_2 - O$ case following with increasing magnitude. The reason for this order lies in the relaxation time of the vibrational mode. When a fluid element is displaced upward from higher temperature to lower temperature gas due the vortical motion of the disturbance, the higher temperature gas begins to cool due to thermal diffusion. This cooling results in a lower disturbance magnitude. In the $O_2 - O$ case, the relaxation time allows for vibrational mode to return the energy previously absorbed to the translational energy, thus maintaining the translational temperature at higher levels. While having a higher energy capacity, the $CO_2 - CO_2$ is not able to transfer energy as fast as the $O_2 - O$ case, therefore the translation energy in the disturbance diffuses faster. Finally, the O_2 -Air case has the least disturbance energy because it has one of the smaller thermal energy gradients and second slowest vibrational relaxation time.

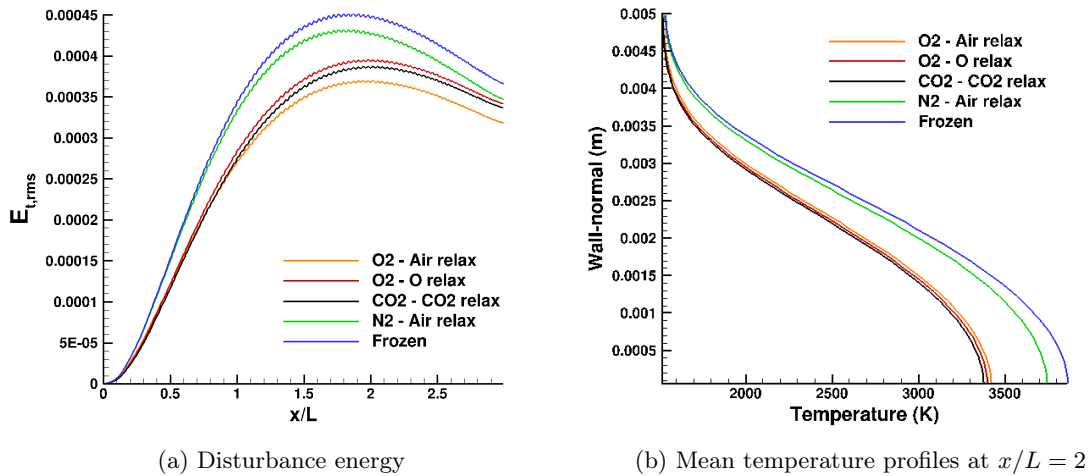


Figure 8.21: Disturbance energy of the translational temperature disturbance versus normalized streamwise distance and the mean translational temperature versus wall-normal distance at a normalized streamwise distance of 2.

Using the proposed value of vibrational disturbance energy given in Eq. 3.60, the variation of vibrational energy disturbance is directly related to the amount of energy the vibrational mode has absorbed from the translational, as shown in Fig. 8.22a. Although the relaxation time of the $CO_2 - CO_2$ vibrational mode is slower than $O_2 - O$, the higher specific heat of vibration allows

the $CO_2 - CO_2$ vibrational mode to absorb more energy from translation. This is also reflected in the translational and vibrational temperatures of the mean shown in Fig. 8.21b and Fig. 8.22b. Thus, the $CO_2 - CO_2$ vibrational mode has the largest vibrational disturbance energy. The peak of each vibrational disturbance energy is directly related to the relaxation time of the mode. The $O_2 - O$ has shortest relaxation time, therefore, this mode peaks first at an approximate streamwise distance of 1.25. The $CO_2 - CO_2$ vibrational mode peaks next at approximately 1.29, followed by the O_2 -Air vibrational mode at approximately 1.5. Lastly, the slowest vibrational mode, N_2 -Air, peaks at approximately 1.98.

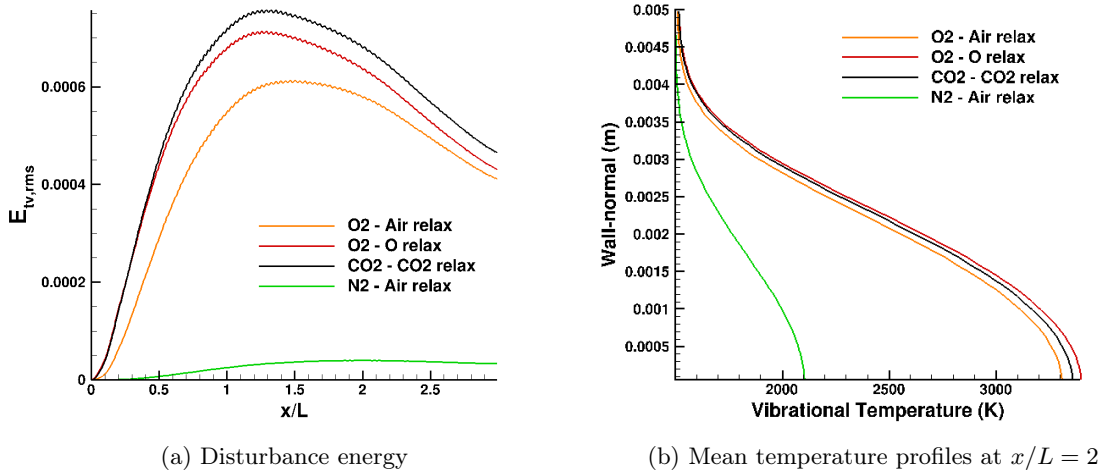


Figure 8.22: Disturbance energy of the vibrational temperature disturbance versus normalized streamwise distance and the mean vibrational temperature versus wall-normal distance at a normalized streamwise distance of 2.

As shown in Eq. 3.62, the growth factor is based on the output disturbance energy, which is dependent on the sum of the streamwise velocity and translational temperature disturbance in the case of frozen, compressible disturbances. Applying this same output disturbance energy to the current simulation, we obtain the disturbance energy profiles shown in Fig. 8.23a. From this, the effect of adding a vibrational mode is to increase the disturbance energy, thus decreasing the stability of the boundary layer. However, because this energy does not take into account the disturbance of vibrational energy, it does not capture the full disturbance profile of the boundary layer. The interaction of the vibrational and translational temperature disturbances with each other as well as the mean flow observed in previous chapters, especially in Section 7.5, would indicate that the addition of the vibrational energy disturbance is essential, from a physical standpoint, to

properly describe the stability of a boundary layer with respect to transient growth disturbances. Mathematically, adding a component of the vibrational energy disturbance is required to fully define the space of disturbances due to the addition of the vibrational energy eigenfunction. With the component of vibration, a disturbance norm would describe the full length of a vector in the space, thus would not accurately describe the disturbance energy. Adding the proposed vibrational disturbance energy to the output disturbance energy, the disturbance energy profiles separate out and clearly show a decrease in stability with the addition of a vibrational mode. As expected, this trend is reflected in the growth factor, shown in Fig. 8.24a. As another indicator of boundary layer stability, the disturbance amplitude also indicates a decrease in boundary layer stability with the addition of a vibrational mode, shown in Fig. 8.24b

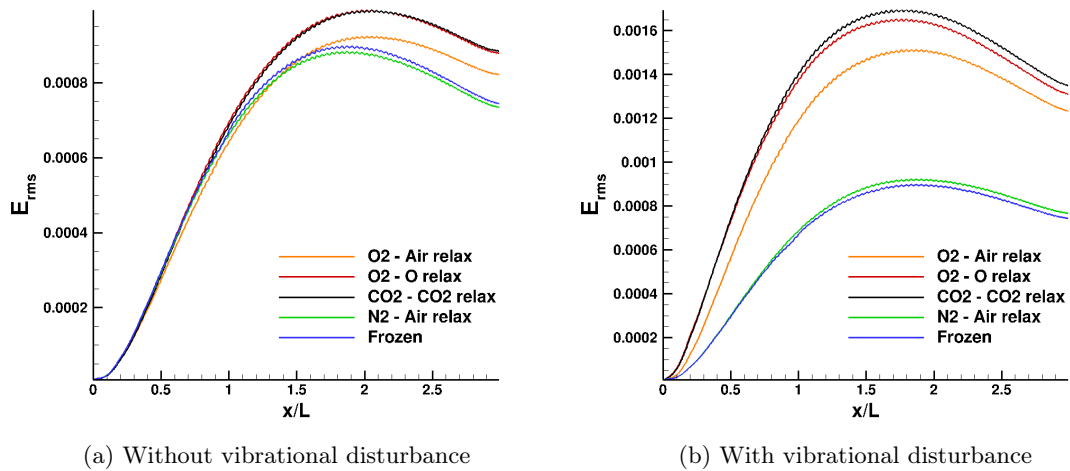


Figure 8.23: Total disturbance energy versus normalized streamwise distance without and with the contribution of the vibrational disturbance energy.

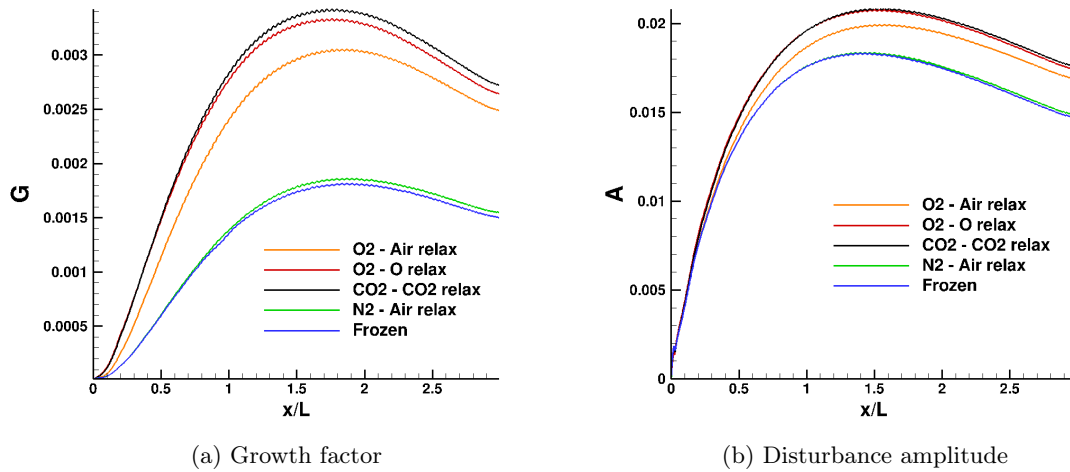


Figure 8.24: Growth factor and the disturbance amplitude function versus normalized streamwise distance.

8.3.3 Non-equilibrium Freestream

The previous set of vibrationally active cases provides insight into the effect of an internal process on transient growth, a general fluid flow is not necessarily in thermal or chemical equilibrium, such as the flow from the stagnation region of a blunt body over a roughness element. Therefore we add an additional degree of freedom to the transient growth problem by adding two cases with a freestream in thermal non-equilibrium. Both cases have a vibrational mode based on the O_2 -Air case given above as well as a translational temperature of 1500 K . The first case labeled 'Low' has a freestream vibrational temperature of 1000 K and the second case, labeled 'High', has a freestream vibrational temperature of 2000 K . Using the vibrational disturbance energy, the growth factor of the resulting disturbance field shows an increase in maximum gain in the 'Low' case and a decrease in maximum gain in the 'High' case, shown in Fig. 8.25a. The reason for these effects on the maximum gain lie in the primary method by which transient growth causes a disturbance. The streamwise vortices redistribute the fluid in the boundary layer causing low momentum, high temperature fluid to move from near the wall to higher in the boundary layer and vice versa. Thus the mean flow gradient plays a large roll in determining the disturbance energy gain for a given boundary layer. In the current study, the case with a higher freestream vibrational temperature heats the boundary causing it to become thick, which results in smaller gradients. In the case with a lower freestream vibrational temperature, the boundary layer is cooled and the gradients increase in magnitude. As the first

series of vibrationally active cases, cooling the boundary layer results in a larger growth factor. A similar trend is seen in the disturbance amplitude, which is directly reflective of the change in the mean gradients of streamwise velocity.

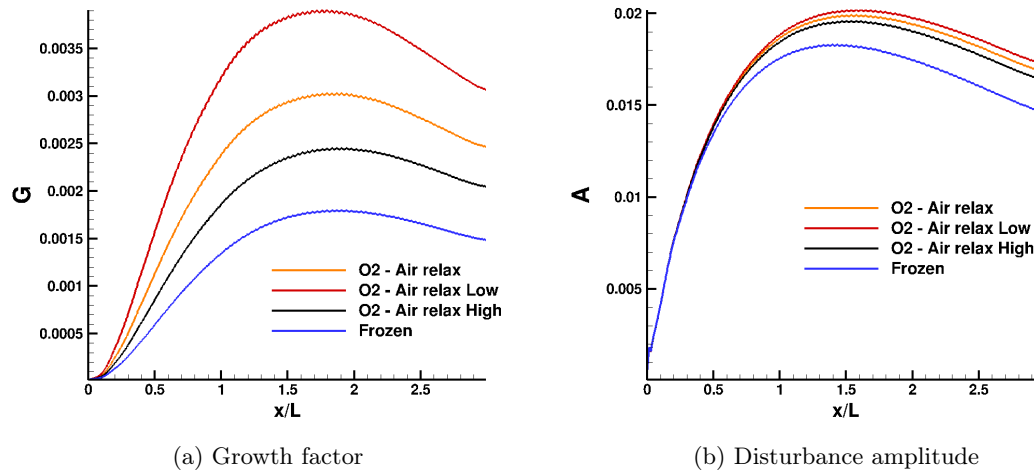


Figure 8.25: Growth factor and disturbance amplitude versus normalized streamwise distance.

8.4 Conclusion

Using a compressible optimal disturbance solver based on linear theory and validated against published data, various properties of optimal transient growth disturbances in compressible flow over a flat plate were explored. Based on the data generated from the linear solver, US3D was validated for capturing the transient growth phenomenon, allowing the effect of an increasing input energy of the linear transient growth disturbance to be tested. It was found that the compressible flowfield develops in a similar manner to that of the incompressible cases[16], with the addition of a temperature field. The theory described by Landahl[95], in which any three-dimensional disturbance with a non-zero velocity disturbance parallel to the mean velocity gradient causes transient growth, was tested using a single streamwise vortex and found to be correct. The addition of an internal mode such as vibration results in a larger gain in the disturbance energy for a given set of flow conditions. A non-equilibrium freestream showed a decrease in boundary layer stability when the mean flow has a lower vibrational temperature than the translational temperature and an increase in stability when the mean flow has a higher vibrational temperature. The effects of a vibrational mode are similar to those seen in the mean flow effects

on disturbance amplification of second mode disturbances in Chapter 6. Because a transient growth disturbance is essentially a steady state flow feature with respect to roughness element flows and the response of a transient growth disturbance to the presence of an internal mode, calling transient growth a mean disturbance, as is done by Ergin and White[80], is well justified. This demonstrates the importance of a secondary disturbance in the case of transient growth disturbances for causing the eventual transition of the boundary layer to turbulent flow.

Chapter 9

Summary and Conclusions

In this thesis, the interactions of two types of disturbances found in supersonic and hypersonic flows with the high enthalpy flow environment were investigated. The first disturbance considered was Mack's[20] second mode disturbance, which is acoustic in nature. The second disturbance considered was the transient growth disturbance observed. The motivation for this work was based on the need to understand, predict, and manipulate the boundary layer transition process in order to optimize high speed vehicle design. The tools employed in this work included theoretical analyses, linear stability analyses, and computational fluid dynamics simulations.

A brief introduction to boundary layer transition was given, followed by a more focused study of previous research in the areas of second mode and transient growth disturbances. Throughout this study, trends previously identified for each of these disturbances are discussed to develop an understanding for the interaction of these disturbances with fluid flow. Next, the governing equations of a general, reacting fluid flow were presented. From these equations, the acoustic wave relations based on a pressure disturbance were derived for reacting flow with a mean flow velocity. Lastly, the equations governing an optimal compressible transient growth were presented. The extension to these equations to a reacting, vibrationally active flow were laid out.

The results of the current thesis began with a theoretical analysis of acoustic waves with the assumptions of a static gas in equilibrium. The frequency at which the acoustic damping rate per wavelength is a maximum was found for a general internal molecular process and applied to molecular vibration and chemical dissociation. The acoustic damping theory was then extended to include a constant mean flow velocity and the consequences of the extension were tested. The results from theory were then compared against highly resolved acoustic wave simulations using the

CFD solver US3D. These two methods of calculation showed very good agreement indicating the accuracy of the theoretical approach and the ability of the CFD solver to capture the interaction of acoustic waves with the high enthalpy environment. The CFD solver also verified the accuracy of the theoretical extension of acoustic damping theory to flows with a mean flow velocity. Lastly, using the acoustic wave simulations, the various aspect of slow and fast acoustic wave experiencing damping due to internal molecular processes were identified.

The study of acoustic waves lead to a computational investigation of a novel idea used to delay transition on a sharp cone in the T5 reflected shock tunnel, a high-enthalpy experimental facility. This investigation began with an attempt to simulate the flow through the tunnel itself using two different CFD solvers. These simulations highlighted center-line and wall normal variations of the flow caused by the presence of a compression wave. This compression wave eventually caused an oscillation to occur in the tunnel wall boundary layer that resulted in a series of compression waves that could potentially interact with tunnel test body. A comparison of experimentally measured heat flux show the numerical solvers are under-predicted the wall heat flux to the T5 test body, which is a 5° half-angle sharp cone. Next, several previous experimental test cases, known as shots, were examined using linear stability analysis to determine the accuracy of the flow and disturbance modeling. Results showed an increasing trend in transition N factor for air shots and a decreasing trend in transition N factor for carbon dioxide shots. Several of these transition N factors were larger than expected for a conventional wind tunnel, however, a more accurate simulation showed a reduction in transition N factor. This along with several other potential causes for high transition N factors was discussed. Using the reference transition Reynolds number, a comparison derived by Germain[131] and used by Adam[12], the current cases showed similar values and an increasing trend with respect to the flow's total enthalpy for air shots as compared to data obtained by Adam[12]. The comparison of data for carbon dioxide shots showed largely different values of reference transition Reynolds number as well as opposing trend with respect to the flow's total enthalpy.

Despite the disagreement with the experiments and tunnel simulations, a theoretical injection case based on two different tunnel shots was examined to determine the stability characteristics of a porous injection process. Results highlighted three dimensions of the high-enthalpy injection process. The first was that in general injection tends to reduce the stability of a boundary layer. Next, these simulations demonstrated the ability of the flow's molecular vibration to stabilize or destabilize the mean flow depending on the vibrational relaxation parameters. Lastly, a difference in disturbance

amplification were seen with the presence of molecular vibration indicating a second means for an internal molecular process to affect flow stability. However, the injection profile specified did not introduce a sufficient amount of carbon dioxide to produce a significant amount of disturbance damping due to vibration. With the basic understanding of porous injection, an attempt was made at simulating the injection experiments that produced a delay in transition. Results showed the inadequacy of the linear stability analysis to gauge the amplification of disturbances through a region of strong injection. Ignoring the injection region, a stability analysis of the flow after the injector showed early transition relative to smooth cone case. These results contradicted the results of the experiments and indicated that the numerical methods were either inadequate to model the experimental flow or that some critical aspect of the flow was not being modeled.

Based on the disagreement between stability analyses and experiment, direct numerical simulations of acoustic waves were pursued in order to lay the ground work for high-fidelity simulations of the injection process. These simulations tested the effect of adding a molecular vibrational to a gas on acoustic disturbances passing over a cone in hypersonic flow. Using the PSE stability analysis, the presence of disturbance damping due to molecular vibration was verified for a particular set of flow conditions. A comparison between DNS and PSE shows good agreement on the location and growth of boundary layer disturbances for three different frequencies. Both calculations show a cyclic growth and decay behind the initial period of growth. In the DNS, the data show these cycles to be caused by a varying phase speed of the disturbance across the boundary layer, which results in a behavior similar to that of acoustic beating. An analysis of the numerical method shows that it incurs essentially zero dispersion error. However, the numerical method could be adding artificial dissipation that limits the ability of the simulations to obtain excellent agreement with the PSE analysis. Further investigation is required to determine the exact cause for the disagreement observed. The limitations of the numerical method and grid were demonstrated by attempting to simulate a frequency higher than what was intended. Based on extracted disturbance profiles from different wall-normal locations as well as a review of general linear disturbance evolution, the DNS data show that the vibrational temperature disturbance is largely driven by mean flow energy exchanges, rather than the effects of acoustic damping.

Finally, the linear, optimal compressible disturbance solver for transient growth disturbances was validated to published data. The solver was then used to explore some additional properties of transient growth disturbances on a flat plate, including the effect of an adiabatic wall boundary

condition. Using the linear solver, the CFD solver US3D was validated for simulating transient growth disturbances. Once this validation was complete, the CFD solver was used to investigate the effect of increasing the input energy of disturbances. Using metrics based on incompressible transient growth disturbance, the secondary stability of the compressible disturbances was gauged. The theory about three-dimensional disturbances put forth by Landahl[95] was found to hold for a single streamwise vortex, implying that any vortex present in a shear layer undergoes transient growth. Next, the effect of adding an internal molecular process was investigated by manipulating the vibrational relaxation parameters of a fictitious diatomic molecule. Assuming thermal equilibrium in the freestream, simulations show the effect of vibrational was only to increase the relative distortion of the boundary layer caused by the transient growth disturbances. Using a proposed addition to the full disturbance norm, this effect of molecular vibration is clearly demonstrated. The effect of non-equilibrium in the freestream was also tested. Results show that when the vibrational temperature was higher than the translational-rotational temperature, the boundary layer stability was increased. When the vibrational temperature was less than the translational-rotational temperature, the boundary layer stability was decreased. The convention of labeling transient growth a mean disturbance (other than the steady nature of optimal disturbances) was further justified because of the similar response of transient growth to that of mean flow response to the presence of an internal molecular process for second mode disturbance transition.

This thesis demonstrates the difficulty and complexity caused by the high-enthalpy flow environment on modeling and understanding supersonic and hypersonic flow disturbances. Although the current conclusions are similar to previous studies in this area, they emphasize the critical importance of accurately modeling the “real gas” effects in order to properly represent and simulate high enthalpy flows. Only with an accurate understanding of the high-enthalpy boundary layer transition process case scientists and engineers begin to predict and manipulate transition on realistic flight vehicles.

9.1 Recommendations for Future Work

The need for chemical and vibrational models that accurately represent physical processes in the presence of non-equilibrium cannot be emphasized enough. The sensitive nature of the interaction between acoustic waves and the high-enthalpy flow environment demonstrated in Chapter 5 illustrate the dependency of boundary layer transition on the parameters contained in the current models.

To this end, the theory describing the acoustic interaction with the gas in the presence of non-equilibrium should be developed. The multiple interactions observed between the acoustic waves and the flowfield in Chapter 7 demonstrate that the assumptions of equilibrium and constant flow properties are too restrictive to truly understand the effects of acoustic damping in realistic flows.

Also, accurately modeling the experiments of Jewell et al.[13] begins with an accurate representation of the experimental facility in which the experiments were performed. This requires a better understanding of the flow in reflected shock tunnels. Methods to determine the fluid properties and composition as well as the noise environment in the tunnel must be employed in order to provide validation data for numerical solvers as well as the physical model used to simulate these flows.

With the groundwork laid for directly simulating acoustic waves in the high-enthalpy environment, the envelope must be pushed. The disturbances generated in these simulation need to be further validated against those calculated by PSE stability analyses. Higher enthalpies as well as more complex gas compositions should be tested to expand our knowledge of second mode disturbances in high-enthalpy boundary layers and further validate stability analyses using the linear PSE. This will allow for the direct simulation the experiments of Adam and Hornung[58] as well as those by Casper et al.[138]. Also, the experiments of Jewell et al.[13] should be simulated with higher fidelity in order to more thorough understand the flow physics present in these experiments.

Lastly, a more general expression for the disturbance norm is needed to extend the application of transient to reacting and vibrationally active. This will allow for the rapid estimation of boundary layer stability to transient growth type disturbances caused by roughness elements. Additionally, this goal requires a more thorough investigation of roughness elements in compressible reacting flow in order to determine correlations between roughness parameters and the energy input into the transient growth disturbances caused by roughness elements

Bibliography

- [1] M. V. Morkovin, E. Reshotko, and T. Herbert. Transition in open flow systems-a reassessment. *Bull. Am. Phys. Soc.*, 39:1882, 1994.
- [2] A. Fedorov. Transition and stability of high-speed boundary layers. *Annu.Rev.FluidMech.*, (43):79–95, 2011.
- [3] F. M. White. *Viscous Fluid Flow*. McGraw-Hill, Inc., 2nd edition, 1991.
- [4] K. Fujii. *An Experimental Investigation of the Attachment Line Boundary Layer Transition on Swept Cylinders in Hypervelocity Flow*. PhD thesis, California Institute of Technology, 2001.
- [5] K. Fujii and H. G. Hornung. A Procedure to Estimate the Absorption Rate of Sound Propagating Through High Temperature Gas. GALCIT TR FM 2001-004, California Institute of Technology, Pasadena, CA, August 2001.
- [6] K. Fujii and H. G. Hornung. Experimental Investigation of High Enthalpy Effects on Attachment-line Boundary Layer Transition. *AIAA Journal*, 41, No. 7(7), July 2003.
- [7] C. J. Baker. The laminar horseshoe vortex. *Journal of Fluid Mechanics*, 95:347–367, October 1979.
- [8] M. D. Bartkowicz, P. K. Subbareddy, and G. V. Candler. Numerical Simulations of Roughness Induced Instability in the Purdue Mach 6 Wind Tunnel. AIAA Paper 2010-4723, June 2010.
- [9] P. Fischer and M. Choudhari. Numerical Simulation of Roughness-Induced Transient Growth in a Laminar Boundary Layer. AIAA Paper 2004-2539, June 2004.
- [10] E. B. White and F. G. Ergin. Receptivity and transient growth of roughness-induced disturbances. Paper 2011-4243, AIAA, June 2003.

-
- [11] S. P. Schneider. Effects of roughness on hypersonic boundary-layer transition. *Journal of Spacecraft and Rockets*, 45(2):193, 2008.
- [12] P. H. Adam. *Enthalpy Effects on Hypervelocity Boundary Layers*. PhD thesis, California Institute of Technology, 1997.
- [13] J. Jewell, I. A. Leyva, N. Parziale, and J. E. Shepherd. Effect of gas injection on transition in hypervelocity boundary layers. In *Proceedings of the 28th International Symposium on Shock Waves, University of Manchester, July 17-22, 2011*, 2011.
- [14] P. Balakumar and M. A. Kegerise. Receptivity of Hypersonic Boundary Layers over Straight and Flared Cones. Paper 2010-1065, AIAA, January 2010.
- [15] A. Tumin and E. Reshotko. Optimal Disturbances in Compressible Boundary Layers. *AIAA Journal*, 41(12), December 2003.
- [16] P. Andersson, L. Brandt, A. Bottaro, and D. S. Henningson. On the breakdown of boundary layer streaks. *Journal of Fluid Mechanics*, 428:29–60, 2001.
- [17] N. A. Denissen and E. B. White. Secondary instability of roughness wakes and optimal disturbances. AIAA Paper 2011-562, January 2011.
- [18] W. Tollmien. Ueber die entstehung der turbulenz. *Nachr. Ges. Wiss. Goettingen, Math.-Phys. Kl.*, pages 21–44, 1929.
- [19] H. Schlichting. Zur entstehung der turbulenz bei der plattenstroemung. *Nachr. Ges. Wiss. Goettingen, Math.-Phys. Kl.*, pages 181–208, 1933.
- [20] L. M. Mack. Boundary layer stability theory. JPL Report 900-277, 1969.
- [21] J. W. S. Rayleigh. On the stability, or instability, or certain fluid motions. *Proc. Lond. Math. Soc.*, 11:57–70, 1880.
- [22] Mujeeb R. Malik. Hypersonic Flight Transition Data Analysis Using Parabolized Stability Equations with Chemistry Effects. *Journal of Spacecraft and Rockets*, 40, No. 3(3):332–344, May-June 2003.
- [23] L. M. Mack. Stability of the compressible boundary layer according to a direct numerical solution. AGARDograph 97, Part I, pp. 329-362, NATO, Neuilly Sur Seine, France, 1965.

- [24] A. Demetriades. Hypersonic viscous flow over a slender cone; part iii: Laminar instability and transition. Paper 74-535, AIAA, June 1974.
- [25] J. M. Kendall. Wind tunnel experiments relating to supersonic and hypersonic boundary-layer transition. *AIAA Journal*, 13(3):290–299, 1975.
- [26] K. F. Stetson, E. R. Thompson, J. C. Donaldson, and L. G. Siler. Laminar boundary layer stability experiments on a cone at mach8. part 1: Sharp cone. Paper 83-1761, AIAA, 1983.
- [27] M. R. Malik, R. E. Spall, and C.-L. Chang. Effect of nose bluntness on boundary layer stability and transition. Paper 90-0112, AIAA, January 1990.
- [28] H. Goertler. Ueber eine dreedimensionale instabilitaet laminarer grenzsichten an konkaven waenden. *Nachr. Ges. Wiss. Goettingen, N.F.*, 2:1–26, 1940.
- [29] E. Reshotko. Transient growth: A factor in bypass transition. *Physics of Fluids*, 13(5):1067–1075, 2001.
- [30] P. Andersson, M. Berggren, and D. S. Henningson. Optimal disturbances and bypass transition in boundary layers. *Physics of Fluids*, 11(1):134, 1999.
- [31] K. M. Butler and B. F. Farrell. Three-dimensional optimal perturbations in viscous shear flow. *Physics of Fluids A*, 4:1637, 1992.
- [32] L. Boberg and U. Brosa. Onset of turbulence in a pipe. *Z. Naturforschung*, 43a:697–726, 1988.
- [33] P. Schlatter, L. Brandt, H. C. de Lange, and D. S. Henningson. On streak breakdown in bypass transistion. *Physics of Fluids*, 20, 2008.
- [34] P. J. Schmid and D. S. Henningson. *Stability and Transition in Shear Flows*. Springer, New York, 2001.
- [35] P. S. Klebanoff. Effect of free-stream turbulence on the laminar boundary layer. *Bull. Am. Phys. Soc.*, 10, 1971.
- [36] J. M. Kendall. Experimental study of disturbances produced in a pre-transitional laminar boundary layer by weak free-stream turbulence. Paper 85-1695, AIAA, 1985.

- [37] E. Reshotko. Roughness-induced transition, experiment and modeling. Paper 2008-4294, AIAA, June 2008.
- [38] E. Reshotko. Roughness-induced transition transient growth in 3-d supersonic flow. In *Advances in Laminar-Turbulent Transition Modelling*. RTO-EN-AVT-151-12 NATO, June 2008.
- [39] J. D. Anderson Jr. *Hypersonic and High Temperature Gas Dynamics*. McGraw-Hill, 1989.
- [40] C. F. Hansen and S. P. Heims. A review of the thermodynamic transport, and chemical reactionrate properties of high-temperature air. Technical Note TN-4359, NACA, July 1958.
- [41] S. Doraiswamy, J. D. Kelley, and G. V. Candler. Vibrational modeling of co2 in high-enthalpy nozzle flows. *Journal of Thermophysics and Heat Transfer*, 24(1), January 2010.
- [42] I. Nompelis. *Computational Study of Hypersonic Double-Cone Experiments for Code Validation*. PhD thesis, University of Minnesota, 2004.
- [43] C. Clanet, G. Searby, and P. Clavin. Primary acoustic instability of flames propagating in tubes: cases of spray and premixed gas combustion. *Journal of Fluid Mech.*, 385:157–197, 1999.
- [44] M. J. Nusca. Modeling combustion instability in small mmh-nto liquid rocket engines using cfd: Injector-chamber coupling. Paper 2010-1518, AIAA, January 2010.
- [45] L. Lees and H. Gold. Stability of laminar boundary layers and wakes at hypersonic speeds part i. stability of laminar wakes. Galcit memo, California Institute of Technology, 1964.
- [46] M. R. Malik. Prediction and control of transition in supersonic and hypersonic boundary layers. *AIAA Journal*, 27(11):1487–1493, November 1989.
- [47] L. M. Mack. Boundary-layer stability theory. In *Special Course on Stability and Transition of Laminar Flow*, number AGARD Report Number 709, 1984.
- [48] L. M. Mack. Transition and laminar instability. Publication 77-15, JPL, 1977.
- [49] A. M. O. Smith and N. Gamberoni. Transition, pressure gradient, and stability theory. Rept. ES 26388, Douglas Aircraft Co., Inc., Long Beach, CA, 1956.
- [50] T. Herbert and F. P. Bertolotti. Stability analysis of nonparallel boundary layers. *Bull. Am. Phys. Soc.*, 32:2079, 1987.

- [51] F. P. Bertolotti and T. Herbert. Analysis of the linear stability of compressible boundary layers using the pse. *Theor. Comp. Fluid Dyn.*, 3(117-124), 1991.
- [52] T. Herbert. Parabolized stability equations. *Annu. Rev. Fluid Mech.*, 29:245–283, 1997.
- [53] M. R. Malik and E. C. Anderson. Real gas effects on hypersonic boundary layer stability. *Phys. Fluids A*, 3:803, 1991.
- [54] G. K. Stuckert and H. L. Reed. Linear disturbances in hypersonic, chemically reacting shock layers. *AIAA Journal*, 32:1384, 1994.
- [55] M. L. Hudson, N. Chokani, and G. V. Candler. Linear stability of hypersonic flow in thermochemical nonequilibrium. *AIAA Journal*, 35:958, 1997.
- [56] Heath B. Johnson, Trevor G. Seipp, and Graham V. Candler. Numerical Study of Hypersonic Reacting Boundary Layer Transition on Cones. *Physics of Fluids*, 10, No. 10(10), October 1998.
- [57] P. Germain and H. G. Hornung. Transition on a Slender Cone in Hypervelocity Flow. *Experiments in Fluids*, 22(3):183–190, 1997.
- [58] P. H. Adam and H. G. Hornung. Enthalpy Effects on Hypervelocity Boundary-Layer Transition: Ground Test and Flight Data. *Journal of Spacecraft and Rockets*, 34(5), 1997.
- [59] C.-L. Chang and M. R. Malik. Oblique-mode breakdown and secondary instability in supersonic boundary layer. *J. Fluid Mech.*, 273:323–360, 1994.
- [60] C. R. Alba, H. B. Johnson, M. D. Bartkowicz, G. V. Candler, and K. T. Berger. Boundary-layer stability calculations for the hifire-1 transition experiment. *Journal of Spacecraft and Rockets*, 45(6):1125, November 2008.
- [61] M. J. Lighthill. Viscosity effects in sound waves of finite amplitude. In G. K. Batchelor and R. M. Davies, editors, *Surveys in Mechanics*, pages 250–351. Cambridge University Press, 1956.
- [62] W. G. Vincenti and C. H. Kruger. *Introduction to Physical Gas Dynamics*. Krieger Publishing Company, 1965.
- [63] J. F. Clarke and M. McChesney. *The Dynamics of Real Gases*. Butterworths, 1964.

- [64] P. F. Bertolotti. The influence of rotational and vibrational energy relaxation on boundary layer stability. *Journal of Fluid Mechanics*, 372:93–118, 1998.
- [65] S. A. Gaponov. Influence of gas compressibility on stability of boundary layer on porous surface at subsonic speeds. *Zhurnal Prikladnoi Mekhaniki i Technicheskoi Fiziki*, (1):121–125, 1975.
- [66] A. V. Fedorov, N. D. Malmuth, A. Rasheed, and H. G. Hornung. Stabilization of hypersonic boundary layers by porous coatings. *AIAA Journal*, 39(4):605, 2001.
- [67] A. Rasheed, H. G. Hornung, A. V. Fedorov, and N. D. Malmuth. Experiments on passive hypervelocity boundary-layer control using an ultrasonically absorptive surface. *AIAA Journal*, 40(3):481, March 2002.
- [68] P. Balakumar. Receptivity of a Supersonic Boundary Layer to Acoustic Disturbances. *AIAA Journal*, 47(5):1069–1078, May 2009.
- [69] P. Balakumar and M. A. Kegerise. Receptivity of hypersonic boundary layers to acoustic and vortical disturbances. Paper 2011-371, AIAA, January 2011.
- [70] E. R. G. Eckert. Engineering relations for friction and heat transfer to surfaces in high velocity flow. *Journal of the Aeronautical Sciences*, 22:585–587, August 1955.
- [71] I. A. Leyva, S. Laurence, A. W. Beierholm, H. G. Hornung, R. Wagnild, and G. V. Candler. Transition Delay in Hypervelocity Boundary Layers by Means of CO₂/acoustic Instability Interactions. Paper 2009-1287, AIAA, January 2009.
- [72] I. A. Leyva, J. S. Jewell, S. Laurence, H. G. Hornung, and J. E. Shepherd. On the impact of injection schemes on transition in hypersonic boundary layers. Paper 2009-7204, AIAA, 2009.
- [73] D. C. Reda. Review and synthesis of roughness-dominated transition correlations for reentry applications. *Journal of Spacecraft and Rockets*, 39(2):161, 2002.
- [74] E. R. van Driest, C. B. Blumer, and C. S. Wells Jr. Boundary-layer transition on blunt bodies-effects of roughness. *AIAA Journal*, 5(10):1913, October 1967.
- [75] A. L. Braslow and E. A. Horton. Effects of surface roughness on transition. In *NACA Conference on High-Speed Aerodynamics*, pages 439–450, Washington, D.C., March 1958. NACA. From Schneider 2008.

- [76] A. L. Braslow. A review of factors affecting boundary-layer transition. NASA TN D-3384, NASA, August 1966.
- [77] A. H. Whitehead Jr. Flow-field and drag characteristics of several boundary-layer tripping elements in hypersonic flow. NASA TN D-5454, NASA, October 1969.
- [78] J. E. Gronvall, H. B. Johnson, and G. V. Candler. Hypersonic three-dimensional boundary layer transition on a cone at angle of attack. Paper 2011-3561, AIAA, June 2011.
- [79] D. P. Rizzetta and M. R. Visbal. Direct numerical simulations of flow past an array of distributed roughness elements. *AIAA Journal*, 45(8):1967–1976, August 2007.
- [80] F. G. Ergin and E. B. White. Unsteady and transitional flows behind roughness elements. *AIAA Journal*, 44(11):2504–2513, 2006.
- [81] M. S. Acarlar and C. R. Smith. Study of hairpin vortices in a laminar boundary layer. part 1. hairpin vortices generated by a hemisphere protuberance. *Journal of Fluid Mechanics*, 175:1–41, 1987.
- [82] P. S. Klebanoff, W. G. Cleveland, and K. D. Tidstrom. On the evolution of a turbulent boundary layer induced by a three-dimensional roughness element. *Journal of Fluid Mechanics*, 237:101–187, 1992.
- [83] N. A. Denissen, R. S. Downs III, and E. B. White. Transient Growth due to Surface Roughness: Theory, Simulation and Experiment. AIAA Paper 2009-175, January 2009.
- [84] E. B. White. Transient growth of stationary disturbances in a flat plate boundary layer. *Physics of Fluids*, 14(12):4429–4439, 2002.
- [85] A. Tumin and E. Reshotko. The problem of boundary-layer flow encountering a three-dimensional hump revisited. Paper 2004-101, AIAA, January 2004.
- [86] C.-L. Chang and M. M. Choudhari. Hypersonic viscous flow over large roughness elements. Paper 2009-0173, AIAA, 2009.
- [87] C.-L. Chang, M. M. Choudhari, and F. Li. Numerical computations of hypersonic boundary-layer over surface irregularities. Paper 2010-1572, AIAA, January 2010.

- [88] M. M. Choudhari, F. Li, M. Wu, C.-L. Change, J. Edwards, M. Kegerise, and R. King. Laminar-turbulent transition behind discrete roughness elements in a high-speed boundary layer. Paper 2010-1575, AIAA, January 2010.
- [89] M. M. Choudhari, F. Li, and J. E. Edwards. Stability analysis of roughne array wake in a high-speed boundary layer. Paper 2009-0170, AIAA, 2009.
- [90] L. H. Gustavsson. Energy growth of three-dimensional disturbances in plane Poiseuille flow. *Journal of Fluid Mechanics*, 224:241–260, 1991.
- [91] H. B. Squire. On the stability for three-dimensional disturbances of viscous fluid flow between parallel walls. *Proc. R. Soc. London Ser. A*, 142:621, 1933.
- [92] S. Zuccher, A. Tumin, and E. Reshotko. Optimal disturbances in compressible boundary layers - complete energy norm analysis. AIAA Paper 2005-5314, AIAA, June 2005.
- [93] L. N. Trefethen, A. E. Trefethen, S. C. Reddy, and T. A. Driscoll. Hydrodynamic Stability Without Eigenvalues. *Science*, 261:578, 1993.
- [94] T. Ellingsen and E. Palm. Stability of linear flow. *Physics of Fluids*, 18:487, 1975.
- [95] M. T. Landahl. A note on an algebraic instability of inviscid parallel shear flows. *Journal of Fluid Mechanics*, 98:243, 1980.
- [96] L. S. Hultgren and L. H. Gustavsson. Algebraic growth of disturbances in a laminar boundary layer. *Physics of Fluids*, 24:1000, 1981.
- [97] B. Farrell. Optimal excitation of perturbations in viscous shear flow. *Physics of Fluids*, 31(8):2093–2102, 1988.
- [98] A. Hanifi, P. J. Schmid, and D. S. Henningson. Transient growth in compressible boundary layer flow. *Physics of Fluids*, 8:826, 1996.
- [99] S. C. Reddy and D. S. Henningson. Energy growth in viscous channel flows. *Journal of Fluid Mechanics*, 252:209, 1993.
- [100] P. J. Schmid, A. Lundbladh, and D. S. Henningson. Spatial evolution of disturbances in plane Poiseuille flow. In M. Y. Hussaini, T. B. Gatski, and T. L. Jackson, editors, *Transition, Turbulence and Combustion*, volume 1, pages 287–297, 1994.

- [101] A. Tumin and E. Reshotko. Spatial theory of optimal disturbances in boundary layers. *Physics of Fluids*, 13(7):2097, 2001.
- [102] E. Reshotko and A. Tumin. The blunt body paradox-A case for transient growth. In H. F. Fasel and W. S. Saric, editors, *Laminar-Turbulent Transition*, page 403. Springer, New York, 2000.
- [103] P. Luchini. Reynolds-number-independent instability of the boundary layer over a flat surface: optimal perturbations. *Journal of Fluid Mechanics*, 404:289, 2000.
- [104] M. T. Landahl. Dynamics of boundary layer turbulence and the mechanism of drag reduction. *Physics of Fluids*, 22:55, 1977.
- [105] L. Brandt, C. Cossu, J. Chomaz, P. Huerre, and D. S. Henningson. On the convectively unstable nature of optimal streaks in boundary layers. *Journal of Fluid Mechanics*, 485:221–242, 2003.
- [106] B. M. Wheaton and S. P. Schneider. Roughness-induced instability in a laminar boundary layer at mach 6. Paper 2010-1574, AIAA, January 2010.
- [107] B. M. Wheaton, M. D. Bartkowicz, P. K. Subbareddy, S. P. Schneider, and G. V. Candler. Roughness-induced instabilities at mach 6: A combined numerical and experimental study. Paper 2011-3248, AIAA, June 2011.
- [108] P. S. Iyer, S. Muppidi, and K. Mahesh. Transition of hypersonic flow past flat plate with roughness elements. Paper 2010-5015, AIAA, June 2010.
- [109] P. S. Iyer, S. Muppidi, and K. Mahesh. Roughness-induced transition in high speed flows. Paper 2011-566, AIAA, January 2011.
- [110] P. M. Danehy, B. Bathel, C. Ivey, J. A. Inman, and S. B. Jones. No plif study of hypersonic transition over a discrete hemispherical roughness element. Paper 2009-394, AIAA, 2009.
- [111] F. Li, M. Choudhari, C.-L. Chang, M. Wu, and P. T. Greene. Development and breakdown of goertler vortices in high speed boundary layers. Paper 2010-705, AIAA, January 2010.
- [112] Chul Park. *Nonequilibrium Hypersonic Aerodynamics*. Wiley, 1990.

- [113] C. Park. Assessment of two-temperature kinetic model for dissociating and weakly ionizing nitrogen. Paper 86-1347, AIAA, 1986.
- [114] Deepak Bose and Graham V. Candler. Thermal Rate Constants of the $\text{N}_2 + \text{O} \rightarrow \text{NO} + \text{N}$ Reaction Using ab initio $3A''$ and $3A'$ Potential Energy Surfaces. *Journal of Chemical Physics*, 104, No. 8(8):2825–2833, 1996.
- [115] Deepak Bose and Graham V. Candler. Thermal Rate Constants of the $\text{O}_2 + \text{N} \rightarrow \text{NO} + \text{O}$ Reaction Based on the $2A'$ and $4A'$ Potential Energy Surfaces. *Journal of Chemical Physics*, 107, No. 16(16):6136–6145, 1997.
- [116] R. A. Mitcheltree and P. A. Gnoffo. Wake flow about the mars pathfinder entry vehicle. *Journal of Spacecraft and Rockets*, 32(5):771, 1995.
- [117] B. J. McBride, M. J. Zehe, and S. Gordon. NASA Glenn Coefficients for Calculating Thermodynamic Properties of Individual Species. Paper 2002-211556, NASA, September 2002.
- [118] C. Park. Review of Chemical-Kinetic Problems of Future NASA Missions, I: Earth Entries. *Journal of Thermophysics and Heat Transfer*, 7, No. 3(3):385–398, 1993.
- [119] M. Camac. CO_2 Relaxation Processes in Shock Waves. In J. G. Hall, editor, *Fundamental Phenomena in Hypersonic Flow*, pages 195–215. Cornell University Press, Ithaca, NY, 1966.
- [120] H. B. Johnson. *Thermochemical Interactions in Hypersonic Boundary Layer Stability*. PhD thesis, University of Minnesota, 2000.
- [121] H. B. Johnson and G. V. Candler. Hypersonic Boundary Layer Stability Analysis Using PSE-Chem. Paper 2005-5023, AIAA, June 2005.
- [122] H. B. Johnson, G. V. Candler, and M. J. Wright. Boundary Layer Stability Analysis of Mars Science Laboratory Aeroshell. Paper 2006-0920, AIAA, January 2006.
- [123] I. Nompelis, T.W. Drayna, and G.V. Candler. Development of a Hybrid Unstructured Implicit Solver for the Simulation of Reacting Flow Over Complex Geometries. Paper 2004-2227, AIAA, June 2004.
- [124] J. L. Steger and R. F. Warming. Flux vector splitting for the inviscid gasdynamic equations with application to finite difference methods. *Journal of Computational Physics*, 40:263–293, 1981.

- [125] R. W. MacCormack and G. V. Candler. The solution of the navier-stokes equations using gauss-seidel line relaxation. *Computers and Fluids*, 17(1):135–150, 1989.
- [126] M. J. Wright, G. V. Candler, and M. Prampolini. Data Parallel Lower-Upper Relaxation Method for the Navier-Stokes Equations. *AIAA Journal*, 34(7):1371–1377, July 1996.
- [127] M. J. Wright, G. V. Candler, and D. Bose. A Data-Parallel Line-Relaxation Method for the Navier-Stokes Equations. Paper 97-2046CP, AIAA, June 1997.
- [128] F. Ducros, V. Ferrand, F. Nicoud, C. Weber, D. Darracq, C. Gacherieu, and T. Poinsot. Large-eddy Simulation of Shock/Turbulence Interaction. *Journal of Computational Physics*, 152:517–549, 1999.
- [129] P. Subbareddy and G. V. Candler. A Fully Discrete, Kinetic Energy Consistent Finite-Volume Scheme for Compressible Flows. *Journal of Computational Physics*, 228(5):1347–1364, 2009.
- [130] R. C. Millikan and D. R. White. Systematics of Vibrational Relaxation. *Journal of Chemical Physics*, 39(12):3209–3213, 1963.
- [131] P. Germain. *The boundary layer on a sharp cone in high-enthalpy flow*. PhD thesis, California Institute of Technology, 1994.
- [132] A. Rasheed. *Passive Hypervelocity Boundary Layer Control Using an Ultrasonically Absorptive Surface*. PhD thesis, California Institute of Technology, 2001.
- [133] M. S. Holden, T. P. Wadhams, M. MacLean, A. Dufrene, E. Mundy, and E. Marineau. Review of basic research and development programs conducted in the lens facilities in hypervelocity flows. Paper 2012-0469, AIAA, 2012.
- [134] K. Hannemann, M. Schnieder, B. Reimann, and J. M. Schramm. The influence and the delay of driver gas contamination in heg. Paper 2000-2593, AIAA, 2000.
- [135] P. R. Spalart and S. R. Allmaras. A one-equation turbulence model for aerothermodynamic flows. Paper 92-0439, AIAA, 1992.
- [136] H. B. Johnson, J. E. Gronvall, and G. V. Candler. Reacting hypersonic boundary layer stability with blowing and suction. Paper 2009-938, AIAA, January 2009.

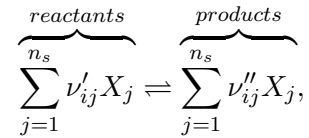
-
- [137] M. J. Wright, G. V. Candler, and M. Prampolini. Data Parallel Lower-Upper Relaxation Method for the Navier-Stokes Equations. *AIAA*, 34(7):1371, July 1996.
- [138] K. M. Casper, S. J. Beresh, J. F. Henfling, R. W. Spillers, B. Pruett, and S. P. Schneider. Hypersonic Wind-Tunnel Measurements of Boundary-Layer Pressure Fluctuations. Paper 2009-4054, AIAA, June 2009.
- [139] S. R. Turns. *Combustion*. McGraw-Hill, 2000.

Appendix A

Fujii's Method : Full Problem Derivation

A.1 Definitions of Variables and Description of the System

A linearly independent set of chemical reactions can be represented by



$$\nu_{ij} = \nu''_{ij} - \nu'_{ij}.$$

Define $\vec{\alpha}$ as a vector of the degree of advancement of the reactions per unit mass of mixture (mole/kg), each species concentration, N_j , moles per unit mass of mixture, can be written as

$$N_j = \sum_{i=1}^{n_{re}} \alpha_i \nu_{ij} + N_{0,j}, \quad (\text{A.1})$$

note also that

$$N_j = \frac{\rho_j}{\rho}; \quad \rho_j = \rho M_j N_j; \quad M_{mix} = \frac{1}{\sum_{j=1}^{n_s} N_j},$$

where $[]_j$ is the molar concentration of species j and M_j is the molecular weight of species j . The non-equilibrium variables, \vec{q} , can be defined as

$$\vec{q} \equiv \begin{pmatrix} \vec{\alpha} \\ e_v(1) \\ \vdots \\ e_v(n_s) \end{pmatrix}, \quad (\text{A.2})$$

where e_v is the vibrational energy per unit mass. To account for all reactions in the chemistry model for a particular mixture, a matrix \mathbf{R}' is introduced to relate the linearly independent reactions (n_{re}) and the remaining reactions $n_{re} + 1 \rightarrow n_r$ such that

$$\nu^* = \begin{pmatrix} \mathbf{I} \\ \mathbf{R}' \end{pmatrix} \nu, \quad (\text{A.3})$$

where ν^* is a $n_r \times n_s$ coefficient matrix for all reactions and \mathbf{R}' is a $(n_r - n_{re}) \times n_{re}$. Letting $\vec{\alpha}'$ express the degrees of advancement of reactions ν^* ,

$$\vec{\alpha} = \left(\mathbf{I} (\mathbf{R}')^\dagger \right) \vec{\alpha}' \equiv \mathbf{R} \vec{\alpha}'. \quad (\text{A.4})$$

A.2 Calculation of derivative values

The pressure and density dependence of \vec{q} in equilibrium can be determined by calculating the appropriate partial derivatives.

A.2.1 Extent of Reaction

From Turns[139] page 123, the equilibrium constant for reaction i , K_i , is

$$K_i = K_i(T) = \prod_j [X]_j^{*\nu_{ij}} = \rho^{\sum_j \nu_{ij}} \prod_j N_j^{*\nu_{ij}}, \quad (\text{A.5})$$

which must be satisfied for a given p , ρ , and $\vec{\alpha}$. Starting from the equation of state

$$T = \frac{p}{\rho R_{mix}} = \frac{p M_{mix}}{\rho R_u} = \frac{p}{R_u \rho \sum_j N_j}$$

and differentiating

$$dT = \frac{dp}{p} \underbrace{\frac{p}{R_u \rho \sum_j N_j}}_T - \frac{d\rho}{\rho} \underbrace{\frac{p}{R_u \rho \sum_j N_j}}_T + \sum_i \frac{-d\alpha_i}{\sum_j N_j} \underbrace{\frac{p}{R_u \rho \sum_j N_j}}_T \sum_j \frac{\partial N_j}{\partial \alpha_i},$$

with

$$\frac{\partial N_j}{\partial \alpha_i} = \frac{\partial}{\partial \alpha_i} \left(\sum_i \alpha_i \nu_{ij} + N_{o,j} \right) = \nu_{ij},$$

we obtain

$$\begin{aligned} dT &= \frac{dp}{p} T - \frac{d\rho}{\rho} T - T \sum_i \sum_j \nu_{ij} d\alpha_i \left(\overbrace{\frac{1}{\sum_j N_j}}^{M_{mix}} \right) \\ &\Leftrightarrow \frac{dT}{T} = \frac{dp}{p} - \frac{d\rho}{\rho} - M_{mix} \sum_i \sum_j \nu_{ij} d\alpha_i. \end{aligned} \quad (\text{A.6})$$

Differentiating Equation A.5, we get

$$\begin{aligned} dK_i &= \frac{dK_i}{dT} dT = \frac{\partial K_i}{\partial p} dp + \frac{\partial K_i}{\partial \rho} d\rho + \frac{\partial K_i}{\partial \alpha_j} d\alpha_j^* \\ &\Leftrightarrow \frac{dK_i}{dT} dT - \frac{\partial K_i}{\partial p} dp - \frac{\partial K_i}{\partial \rho} d\rho - \frac{\partial K_i}{\partial \alpha_j} d\alpha_j^* = 0 \end{aligned}$$

and using Equation A.6;

$$\frac{dK_i}{dT} \frac{T}{p} dp - \frac{dK_i}{dT} \frac{T}{\rho} d\rho - \frac{dK_i}{dT} T M_{mix} \sum_j \sum_k \nu_{jk} d\alpha_j^* - \frac{\partial K_i}{\partial p} dp - \frac{\partial K_i}{\partial \rho} d\rho - \frac{\partial K_i}{\partial \alpha_j} d\alpha_j^* = 0.$$

The partial derivatives are

$$\frac{\partial K_i}{\partial p} = 0; \quad \frac{\partial K_i}{\partial p} = \sum_j \nu_{ij} \rho^{\sum_j \nu_{ij} - 1} \prod_j N_j^{*\nu_{ij}} = \frac{\sum_j \nu_{ij}}{\rho} \rho^{\sum_j \nu_{ij}} \prod_j N_j^{*\nu_{ij}} = \frac{\sum_j \nu_{ij}}{\rho} K_i,$$

and

$$\frac{\partial K_i}{\partial \alpha_j} = \frac{\partial}{\partial \alpha_j} \left(\rho^{\sum_k \nu_{ik}} \prod_k N_k^{*\nu_{ik}} \right) = \rho^{\sum_k \nu_{ik}} \prod_k N_k^{*\nu_{ik}} \left(\sum_k \frac{\partial N_k}{\partial \alpha_j} \frac{\nu_{ik}}{N_k} \right) = K_i \sum_k \frac{\nu_{ik} \nu_{jk}}{N_k}.$$

Substituting these into the equation for a change in the equilibrium constant, we have

$$\begin{aligned} \frac{dK_i}{dT} \frac{T}{p} dp - \left(\frac{dK_i}{dT} \frac{T}{\rho} + K_i \frac{\sum_j \nu_{ij}}{\rho} \right) d\rho - \sum_j \left(\frac{dK_i}{dT} T M_{mix} \sum_k \nu_{jk} + K_i \sum_k \frac{\nu_{ik} \nu_{jk}}{N_k} \right) d\alpha_j^* &= 0 \\ \left(\frac{1}{K_i} \frac{dK_i}{dT} \frac{T}{p} \right) dp + \left(- \left(\frac{1}{K_i} \frac{dK_i}{dT} \frac{T}{\rho} + \frac{\sum_j \nu_{ij}}{\rho} \right) \right) d\rho \\ - \sum_j \left(\frac{1}{K_i} \frac{dK_i}{dT} T M_{mix} \sum_k \nu_{jk} + \sum_k \frac{\nu_{ik} \nu_{jk}}{N_k} \right) d\alpha_j^* &= 0 \quad (\text{no sum on } i) \\ \Leftrightarrow A_{p,i} dp + A_{\rho,i} d\rho - A_{\alpha,i,j} d\alpha_j^* &= 0, \end{aligned}$$

implying that

$$\begin{aligned} A_{p,i} &= \frac{1}{K_i} \frac{dK_i}{dT} \frac{T}{p} = \frac{d(\ln K_i)}{dT} \frac{T}{p}, \\ A_{\rho,i} &= - \left(\frac{d(\ln K_i)}{dT} \frac{T}{\rho} + \frac{\sum_j \nu_{ij}}{\rho} \right), \end{aligned}$$

and

$$A_{\alpha,i,j} = \frac{d(\ln K_i)}{dT} T M_{mix} \sum_k \nu_{jk} + \sum_k \frac{\nu_{ik} \nu_{jk}}{N_k}.$$

Solving for $d\alpha_j^*$, we can determine how a change in $\vec{\alpha}$ corresponds to a changes in pressure and density,

$$d\alpha_j^* = A_{\alpha,i,j}^{-1} A_{p,i} dp + A_{\alpha,i,j}^{-1} A_{\rho,i} d\rho,$$

so

$$\frac{\partial \alpha_j^*}{\partial p} = A_{\alpha,i,j}^{-1} A_{p,i}$$

and

$$\frac{\partial \alpha_j^*}{\partial \rho} = A_{\alpha,i,j}^{-1} A_{\rho,i}$$

A.2.2 Vibrational Energy

Changes in the vibrational energy follow

$$de_{v,i}^* = \frac{de_{v,i}^*}{dT} dT = \frac{de_{v,i}^*}{dT} \frac{\partial T}{\partial p} dp + \frac{de_{v,i}^*}{dT} \frac{\partial T}{\partial \rho} d\rho + \frac{de_{v,i}^*}{dT} \frac{\partial T}{\partial \alpha_j} d\alpha_j^*,$$

where

$$\begin{aligned} \frac{de_{v,i}^*}{dT} &= \frac{d}{dT} \left(\frac{R_u}{M_i} \frac{\theta_{v,i}}{\exp(\theta_{v,i}/T) - 1} \right) = \underbrace{\frac{R_u}{M_i} \frac{\theta_{v,i}}{\exp(\theta_{v,i}/T) - 1}}_{e_{v,i}^*} \left(\frac{-1}{\exp(\theta_{v,i}/T) - 1} \right) \exp(\theta_{v,i}/T) \frac{-\theta_{v,i}}{T^2} \\ &= e_{v,i}^* \frac{\left(\frac{\theta_{v,i}}{T^2} \right) \exp(\theta_{v,i}/T)}{\exp(\theta_{v,i}/T) - 1} \\ \Rightarrow de_{v,i}^* &= e_{v,i}^* \frac{\left(\frac{\theta_{v,i}}{T^2} \right) \exp(\theta_{v,i}/T)}{\exp(\theta_{v,i}/T) - 1} \left(\left(\frac{T}{p} + \frac{\partial T}{\partial \alpha_j} \frac{\partial \alpha_j^*}{\partial p} \right) dp + \left(-\frac{T}{\rho} + \frac{\partial T}{\partial \alpha_j} \frac{\partial \alpha_j^*}{\partial \rho} \right) d\rho \right), \end{aligned}$$

where

$$\frac{\partial T}{\partial \alpha_j} = -M_{mix} T \sum_k \nu_{jk}$$

and $\theta_{v,i}$ is the characteristic vibrational temperature of vibrational mode i .

A.2.3 Enthalpy Derivatives

Equation 3.27 requires various partial derivatives of enthalpy. Starting from the definition of enthalpy,

$$h = \sum_{j=1}^{n_s} N_j \hat{C}_{v,t+r} T + \sum_{i=1}^{n_v} N_{s,i} M_{s,i} e_{v,i} + \sum_{j=1}^{n_s} N_j \hat{e}_{0,j} + \frac{p}{\rho},$$

we have

$$\frac{\partial h}{\partial p} = \sum_{j=1}^{n_s} N_j \hat{C}_{v,t+r} \frac{\partial T}{\partial p} + \frac{1}{\rho} = \sum_{j=1}^{n_s} N_j \hat{C}_{v,t+r} \frac{T}{p} + \frac{1}{\rho},$$

$$\frac{\partial h}{\partial \rho} = \sum_{j=1}^{n_s} N_j \hat{C}_{v,t+r} \frac{\partial T}{\partial \rho} - \frac{p}{\rho^2} = -\sum_{j=1}^{n_s} N_j \hat{C}_{v,t+r} \frac{T}{\rho} - \frac{p}{\rho^2},$$

$$\frac{\partial h}{\partial e_{v,i}} = N_{s,i} M_{s,i},$$

and

$$\begin{aligned} \frac{\partial h}{\partial \alpha_i} &= \sum_{j=1}^{n_s} \frac{\partial N_j}{\partial \alpha_i} \hat{C}_{v,t+r} T + \sum_{j=1}^{n_s} N_j \hat{C}_{v,t+r} \frac{\partial T}{\partial \alpha_i} + \sum_{j=1}^{n_s} \frac{\partial N_j}{\partial \alpha_i} M_j \sum_{s=1}^{n_{v,j}} e_{v,s,j} + \sum_{j=1}^{n_s} \frac{\partial N_j}{\partial \alpha_i} \hat{e}_{0,j} \\ &= \sum_{j=1}^{n_s} \left(\frac{\partial N_j}{\partial \alpha_i} \left(\underbrace{\hat{C}_{v,t+r} T + M_j \sum_{s=1}^{n_{v,j}} e_{v,s,j}}_{\hat{e}_j} + \hat{e}_{0,j} \right) - N_j M_{mix} T \sum_k \nu_{ik} \hat{C}_{v,t+r} \right) \end{aligned}$$

$$\Leftrightarrow \frac{\partial h}{\partial \alpha_i} = \sum_{j=1}^{n_s} \left(\nu_{ij} (\hat{e}_j + \hat{e}_{0,j}) - N_j M_{mix} T \sum_k \nu_{ik} \hat{C}_{v,t+r} \right),$$

where $(\)_{s,i}$ is the species associated with vibrational mode i , n_v is the number of vibrational modes, $n_{v,j}$ is the number of vibrational modes of species j , and $e_{v,s,j}$ is the energy of vibration of the s th vibrational mode of species j . In Fujii's code, he also includes the electronic energy into the term \hat{e}_j . However, there are no other dependencies on this component of the energy, thus omitting this term in the derivation has little effect on the calculated damping rate.

A.2.4 Relaxation Time

For a chemical reaction the relaxation time is related to the reaction rate,

$$\begin{aligned} \rho \frac{d\alpha'_i}{dt} &= k_{f,i} \left[\prod_s [X]_s^{\nu'_{is}} - \frac{1}{K_i} \prod_s [X]_s^{\nu''_{is}} \right] \\ \Leftrightarrow \rho \frac{d\alpha'_i}{dt} &= k_{f,i} \left[\prod_s (\rho N_s)^{\nu'_{is}} - \frac{1}{K_i} \prod_s (\rho N_s)^{\nu''_{is}} \right], \end{aligned} \quad (\text{A.7})$$

where $k_{f,i}$ is the forward reaction rate coefficient,

$$k_{f,i} = C_{f,i} T^{\eta_{f,i}} \exp \left(\frac{-\theta_{f,i}}{T} \right). \quad (\text{A.8})$$

The reaction rates for the linearly independent reactions are derived using Equation A.4,

$$\frac{d\alpha_i}{dt} = \left(I_{ij} (R'_{ij})^\dagger \right) \frac{d\alpha'_j}{dt} = R_{ij} \frac{d\alpha'_j}{dt}. \quad (\text{A.9})$$

Differentiating Equation A.9 with respect to α_j , we obtain

$$\begin{aligned} \frac{\partial}{\partial \alpha_j} \left(\frac{d\alpha_i}{dt} \right) &= \sum_k R_{ik} \frac{k_{f,k}}{\rho} \left[\sum_m \left(\frac{\nu'_{km}}{N_m} \frac{\partial N_m}{\partial \alpha_j} \right) \prod_s (\rho N_s)^{\nu'_{ks}} - \frac{1}{K_k} \sum_m \left(\frac{\nu''_{km}}{N_m} \frac{\partial N_m}{\partial \alpha_j} \right) \prod_s (\rho N_s)^{\nu''_{ks}} \right] \\ &= \sum_k R_{ik} \frac{k_{f,k}}{\rho} \left[\sum_m \left(\frac{\nu'_{km} \nu_{jm}}{N_m} \right) \prod_s (\rho N_s)^{\nu'_{ks}} - \frac{1}{K_k} \sum_m \left(\frac{\nu''_{km} \nu_{jm}}{N_m} \right) \prod_s (\rho N_s)^{\nu''_{ks}} \right]. \end{aligned}$$

When the undisturbed condition is in equilibrium, $N_s = N_s^*$, we have

$$\frac{1}{K_k} = \frac{\prod_s (\rho N_s)^{\nu'_{ks}}}{\prod_s (\rho N_s)^{\nu''_{ks}}}$$

$$\begin{aligned}
\Rightarrow \frac{\partial}{\partial \alpha_j} \left(\frac{d\alpha_i}{dt} \right) &= \sum_k R_{ik} \frac{k_{f,k}}{\rho} \left[\sum_m \left(\frac{\nu'_{km} \nu_{jm}}{N_m} \right) \prod_s (\rho N_s)^{\nu'_{ks}} \right. \\
&\quad \left. - \frac{\prod_s (\rho N_s)^{\nu'_{ks}}}{\prod_s (\rho N_s)^{\nu''_{ks}}} \sum_m \left(\frac{\nu''_{km} \nu_{jm}}{N_m} \right) \prod_s (\rho N_s)^{\nu''_{ks}} \right] \\
&= \sum_k R_{ik} \frac{k_{f,k}}{\rho} \left[\sum_m \left(\frac{(\nu'_{km} - \nu''_{km}) \nu_{jm}}{N_m} \right) \prod_s (\rho N_s)^{\nu'_{ks}} \right] \\
\frac{\partial}{\partial \alpha_j} \left(\frac{d\alpha_i}{dt} \right) &= - \sum_k R_{ik} \frac{k_{f,k}}{\rho} \left[\sum_m \left(\frac{\nu_{km} \nu_{jm}}{N_m} \right) \prod_s (\rho N_s)^{\nu'_{ks}} \right],
\end{aligned}$$

assuming the rate constants are frozen.

The vibrational energy relaxation for species s due to collisions with species r is determined from the expression given by Millikan and White[130],

$$\ln A_1 \tau_{sr} p = A_2 \mu_{sr}^{1/2} \theta_{v,s}^{4/3} \left(T^{1/3} - A_3 \mu_{sr}^{1/4} \right),$$

where μ_{sr} is the equivalent molecular weight between the two species. The constants in the relaxation time equation are

$$A_1 = 9.8625 \cdot 10^2 \text{Pa}^{-1} \text{s}^{-1}; \quad A_2 = 0.0367 \text{kg}^{1/2} \text{mol}^{1/2} \text{K}^{-5/3}; \quad A_3 = 0.08435 \text{kg}^{-1/4} \text{mol}^{-1/4} \text{K}^{1/3}.$$

The relaxation time of species s is determined by taking the number-weighted average of τ_{sr} ,

$$\tau_s = \frac{\sum_r N_r}{\sum_r \frac{N_r}{\tau_{sr}}}.$$

For CO₂, the four vibrational modes relax at the same rate given by Camac[119],

$$\ln A_4 \tau_{CO_2} p = A_5 T^{-1/3},$$

where

$$A_4 = 4.8488 \cdot 10^2 \text{Pa}^{-1} \text{s}^{-1}; \quad A_5 = 36.5 \text{K}^{1/3}.$$

The vibrational relaxation time might be a function of concentration, however, it is assumed that the effect of the disturbance wave is small and the relaxation time is constant through the disturbance wave.

The \mathbf{A} matrix becomes

$$A_{ij} = \frac{\partial}{\partial \alpha_j} \left(\frac{d\alpha_i}{dt} \right) \quad i, j : 1 \rightarrow n_{re}$$

for chemical relaxation and

$$A_{ij} = \frac{1}{\tau_s} \delta_{ij}$$

for vibrational relaxation.

A.3 Proof of frozen speed of sound formula

We start from the formula given by Vincenti and Kruger[62] in Eq. 3.28, which is

$$a_f^2 = \frac{\left. \frac{\partial h}{\partial \rho} \right|_{\rho_0}}{\left. \frac{1}{\rho_0} - \frac{\partial h}{\partial p} \right|_{p_0}}.$$

From Eq. 3.36, we have that

$$\left. \frac{\partial h}{\partial p} \right|_{p_0} = c_p \frac{T_0}{P_0}$$

and

$$\left. \frac{\partial h}{\partial \rho} \right|_{\rho_0} = -c_p \frac{T_0}{\rho_0}$$

for a frozen or thermally perfect gas. Plugging these values into the frozen speed of sound equation, we have the following

$$\frac{\left. \frac{\partial h}{\partial \rho} \right|_{\rho_0}}{\left. \frac{1}{\rho_0} - \frac{\partial h}{\partial p} \right|_{p_0}} = \frac{-c_p \frac{T_0}{\rho_0}}{\frac{1}{\rho_0} - c_p \frac{T_0}{P_0}} = \frac{c_p T_0}{c_p \frac{T_0 \rho_0}{P_0} - 1} = \frac{c_p T_0}{\frac{c_p}{R} - 1} = \frac{c_p R T_0}{c_p - R} = \frac{c_p}{c_v} R T_0 = a_f^2.$$

A.4 Derivation of single mode formula

Starting with wavenumber equation, Eq. 3.27, we have for a single relaxation mode

$$\begin{aligned}
D^2 &= \frac{-\omega^2 \left(\frac{1}{a_f^2} - \frac{1}{\frac{\partial h}{\partial \rho}} \Big|_{\rho_0} \frac{\partial h}{\partial q_i} \Big|_{q_{i,0}} (\omega I_{ji} + A_{ji})^{-1} A_{ji} \frac{\partial q_i^*}{\partial p} \Big|_{p_0} \right)}{1 + \frac{1}{\frac{\partial h}{\partial \rho}} \Big|_{\rho_0} \frac{\partial h}{\partial q_i} \Big|_{q_{i,0}} (\omega I_{ji} + A_{ji})^{-1} A_{ji} \frac{\partial q_i^*}{\partial p} \Big|_{p_0}} \\
&= \frac{\omega^2 \left(\frac{\partial h}{\partial p} \Big|_{p_0} - \frac{1}{\rho_0} + \frac{\partial h}{\partial q_i} \Big|_{q_{i,0}} (\omega + \frac{1}{\tau})^{-1} \frac{1}{\tau} \frac{\partial q_i^*}{\partial p} \Big|_{p_0} \right)}{\frac{\partial h}{\partial \rho} \Big|_{\rho_0} + \frac{\partial h}{\partial q_i} \Big|_{q_{i,0}} (\omega + \frac{1}{\tau})^{-1} \frac{1}{\tau} \frac{\partial q_i^*}{\partial p} \Big|_{p_0}} \\
&= \frac{\omega^2 \left(\frac{\partial h}{\partial p} \Big|_{p_0} - \frac{1}{\rho_0} + \frac{\partial h}{\partial q_i} \Big|_{q_{i,0}} \frac{1}{\omega\tau+1} \frac{\partial q_i^*}{\partial p} \Big|_{p_0} \right)}{\frac{\partial h}{\partial \rho} \Big|_{\rho_0} + \frac{\partial h}{\partial q_i} \Big|_{q_{i,0}} \frac{1}{\omega\tau+1} \frac{\partial q_i^*}{\partial p} \Big|_{p_0}} \\
&= \frac{\omega^2 \left(\omega\tau \left(\frac{\partial h}{\partial p} \Big|_{p_0} - \frac{1}{\rho_0} \right) + \left(\frac{\partial h}{\partial p} \Big|_{p_0} - \frac{1}{\rho_0} \right) + \frac{\partial h}{\partial q_i} \Big|_{q_{i,0}} \frac{\partial q_i^*}{\partial p} \Big|_{p_0} \right)}{\omega\tau \frac{\partial h}{\partial \rho} \Big|_{\rho_0} + \frac{\partial h}{\partial \rho} \Big|_{\rho_0} + \frac{\partial h}{\partial q_i} \Big|_{q_{i,0}} \frac{\partial q_i^*}{\partial p} \Big|_{p_0}}.
\end{aligned}$$

Using the equation for τ^+

$$\tau^+ = \frac{\tau \left(\frac{\partial h}{\partial p} - \frac{1}{\rho} \right)}{\frac{\partial h}{\partial p} + \frac{\partial h}{\partial q_i} \frac{\partial q_i^*}{\partial p} - \frac{1}{\rho}},$$

we have the following relationships:

$$\tau^+ \left(\frac{\partial h}{\partial p} + \frac{\partial h}{\partial q_i} \frac{\partial q_i^*}{\partial p} - \frac{1}{\rho} \right) = \tau \left(\frac{\partial h}{\partial p} - \frac{1}{\rho} \right)$$

and

$$-a_f^2 \tau^+ \left(\frac{\partial h}{\partial p} + \frac{\partial h}{\partial q_i} \frac{\partial q_i^*}{\partial p} - \frac{1}{\rho} \right) = \tau \frac{\partial h}{\partial \rho}.$$

Substituting these formulas into the equation for wavenumber, we have

$$D^2 = \frac{\omega^2 \left(\frac{\partial h}{\partial p} \Big|_{p_0} - \frac{1}{\rho_0} + \frac{\partial h}{\partial q_i} \Big|_{q_{i,0}} \frac{\partial q_i^*}{\partial p} \Big|_{p_0} \right) (\omega\tau^+ + 1)}{-\omega a_f^2 \tau^+ \left(\frac{\partial h}{\partial p} + \frac{\partial h}{\partial q_i} \frac{\partial q_i^*}{\partial p} - \frac{1}{\rho} \right) + \frac{\partial h}{\partial \rho} \Big|_{\rho_0} + \frac{\partial h}{\partial q_i} \Big|_{q_{i,0}} \frac{\partial q_i^*}{\partial \rho} \Big|_{\rho_0}} = \frac{\omega^2 (\omega\tau^+ + 1)}{-\omega a_f^2 \tau^+ + \frac{\frac{\partial h}{\partial \rho} \Big|_{\rho_0} + \frac{\partial h}{\partial q_i} \Big|_{q_{i,0}} \frac{\partial q_i^*}{\partial \rho} \Big|_{\rho_0}}{\frac{\partial h}{\partial p} \Big|_{p_0} - \frac{1}{\rho_0} + \frac{\partial h}{\partial q_i} \Big|_{q_{i,0}} \frac{\partial q_i^*}{\partial p} \Big|_{p_0}}$$

$$\Leftrightarrow D^2 = \frac{-\omega^2 (\omega\tau^+ + 1)}{\omega\tau^+ a_f^2 + a_e^2}.$$

$$\Leftrightarrow D^2 = \frac{-\omega^2}{a_e^2} \left[\frac{1 + X(\omega\tau^+)}{1 + X^2(\omega\tau^+)^2} + i \frac{(1 - X)\omega\tau^+}{1 + X^2(\omega\tau^+)^2} \right]$$

In addition to this formula based on the equilibrium sound speed, we can derive another formula based on the frozen sound speed as follows. We start again with the wavenumber equation

$$D^2 = \frac{-\omega^2 \left(\frac{1}{a_f^2} - \frac{1}{\frac{\partial h}{\partial \rho} \Big|_{\rho_0}} \frac{\partial h}{\partial q_i} \Big|_{q_{i,0}} \frac{\partial q_i^*}{\partial p} \Big|_{p_0} \right) (\omega\tau + 1)^{-1}}{1 + \frac{1}{\frac{\partial h}{\partial \rho} \Big|_{\rho_0}} \frac{\partial h}{\partial q_i} \Big|_{q_{i,0}} \frac{\partial q_i^*}{\partial \rho} \Big|_{\rho_0}} (\omega\tau + 1)^{-1}}{a_f^2 \frac{\omega\tau + 1 - \frac{a_f^2}{\frac{\partial h}{\partial \rho} \Big|_{\rho_0}} \frac{\partial h}{\partial q_i} \Big|_{q_{i,0}} \frac{\partial q_i^*}{\partial p} \Big|_{p_0}}{\omega\tau + 1 + \frac{1}{\frac{\partial h}{\partial \rho} \Big|_{\rho_0}} \frac{\partial h}{\partial q_i} \Big|_{q_{i,0}} \frac{\partial q_i^*}{\partial \rho} \Big|_{\rho_0}}}$$

$$h_{q,p} = \frac{\frac{\partial h}{\partial q_i} \Big|_{q_{i,0}} \frac{\partial q_i^*}{\partial p} \Big|_{p_0}}{\frac{\partial h}{\partial \rho} \Big|_{\rho_0}}$$

$$h_{q,\rho} = \frac{\frac{\partial h}{\partial q_i} \Big|_{q_{i,0}} \frac{\partial q_i^*}{\partial \rho} \Big|_{\rho_0}}{\frac{\partial h}{\partial \rho} \Big|_{\rho_0}}$$

$$D^2 = \frac{-\omega^2}{a_f^2} \frac{\omega\tau + 1 - a_f^2 h_{q,p}}{\omega\tau + 1 + h_{q,\rho}} = \frac{-\omega^2}{a_f^2} \left(\frac{(\omega\tau + 1 - a_f^2 h_{q,p}) * (1 + h_{q,\rho} - \omega\tau)}{(\omega\tau)^2 + (1 + h_{q,\rho})^2} \right)$$

$$= \frac{-\omega^2}{a_f^2} \left(\frac{(\omega\tau)^2 + \omega\tau h_{q,\rho} + 1 + h_{q,\rho} - a_f^2 h_{q,p} - a_f^2 h_{q,p} h_{q,\rho} + a_f^2 h_{q,p} \omega\tau}{(\omega\tau)^2 + (1 + h_{q,\rho})^2} \right)$$

$$\begin{aligned}
&= \frac{-\omega^2}{a_f^2} \left(\frac{(\omega\tau)^2 + 1 + h_{q,\rho} - a_f^2 h_{q,p} (1 + h_{q,\rho}) + i\omega\tau (h_{q,\rho} + a_f^2 h_{q,p})}{(\omega\tau)^2 + (1 + h_{q,\rho})^2} \right) \\
&= \frac{\omega^2}{a_f^2} \left(\frac{a_f^2 h_{q,p} (1 + h_{q,\rho}) - (\omega\tau)^2 - (1 + h_{q,\rho}) - i\omega\tau (h_{q,\rho} + a_f^2 h_{q,p})}{(\omega\tau)^2 + (1 + h_{q,\rho})^2} \right) \\
D^2 &= \frac{\omega^2}{a_f^2} \left(\frac{(a_f^2 h_{q,p} - 1)(1 + h_{q,\rho}) - (\omega\tau)^2}{(\omega\tau)^2 + (1 + h_{q,\rho})^2} - \frac{i\omega\tau (h_{q,\rho} + a_f^2 h_{q,p})}{(\omega\tau)^2 + (1 + h_{q,\rho})^2} \right) \tag{A.10}
\end{aligned}$$

Vincenti and Kruger define

$$\tau_0^+ = \frac{\tau_0}{1 + \frac{\frac{\partial h}{\partial a_i} \Big|_{q_{i,0}} \frac{\partial q_i^*}{\partial \rho} \Big|_{\rho_0}}{\frac{\partial h}{\partial \rho} \Big|_{\rho_0}}} = \frac{\tau_0}{1 + h_{q,\rho}} \tag{A.11}$$

where τ_0 is the calculated relaxation time for a particular gas composition. This relaxation time is related to the relaxation time used in the equilibrium speed of sound through the following relationship

$$a_e^2 \tau^+ = a_f^2 \tau_0^+.$$

Substituting the new relaxation time into Eq. A.10, we have

$$D^2 = \frac{\omega^2}{a_f^2} \left(\frac{\frac{-(1 - a_f^2 h_{q,p})}{(1 + h_{q,\rho})} - (\omega\tau_0^+)^2}{(\omega\tau_0^+)^2 + 1} - \frac{i\omega\tau_0^+ \frac{(1 + h_{q,\rho} + a_f^2 h_{q,p} - 1)}{(1 + h_{q,\rho})}}{(\omega\tau_0^+)^2 + 1} \right).$$

Vincenti and Kruger also introduce the following parameters to help simplify this formula

$$k = \omega\tau_0^+,$$

$$b = \frac{a_f^2}{a_e^2}.$$

The ratio of the speeds of sound can be rewritten as

$$\frac{a_f^2}{a_e^2} = \frac{\frac{\partial h}{\partial \rho} \Big|_{\rho_0}}{\frac{\partial h}{\partial \rho} \Big|_{\rho_0} - \frac{1}{\rho_0}} \frac{\frac{\partial h}{\partial p} \Big|_{p_0} - \frac{1}{\rho_0} + \frac{\partial h}{\partial q_i} \Big|_{q_{i,0}} \frac{\partial q_i^*}{\partial p} \Big|_{p_0}}{\frac{\partial h}{\partial \rho} \Big|_{\rho_0} + \frac{\partial h}{\partial q_i} \Big|_{q_{i,0}} \frac{\partial q_i^*}{\partial \rho} \Big|_{\rho_0}} = \frac{1}{\frac{\frac{\partial h}{\partial p} \Big|_{p_0} - \frac{1}{\rho_0}}{\frac{\partial h}{\partial \rho} \Big|_{\rho_0}}} \frac{\frac{\frac{\partial h}{\partial p} \Big|_{p_0} - \frac{1}{\rho_0}}{\frac{\partial h}{\partial \rho} \Big|_{\rho_0}} + h_{q,p}}{1 + h_{q,p}} = \frac{1 - \frac{\frac{\partial h}{\partial p} \Big|_{p_0}}{\frac{\partial h}{\partial \rho} \Big|_{\rho_0}} h_{q,p}}{1 + h_{q,p}}$$

$$\frac{a_f^2}{a_e^2} = \frac{1 - a_f^2 h_{q,p}}{1 + h_{q,p}}. \quad (\text{A.12})$$

Substituting this into the current form of the wavenumber equation, we have

$$D^2 = \frac{\omega^2}{a_f^2} \left(-\frac{\frac{a_f^2}{a_e^2} + (\omega\tau_0^+)^2}{(\omega\tau_0^+)^2 + 1} - \frac{i\omega\tau_0^+ \left(1 - \frac{a_f^2}{a_e^2}\right)}{(\omega\tau_0^+)^2 + 1} \right) = \frac{\omega^2}{a_f^2} \left(-\frac{\frac{a_f^2}{a_e^2} + (\omega\tau_0^+)^2}{(\omega\tau_0^+)^2 + 1} + \frac{i\omega\tau_0^+ \left(\frac{a_f^2}{a_e^2} - 1\right)}{(\omega\tau_0^+)^2 + 1} \right) \quad (\text{A.13})$$

We can rewrite Eq. A.13 with the variables used by Vincenti and Kruger, which looks as

$$D^2 = \frac{\omega^2}{a_f^2} \left(-\frac{b + k^2}{1 + k^2} + i \frac{k(b - 1)}{1 + k^2} \right). \quad (\text{A.14})$$

A.5 Acoustic absorption rate for a single mode

Vincenti and Kruger also solve a one dimensional acoustic equation on page 264 of their book as

$$\left. \begin{array}{l} \delta \\ \lambda \end{array} \right\} = \left\{ \frac{1}{2(1+k^2)} \left[\mp (b+k^2) + \sqrt{(1+k^2)(b^2+k^2)} \right] \right\}^{1/2},$$

where

$$\text{Re}(D) = \frac{\omega}{a_f} \delta, \quad \text{Im}(D) = \frac{\omega}{a_f} \lambda.$$

Fujii shows that the absorption rate per wavelength, ε_λ , is given by the formula

$$\varepsilon_\lambda = \frac{2\pi \text{Re}(D)}{\text{Im}(D)},$$

therefore we write the absorption rate per wavelength as

$$\varepsilon_\lambda = 2\pi \frac{\delta}{\lambda}. \quad (\text{A.15})$$

The derivation of this result is also given in the book, however, an alternate derivation is as follows.

We start by introducing the following variables:

$$\begin{aligned} x &= -\frac{b+k^2}{1+k^2}, \\ y &= -\frac{k(1-b)}{1+k^2}, \\ r &= \sqrt{x^2+y^2}, \end{aligned}$$

where

$$\begin{aligned} r &= \left(\frac{(b+k^2)^2 + k^2(1-b)^2}{(1+k^2)^2} \right)^{1/2} = \frac{\sqrt{b^2 + 2bk^2 + k^4 + k^2 - 2bk^2 + k^2b^2}}{(1+k^2)} = \frac{\sqrt{b^2 + k^2 + k^2b^2 + k^4}}{(1+k^2)} \\ &\Leftrightarrow r = \frac{\sqrt{(1+k^2)(b^2+k^2)}}{(1+k^2)} \end{aligned}$$

and substitute them into Eq. A.14. Using the standard formula for the square root of a complex number, we have

$$D = \frac{\omega}{a_f} \left(\left(\frac{r+x}{2} \right)^{1/2} \pm i \left(\frac{r-x}{2} \right)^{1/2} \right),$$

with

$$\begin{aligned} \text{Re}(D) &= \frac{\omega}{a_f} \left(\frac{r+x}{2} \right)^{1/2} = \frac{\omega}{a_f} \left(\frac{\sqrt{(1+k^2)(b^2+k^2)} - (b+k^2)}{2(1+k^2)} \right)^{1/2}, \\ \text{Im}(D) &= \frac{\omega}{a_f} \left(\frac{r-x}{2} \right)^{1/2} = \frac{\omega}{a_f} \left(\frac{\sqrt{(1+k^2)(b^2+k^2)} + (b+k^2)}{2(1+k^2)} \right)^{1/2}. \end{aligned}$$

Now the absorption rate per wavelength is

$$\varepsilon_\lambda = 2\pi \left\{ \frac{\sqrt{(1+k^2)(b^2+k^2)} - (b+k^2)}{\sqrt{(1+k^2)(b^2+k^2)} + (b+k^2)} \right\}^{1/2},$$

which is identical to Eq. A.15.

It is instructive to find the maximum of ε_λ with respect to both k and b in order to understand

how the absorption rate varies with frequency, relaxation time, and other parameters describing the gas. To do this we use the standard method of determine the extrema of a function with its first derivatives. The derivative of ε_λ^2 with respect to k is

$$\begin{aligned} \frac{\partial \varepsilon_\lambda^2}{\partial k} &= 4\pi^2 \frac{\partial}{\partial k} \left(\frac{r - |x|}{r + |x|} \right) = \frac{\partial}{\partial k} \left(\frac{\sqrt{(1+k^2)(b^2+k^2)} - (b+k^2)}{\sqrt{(1+k^2)(b^2+k^2)} + (b+k^2)} \right) \\ &= \frac{b^2 + 2k^2 + 1}{\sqrt{(1+k^2)(b^2+k^2)}} - 2 - \frac{\sqrt{(1+k^2)(b^2+k^2)} - (b+k^2)}{\sqrt{(1+k^2)(b^2+k^2)} + (b+k^2)} \left(\frac{b^2 + 2k^2 + 1}{\sqrt{(1+k^2)(b^2+k^2)}} + 2 \right) = 0. \end{aligned}$$

The derivative with respect to b is

$$\begin{aligned} \frac{\partial \varepsilon_\lambda^2}{\partial b} &= 4\pi^2 \frac{\partial}{\partial b} \left(\frac{r - |x|}{r + |x|} \right) = \frac{\partial}{\partial b} \left(\frac{\sqrt{(1+k^2)(b^2+k^2)} - (b+k^2)}{\sqrt{(1+k^2)(b^2+k^2)} + (b+k^2)} \right) \\ &= \frac{b(1+k^2)}{\sqrt{(1+k^2)(b^2+k^2)}} - 1 - \frac{\sqrt{(1+k^2)(b^2+k^2)} - (b+k^2)}{\sqrt{(1+k^2)(b^2+k^2)} + (b+k^2)} \left(\frac{b(1+k^2)}{\sqrt{(1+k^2)(b^2+k^2)}} + 2 \right) = 0. \end{aligned}$$

The derivative of ε_λ^2 with respect to both k and b takes the following form

$$\begin{aligned} 0 &= \frac{a}{r} - c - \frac{r - |x|}{r + |x|} \left(\frac{a}{r} + c \right) \\ &= a - rc - \frac{r - |x|}{r + |x|} (a + rc) = a(r + |x|) - rc(r + |x|) - a(r - |x|) - rc(r - |x|) \\ &= a|x| - cr^2 = 0, \end{aligned} \tag{A.16}$$

where

$$a = \begin{cases} b^2 + 2k^2 + 1 & \text{for } \frac{\partial}{\partial k} \\ b(1+k^2) & \text{for } \frac{\partial}{\partial b} \end{cases}$$

and

$$c = \begin{cases} 2 & \text{for } \frac{\partial}{\partial k} \\ 1 & \text{for } \frac{\partial}{\partial b} \end{cases}.$$

Expanding out Eq. A.16 for the derivative with respect to k , we have

$$0 = (b^2 + 2k^2 + 1)(b + k^2) - 2(1 + k^2)(b^2 + k^2)$$

$$\begin{aligned}\Leftrightarrow 0 &= -k^2 (b^2 - 2b + 1) + b^3 - 2b^2 + b = -k^2 (b - 1)^2 + b(b - 1)^2 \\ &\Leftrightarrow k = \pm\sqrt{b}.\end{aligned}$$

Since k depends on the adjusted relaxation time τ_0^+ and ω , it must always be positive. Therefore we take the positive root and have the result that

$$k_{max} = \sqrt{b}. \quad (\text{A.17})$$

It can be shown, either with calculus or by plotting, that ε_λ is concave down at this value of k , making it a maximum. Continuing on with the derivative with respect to b , we have

$$\begin{aligned}0 &= (b(1 + k^2))(b + k^2) - (1 + k^2)(b^2 + k^2) \\ 0 &= b^2 + b^2k^2 + bk^2 + bk^4 - (b^2 + k^2 + b^2k^2 + k^4) = b(k^2 + k^4) - (k^2 + k^4) \\ &b = 1.\end{aligned}$$

To determine if this is a maximum or minimum of ε_λ , we can simply look at the nature of the function ε_λ^2 . When written in terms of r and $|x|$, we have

$$\varepsilon_\lambda^2 = (2\pi)^2 \frac{r - |x|}{r + |x|}.$$

From this expression, we can see that ε_λ^2 is always non-negative because $r \geq x$ and that ε_λ^2 is a minimum when $r = x$ and $y = 0$. The condition of $y = 0$ occurs when $b = 1$. Therefore we have

$$b_{min} = 1. \quad (\text{A.18})$$

This also implies that the maximum of ε_λ will occur on the border of the range of b . We have that

$$b = \frac{a_f^2}{a_e^2},$$

and knowing that $a_f \geq a_e$, b must be equal to one at a minimum and bounded on the right by the non-equilibrium parameters of the system. Therefore the maximum of ε_λ with respect to b occurs at the upper bound of b itself.

It is also interesting to track the maximum absorption rate as b varies. Taking the value of k_{max} and substituting it into the equation for ε_λ , we find that

$$\varepsilon_{\lambda,max(f)} = 2\pi \frac{\sqrt{b} - 1}{\sqrt{b} + 1} = 2\pi \frac{\frac{a_f}{a_e} - 1}{\frac{a_f}{a_e} + 1} = 2\pi \frac{a_f - a_e}{a_f + a_e}.$$

Again we see that the maximum value of ε_λ occurs at the largest difference in a_f and a_e , which corresponds to the largest value of b .

A.5.1 Dissipation per wavelength for a single vibrational mode

For a diatomic gas with a single mode of vibration (assuming a temperature range for which dissociation does not occur), the partial derivatives in this formula are as follows

$$\left. \frac{\partial h}{\partial \rho} \right|_{\rho_0} = -\frac{c_p T}{\rho},$$

$$\left. \frac{\partial h}{\partial p} \right|_{p_0} = \frac{c_p T}{p},$$

$$\left. \frac{\partial h}{\partial q_i} \right|_{q_{i,0}} = \left. \frac{\partial h}{\partial e_v} \right|_{e_{v,0}} = 1,$$

$$\left. \frac{\partial q_i^*}{\partial \rho} \right|_{\rho_0} = \left. \frac{\partial e_v^*}{\partial \rho} \right|_{\rho_0} = \overbrace{\frac{R_u}{M_s} \left(\frac{\theta_{vs}}{T} \right)^2 \frac{\exp(\theta_{vs}/T)}{\exp(\theta_{vs}/T) - 1}}^{c_{vv}^*} \left(-\frac{T}{\rho} \right) = -c_{vv}^* \frac{T}{\rho},$$

$$\left. \frac{\partial q_i^*}{\partial p} \right|_{p_0} = \left. \frac{\partial e_v^*}{\partial p} \right|_{p_0} = \overbrace{\frac{R_u}{M_s} \left(\frac{\theta_{vs}}{T} \right)^2 \frac{\exp(\theta_{vs}/T)}{\exp(\theta_{vs}/T) - 1}}^{c_{vv}^*} \left(\frac{T}{p} \right) = c_{vv}^* \frac{T}{p},$$

where the enthalpy is assumed to be

$$h = c_p T + e_v.$$

With these derivatives defined we can also write the more complex enthalpy derivative terms as

$$h_{q,p} = \frac{\left. \frac{\partial h}{\partial q_i} \right|_{q_{i,0}} \left. \frac{\partial q_i^*}{\partial p} \right|_{p_0}}{\left. \frac{\partial h}{\partial \rho} \right|_{\rho_0}} = \frac{c_{vv}^* \frac{T}{P}}{-c_p \frac{T}{\rho}} = -\frac{c_{vv}^* \frac{\rho}{P}}{c_p} = -\frac{c_{vv}^*}{a_f^2 \gamma c_p} = -\frac{c_{vv}^*}{a_f^2 c_v},$$

$$h_{q,\rho} = \frac{\left. \frac{\partial h}{\partial q_i} \right|_{q_{i,0}} \left. \frac{\partial q_i^*}{\partial \rho} \right|_{\rho_0}}{\left. \frac{\partial h}{\partial \rho} \right|_{\rho_0}} = \frac{-c_{vv}^* \frac{T}{\rho}}{-c_p \frac{T}{\rho}} = \frac{c_{vv}^*}{c_p}.$$

Substituting these into Eq. A.11, we have

$$\tau_0^+ = \frac{\tau_0}{1 + h_{q,\rho}} = \frac{\tau_0}{1 + \frac{c_{vv}^*}{c_p}},$$

therefore, the variable k is

$$k = \frac{\omega \tau_0}{1 + \frac{c_{vv}^*}{c_p}}.$$

The ratio of the speeds of sound can be determined from Eq. A.12. Substituting the enthalpy derivative terms for a vibrational mode we have

$$\frac{a_f^2}{a_e^2} = \frac{1 + \frac{c_{vv}^*}{c_v}}{1 + \frac{c_{vv}^*}{c_p}}.$$

We can now find the frequency of maximum damping for a vibrational mode. Using the formula in Eq. A.17, we have

$$k_{max} = \sqrt{b} = \sqrt{\frac{1 + \frac{c_{vv}^*}{c_v}}{1 + \frac{c_{vv}^*}{c_p}}} = \frac{\omega \tau_0}{1 + \frac{c_{vv}^*}{c_p}} \Leftrightarrow \sqrt{\left(1 + \frac{c_{vv}^*}{c_p}\right) \left(1 + \frac{c_{vv}^*}{c_v}\right)} = \omega \tau_0$$

$$\Leftrightarrow \omega_{max} = \frac{\sqrt{\left(1 + \frac{c_{vv}^*}{c_p}\right) \left(1 + \frac{c_{vv}^*}{c_v}\right)}}{\tau_0}.$$

Therefore the frequency of maximum damping is

$$f_{max} = \frac{\sqrt{\left(1 + \frac{c_{vv}^*}{c_p}\right) \left(1 + \frac{c_{vv}^*}{c_v}\right)}}{2\pi \tau_0}.$$

The absorption rate per wavelength of the vibrational mode is

$$\varepsilon_{\lambda,max}(f) = 2\pi \frac{\sqrt{1 + \frac{c_{vv}^*}{c_v}} - \sqrt{1 + \frac{c_{vv}^*}{c_p}}}{\sqrt{1 + \frac{c_{vv}^*}{c_v}} + \sqrt{1 + \frac{c_{vv}^*}{c_p}}}.$$

An interesting result of these formulas is that for all diatomic gases the maximum damping rate

is the same and limited to approximately 13.4 percent. When $T \gg \theta_v$ and T is large, c_{vv}^* limits to R_s , therefore we have

$$\lim_{T \rightarrow \infty} \left(1 + \frac{c_{vv}^*}{c_v} \right) = \frac{7}{5},$$

$$\lim_{T \rightarrow \infty} \left(1 + \frac{c_{vv}^*}{c_p} \right) = \frac{9}{7}.$$

Substituting these values into the equation for the maximum damping frequency, we have

$$f_{max} = \frac{\sqrt{\frac{9}{7} \frac{7}{5}}}{2\pi\tau_0} = \frac{3}{2\sqrt{5}\pi\tau_0} \simeq \frac{0.2135}{\tau_0}.$$

The maximum absorption rate limits to

$$\max(\varepsilon_\lambda) = 2\pi \frac{\sqrt{\frac{7}{5} \frac{7}{9}} - 1}{\sqrt{\frac{7}{5} \frac{7}{9}} + 1} = 2\pi \frac{7 - 3\sqrt{5}}{7 + 3\sqrt{5}} \simeq 0.133745.$$

A.5.2 Dissipation per wavelength for an dissociating gas

For a dissociating gas, we can repeat the process used for determining the optimal damping parameters in the vibrational by beginning with the definition of the enthalpy derivatives,

$$\begin{aligned} \left. \frac{\partial h}{\partial \rho} \right|_{\rho_0} &= - \sum_{j=1}^{n_s} N_j \hat{C}_{v,t+r} \frac{T}{\rho} - \frac{p}{\rho^2} = - (N_1 + N_2) \hat{C}_{v,t} \frac{T}{\rho} - \left(N_1 \hat{C}_{v,r} + N_2(0) \right) \frac{T}{\rho} - \frac{p}{\rho^2}, \\ \left. \frac{\partial h}{\partial \rho} \right|_{\rho_0} &= - \frac{\hat{C}_{v,t}}{M_{mix}} \frac{T}{\rho} - \frac{R_u}{M_{mix}} \frac{T}{\rho} - \frac{Y_1 \hat{C}_{v,r}}{M_1} \frac{T}{\rho} = - \frac{\hat{C}_{p,t}}{M_{mix}} \frac{T}{\rho} - Y_1 c_{p,r,1} \frac{T}{\rho} = - c_{p,t+r,mix} \frac{T}{\rho}, \\ \left. \frac{\partial h}{\partial p} \right|_{p_0} &= \sum_{j=1}^{n_s} N_j \hat{C}_{v,t+r} \frac{T}{p} + \frac{1}{\rho} = - \frac{\hat{C}_{v,t}}{M_{mix}} \frac{T}{p} + \frac{R_u}{M_{mix}} \frac{T}{p} + \frac{Y_1 \hat{C}_{v,r}}{M_1} \frac{T}{p} = c_{p,t+r,mix} \frac{T}{p}, \\ \left. \frac{\partial h}{\partial q_i} \right|_{q_{i,0}} &= \frac{\partial h}{\partial \alpha_i} = \sum_{j=1}^{n_s} \nu_{1j} \hat{C}_{v,t+r} T + \sum_{j=1}^{n_s} \nu_{1j} M_j \sum_{s=1}^{n_{v,j}} e_{v,s,j} + \overbrace{\sum_{j=1}^{n_s} \nu_{1j} \hat{e}_{0,j}}^{\Delta H_r} - \sum_{j=1}^{n_s} N_j M_{mix} T \sum_k \nu_{1k} \hat{C}_{v,t+r}, \\ &= \sum_{j=1}^{n_s} \nu_{1j} \hat{C}_{v,t+r} T + \nu_{11} M_1 e_{v,1} + \Delta H_r - N_1 M_{mix} T (1) \hat{C}_{v,t+r} - N_2 M_{mix} T (1) \hat{C}_{v,t}, \end{aligned}$$

$$\begin{aligned}
&= -\hat{C}_{v,t}T - \hat{C}_{v,r}T + 2\hat{C}_{v,t}T + \nu_{11}M_1e_{v,1} + \Delta H_r - N_1M_{mix}T\hat{C}_{v,r} - \overbrace{(N_1 + N_2)}^{1/M_{mix}}M_{mix}T\hat{C}_{v,t}, \\
&= -\hat{C}_{v,r}T + \hat{C}_{v,t}T + \nu_{11}M_1e_{v,1} + \Delta H_r - N_1M_{mix}T\hat{C}_{v,r} - \hat{C}_{v,t}T, \\
&= \Delta H_r - M_1e_{v,1} - \hat{C}_{v,r}T - N_1M_{mix}T\hat{C}_{v,r} = \Delta H_r - M_1e_{v,1} - (1 + N_1M_{mix})\hat{C}_{v,r}T, \\
&= \Delta H_r - M_1e_{v,1} - (2N_1 + N_2)M_{mix}\hat{C}_{v,r}T, \\
&\Leftrightarrow \frac{\partial h}{\partial \alpha_i} = \Delta H_r - M_1e_{v,1} - (2N_1 + N_2)M_{mix}\hat{C}_{v,r}T = \Delta H_{r2}
\end{aligned}$$

$$A_p = \frac{d(\ln K)T}{dT} \frac{1}{p} = \frac{1}{p} \frac{\Delta H_{r2}}{R_u T},$$

$$A_\rho = - \left(\frac{d(\ln K)T}{dT} \frac{1}{\rho} + \frac{\sum_j \nu_{1j}}{\rho} \right) = - \frac{1}{\rho} \left(\frac{\Delta H_{r2}}{R_u T} + 1 \right),$$

using the Van't Hoff relation or we can leave it as the derivative of the equilibrium constant

$$A_\rho = - \frac{1}{\rho} \left(\frac{d(\ln K)}{dT} T + 1 \right),$$

$$A_\alpha = \frac{d(\ln K)}{dT} T M_{mix} \sum_k \nu_{1k} + \sum_k \frac{\nu_{1k} \nu_{1k}}{N_k}$$

$$A_\alpha = \frac{\Delta H_{r2}}{R_u T} M_{mix} (1) + \left(\frac{(-1)^2}{N_1} + \frac{2^2}{N_2} \right)$$

$$A_\alpha = \frac{\Delta H_{r2}}{R_u T} M_{mix} + \left(\frac{1}{N_1} + \frac{4}{N_2} \right)$$

or

$$A_\alpha = \frac{d(\ln K)}{dT} T M_{mix} + \left(\frac{1}{N_1} + \frac{4}{N_2} \right)$$

$$\left. \frac{\partial q_i^*}{\partial \rho} \right|_{p_0} = \left. \frac{\partial \alpha^*}{\partial \rho} \right|_{p_0} = A_\alpha^{-1} A_\rho = \frac{-\frac{1}{\rho} \left(\frac{\Delta H_{r2}}{R_u T} + 1 \right)}{\frac{\Delta H_{r2}}{R_u T} M_{mix} + \left(\frac{1}{N_1} + \frac{4}{N_2} \right)},$$

$$\left. \frac{\partial q_i^*}{\partial p} \right|_{p_0} = \left. \frac{\partial \alpha^*}{\partial p} \right|_{p_0} = A_\alpha^{-1} A_p = \frac{\frac{\Delta H_{r2}}{R_u T p}}{\frac{\Delta H_{r2}}{R_u T} M_{mix} + \left(\frac{1}{N_1} + \frac{4}{N_2} \right)},$$

$$\left. \frac{\partial q_i^*}{\partial \rho} \right|_{\rho_0} = \left. \frac{\partial \alpha^*}{\partial \rho} \right|_{\rho_0} = A_\alpha^{-1} A_\rho = \frac{-\frac{1}{\rho} \left(\frac{d(\ln K)}{dT} T + 1 \right)}{\frac{d(\ln K)}{dT} T M_{mix} + \left(\frac{1}{N_1} + \frac{4}{N_2} \right)},$$

$$\left. \frac{\partial q_i^*}{\partial p} \right|_{p_0} = \left. \frac{\partial \alpha^*}{\partial p} \right|_{p_0} = A_\alpha^{-1} A_p = \frac{\frac{d(\ln K)}{dT} \frac{T}{P}}{\frac{d(\ln K)}{dT} T M_{mix} + \left(\frac{1}{N_1} + \frac{4}{N_2} \right)},$$

where the enthalpy is assumed to be

$$h = c_p T + e_v.$$

$$h_{q,p} = \frac{\left. \frac{\partial h}{\partial q_i} \right|_{q_{i,0}} \left. \frac{\partial q_i^*}{\partial p} \right|_{p_0}}{\left. \frac{\partial h}{\partial \rho} \right|_{\rho_0}} = \frac{\Delta H_{r2} \frac{\Delta H_{r2} T}{R_u T^2 p}}{-c_{p,t+r,mix} \frac{T}{\rho} \frac{\Delta H_{r2}}{R_u T} M_{mix} + \left(\frac{1}{N_1} + \frac{4}{N_2} \right)}$$

$$= \frac{\frac{\rho}{p} \frac{\Delta H_{r2}}{R_u T^2} \Delta H_{r2}}{-c_{p,t+r,mix} \frac{\Delta H_{r2}}{R_u T^2} T M_{mix} + \left(\frac{1}{N_1} + \frac{4}{N_2} \right)} = \frac{1}{a_f^2 c_{v,t+r,mix} T M_{mix} + \frac{R_u T^2}{\Delta H_{r2}} \left(\frac{1}{N_1} + \frac{4}{N_2} \right)} \Delta H_{r2}$$

$$h_{q,p} = \frac{\left. \frac{\partial h}{\partial q_i} \right|_{q_{i,0}} \left. \frac{\partial q_i^*}{\partial \rho} \right|_{\rho_0}}{\left. \frac{\partial h}{\partial \rho} \right|_{\rho_0}} = \frac{\Delta H_{r2} \frac{-\frac{1}{\rho} \left(\frac{\Delta H_{r2}}{R_u T} + 1 \right)}{\rho}}{-c_{p,t+r,mix} \frac{T}{\rho} \frac{\Delta H_{r2}}{R_u T} M_{mix} + \left(\frac{1}{N_1} + \frac{4}{N_2} \right)}$$

$$= \frac{\frac{T}{\rho} \frac{-\left(\frac{\Delta H_{r2}}{R_u T^2} + \frac{1}{T} \right) \Delta H_{r2}}{-c_{p,t+r,mix} \frac{T}{\rho} \frac{\Delta H_{r2}}{R_u T} M_{mix} + \left(\frac{1}{N_1} + \frac{4}{N_2} \right)}}{c_{p,t+r,mix} \frac{\Delta H_{r2}}{R_u T^2} T M_{mix} + \left(\frac{1}{N_1} + \frac{4}{N_2} \right)} \frac{\left(\frac{\Delta H_{r2}}{R_u T^2} + \frac{1}{T} \right) \Delta H_{r2}}{1}$$

$$= \frac{1}{c_{p,t+r,mix} T M_{mix} + \frac{R_u T^2}{\Delta H_{r2}} \left(\frac{1}{N_1} + \frac{4}{N_2} \right)} \left(1 + \frac{R_u T}{\Delta H_{r2}} \right) \Delta H_{r2}$$

or

$$h_{q,p} = \frac{\left. \frac{\partial h}{\partial q_i} \right|_{q_{i,0}} \left. \frac{\partial q_i^*}{\partial p} \right|_{p_0}}{\left. \frac{\partial h}{\partial \rho} \right|_{\rho_0}} = \frac{\Delta H_{r2} \frac{\frac{d(\ln K)}{dT} T}{p}}{-c_{p,t+r,mix} \frac{T}{\rho} \frac{d(\ln K)}{dT} T M_{mix} + \left(\frac{1}{N_1} + \frac{4}{N_2} \right)}$$

$$= \frac{\frac{\rho}{p} \frac{\frac{d(\ln K)}{dT} \Delta H_{r2}}{\frac{d(\ln K)}{dT}}}{-c_{p,t+r,mix} \frac{d(\ln K)}{dT} T M_{mix} + \left(\frac{1}{N_1} + \frac{4}{N_2} \right)} = \frac{1}{a_f^2 c_{v,t+r,mix} T M_{mix} + \left(\frac{d(\ln K)}{dT} \right)^{-1} \left(\frac{1}{N_1} + \frac{4}{N_2} \right)} \Delta H_{r2}$$

$$\begin{aligned}
h_{q,\rho} &= \frac{\left. \frac{\partial h}{\partial q_i} \right|_{q_{i,0}} \left. \frac{\partial q_i^*}{\partial \rho} \right|_{\rho_0}}{\left. \frac{\partial h}{\partial \rho} \right|_{\rho_0}} = \frac{\Delta H_{r2}}{-c_{p,t+r,mix} \frac{T}{\rho} \frac{d(\ln K)}{dT} TM_{mix} + \left(\frac{1}{N_1} + \frac{4}{N_2} \right)} \frac{-\frac{1}{\rho} \left(\frac{d(\ln K)}{dT} T + 1 \right)}{\left(\frac{1}{N_1} + \frac{4}{N_2} \right)} \\
&= \frac{\frac{T}{\rho}}{-c_{p,t+r,mix} \frac{T}{\rho} \frac{d(\ln K)}{dT} TM_{mix} + \left(\frac{1}{N_1} + \frac{4}{N_2} \right)} - \frac{\left(\frac{d(\ln K)}{dT} + \frac{1}{T} \right) \Delta H_{r2}}{c_{p,t+r,mix} \frac{d(\ln K)}{dT} TM_{mix} + \left(\frac{1}{N_1} + \frac{4}{N_2} \right)} = \frac{1}{c_{p,t+r,mix} \frac{d(\ln K)}{dT} TM_{mix} + \left(\frac{1}{N_1} + \frac{4}{N_2} \right)} \frac{\left(\frac{d(\ln K)}{dT} + \frac{1}{T} \right) \Delta H_{r2}}{\left(\frac{d(\ln K)}{dT} + \frac{1}{T} \right) \Delta H_{r2}} \\
&= \frac{1}{c_{p,t+r,mix} TM_{mix} + \left(\frac{d(\ln K)}{dT} \right)^{-1} \left(\frac{1}{N_1} + \frac{4}{N_2} \right)} \frac{\left(1 + \left(\frac{d(\ln K)}{dT} \right)^{-1} \frac{1}{T} \right) \Delta H_{r2}}{\left(1 + \left(\frac{d(\ln K)}{dT} \right)^{-1} \frac{1}{T} \right) \Delta H_{r2}}
\end{aligned}$$

Using the formula for the optimal damping angular frequency, we have

$$\begin{aligned}
\omega_{opt} \tau_0 &= \sqrt{(1 + h_{q,\rho}) \left(1 - a_f^2 h_{q,p} \right)}, \\
\omega_{opt} \tau_0 &= \sqrt{\left(1 + \frac{\left(1 + \frac{R_u T}{\Delta H_{r2}} \right) c_{chem}}{c_{p,t+r,mix}} \right) \left(1 + \frac{c_{chem}}{c_{v,t+r,mix}} \right)},
\end{aligned}$$

where

$$c_{chem} = \frac{\Delta H_{r2}}{TM_{mix} + \frac{R_u T^2}{\Delta H_{r2}} \left(\frac{1}{N_1} + \frac{4}{N_2} \right)}.$$

This could also be written as

$$\omega_{opt} \tau_0 = \sqrt{\left(1 + \frac{\left(1 + \left(\frac{d(\ln K)}{dT} \right)^{-1} \frac{1}{T} \right) c_{chem}}{c_{p,t+r,mix}} \right) \left(1 + \frac{c_{chem}}{c_{v,t+r,mix}} \right)},$$

where

$$c_{chem} = \frac{\Delta H_{r2}}{TM_{mix} + \left(\frac{d(\ln K)}{dT} \right)^{-1} \left(\frac{1}{N_1} + \frac{4}{N_2} \right)}.$$

To determine the derivative of the equilibrium coefficient, we start with

$$\begin{aligned}
\rho \frac{d\alpha'_i}{dt} &= k_{f,i} \left[\prod_s [X]_s^{\nu'_{is}} - \frac{1}{K_i} \prod_s [X]_s^{\nu''_{is}} \right] \\
\Leftrightarrow \rho \frac{d\alpha'}{dt} &= k_f \left[(\rho N_1) - \frac{1}{K_{eq}} (\rho N_2)^2 \right], \tag{A.19}
\end{aligned}$$

where k_f is the forward reaction rate coefficient,

$$k_f = C_f T^{\eta_f} \exp\left(\frac{-\theta_f}{T}\right). \quad (\text{A.20})$$

Differentiating Equation A.19 with respect to α , we obtain

$$\begin{aligned} \frac{\partial}{\partial \alpha} \left(\frac{d\alpha}{dt} \right) &= \frac{k_f}{\rho} \left[\left(\frac{1}{N_1} \frac{\partial N_1}{\partial \alpha} \right) (\rho N_1) - \frac{1}{K_{eq}} \left(\frac{2}{N_2} \frac{\partial N_2}{\partial \alpha} \right) (\rho N_2)^2 \right] \\ &= \frac{k_f}{\rho} \left[\left(\frac{1 * \nu_{11}}{N_1} \right) (\rho N_1) - \frac{1}{K_k} \left(\frac{2 * \nu_{12}}{N_2} \right) (\rho N_2)^2 \right]. \end{aligned}$$

When the undisturbed condition is in equilibrium, $N_s = N_s^*$, we have

$$\begin{aligned} \frac{1}{K_{eq}} &= \frac{\rho N_1}{(\rho N_2)^2} \\ \Rightarrow \frac{\partial}{\partial \alpha} \left(\frac{d\alpha}{dt} \right) &= \frac{k_f}{\rho} \left[\left(\frac{1 * (-1)}{N_1} \right) (\rho N_1) - \frac{\rho N_1}{(\rho N_2)^2} \left(\frac{2 * (2)}{N_2} \right) (\rho N_2)^2 \right] \\ &= \frac{k_f}{\rho} \left[\left(\frac{-1}{N_1} - \frac{4}{N_2} \right) (\rho N_1) \right] \\ \frac{\partial}{\partial \alpha} \left(\frac{d\alpha}{dt} \right) &= -k_f N_1 \left(\frac{1}{N_1} + \frac{4}{N_2} \right), \\ \frac{\partial}{\partial \alpha} \left(\frac{d\alpha}{dt} \right) &= \frac{1}{\tau_0} = C_f T^{\eta_f} \exp\left(\frac{-\theta_f}{T}\right) N_1 \left(\frac{1}{N_1} + \frac{4}{N_2} \right) \end{aligned}$$

or

$$\frac{\partial}{\partial \alpha} \left(\frac{d\alpha}{dt} \right) = \frac{1}{\tau_0} = C_f T^{\eta_f} \exp\left(\frac{-\theta_f}{T}\right) \left(\frac{4N_1 + N_2}{N_2} \right).$$

Finally, we have the optimum frequency as

$$\omega_{opt} = C_f T^{\eta_f} \exp\left(\frac{-\theta_f}{T}\right) \left(\frac{4N_1 + N_2}{N_2} \right) \sqrt{\left(1 + \frac{\left(1 + \frac{R_u T}{\Delta H_{r2}} \right) c_{chem}}{c_{p,t+r,mix}} \right) \left(1 + \frac{c_{chem}}{c_{v,t+r,mix}} \right)}.$$

or

$$\omega_{opt} = C_f T^{\eta_f} \exp\left(\frac{-\theta_f}{T}\right) \left(\frac{4N_1 + N_2}{N_2} \right) \sqrt{\left(1 + \frac{\left(1 + \left(\frac{d(\ln K)}{dT} \right)^{-1} \frac{1}{T} \right) c_{chem}}{c_{p,t+r,mix}} \right) \left(1 + \frac{c_{chem}}{c_{v,t+r,mix}} \right)}.$$

An interesting consequence of this formula is the dissociated species, N_2 , must be present in the mean state of the gas in order for damping to occur.

Using the formula for the damping rate per wavelength at the optimum frequency, we have

$$\frac{a_f^2}{a_e^2} = \frac{1 + \frac{c_{chem}}{c_{v,t+r,mix}}}{1 + \frac{\left(1 + \frac{R_u T}{\Delta H_{r2}}\right) c_{chem}}{c_{p,t+r,mix}}}$$

$$\varepsilon_{\lambda,max(f)} = 2\pi \frac{\sqrt{1 + \frac{c_{chem}}{c_{v,t+r,mix}}} - \sqrt{1 + \frac{\left(1 + \frac{R_u T}{\Delta H_{r2}}\right) c_{chem}}{c_{p,t+r,mix}}}}{\sqrt{1 + \frac{c_{chem}}{c_{v,t+r,mix}}} + \sqrt{1 + \frac{\left(1 + \frac{R_u T}{\Delta H_{r2}}\right) c_{chem}}{c_{p,t+r,mix}}}}$$

or

$$\frac{a_f^2}{a_e^2} = \frac{1 + \frac{c_{chem}}{c_{v,t+r,mix}}}{1 + \frac{\left(1 + \left(\frac{d(\ln K)}{dT}\right)^{-1} \frac{1}{T}\right) c_{chem}}{c_{p,t+r,mix}}}$$

$$\varepsilon_{\lambda,max(f)} = 2\pi \frac{\sqrt{1 + \frac{c_{chem}}{c_{v,t+r,mix}}} - \sqrt{1 + \frac{\left(1 + \left(\frac{d(\ln K)}{dT}\right)^{-1} \frac{1}{T}\right) c_{chem}}{c_{p,t+r,mix}}}}{\sqrt{1 + \frac{c_{chem}}{c_{v,t+r,mix}}} + \sqrt{1 + \frac{\left(1 + \left(\frac{d(\ln K)}{dT}\right)^{-1} \frac{1}{T}\right) c_{chem}}{c_{p,t+r,mix}}}}.$$

This formula is considerably more complicated than the vibrational damping case, however, it still maintains a strong dependence of the factor of c_{chem}

A.5.3 Frozen Wave Dispersion Relation from Disturbance Energy

We can also use the conservation of disturbance energy equation to determine the dispersion relation.

This equation is

$$\rho_0 \frac{\partial e'}{\partial t} + \rho_0 U_{0,j} \frac{\partial e'}{\partial x_j} + P_0 \frac{\partial u'_i}{\partial x_i} = 0, \quad (\text{A.21})$$

where

$$e = c_v T,$$

which implies

$$de = c_v dT.$$

Using a reduced form Equation A.6, this equation becomes

$$de = c_v T \left(\frac{dp}{p} - \frac{d\rho}{\rho} \right) = \frac{a_f^2}{\gamma(\gamma-1)} \left(\frac{dp}{p} - \frac{d\rho}{\rho} \right).$$

From this we have

$$e' = \frac{a_f^2}{\gamma(\gamma-1)} \left(\frac{p'}{p_0} - \frac{\rho'}{\rho_0} \right) = \frac{a_f^2}{\gamma(\gamma-1)} \left(\frac{1}{p_0} - \frac{k_i k_i}{(U_{0,j} k_j - \omega)^2} \frac{1}{\rho_0} \right) p'.$$

After substituting this into Equation A.21, we obtain

$$\begin{aligned} & -i\omega\rho_o \frac{\partial e}{\partial p} \Big|_{p_0} p' + i k_j U_{0,j} \rho_o \frac{\partial e}{\partial p} \Big|_{p_0} p' + i \rho_o R T_0 k_i \left(-\frac{k_i p'}{\rho_o (U_{0,j} k_j - \omega)} \right) \\ & = \rho_o \frac{\partial e}{\partial p} \Big|_{p_0} - R T_0 \frac{k_i k_i}{(U_{0,j} k_j - \omega)^2} = 0 \\ & \Leftrightarrow \frac{a_f^2}{\gamma(\gamma-1)} \left(\frac{\rho_o}{p_0} - \frac{k_i k_i}{(U_{0,j} k_j - \omega)^2} \right) - R T_0 \frac{k_i k_i}{(U_{0,j} k_j - \omega)^2} = 0 \\ & \Leftrightarrow \frac{a_f^2}{(\gamma-1)} \left(\frac{\rho_o}{p_0} - \frac{k_i k_i}{(U_{0,j} k_j - \omega)^2} \right) - \gamma R T_0 \frac{k_i k_i}{(U_{0,j} k_j - \omega)^2} \\ & = \frac{1}{(\gamma-1)} \left(\frac{\rho_o}{p_0} - \frac{k_i k_i}{(U_{0,j} k_j - \omega)^2} \right) - \frac{k_i k_i}{(U_{0,j} k_j - \omega)^2} = \frac{\rho_o}{p_0} \frac{1}{(\gamma-1)} - \left(\frac{1}{(\gamma-1)} + 1 \right) \frac{k_i k_i}{(U_{0,j} k_j - \omega)^2} \\ & = \frac{\rho_o}{p_0} \frac{1}{(\gamma-1)} - \left(\frac{1}{(\gamma-1)} + \frac{\gamma-1}{(\gamma-1)} \right) \frac{k_i k_i}{(U_{0,j} k_j - \omega)^2} = \frac{\rho_o}{p_0} - \gamma \frac{k_i k_i}{(U_{0,j} k_j - \omega)^2} = 0 \\ & \Leftrightarrow (U_{0,j} k_j - \omega)^2 = \gamma \frac{p_0}{\rho_o} k_i k_i \\ & \Leftrightarrow (U_{0,j} k_j - \omega)^2 = a_f^2 k_i k_i. \end{aligned} \tag{A.22}$$

A.5.4 The nature of the acoustic dispersion relation with a mean flow

To investigate the nature of the acoustic dispersion relation with a mean flow, Eq. 3.45, we must simplify the system to involve a single relaxation mode. This allows us to rearrange the equation to isolate the various powers of the wavenumber k_i . This looks as

$$\frac{k_i k_i}{(U_{0,j} k_j - \omega)^2} = \frac{1}{a_f^2} \frac{1 - ((U_{0,j} k_j - \omega) \tau \iota + 1)^{-1} h_{q,p} a_f^2}{1 + ((U_{0,j} k_j - \omega) \tau \iota + 1)^{-1} h_{q,\rho}}$$

$$\begin{aligned}
&\Leftrightarrow \frac{k_i k_i}{(U_{0,j} k_j - \omega)^2} = \frac{1}{a_f^2} \frac{(U_{0,j} k_j - \omega) \tau_l + 1 - h_{q,p} a_f^2}{(U_{0,j} k_j - \omega) \tau_l + 1 + h_{q,p}} \\
&\Leftrightarrow \frac{k_i k_i}{(U_{0,j} k_j - \omega)^2} = \frac{1}{a_f^2} \frac{(U_{0,j} k_j - \omega) \tau_0^{+l} + \frac{a_f^2}{a_e^2}}{(U_{0,j} k_j - \omega) \tau_0^{+l} + 1} \\
&\Leftrightarrow ((U_{0,j} k_j - \omega) \tau_0^{+l} + 1) k_i k_i = \frac{1}{a_f^2} (U_{0,j} k_j - \omega)^2 \left((U_{0,j} k_j - \omega) \tau_0^{+l} + \frac{a_f^2}{a_e^2} \right).
\end{aligned}$$

We now assume that the problem is one dimensional or in other words that the wave is travelling parallel with the mean velocity. Continuing on with this assumption, we have

$$\begin{aligned}
k^3 U_0 \tau_0^{+l} + (1 - \omega \tau_0^{+l}) k^2 &= \frac{1}{a_f^2} \left((U_0 k)^2 - 2U_0 k \omega + \omega^2 \right) \left((U_0 k - \omega) \tau_0^{+l} + \frac{a_f^2}{a_e^2} \right) \\
&= \frac{1}{a_f^2} \left((U_0 k)^2 - 2U_0 k \omega + \omega^2 \right) \left(U_0 k \tau_0^{+l} + \frac{a_f^2}{a_e^2} - \omega \tau_0^{+l} \right) \\
&= U_0 k^3 M_f^2 \tau_0^{+l} - 2M_f^2 k^2 \omega \tau_0^{+l} + \frac{1}{a_f^2} \omega^2 U_0 k \tau_0^{+l} + M_f^2 k^2 \left(\frac{a_f^2}{a_e^2} - \omega \tau_0^{+l} \right) \\
&\quad - \frac{1}{a_f^2} 2U_0 k \omega \left(\frac{a_f^2}{a_e^2} - \omega \tau_0^{+l} \right) + \frac{1}{a_f^2} \omega^2 \left(\frac{a_f^2}{a_e^2} - \omega \tau_0^{+l} \right) \\
&\Leftrightarrow 0 = k^3 U_0 (M_f^2 - 1) \tau_0^{+l} + k^2 \left((M_e^2 - 1) - (3M_f^2 - 1) \omega \tau_0^{+l} \right) \\
&\quad + k \left(\frac{3}{a_f} M_f \omega^2 \tau_0^{+l} - \frac{2}{a_e} M_e \omega \right) + \omega^2 \left(\frac{1}{a_e^2} - \frac{\omega \tau_0^{+l}}{a_f^2} \right)
\end{aligned}$$

We now have a cubic equation for the complex wavenumber k . This implies that there exists three solutions to the acoustic equation. As it turns out, the familiar solutions of

$$k_{re} = \frac{\omega}{U_0 \pm a},$$

are two of these possible solutions, while the mathematical form and physical meaning of the third root are currently unknown. Numerical testing shows consistently that this third root has a significant amount of damping per wavelength and therefore, if it were physically possible, would damp out within a few wavelengths. As expected the nature of the equation changes when the frozen Mach number exceeds one. When the frozen Mach number equals one, the cubic term is eliminated, resulting in a quadratic equation with only two possible roots. This reflects the impossibility of

describing a slow acoustic wave at this condition using this formulation. Another important aspect of this equation is the inter-dependence of the real and imaginary parts of the wavenumber k . To demonstrate this, we separate the real and imaginary parts

$$\operatorname{Re} (k^3 U_0 (M_f^2 - 1) \tau_0^+ \iota) = (k_{im}^3 - 3k_{re}^2 k_{im}) U_0 (M_f^2 - 1) \tau_0^+$$

$$\operatorname{Im} (k^3 U_0 (M_f^2 - 1) \tau_0^+ \iota) = (k_{re}^3 - 3k_{re} k_{im}^2) U_0 (M_f^2 - 1) \tau_0^+$$

$$\operatorname{Re} (k^2 ((M_e^2 - 1) - (3M_f^2 - 1) \omega \tau_0^+ \iota)) = (k_{re}^2 - k_{im}^2) (M_e^2 - 1) + 2k_{re} k_{im} (3M_f^2 - 1) \omega \tau_0^+$$

$$\operatorname{Im} (k^2 ((M_e^2 - 1) - (3M_f^2 - 1) \omega \tau_0^+ \iota)) = (k_{im}^2 - k_{re}^2) (3M_f^2 - 1) \omega \tau_0^+ - 2k_{re} k_{im} (M_e^2 - 1)$$

$$\operatorname{Re} \left(k \left(\frac{3}{a_f} M_f \omega^2 \tau_0^+ \iota - \frac{2}{a_e} M_e \omega \right) \right) = -\frac{2}{a_e} M_e \omega k_{re} - \frac{3}{a_f} M_f \omega^2 \tau_0^+ k_{im}$$

$$\operatorname{Im} \left(k \left(\frac{3}{a_f} M_f \omega^2 \tau_0^+ \iota - \frac{2}{a_e} M_e \omega \right) \right) = -\frac{2}{a_e} M_e \omega k_{im} + \frac{3}{a_f} M_f \omega^2 \tau_0^+ k_{re}$$

This makes the real part of the equation

$$\begin{aligned} & (k_{im}^3 - 3k_{re}^2 k_{im}) U_0 (M_f^2 - 1) \tau_0^+ + (k_{re}^2 - k_{im}^2) (M_e^2 - 1) + 2k_{re} k_{im} (3M_f^2 - 1) \omega \tau_0^+ \\ & - \frac{2}{a_e} M_e \omega k_{re} - \frac{3}{a_f} M_f \omega^2 \tau_0^+ k_{im} + \frac{\omega^2}{a_e^2} = 0 \end{aligned}$$

and the imaginary part of the equation

$$\begin{aligned} & (k_{re}^3 - 3k_{re} k_{im}^2) U_0 (M_f^2 - 1) \tau_0^+ + (k_{im}^2 - k_{re}^2) (3M_f^2 - 1) \omega \tau_0^+ - 2k_{re} k_{im} (M_e^2 - 1) \\ & - \frac{2}{a_e} M_e \omega k_{im} + \frac{3}{a_f} M_f \omega^2 \tau_0^+ k_{re} - \frac{\omega^3 \tau_0^+}{a_f^2} = 0. \end{aligned}$$

Appendix B

Transient Growth Formulation

B.1 Definition of the Derivatives for the Species Density Equations

Taking the derivative of c_s with respect to ϕ , we have

$$\frac{\partial c_s}{\partial \phi} = \begin{cases} (\delta_{rs} - c_s) \frac{1}{\rho} & \phi = \rho_r; r = 1 \rightarrow ns \\ 0 & \phi \neq \rho_r \end{cases}.$$

Following the derivation given in the appendix, the derivative of the mixture viscosity is as follows,

$$\frac{\partial \mu}{\partial \phi} = \begin{cases} \frac{M}{\rho M_l} \left(\frac{\mu_l}{\phi_{w,l}} - \sum_s \frac{\mu_s X_s}{\phi_{w,s}^2} a_{sl}^2 c_{sl} \right) & \phi = \rho_l; l = 1 \rightarrow ns \\ \sum_s \frac{\mu_s X_s}{\phi_{w,s}} \left(\frac{(2A_s \ln T + B_s)}{T} - \frac{1}{\phi_{w,s}} \frac{\partial \phi_{w,s}}{\partial T} \right) & \phi = T \\ 0 & \phi = u_i, T_v \end{cases},$$

where we have made the following substitutions

$$a_{sl} = 1 + \sqrt{\frac{\mu_s}{\mu_l}} \left(\frac{M_l}{M_s} \right)^{1/4}$$

and

$$c_{sl} = \left(8 \left(1 + \frac{M_s}{M_l} \right) \right)^{-1/2}.$$

The derivative of the chemical reaction rates with respect to a disturbance variable for the dissociation reactions is

$$\frac{\partial R_r}{\partial \phi} = \begin{cases} \sum_m k_{fm}(T_{eff}) [M] \frac{\delta_{sAB}}{M_{AB}} - \sum_m k_{bm}(T) [M] \left([B] \frac{\delta_{sA}}{M_A} + [A] \frac{\delta_{sB}}{M_B} \right) & \phi = \rho_l; l = 1 \rightarrow ns \\ \quad + \frac{\delta_{sm}}{M_m} (k_{fm}(T_{eff}) [AB] - k_{bm}(T) [A][B]) & \\ \sum_m \frac{\partial k_{fm}(T_{eff})}{\partial T_{eff}} \frac{\partial T_{eff}}{\partial T} [AB][M] - \frac{\partial k_{bm}}{\partial T} [A][B][M] & \phi = T \\ \sum_m \frac{\partial k_{fm}(T_{eff})}{\partial T_{eff}} \frac{\partial T_{eff}}{\partial T_v} [AB][M] & \phi = T_v \\ 0 & \phi = u_i \end{cases},$$

where the remaining partial derivatives are defined in the appendix. For the exchange reactions, we have

$$\frac{\partial R_r}{\partial \phi} = \begin{cases} \frac{\partial k_f(T)}{\partial T} [AB][CD] - \frac{\partial k_b}{\partial T} [AD][CB] & \phi = \rho_l; l = 1 \rightarrow ns \\ \frac{\partial k_f(T)}{\partial T} [AB][CD] - \frac{\partial k_b}{\partial T} [AD][CB] & \phi = T \\ 0 & \phi = u_i, T_v \end{cases}.$$

B.2 Definition of the Derivatives for the Temperature Equation

We start with the partial derivative of the internal enthalpy of the species s , h_s , which is

$$\frac{\partial h_s}{\partial \phi} = \begin{cases} c_{ps} & \phi = T \\ \frac{\partial e_{vs}}{\partial T_v} = c_{vvs} & \phi = T_v \\ 0 & \phi = \rho_s, u_i \end{cases}.$$

Next, we need to partial derivative of the thermal conductivities with respect to the set of disturbance variables. Because the mixture thermal conductivities are determined in the same manner as the mixture viscosity, the partial derivatives are very similar. For the translational-rotational conductivity, we have

$$\frac{\partial \kappa}{\partial \phi} = \begin{cases} \frac{M}{\rho M_l} \left(\frac{\mu_l}{\phi_{w,l}} \frac{\partial \kappa_l}{\partial \mu_l} - \sum_s \frac{\mu_s X_s}{\phi_{w,s}^2} \frac{\partial \kappa_s}{\partial \mu_s} a_{sl}^2 c_{sl} \right) & \phi = \rho_l; l = 1 \rightarrow ns \\ \sum_s \frac{\mu_s X_s}{\phi_{w,s}} \frac{\partial \kappa_s}{\partial \mu_s} \left(\frac{(2A_s \ln T + B_s)}{T} - \frac{1}{\phi_{w,s}} \frac{\partial \phi_{w,s}}{\partial T} \right) & \phi = T \\ 0 & \phi = u_i, T_v \end{cases},$$

where

$$\frac{\partial \kappa_s}{\partial \mu_s} = \begin{cases} \frac{7}{2} c_v & s = 1 \rightarrow nd \\ \frac{5}{2} c_v & s = nd + 1 \rightarrow ns \end{cases}.$$

For the vibrational conductivity, we have

$$\frac{\partial \kappa_v}{\partial \phi} = \begin{cases} \frac{M}{\rho M_l} \left(\frac{\mu_l c_{vvs}}{\phi_{w,l}} - \sum_s \frac{\mu_s X_s c_{vvs}}{\phi_{w,s}^2} a_{sl}^2 c_{sl} \right) & \phi = \rho_l; l = 1 \rightarrow ns \\ \sum_s \frac{\mu_s X_s c_{vvs}}{\phi_{w,s}} \left(\frac{(2A_s \ln T + B_s)}{T} - \frac{1}{\phi_{w,s}} \frac{\partial \phi_{w,s}}{\partial T} \right) & \phi = T \\ \sum_s \frac{\mu_s X_s c_{vvs}}{\phi_{w,s} T_v} \left(\frac{\theta_{v,s}}{T_v} \left[\frac{\exp\left(\frac{\theta_{v,s}}{T_v}\right) + 1}{\exp\left(\frac{\theta_{v,s}}{T_v}\right) - 1} \right] - 2 \right) & \phi = T_v \\ 0 & \phi = u_i \end{cases}.$$

All the partial derivative in this equation have been defined above, except for the partial derivative of the translational-vibrational exchange term. This term looks as

$$\frac{\partial Q_{t-v}}{\partial \phi} = \begin{cases} \frac{e_{vl}^* - e_{vl}}{\langle \tau_l \rangle} + \frac{M}{\rho M_l} \sum_s \rho_s \frac{(e_{vs}^* - e_{vs})}{\tau_{sl}} & \phi = \rho_l; l = 1 \rightarrow ns \\ \sum_s \frac{\rho_s c_{vvs}^*}{\langle \tau_s \rangle} + \rho_s (e_{vs}^* - e_{vs}) \left(\frac{1}{3} T^{-4/3} \sum_r \frac{A_{sr} X_r}{\tau_{sr}} \right) & \phi = T \\ - \sum_s \frac{\rho_s c_{vvs}}{\langle \tau_s \rangle} & \phi = T_v \\ 0 & \phi = u_i \end{cases}.$$

B.3 Non-dimensional Disturbance Equations

Beginning with the disturbance form of the conservation of mass equation, Equation 3.47, we have

$$\frac{\partial}{\partial t} \left(\frac{\partial \rho}{\partial \phi} \phi' \right) + \frac{\partial}{\partial x_i} (\rho_0 u_i') + \frac{\partial}{\partial x_i} \left(u_{0,i} \frac{\partial \rho}{\partial \phi} \phi' \right) = 0. \quad (\text{B.1})$$

Since all of the terms are of order 1, we retain all terms for this equation.

Continuing on with the disturbance form of the conservation of species density equations, Equations 3.48, we have

$$\begin{aligned} \frac{\partial \rho_s}{\partial t} + \frac{\partial}{\partial x_i} (\rho_s u_i) &= \frac{\partial}{\partial x_i} \left(\frac{1}{Sc} \mu \frac{\partial c_s}{\partial x_i} \right) \delta'_{i1} \\ &+ M_s \left(\sum_{r,diss} v_{sr} \left(R_{fr} \frac{\rho_\infty L}{u_\infty} - R_{br} \frac{\rho_\infty^2 L}{u_\infty} \right) + \sum_{r,exch} v_{sr} R_r \frac{\rho_\infty L}{u_\infty} \right) \end{aligned} \quad (\text{B.2})$$

For now, we will leave the dimensional coefficient on the chemical source terms. Based on eq. B.2,

we can expand and eliminate a few terms in the species disturbance conservation equations. To do this, we introduce the following relations to simplify our notation,

$$\begin{pmatrix} x_1 \\ x_2 \\ x_3 \end{pmatrix} = \begin{pmatrix} x \\ y \\ z \end{pmatrix}; \quad \begin{pmatrix} u_1 \\ u_2 \\ u_3 \end{pmatrix} = \begin{pmatrix} u \\ v \\ w \end{pmatrix}. \quad (\text{B.3})$$

It is also important to note two properties of a flat-plate boundary layer. First, all mean flow properties are constant with respect the spanwise, or z , direction, which means all spanwise derivatives of mean flow properties are zero, including the partial derivatives with respect to ϕ . Second, the mean flow spanwise velocity, w_0 , is equal to zero. Applying these relations eq 3.48 we have

$$\begin{aligned} & \frac{\partial \rho'_s}{\partial t} + \frac{\partial}{\partial x} (\rho'_s u_0) + \frac{\partial}{\partial y} (\rho'_s v_0) + \frac{\partial}{\partial x} (\rho_{s,0} u') + \frac{\partial}{\partial y} (\rho_{s,0} v') + \frac{\partial}{\partial z} (\rho_{s,0} w') \\ & = \left[\frac{1}{Sc} \frac{\partial}{\partial y} \left(\frac{\partial \mu}{\partial \phi} \frac{\partial c_{s,0}}{\partial y} + \mu_0 \frac{\partial}{\partial y} \left(\frac{\partial c_s}{\partial \phi} \right) \right) \right. \\ & \quad \left. + M_s \left(\sum_{r,diss} v_{sr} \left(\frac{\partial R_{fr}}{\partial \phi} \frac{\rho_\infty L}{u_\infty} - \frac{\partial R_{br}}{\partial \phi} \frac{\rho_\infty^2 L}{u_\infty} \right) + \sum_{r,exch} v_{sr} \frac{\partial R_r}{\partial \phi} \frac{\rho_\infty L}{u_\infty} \right) \right] \phi' \\ & + \frac{1}{Sc} \left(2\mu_0 \frac{\partial}{\partial y} \left(\frac{\partial c_s}{\partial \phi} \right) + \frac{\partial \mu_0}{\partial y} \frac{\partial c_s}{\partial \phi} + \frac{\partial \mu}{\partial \phi} \frac{\partial c_{s,0}}{\partial y} \right) \frac{\partial \phi'}{\partial y} + \frac{1}{Sc} \mu_0 \frac{\partial c_s}{\partial \phi} \frac{\partial^2 \phi'}{\partial y^2} + \frac{1}{Sc} \mu_0 \frac{\partial c_s}{\partial \phi} \frac{\partial^2 \phi'}{\partial z^2}. \end{aligned} \quad (\text{B.4})$$

Next, we non-dimensionalize the disturbance momentum equations, Equations 3.49, as

$$\frac{\partial}{\partial t} (\rho u_i) + \frac{\partial}{\partial x_j} (\rho u_i u_j) = -\frac{\partial P}{\partial x_i} \delta'_{i1} + \frac{\partial}{\partial x_j} \left(\mu_s \left(\frac{\partial u_i}{\partial x_j} \delta'_{j1} + \frac{\partial u_j}{\partial x_i} \delta'_{i1} - \frac{2}{3} \frac{\partial u_k}{\partial x_k} \delta_{ij} \delta'_{i1} \right) \right). \quad (\text{B.5})$$

Due to the different treatment of the spatial directions, it is useful to separate Equations B.5 into an equation for each direction. For this part of the derivation, we use the following relations to simplify our notation, With this in mind, we first look at the case when $i = 1$, which is the x or streamwise direction. We have

$$\begin{aligned} & \frac{\partial}{\partial t} \left(u_0 \frac{\partial \rho}{\partial \phi} \phi' \right) + \frac{\partial}{\partial t} (\rho_0 u') + \frac{\partial}{\partial x} \left(u_0 u_0 \frac{\partial \rho}{\partial \phi} \phi' \right) + \frac{\partial}{\partial y} \left(u_0 v_0 \frac{\partial \rho}{\partial \phi} \phi' \right) + \frac{\partial}{\partial x} (2\rho_0 u_0 u') + \frac{\partial}{\partial y} (\rho_0 v_0 u') \\ & + \frac{\partial}{\partial y} (\rho_0 u_0 v') + \frac{\partial}{\partial z} (\rho_0 u_0 w') = \frac{\partial}{\partial y} \left(\mu_0 \frac{\partial u'}{\partial y} + \frac{\partial \mu}{\partial \phi} \phi' \frac{\partial u_0}{\partial y} \right) + \frac{\partial}{\partial z} \left(\mu_0 \frac{\partial u'}{\partial z} \right). \end{aligned} \quad (\text{B.6})$$

Next, for $i = 2$, the y or wall-normal direction, we have

$$\begin{aligned} & \frac{\partial}{\partial t} \left(v_0 \frac{\partial \rho}{\partial \phi} \phi' \right) + \frac{\partial}{\partial t} (\rho_0 v') + \frac{\partial}{\partial x} \left(u_0 v_0 \frac{\partial \rho}{\partial \phi} \phi' \right) + \frac{\partial}{\partial y} \left(v_0 v_0 \frac{\partial \rho}{\partial \phi} \phi' \right) + \frac{\partial}{\partial x} (\rho_0 u_0 v') + \frac{\partial}{\partial y} (2\rho_0 v_0 v') \\ & \quad + \frac{\partial}{\partial x} (\rho_0 v_0 u') + \frac{\partial}{\partial z} (\rho_0 v_0 w') = -\frac{\partial}{\partial y} \left(\frac{\partial P}{\partial \phi} \phi' \right) + \frac{\partial}{\partial x} \left(\mu_0 \frac{\partial u'}{\partial y} + \frac{\partial \mu}{\partial \phi} \phi' \frac{\partial u_0}{\partial y} \right) \\ & + \frac{\partial}{\partial y} \left(\mu_0 \left(\frac{4}{3} \frac{\partial v'}{\partial y} - \frac{2}{3} \frac{\partial u'}{\partial x} - \frac{2}{3} \frac{\partial w'}{\partial z} \right) \right) + \frac{\partial}{\partial y} \left(\frac{\partial \mu}{\partial \phi} \phi' \left(\frac{4}{3} \frac{\partial v_0}{\partial y} - \frac{2}{3} \frac{\partial u_0}{\partial x} \right) \right) + \frac{\partial}{\partial z} \left(\mu_0 \left(\frac{\partial v'}{\partial z} + \frac{\partial w'}{\partial y} \right) \right). \end{aligned} \quad (\text{B.7})$$

Finally, for $i = 3$, the z direction, we have

$$\begin{aligned} & \frac{\partial}{\partial t} (\rho_0 w') + \frac{\partial}{\partial x} (\rho_0 w' u_0) + \frac{\partial}{\partial y} (\rho_0 w' v_0) = -\frac{\partial}{\partial z} \left(\frac{\partial P}{\partial \phi} \phi' \right) + \frac{\partial}{\partial x} \left(\mu_0 \frac{\partial u'}{\partial z} \right) + \frac{\partial}{\partial y} \left(\mu_0 \left(\frac{\partial w'}{\partial y} + \frac{\partial v'}{\partial z} \right) \right) \\ & \quad + \frac{\partial}{\partial z} \left(\mu_0 \left(\frac{4}{3} \frac{\partial w'}{\partial z} - \frac{2}{3} \frac{\partial u'}{\partial x} - \frac{2}{3} \frac{\partial v'}{\partial y} \right) + \frac{\partial \mu}{\partial \phi} \phi' \left(-\frac{2}{3} \frac{\partial u_0}{\partial x} - \frac{2}{3} \frac{\partial v_0}{\partial y} \right) \right). \end{aligned} \quad (\text{B.8})$$

Next, applying the same treatment of Equation 3.52, we have

$$\begin{aligned} & \frac{\partial}{\partial t} \left(\sum_s \rho_s h_s \right) - \frac{\partial P}{\partial t} \varepsilon^2 (\gamma_\infty - 1) Ma_\infty^2 + \frac{\partial}{\partial x_j} \left(u_j \sum_s \rho_s h_s \right) = u_i \frac{\partial P}{\partial x_i} \varepsilon^2 (\gamma_\infty - 1) Ma_\infty^2 \\ & + \mu \left(\frac{\partial u_i}{\partial x_j} (\gamma_\infty - 1) Ma_\infty^2 \varepsilon^{2(1+\delta_{j1}-\delta_{i1})} + \frac{\partial u_j}{\partial x_i} (\gamma_\infty - 1) Ma_\infty^2 \varepsilon^2 - \frac{2}{3} \frac{\partial u_k}{\partial x_k} \delta_{ij} (\gamma_\infty - 1) Ma_\infty^2 \varepsilon^2 \right) \frac{\partial u_i}{\partial x_j} \\ & \quad - \frac{\partial}{\partial x_i} \left(-\kappa \frac{\partial T}{\partial x_i} \right) \varepsilon^{2\delta_{i1}} - \frac{\partial}{\partial x_i} \left(-\kappa_v \frac{\partial T_v}{\partial x_i} \right) \varepsilon^{2\delta_{i1}} + \frac{\partial}{\partial x_i} \left(\sum_s \frac{1}{Sc} \mu \frac{\partial c_s}{\partial x_i} h_s \right) \varepsilon^{2\delta_{i1}} \end{aligned}$$

After eliminating the term always proportional to ε^2 , we arrive at final form of the non-dimensionalized energy equation

$$\begin{aligned} & \frac{\partial}{\partial t} \left(\sum_s \rho_s h_s \right) + \frac{\partial}{\partial x_j} \left(u_j \sum_s \rho_s h_s \right) = \mu \left(\frac{\partial u_i}{\partial x_j} (\gamma_\infty - 1) Ma_\infty^2 \varepsilon^{2(1+\delta_{j1}-\delta_{i1})} \right) \frac{\partial u_i}{\partial x_j} \\ & \quad + \left(\frac{\partial}{\partial x_i} \left(\kappa \frac{\partial T}{\partial x_i} \right) + \frac{\partial}{\partial x_i} \left(\kappa_v \frac{\partial T_v}{\partial x_i} \right) + \frac{\partial}{\partial x_i} \left(\sum_s \frac{1}{Sc} \mu \frac{\partial c_s}{\partial x_i} h_s \right) \right) \delta'_{i1}. \end{aligned} \quad (\text{B.9})$$

In this equation, Ma is the Mach number and γ is the ratio of specific heats. Applying this non-dimensionalization to the disturbance enthalpy equation, eq. 3.52, we obtain

$$\begin{aligned}
& \frac{\partial}{\partial t} \left(\sum_s \rho'_s h_{s,0} \right) + \frac{\partial}{\partial t} \left(\sum_s \rho_{s,0} \frac{\partial h_s}{\partial \phi} \phi' \right) + \frac{\partial}{\partial x_j} \left(\sum_s (u'_j \rho_{s,0} + u_{0,j} \rho'_s) h_{s,0} \right) \\
& + \frac{\partial}{\partial x_j} \left(u_{0,j} \sum_s \rho_{s,0} \frac{\partial h_s}{\partial \phi} \phi' \right) = 2\mu_0 (\gamma_\infty - 1) Ma_\infty^2 \frac{\partial u_0}{\partial y} \frac{\partial u'}{\partial y} + \frac{\partial \mu}{\partial \phi} \phi' (\gamma_\infty - 1) Ma_\infty^2 \left(\frac{\partial u_0}{\partial y} \right)^2 \\
& + \frac{\partial}{\partial y} \left(\frac{\partial \kappa}{\partial \phi} \phi' \frac{\partial T_0}{\partial y} + \kappa_0 \frac{\partial T'}{\partial y} \right) + \frac{\partial}{\partial z} \left(\kappa_0 \frac{\partial T'}{\partial z} + \kappa_{v,0} \frac{\partial T'_v}{\partial z} \right) + \frac{\partial}{\partial y} \left(\frac{\partial \kappa_v}{\partial \phi} \phi' \frac{\partial T_{v,0}}{\partial y} + \kappa_{v,0} \frac{\partial T'_v}{\partial y} \right) \\
& + \frac{\partial}{\partial y} \left(\sum_s \frac{1}{Sc} \frac{\partial \mu}{\partial \phi} \phi' \frac{\partial c_{s,0}}{\partial y} h_{s,0} \right) + \frac{\partial}{\partial y} \left(\sum_s \frac{1}{Sc} \mu_0 \frac{\partial}{\partial y} \left(\frac{\partial c_s}{\partial \phi} \phi' \right) h_{s,0} \right) \\
& + \frac{\partial}{\partial y} \left(\sum_s \frac{1}{Sc} \mu_0 \frac{\partial c_{s,0}}{\partial y} \frac{\partial h_s}{\partial \phi} \phi' \right) + \frac{\partial}{\partial z} \left(\sum_s \frac{1}{Sc} \mu_0 \frac{\partial c_s}{\partial \phi} \frac{\partial \phi'}{\partial z} h_{s,0} \right). \tag{B.10}
\end{aligned}$$

Moving on to the vibrational equation, we non-dimensionalize according to eqs. 3.55 as

$$\begin{aligned}
& \frac{\partial}{\partial t} \left(\sum_s \rho_s e_{vs} \right) + \frac{\partial}{\partial x_j} \left(u_j \sum_s \rho_s e_{vs} \right) = \frac{\partial}{\partial x_i} \left(\kappa_v \frac{\partial T_v}{\partial x_i} \right) \varepsilon^{2\delta_{i1}} \\
& + \frac{\partial}{\partial x_i} \left(\sum_s \frac{1}{Sc} \mu \frac{\partial c_s}{\partial x_i} e_{vs} \right) \varepsilon^{2\delta_{i1}} + Q_{t-v} \frac{L}{u_\infty} \\
& + \sum_s e_{vs} M_s \left(\sum_{r,diss} v_{sr} \left(R_{fr} \frac{\rho_\infty L}{u_\infty} - R_{br} \frac{\rho_\infty^2 L}{u_\infty} \right) + \sum_{r,exch} v_{sr} R_r \frac{\rho_\infty L}{u_\infty} \right)
\end{aligned}$$

Applying these changes to the disturbance vibrational energy equation, we have

$$\begin{aligned}
& \frac{\partial}{\partial t} \left(\sum_s \rho'_s e_{vs,0} \right) + \frac{\partial}{\partial t} \left(\sum_s \rho_{s,0} c_{vvs} T'_v \right) + \frac{\partial}{\partial x_j} \left(\sum_s (u'_j \rho_{s,0} + u_{0,j} \rho'_s) e_{vs,0} \right) \\
& + \frac{\partial}{\partial x_j} \left(u_{0,j} \sum_s \rho_{s,0} c_{vvs} T'_v \right) = \frac{\partial}{\partial y} \left(\frac{\partial \kappa_v}{\partial \phi} \phi' \frac{\partial T_{v,0}}{\partial y} + \kappa_{v,0} \frac{\partial T'_v}{\partial y} \right) + \frac{\partial}{\partial z} \left(\kappa_{v,0} \frac{\partial T'_v}{\partial z} \right) \\
& + \frac{\partial Q_{t-v}}{\partial \phi} \phi' \frac{L}{u_\infty} + \sum_s c_{vvs} T'_v M_s \left(\sum_{r,diss} v_{sr} \left(R_{fr} \frac{\rho_\infty L}{u_\infty} - R_{br} \frac{\rho_\infty^2 L}{u_\infty} \right) + \sum_{r,exch} v_{sr} R_r \frac{\rho_\infty L}{u_\infty} \right)
\end{aligned}$$

$$\begin{aligned}
& + \sum_s e_{vs,0} M_s \left(\sum_{r,diss} v_{sr} \left(\frac{\partial R_{fr}}{\partial \phi} \frac{\rho_\infty L}{u_\infty} - \frac{\partial R_{br}}{\partial \phi} \frac{\rho_\infty^2 L}{u_\infty} \right) + \sum_{r,exch} v_{sr} \frac{\partial R_r}{\partial \phi} \frac{\rho_\infty L}{u_\infty} \right) \phi' \\
& + \frac{\partial}{\partial y} \left(\sum_s \frac{1}{S_c} \frac{\partial \mu}{\partial \phi} \phi' \frac{\partial c_{s,0}}{\partial y} e_{vs,0} \right) + \frac{\partial}{\partial y} \left(\sum_s \frac{1}{S_c} \mu_0 \frac{\partial}{\partial y} \left(\frac{\partial c_s}{\partial \phi} \phi' \right) e_{vs,0} \right) \\
& + \frac{\partial}{\partial y} \left(\sum_s \frac{1}{S_c} \mu_0 \frac{\partial c_{s,0}}{\partial y} c_{vvs} T'_v \right) + \frac{\partial}{\partial z} \left(\sum_s \frac{1}{S_c} \mu_0 \frac{\partial c_s}{\partial \phi} \frac{\partial \phi'}{\partial z} e_{vs,0} \right) \tag{B.11}
\end{aligned}$$

For the non-reacting disturbance equations, a few terms of the previous equation can be eliminated using the non-dimensionalized ideal gas law. First, the mean ideal gas law is

$$\begin{aligned}
P_0 \rho_\infty u_\infty^2 & = \rho_0 \rho_\infty \bar{R} T_0 T_\infty \Leftrightarrow P_0 \frac{u_\infty^2}{\bar{R} T_\infty} = \rho_0 T_0 \\
& \Leftrightarrow \gamma M a^2 P_0 = \rho_0 T_0. \tag{B.12}
\end{aligned}$$

For boundary layers, we have the relation $P_0 = 1/\gamma M a^2$ [22], which shows that

$$\rho_0 T_0 = 1. \tag{B.13}$$

Using Equation 3.54, we give the disturbance ideal gas law similar treatment, which looks as

$$\begin{aligned}
P' \varepsilon^2 \rho_\infty u_\infty^2 & = (\rho' T_0 + \rho_0 T') \rho_\infty \bar{R} T_\infty \Leftrightarrow P' \gamma M^2 \varepsilon^2 = \rho' T_0 + \rho_0 T' \\
\rho' T_0 = -\rho_0 T' & \Leftrightarrow \rho' = -\frac{\rho_0}{T_0} T' = -\rho_0^2 T' = -\frac{T'}{T_0^2}. \tag{B.14}
\end{aligned}$$

B.4 Transient Growth Disturbance Equations

Applying the transient growth disturbance to the non-dimensionalized disturbance equations, Equations B.1 B.4, B.6, B.7, B.8, B.10 and B.11, we have

$$\frac{\partial}{\partial x} (\rho_0 \hat{u}') + \frac{\partial}{\partial y} (\rho_0 \hat{v}') + \rho_0 \beta \nu \hat{w}' + \frac{\partial}{\partial x} \left(u_0 \frac{\partial \rho}{\partial \phi} \hat{\phi}' \right) + \frac{\partial}{\partial y} \left(v_0 \frac{\partial \rho}{\partial \phi} \hat{\phi}' \right) = 0 \tag{B.15}$$

$$\frac{\partial}{\partial x} (\hat{\rho}'_s u_0) + \frac{\partial}{\partial y} (\hat{\rho}'_s v_0) + \frac{\partial}{\partial x} (\rho_{s,0} \hat{u}') + \frac{\partial}{\partial y} (\rho_{s,0} \hat{v}') + \rho_{s,0} \beta \nu \hat{w}'$$

$$\begin{aligned}
&= \left[\frac{1}{Sc} \frac{\partial}{\partial y} \left(\frac{\partial \mu}{\partial \phi} \frac{\partial c_{s,0}}{\partial y} + \mu_0 \frac{\partial}{\partial y} \left(\frac{\partial c_s}{\partial \phi} \right) \right) \right. \\
&\quad \left. + M_s \left(\sum_{r,diss} v_{sr} \left(\frac{\partial R_{fr}}{\partial \phi} \frac{\rho_\infty L}{u_\infty} - \frac{\partial R_{br}}{\partial \phi} \frac{\rho_\infty^2 L}{u_\infty} \right) + \sum_{r,exch} v_{sr} \frac{\partial R_r}{\partial \phi} \frac{\rho_\infty L}{u_\infty} \right) \right] \hat{\phi}' \\
&+ \frac{1}{Sc} \left(2\mu_0 \frac{\partial}{\partial y} \left(\frac{\partial c_s}{\partial \phi} \right) + \frac{\partial \mu_0}{\partial y} \frac{\partial c_s}{\partial \phi} + \frac{\partial \mu}{\partial \phi} \frac{\partial c_{s,0}}{\partial y} \right) \frac{\partial \hat{\phi}'}{\partial y} + \frac{1}{Sc} \mu_0 \frac{\partial c_s}{\partial \phi} \frac{\partial^2 \hat{\phi}'}{\partial y^2} - \beta^2 \frac{1}{Sc} \mu_0 \frac{\partial c_s}{\partial \phi} \hat{\phi}' \quad (B.16)
\end{aligned}$$

$$\begin{aligned}
&\frac{\partial}{\partial x} \left(u_0 u_0 \frac{\partial \rho}{\partial \phi} \hat{\phi}' \right) + \frac{\partial}{\partial y} \left(u_0 v_0 \frac{\partial \rho}{\partial \phi} \hat{\phi}' \right) + \frac{\partial}{\partial x} (2\rho_0 u_0 \hat{u}') + \frac{\partial}{\partial y} (\rho_0 v_0 \hat{u}') \\
&+ \frac{\partial}{\partial y} (\rho_0 u_0 \hat{v}') + \rho_0 u_0 \beta \nu \hat{w}' = \frac{\partial}{\partial y} \left(\mu_0 \frac{\partial \hat{u}'}{\partial y} + \frac{\partial \mu}{\partial \phi} \hat{\phi}' \frac{\partial u_0}{\partial y} \right) - \beta^2 \mu_0 \hat{u}' \quad (B.17)
\end{aligned}$$

$$\begin{aligned}
&\frac{\partial}{\partial x} \left(u_0 v_0 \frac{\partial \rho}{\partial \phi} \hat{\phi}' \right) + \frac{\partial}{\partial x} (\rho_0 u_0 \hat{v}') + \frac{\partial}{\partial x} (\rho_0 v_0 \hat{u}') + \frac{\partial}{\partial y} \left(v_0 v_0 \frac{\partial \rho}{\partial \phi} \hat{\phi}' \right) + \frac{\partial}{\partial y} (2\rho_0 v_0 \hat{v}') + \rho_0 v_0 \beta \nu \hat{w}' \\
&= -\frac{\partial}{\partial y} \left(\frac{\partial P}{\partial \phi} \hat{\phi}' \right) + \frac{\partial}{\partial x} \left(\mu_0 \frac{\partial \hat{u}'}{\partial y} + \frac{\partial \mu}{\partial \phi} \hat{\phi}' \frac{\partial u_0}{\partial y} \right) + \frac{\partial}{\partial y} \left(\mu_0 \left(\frac{4}{3} \frac{\partial \hat{v}'}{\partial y} - \frac{2}{3} \frac{\partial \hat{u}'}{\partial x} - \frac{2}{3} \beta \nu \hat{w}' \right) \right) \\
&\quad + \frac{\partial}{\partial y} \left(\frac{\partial \mu}{\partial \phi} \hat{\phi}' \left(\frac{4}{3} \frac{\partial v_0}{\partial y} - \frac{2}{3} \frac{\partial u_0}{\partial x} \right) \right) - \mu_0 \beta^2 \hat{v}' + \mu_0 \beta \frac{\partial \nu \hat{w}'}{\partial y}. \quad (B.18)
\end{aligned}$$

$$\begin{aligned}
&\frac{\partial}{\partial x} (\rho_0 u_0 \hat{w}') + \frac{\partial}{\partial y} (\rho_0 v_0 \hat{w}') = -\iota \beta \frac{\partial P}{\partial \phi} \hat{\phi}' + \frac{\partial}{\partial x} (\mu_0 \iota \beta \hat{u}') + \frac{\partial}{\partial y} \left(\mu_0 \left(\frac{\partial \hat{w}'}{\partial y} + \iota \beta \hat{v}' \right) \right) \\
&\quad - \frac{4}{3} \mu_0 \beta^2 \hat{w}' + \mu_0 \left(-\frac{2}{3} \iota \beta \frac{\partial \hat{u}'}{\partial x} - \frac{2}{3} \iota \beta \frac{\partial \hat{v}'}{\partial y} \right) + \iota \beta \frac{\partial \mu}{\partial \phi} \hat{\phi}' \left(-\frac{2}{3} \frac{\partial u_0}{\partial x} - \frac{2}{3} \frac{\partial v_0}{\partial y} \right). \quad (B.19)
\end{aligned}$$

$$\begin{aligned}
&\frac{\partial}{\partial x} \left(\sum_s (\hat{u}' \rho_{s,0} + u_0 \hat{\rho}'_s) h_{s,0} \right) + \frac{\partial}{\partial y} \left(\sum_s (\hat{v}' \rho_{s,0} + u_0 \hat{\rho}'_s) h_{s,0} \right) + \beta \nu \hat{w}' \sum_s \rho_{s,0} h_{s,0} \\
&\quad + \frac{\partial}{\partial x} \left(u_0 \sum_s \rho_{s,0} \frac{\partial h_s}{\partial \phi} \hat{\phi}' \right) + \frac{\partial}{\partial y} \left(v_0 \sum_s \rho_{s,0} \frac{\partial h_s}{\partial \phi} \hat{\phi}' \right) \\
&= 2\mu_0 (\gamma_\infty - 1) Ma_\infty^2 \frac{\partial u_0}{\partial y} \frac{\partial \hat{u}'}{\partial y} + \frac{\partial \mu}{\partial \phi} \hat{\phi}' (\gamma_\infty - 1) Ma_\infty^2 \left(\frac{\partial u_0}{\partial y} \right)^2 \\
&+ \frac{\partial}{\partial y} \left(\frac{\partial \kappa}{\partial \phi} \hat{\phi}' \frac{\partial T_0}{\partial y} + \kappa_0 \frac{\partial \hat{T}'}{\partial y} \right) - \beta^2 \kappa_0 \hat{T}' - \beta^2 \kappa_{v,0} \hat{T}'_v + \frac{\partial}{\partial y} \left(\frac{\partial \kappa_v}{\partial \phi} \hat{\phi}' \frac{\partial T_{v,0}}{\partial y} + \kappa_{v,0} \frac{\partial \hat{T}'_v}{\partial y} \right)
\end{aligned}$$

$$\begin{aligned}
& + \frac{\partial}{\partial y} \left(\sum_s \frac{1}{Sc} \frac{\partial \mu}{\partial \phi} \hat{\phi}' \frac{\partial c_{s,0}}{\partial y} h_{s,0} \right) + \frac{\partial}{\partial y} \left(\sum_s \frac{1}{Sc} \mu_0 \frac{\partial}{\partial y} \left(\frac{\partial c_s}{\partial \phi} \hat{\phi}' \right) h_{s,0} \right) \\
& + \frac{\partial}{\partial y} \left(\sum_s \frac{1}{Sc} \mu_0 \frac{\partial c_{s,0}}{\partial y} \frac{\partial h_s}{\partial \phi} \hat{\phi}' \right) - \beta^2 \frac{1}{Sc} \mu_0 \sum_s h_{s,0} \frac{\partial c_s}{\partial \phi} \hat{\phi}'. \tag{B.20}
\end{aligned}$$

$$\begin{aligned}
& \frac{\partial}{\partial x} \left(\sum_s (\hat{u}' \rho_{s,0} + u_0 \hat{\rho}'_s) e_{vs,0} \right) + \frac{\partial}{\partial y} \left(\sum_s (\hat{v}' \rho_{s,0} + v_0 \hat{\rho}'_s) e_{vs,0} \right) + \beta \nu \hat{w}' \sum_s \rho_{s,0} e_{vs,0} \\
& + \frac{\partial}{\partial x} \left(u_0 \sum_s \rho_{s,0} c_{vvs} \hat{T}'_v \right) + \frac{\partial}{\partial y} \left(v_0 \sum_s \rho_{s,0} c_{vvs} \hat{T}'_v \right) = \frac{\partial}{\partial y} \left(\frac{\partial \kappa_v}{\partial \phi} \hat{\phi}' \frac{\partial T_{v,0}}{\partial y} + \kappa_{v,0} \frac{\partial \hat{T}'_v}{\partial y} \right) - \beta^2 \kappa_{v,0} \hat{T}'_v \\
& + \frac{\partial Q_{t-v}}{\partial \phi} \hat{\phi}' \frac{L}{u_\infty} + \sum_s c_{vvs} \hat{T}'_v M_s \left(\sum_{r,diss} v_{sr} \left(R_{fr} \frac{\rho_\infty L}{u_\infty} - R_{br} \frac{\rho_\infty^2 L}{u_\infty} \right) + \sum_{r,exch} v_{sr} R_r \frac{\rho_\infty L}{u_\infty} \right) \\
& + \sum_s e_{vs,0} M_s \left(\sum_{r,diss} v_{sr} \left(\frac{\partial R_{fr}}{\partial \phi} \frac{\rho_\infty L}{u_\infty} - \frac{\partial R_{br}}{\partial \phi} \frac{\rho_\infty^2 L}{u_\infty} \right) + \sum_{r,exch} v_{sr} \frac{\partial R_r}{\partial \phi} \frac{\rho_\infty L}{u_\infty} \right) \hat{\phi}' \\
& + \frac{\partial}{\partial y} \left(\sum_s \frac{1}{Sc} \frac{\partial \mu}{\partial \phi} \hat{\phi}' \frac{\partial c_{s,0}}{\partial y} e_{vs,0} \right) + \frac{\partial}{\partial y} \left(\sum_s \frac{1}{Sc} \mu_0 \frac{\partial}{\partial y} \left(\frac{\partial c_s}{\partial \phi} \hat{\phi}' \right) e_{vs,0} \right) \\
& + \frac{\partial}{\partial y} \left(\sum_s \frac{1}{Sc} \mu_0 \frac{\partial c_{s,0}}{\partial y} c_{vvs} \hat{T}'_v \right) - \beta^2 \frac{1}{Sc} \mu_0 \sum_s e_{vs,0} \frac{\partial c_s}{\partial \phi} \hat{\phi}'. \tag{B.21}
\end{aligned}$$

B.5 Optimization Equations

In order to obtain an equation set described in Equation 3.58, we must expand several derivatives to isolate the disturbance amplitude functions. Starting with Equations B.16 and B.17, we have the following two equations

$$\begin{aligned}
& \frac{\partial}{\partial x} (u_0 \hat{\rho}'_s + \rho_{s,0} \hat{u}') = - \frac{\partial v_0}{\partial y} \hat{\rho}'_s - \frac{\partial \rho_{s,0}}{\partial y} \hat{v}' - \rho_{s,0} \beta \hat{w}' - \beta^2 \frac{1}{Sc} \mu_0 \frac{\partial c_s}{\partial \phi} \hat{\phi}' \\
& + \left[\frac{1}{Sc} \frac{\partial}{\partial y} \left(\frac{\partial \mu}{\partial \phi} \frac{\partial c_{s,0}}{\partial y} + \mu_0 \frac{\partial}{\partial y} \left(\frac{\partial c_s}{\partial \phi} \right) \right) \right] + \\
& M_s \left(\sum_{r,diss} v_{sr} \left(\frac{\partial R_{fr}}{\partial \phi} \frac{\rho_\infty L}{u_\infty} - \frac{\partial R_{br}}{\partial \phi} \frac{\rho_\infty^2 L}{u_\infty} \right) + \sum_{r,exch} v_{sr} \frac{\partial R_r}{\partial \phi} \frac{\rho_\infty L}{u_\infty} \right) \hat{\phi}' \\
& - v_0 \frac{\partial \hat{\rho}'_s}{\partial y} - \rho_{s,0} \frac{\partial \hat{v}'}{\partial y} + \frac{1}{Sc} \left(2\mu_0 \frac{\partial}{\partial y} \left(\frac{\partial c_s}{\partial \phi} \right) + \frac{\partial \mu_0}{\partial y} \frac{\partial c_s}{\partial \phi} + \frac{\partial \mu}{\partial \phi} \frac{\partial c_{s,0}}{\partial y} \right) \frac{\partial \hat{\phi}'}{\partial y} + \frac{1}{Sc} \mu_0 \frac{\partial c_s}{\partial \phi} \frac{\partial^2 \hat{\phi}'}{\partial y^2} \tag{B.22}
\end{aligned}$$

and

$$\begin{aligned}
\frac{\partial}{\partial x} \left(2\rho_0 u_0 \hat{u}' + u_0^2 \frac{\partial \rho}{\partial \phi} \hat{\phi}' \right) &= \left(-\frac{\partial}{\partial y} (\rho_0 v_0) - \beta^2 \mu_0 \right) \hat{u}' - \frac{\partial}{\partial y} (\rho_0 u_0) \hat{v}' \\
&\quad - \rho_0 u_0 \beta \hat{w}' + \left(-\frac{\partial}{\partial y} \left(u_0 v_0 \frac{\partial \rho}{\partial \phi} \right) + \frac{\partial}{\partial y} \left(\frac{\partial \mu}{\partial \phi} \frac{\partial u_0}{\partial y} \right) \right) \hat{\phi}' \\
+ \left(-\rho_0 v_0 + \frac{\partial \mu_0}{\partial y} \right) \frac{\partial \hat{u}'}{\partial y} - \rho_0 u_0 \frac{\partial \hat{v}'}{\partial y} &+ \left(-u_0 v_0 \frac{\partial \rho}{\partial \phi} + \frac{\partial \mu}{\partial \phi} \frac{\partial u_0}{\partial y} \right) \frac{\partial \hat{\phi}'}{\partial y} + \mu_0 \frac{\partial^2 \hat{u}'}{\partial y^2} \tag{B.23}
\end{aligned}$$

The wall-normal momentum equation, Equation B.18, requires a few more operations to take the form given in Equation 3.56. We start with

$$\begin{aligned}
\frac{\partial}{\partial x} \left(\rho_0 v_0 \hat{u}' + \rho_0 u_0 \hat{v}' + \left(u_0 v_0 \frac{\partial \rho}{\partial \phi} - \frac{\partial \mu}{\partial \phi} \frac{\partial u_0}{\partial y} \right) \hat{\phi}' \right) &= -\frac{\partial}{\partial y} \left(v_0^2 \frac{\partial \rho}{\partial \phi} \right) \hat{\phi}' - v_0^2 \frac{\partial \rho}{\partial \phi} \frac{\partial \hat{\phi}'}{\partial y} - \frac{\partial}{\partial y} (2\rho_0 v_0) \hat{v}' \\
- 2\rho_0 v_0 \frac{\partial \hat{v}'}{\partial y} - \rho_0 v_0 \beta \hat{w}' - \frac{\partial}{\partial y} \left(\frac{\partial P}{\partial \phi} \right) \hat{\phi}' - \frac{\partial P}{\partial \phi} \frac{\partial \hat{\phi}'}{\partial y} &+ \frac{\partial}{\partial x} \left(\mu_0 \frac{\partial \hat{u}'}{\partial y} \right) - \frac{2}{3} \frac{\partial \mu_0}{\partial y} \frac{\partial \hat{u}'}{\partial x} + \frac{4}{3} \frac{\partial \mu_0}{\partial y} \frac{\partial \hat{v}'}{\partial y} \\
- \frac{2}{3} \frac{\partial \mu_0}{\partial y} \beta \hat{w}' + \mu_0 \frac{4}{3} \frac{\partial^2 \hat{v}'}{\partial y^2} - \frac{2}{3} \beta \mu_0 \frac{\partial \hat{w}'}{\partial y} - \frac{2}{3} \mu_0 \frac{\partial}{\partial y} \left(\frac{\partial \hat{u}'}{\partial x} \right) & \\
+ \frac{\partial}{\partial y} \left(\frac{\partial \mu}{\partial \phi} \left(\frac{4}{3} \frac{\partial v_0}{\partial y} - \frac{2}{3} \frac{\partial u_0}{\partial x} \right) \right) \hat{\phi}' &+ \frac{\partial \mu}{\partial \phi} \left(\frac{4}{3} \frac{\partial v_0}{\partial y} - \frac{2}{3} \frac{\partial u_0}{\partial x} \right) \frac{\partial \hat{\phi}'}{\partial y} - \mu_0 \beta^2 \hat{v}' + \mu_0 \beta \frac{\partial \hat{w}'}{\partial y}. \\
\Leftrightarrow \frac{\partial}{\partial x} \left(\rho_0 v_0 \hat{u}' + \rho_0 u_0 \hat{v}' + \left(u_0 v_0 \frac{\partial \rho}{\partial \phi} - \frac{\partial \mu}{\partial \phi} \frac{\partial u_0}{\partial y} \right) \hat{\phi}' \right) &= \frac{\partial}{\partial x} \left(\mu_0 \frac{\partial \hat{u}'}{\partial y} \right) - \frac{2}{3} \frac{\partial \mu_0}{\partial y} \frac{\partial \hat{u}'}{\partial x} \\
- \frac{2}{3} \mu_0 \frac{\partial}{\partial y} \left(\frac{\partial \hat{u}'}{\partial x} \right) + \left(-\frac{\partial}{\partial y} (2\rho_0 v_0) - \mu_0 \beta^2 \right) \hat{v}' &+ \left(-\rho_0 v_0 \beta - \frac{2}{3} \frac{\partial \mu_0}{\partial y} \beta \right) \hat{w}' \\
+ \left[\frac{\partial}{\partial y} \left(-v_0^2 \frac{\partial \rho}{\partial \phi} - \frac{\partial P}{\partial \phi} \right) + \frac{\partial}{\partial y} \left(\frac{\partial \mu}{\partial \phi} \left(\frac{4}{3} \frac{\partial v_0}{\partial y} - \frac{2}{3} \frac{\partial u_0}{\partial x} \right) \right) \right] \hat{\phi}' &+ \left(-2\rho_0 v_0 + \frac{4}{3} \frac{\partial \mu_0}{\partial y} \right) \frac{\partial \hat{v}'}{\partial y} \\
+ \frac{1}{3} \beta \mu_0 \frac{\partial \hat{w}'}{\partial y} + \left[\left(-v_0^2 \frac{\partial \rho}{\partial \phi} - \frac{\partial P}{\partial \phi} \right) \frac{\partial \hat{\phi}'}{\partial y} + \frac{\partial \mu}{\partial \phi} \left(\frac{4}{3} \frac{\partial v_0}{\partial y} - \frac{2}{3} \frac{\partial u_0}{\partial x} \right) \right] \frac{\partial \hat{\phi}'}{\partial y} &+ \frac{4}{3} \mu_0 \frac{\partial^2 \hat{v}'}{\partial y^2}.
\end{aligned}$$

To reduce the number of terms rewritten, we operate only on the following terms

$$\begin{aligned}
\frac{\partial}{\partial x} \left(\mu_0 \frac{\partial \hat{u}'}{\partial y} \right) - \frac{2}{3} \mu_0 \frac{\partial^2 \hat{u}'}{\partial x \partial y} - \frac{2}{3} \frac{\partial \mu_0}{\partial y} \frac{\partial \hat{u}'}{\partial x} &= \frac{\partial}{\partial x} \left(\mu_0 \frac{\partial \hat{u}'}{\partial y} \right) + \frac{\partial}{\partial x} \left(-\frac{2}{3} \mu_0 \frac{\partial \hat{u}'}{\partial y} \right) \\
+ \frac{2}{3} \frac{\partial \mu_0}{\partial x} \frac{\partial \hat{u}'}{\partial y} + \frac{\partial}{\partial x} \left(-\frac{2}{3} \frac{\partial \mu_0}{\partial y} \hat{u}' \right) &+ \frac{2}{3} \frac{\partial^2 \mu_0}{\partial x \partial y} \hat{u}' \\
\Leftrightarrow \frac{\partial}{\partial x} \left(\frac{1}{3} \mu_0 \frac{\partial \hat{u}'}{\partial y} \right) + \frac{2}{3} \frac{\partial \mu_0}{\partial x} \frac{\partial \hat{u}'}{\partial y} - \frac{\partial}{\partial x} \left(\frac{2}{3} \frac{\partial \mu_0}{\partial y} \hat{u}' \right) &+ \frac{2}{3} \frac{\partial^2 \mu_0}{\partial x \partial y} \hat{u}'.
\end{aligned}$$

Substituting this result into our previous equation, we now have

$$\begin{aligned}
\frac{\partial}{\partial x} \left(\left(\rho_0 v_0 + \frac{2}{3} \frac{\partial \mu_0}{\partial y} \right) \hat{u}' + \rho_0 u_0 \hat{v}' + \left(u_0 v_0 \frac{\partial \rho}{\partial \phi} - \frac{\partial \mu}{\partial \phi} \frac{\partial u_0}{\partial y} \right) \hat{\phi}' \right) &= \frac{\partial}{\partial x} \left(\frac{1}{3} \mu_0 \frac{\partial \hat{u}'}{\partial y} \right) + \frac{2}{3} \frac{\partial^2 \mu_0}{\partial x \partial y} \hat{u}' \\
&+ \left(-\frac{\partial}{\partial y} (2\rho_0 v_0) - \mu_0 \beta^2 \right) \hat{v}' + \left(-\rho_0 v_0 \beta - \frac{2}{3} \frac{\partial \mu_0}{\partial y} \beta \right) \hat{w}' \\
&+ \left[\frac{\partial}{\partial y} \left(-v_0^2 \frac{\partial \rho}{\partial \phi} - \frac{\partial P}{\partial \phi} \right) + \frac{\partial}{\partial y} \left(\frac{\partial \mu}{\partial \phi} \left(\frac{4}{3} \frac{\partial v_0}{\partial y} - \frac{2}{3} \frac{\partial u_0}{\partial x} \right) \right) \right] \hat{\phi}' \\
&+ \frac{2}{3} \frac{\partial \mu_0}{\partial x} \frac{\partial \hat{u}'}{\partial y} + \left(-2\rho_0 v_0 + \frac{4}{3} \frac{\partial \mu_0}{\partial y} \right) \frac{\partial \hat{v}'}{\partial y} + \frac{1}{3} \beta \mu_0 \frac{\partial \hat{w}'}{\partial y} \\
&+ \left[\left(-v_0^2 \frac{\partial \rho}{\partial \phi} - \frac{\partial P}{\partial \phi} \right) \frac{\partial \hat{\phi}'}{\partial y} + \frac{\partial \mu}{\partial \phi} \left(\frac{4}{3} \frac{\partial v_0}{\partial y} - \frac{2}{3} \frac{\partial u_0}{\partial x} \right) \right] \frac{\partial \hat{\phi}'}{\partial y} + \frac{4}{3} \mu_0 \frac{\partial^2 \hat{v}'}{\partial y^2}. \tag{B.24}
\end{aligned}$$

Moving onto the spanwise momentum equation, Equation B.19, multiplied by the factor ι , we have

$$\begin{aligned}
\frac{\partial}{\partial x} (\rho_0 u_0 \hat{w}') &= -\frac{\partial}{\partial y} (\rho_0 v_0) \hat{w}' - \rho_0 v_0 \frac{\partial \hat{w}'}{\partial y} + \beta \frac{\partial P}{\partial \phi} \hat{\phi}' - \beta \frac{\partial \mu_0}{\partial x} \hat{u}' - \mu_0 \beta \frac{\partial \hat{u}'}{\partial x} + \frac{\partial \mu_0}{\partial y} \frac{\partial \hat{w}'}{\partial y} + \mu_0 \frac{\partial^2 \hat{w}'}{\partial y^2} \\
&- \mu_0 \beta \frac{\partial \hat{v}'}{\partial y} - \frac{\partial}{\partial y} (\mu_0 \beta) \hat{v}' - \frac{4}{3} \mu_0 \beta^2 \hat{w}' + \frac{2}{3} \mu_0 \beta \frac{\partial \hat{u}'}{\partial x} + \frac{2}{3} \mu_0 \beta \frac{\partial \hat{v}'}{\partial y} + \beta \frac{\partial \mu}{\partial \phi} \hat{\phi}' \left(\frac{2}{3} \frac{\partial u_0}{\partial x} + \frac{2}{3} \frac{\partial v_0}{\partial y} \right) \\
\frac{\partial}{\partial x} (\rho_0 u_0 \hat{w}') &= -\beta \frac{\partial \mu_0}{\partial x} \hat{u}' - \beta \frac{\partial \mu_0}{\partial y} \hat{v}' - \frac{1}{3} \mu_0 \beta \frac{\partial \hat{u}'}{\partial x} - \frac{1}{3} \mu_0 \beta \frac{\partial \hat{v}'}{\partial y} - \frac{1}{3} \mu_0 \beta^2 \hat{w}' \\
&+ \left(-\frac{\partial}{\partial y} (\rho_0 v_0) - \mu_0 \beta^2 \right) \hat{w}' + \left(-\rho_0 v_0 + \frac{\partial \mu_0}{\partial y} \right) \frac{\partial \hat{w}'}{\partial y} + \left(\beta \frac{\partial P}{\partial \phi} + \frac{2}{3} \beta \frac{\partial \mu}{\partial \phi} \left(\frac{\partial u_0}{\partial x} + \frac{\partial v_0}{\partial y} \right) \right) \hat{\phi}' + \mu_0 \frac{\partial^2 \hat{w}'}{\partial y^2}.
\end{aligned}$$

To further modify this equation, we must first take Equation B.15, multiply it by $-\frac{1}{3}\mu_s\beta$, and rearrange it to obtain

$$\begin{aligned}
-\frac{\mu_0 \beta}{3} \frac{\partial \hat{u}'}{\partial x} - \frac{\mu_0 \beta}{3} \frac{\partial \hat{v}'}{\partial y} - \frac{1}{3} \mu_0 \beta^2 \hat{w}' &= \frac{\partial}{\partial x} \left(\frac{\mu_0 \beta}{3 \rho_0} u_0 \frac{\partial \rho}{\partial \phi} \hat{\phi}' \right) + \frac{\mu_0 \beta}{3 \rho_0} \frac{\partial \rho_0}{\partial x} \hat{u}' + \frac{\mu_0 \beta}{3 \rho_0} \frac{\partial \rho_0}{\partial y} \hat{v}' \\
&+ \left(-u_0 \frac{\partial \rho}{\partial \phi} \frac{\partial}{\partial x} \left(\frac{\mu_0 \beta}{3 \rho_0} \right) + \frac{\mu_0 \beta}{3 \rho_0} \frac{\partial}{\partial y} \left(v_0 \frac{\partial \rho}{\partial \phi} \right) \right) \hat{\phi}' + \frac{\mu_0 \beta v_0}{3 \rho_0} v_0 \frac{\partial \rho}{\partial \phi} \frac{\partial \hat{\phi}'}{\partial y},
\end{aligned}$$

using

$$\frac{\mu_0 \beta}{3 \rho_0} \frac{\partial}{\partial x} \left(u_0 \frac{\partial \rho}{\partial \phi} \hat{\phi}' \right) = \frac{\partial}{\partial x} \left(\frac{\mu_0 \beta}{3 \rho_0} u_0 \frac{\partial \rho}{\partial \phi} \hat{\phi}' \right) - u_0 \frac{\partial \rho}{\partial \phi} \frac{\partial}{\partial x} \left(\frac{\mu_0 \beta}{3 \rho_0} \right) \hat{\phi}'.$$

Substituting this modified conservation of mass in the current form of the spanwise momentum equation, we have

$$\begin{aligned}
& \frac{\partial}{\partial x} \left(\rho_0 u_0 \hat{w}' - \frac{\mu_0 \beta u_0}{3 \rho_0} \frac{\partial \rho}{\partial \phi} \hat{\phi}' \right) = \left(\frac{\mu_0 \beta}{3 \rho_0} \frac{\partial \rho_0}{\partial x} - \beta \frac{\partial \mu_0}{\partial x} \right) \hat{u}' \\
& + \left(\frac{\mu_0 \beta}{3 \rho_0} \frac{\partial \rho_0}{\partial y} - \beta \frac{\partial \mu_0}{\partial y} \right) \hat{v}' + \left(-\frac{\partial}{\partial y} (\rho_0 v_0) - \mu_0 \beta^2 \right) \hat{w}' \\
& + \left(-\frac{u_0 \beta}{3} \frac{\partial \rho}{\partial \phi} \frac{\partial}{\partial x} \left(\frac{\mu_0}{\rho_0} \right) + \frac{\mu_0 \beta}{3 \rho_0} \frac{\partial}{\partial y} \left(v_0 \frac{\partial \rho}{\partial \phi} \right) + \beta \frac{\partial P}{\partial \phi} + \frac{2}{3} \beta \frac{\partial \mu}{\partial \phi} \left(\frac{\partial u_0}{\partial x} + \frac{\partial v_0}{\partial y} \right) \right) \hat{\phi}' \\
& + \left(-\rho_0 v_0 + \frac{\partial \mu_0}{\partial y} \right) \frac{\partial \hat{w}'}{\partial y} + \frac{\mu_0 \beta v_0}{3 \rho_0} v_0 \frac{\partial \rho}{\partial \phi} \frac{\partial \hat{\phi}'}{\partial y} + \mu_0 \frac{\partial^2 \hat{w}'}{\partial y^2}. \tag{B.25}
\end{aligned}$$

The enthalpy disturbance equation, Equation B.20, becomes

$$\begin{aligned}
& \frac{\partial}{\partial x} \left(\sum_s u_0 h_{s,0} \hat{\rho}'_s + \sum_s \rho_{s,0} h_{s,0} \hat{u}' + u_0 \sum_s \rho_{s,0} \frac{\partial h_s}{\partial \phi} \hat{\phi}' \right) = -\frac{\partial}{\partial y} \left(\sum_s u_0 h_{s,0} \right) \hat{\rho}'_s \\
& - \frac{\partial}{\partial y} \left(\sum_s \rho_{s,0} h_{s,0} \right) \hat{v}' - \beta \sum_s \rho_{s,0} h_{s,0} \hat{w}' - \beta^2 \kappa_0 \hat{T}' - \beta^2 \kappa_{v,0} \hat{T}'_v \\
& + \left[-\frac{\partial}{\partial y} \left(v_0 \sum_s \rho_{s,0} \frac{\partial h_s}{\partial \phi} \right) + \frac{\partial \mu}{\partial \phi} (\gamma_\infty - 1) Ma_\infty^2 \left(\frac{\partial u_0}{\partial y} \right)^2 - \beta^2 \frac{1}{Sc} \mu_0 \sum_s h_{s,0} \frac{\partial c_s}{\partial \phi} \right] \hat{\phi}' \\
& + \left[\frac{\partial}{\partial y} \left(\frac{\partial \kappa}{\partial \phi} \frac{\partial T_0}{\partial y} \right) + \frac{\partial}{\partial y} \left(\frac{\partial \kappa_v}{\partial \phi} \frac{\partial T_{v,0}}{\partial y} \right) \right. \\
& \left. + \frac{1}{Sc} \sum_s \frac{\partial}{\partial y} \left(\mu_0 \frac{\partial}{\partial y} \left(\frac{\partial c_s}{\partial \phi} \right) h_{s,0} + \frac{\partial \mu}{\partial \phi} \frac{\partial c_{s,0}}{\partial y} h_{s,0} + \mu_0 \frac{\partial c_{s,0}}{\partial y} \frac{\partial h_s}{\partial \phi} \right) \right] \hat{\phi}' \\
& - \sum_s u_0 h_{s,0} \frac{\partial \hat{\rho}'_s}{\partial y} + 2 \mu_0 (\gamma_\infty - 1) Ma_\infty^2 \frac{\partial u_0}{\partial y} \frac{\partial \hat{u}'}{\partial y} - \sum_s \rho_{s,0} h_{s,0} \frac{\partial \hat{v}'}{\partial y} + \frac{\partial \kappa_0}{\partial y} \frac{\partial \hat{T}'}{\partial y} + \frac{\partial \kappa_{v,0}}{\partial y} \frac{\partial \hat{T}'_v}{\partial y} \\
& + \left[\frac{\partial \kappa}{\partial \phi} \frac{\partial T_0}{\partial y} + \frac{\partial \kappa_v}{\partial \phi} \frac{\partial T_{v,0}}{\partial y} - v_0 \sum_s \rho_{s,0} \frac{\partial h_s}{\partial \phi} \right] \frac{\partial \hat{\phi}'}{\partial y} \\
& + \frac{1}{Sc} \sum_s \left(2 \mu_0 h_{s,0} \frac{\partial}{\partial y} \left(\frac{\partial c_s}{\partial \phi} \right) + \frac{\partial}{\partial y} (\mu_0 h_{s,0}) \frac{\partial c_s}{\partial \phi} + \frac{\partial \mu}{\partial \phi} \frac{\partial c_{s,0}}{\partial y} h_{s,0} + \mu_0 \frac{\partial c_{s,0}}{\partial y} \frac{\partial h_s}{\partial \phi} \right) \frac{\partial \hat{\phi}'}{\partial y} \\
& + \kappa_0 \frac{\partial^2 \hat{T}'}{\partial y^2} + \kappa_{v,0} \frac{\partial^2 \hat{T}'_v}{\partial y^2} + \left(\frac{1}{Sc} \sum_s \mu_0 \frac{\partial c_s}{\partial \phi} h_{s,0} \right) \frac{\partial^2 \hat{\phi}'}{\partial y^2}. \tag{B.26}
\end{aligned}$$

Lastly, we have the vibrational energy disturbance equation, Equation B.21,

$$\begin{aligned}
& \frac{\partial}{\partial x} \left(\sum_s u_0 e_{vs,0} \hat{\rho}_s' + \sum_s \rho_{s,0} e_{vs,0} \hat{u}' + u_0 \sum_s \rho_{s,0} c_{vvs} \hat{T}_v' \right) = - \frac{\partial}{\partial y} \left(\sum_s v_0 e_{vs,0} \right) \hat{\rho}_s' \\
& \quad - \frac{\partial}{\partial y} \left(\sum_s \rho_{s,0} e_{vs,0} \right) \hat{v}' - \beta \sum_s \rho_{s,0} e_{vs,0} \hat{w}' \\
& \quad + \left[-\beta^2 \kappa_{v,0} - \frac{\partial}{\partial y} \left(v_0 \sum_s \rho_{s,0} c_{vvs} \right) + \frac{1}{Sc} \sum_s \frac{\partial}{\partial y} \left(\mu_0 \frac{\partial c_{s,0}}{\partial y} c_{vvs} \right) \right] \hat{T}_v' \\
& \quad + \sum_s c_{vvs} M_s \left(\sum_{r,diss} v_{sr} \left(R_{fr} \frac{\rho_\infty L}{u_\infty} - R_{br} \frac{\rho_\infty^2 L}{u_\infty} \right) + \sum_{r,exch} v_{sr} R_r \frac{\rho_\infty L}{u_\infty} \right) \hat{T}_v' \\
& \quad + \left[\frac{\partial}{\partial y} \left(\frac{\partial \kappa_v}{\partial \phi} \frac{\partial T_{v,0}}{\partial y} \right) + \frac{\partial Q_{t-v}}{\partial \phi} \frac{L}{u_\infty} - \beta^2 \frac{1}{Sc} \mu_0 \sum_s e_{vs,0} \frac{\partial c_s}{\partial \phi} \right. \\
& \quad \left. + \frac{1}{Sc} \sum_s \frac{\partial}{\partial y} \left(\mu_0 \frac{\partial}{\partial y} \left(\frac{\partial c_s}{\partial \phi} \right) e_{vs,0} + \frac{\partial \mu}{\partial \phi} \frac{\partial c_{s,0}}{\partial y} e_{vs,0} \right) \right] \hat{\phi}' \\
& \quad + \sum_s e_{vs,0} M_s \left(\sum_{r,diss} v_{sr} \left(\frac{\partial R_{fr}}{\partial \phi} \frac{\rho_\infty L}{u_\infty} - \frac{\partial R_{br}}{\partial \phi} \frac{\rho_\infty^2 L}{u_\infty} \right) + \sum_{r,exch} v_{sr} \frac{\partial R_r}{\partial \phi} \frac{\rho_\infty L}{u_\infty} \right) \hat{\phi}' \\
& - \sum_s v_0 e_{vs,0} \frac{\partial \hat{\rho}_s'}{\partial y} - \sum_s \rho_{s,0} e_{vs,0} \frac{\partial \hat{v}'}{\partial y} + \left[-v_0 \sum_s \rho_{s,0} c_{vvs} + \frac{\partial \kappa_{v,0}}{\partial y} + \sum_s \frac{1}{Sc} \mu_0 \frac{\partial c_{s,0}}{\partial y} c_{vvs} \right] \frac{\partial \hat{T}_v'}{\partial y} \\
& \quad + \left[\frac{\partial \kappa_v}{\partial \phi} \frac{\partial T_{v,0}}{\partial y} + \frac{1}{Sc} \sum_s \left(2\mu_0 e_{vs,0} \frac{\partial}{\partial y} \left(\frac{\partial c_s}{\partial \phi} \right) + \frac{\partial}{\partial y} (\mu_0 e_{vs,0}) \frac{\partial c_s}{\partial \phi} + \frac{\partial \mu}{\partial \phi} \frac{\partial c_{s,0}}{\partial y} e_{vs,0} \right) \right] \frac{\partial \hat{\phi}'}{\partial y} \\
& \quad + \kappa_{v,0} \frac{\partial^2 \hat{T}_v'}{\partial y^2} + \sum_s \frac{1}{Sc} \mu_0 \frac{\partial c_s}{\partial \phi} e_{vs,0} \frac{\partial^2 \hat{\phi}'}{\partial y^2}. \tag{B.27}
\end{aligned}$$

Appendix C

Chemistry Models and Test Cases

C.1 Chemistry Sets

C.1.1 Five Species Air Model

Species-specific properties : N2,O2,NO,N,O

molwt, hform, cvs, Zc, rm1, rm2

28.01600, 0.0d0, 2.5, 0, 2, 0

32.00000, 0.0d0, 2.5, 0, 2, 0

30.00800, 2.996123d6, 2.5, 0, 2, 0

14.00800, 3.362161d7, 1.5, 0, 1, 0

16.00000, 1.542000d7, 1.5, 0, 1, 0

Vibrational Energy Characteristic Temperatures

3.395d+03, 1 ! N2

2.239d+03, 2 ! O2

2.817d+03, 3 ! NO

Blottner Coefficients for viscosity model

2.6814200d-02, 3.177838d-01,-1.13155513d+01 ! N2

4.4929000d-02,-0.826158d-01,-0.92019475d+01 ! O2

4.3637800d-02,-0.335511d-01,-0.95767430d+01 ! NO

1.1557200d-02, 6.031679d-01,-1.24327495d+01 ! N

2.0314400d-02, 4.294404d-01,-1.16031403d+01 ! O

Reactant/product species (not including generic collision partners)

1, 4, 4 #1 N2 + M <--> N + N + M

2, 5, 5 #2 O2 + M <--> O + O + M

3, 4, 5 #3 NO + M <--> N + O + M

1, 5, 3, 4 #4 N2 + O <--> NO + N

2, 4, 3, 5 #5 O2 + N <--> NO + O

Collision constants for each nrd reaction

7.000d+18, 7.000d+18, 7.000d+18, 3.000d+19, 3.000d+19

2.000d+18, 2.000d+18, 2.000d+18, 1.000d+19, 1.000d+19

5.000d+12, 5.000d+12, 1.100d+14, 1.100d+14, 1.100d+14

Arrhenius parameters for each reaction (Cfm,eta,Ea) (Park ?)

-1.60d+00, 1.1320d+05 #1

-1.50d+00, 5.9500d+04 #2

0.00d+00, 7.5500d+04 #3

5.690d+09, 0.42d+00, 4.2938d+04 #5 ! D.Bose

2.490d+06, 1.18d+00, 4.0055d+03 #4 ! D.Bose

Equilibrium constant curve-fit coefficients (Park 90, n=10^16)

1.60600d+00, 1.57320d+00, 1.39230d+00,-1.15530d+01,-4.54300d-03

6.41830d-01, 2.42530d+00, 1.90260d+00,-6.62770d+00, 3.51510d-02

6.38170d-01, 6.81890d-01, 6.63360d-01,-7.57730d+00,-1.10250d-02

9.67940d-01, 8.91310d-01, 7.29100d-01,-3.95550d+00, 6.48800d-03

3.73200d-03, 1.74340d+00, 1.23940d+00, 9.49520d-01, 4.61820d-02

C.1.2 Six Species Air Model

Species-specific properties : N2,O2,NO,N,O,Ar

molwt, hform, cvs, Zc, rm1, rm2

28.01600, 0.0d0, 2.5, 0, 2, 0
 32.00000, 0.0d0, 2.5, 0, 2, 0
 30.00800, 2.996123d6, 2.5, 0, 2, 0
 14.00800, 3.362161d7, 1.5, 0, 1, 0
 16.00000, 1.542000d7, 1.5, 0, 1, 0
 39.94800, 0.000000d0, 1.5, 0, 1, 0

Vibrational Energy Characteristic Temperatures

3.395d+03, 1 ! N2
 2.239d+03, 2 ! O2
 2.817d+03, 3 ! NO

Blottner Coefficients for viscosity model

2.6814200d-02, 3.177838d-01,-1.13155513d+01 ! N2
 4.4929000d-02,-0.826158d-01,-0.92019475d+01 ! O2
 4.3637800d-02,-0.335511d-01,-0.95767430d+01 ! NO
 1.1557200d-02, 6.031679d-01,-1.24327495d+01 ! N
 2.0314400d-02, 4.294404d-01,-1.16031403d+01 ! O
 -0.22011067538d-01, 0.10103038293d+01, -0.13429828206d+02 ! Argon

Reactant/product species (not including generic collision partners)

1, 4, 4 #1 N2 + M \longleftrightarrow N + N + M
 2, 5, 5 #2 O2 + M \longleftrightarrow O + O + M
 3, 4, 5 #3 NO + M \longleftrightarrow N + O + M
 1, 5, 3, 4 #4 N2 + O \longleftrightarrow NO + N
 2, 4, 3, 5 #5 O2 + N \longleftrightarrow NO + O

Collision constants for each nrd reaction

7.000d+18, 7.000d+18, 7.000d+18, 3.000d+19, 3.000d+19, 3.000d+19
 2.000d+18, 2.000d+18, 2.000d+18, 1.000d+19, 1.000d+19, 1.000d+19
 5.000d+12, 5.000d+12, 1.100d+14, 1.100d+14, 1.100d+14, 1.100d+14

Arrhenius parameters for each reaction (Cfm,eta,Ea) (Park ?)

-1.60d+00, 1.1320d+05 #1

-1.50d+00, 5.9500d+04 #2

0.00d+00, 7.5500d+04 #3

5.690d+09, 0.42d+00, 4.2938d+04 #5 ! D.Bose

2.490d+06, 1.18d+00, 4.0055d+03 #4 ! D.Bose

Equilibrium constant curve-fit coefficients (Park 90, n=10¹⁶)

1.60600d+00, 1.57320d+00, 1.39230d+00,-1.15530d+01,-4.54300d-03

6.41830d-01, 2.42530d+00, 1.90260d+00,-6.62770d+00, 3.51510d-02

6.38170d-01, 6.81890d-01, 6.63360d-01,-7.57730d+00,-1.10250d-02

9.67940d-01, 8.91310d-01, 7.29100d-01,-3.95550d+00, 6.48800d-03

3.73200d-03, 1.74340d+00, 1.23940d+00, 9.49520d-01, 4.61820d-02

C.1.3 Seven Species Air Model

Species-specific properties : CO₂,CO,N₂,O₂,NO,N,O

molwt, hform, cvs, Zc, rm1, rm2

44.01100, -8.932880d6, 2.5, 0, 2, 0 ! CO₂

28.01100,-4.0630824d6, 2.5, 0, 2, 0 ! CO

28.01600, 0.0d0, 2.5, 0, 2, 0 ! N₂

32.00000, 0.0d0, 2.5, 0, 2, 0 ! O₂

30.00800, 2.996123d6, 2.5, 0, 2, 0 ! NO

14.00800, 3.362161d7, 1.5, 0, 1, 0 ! N

16.00000, 1.542000d7, 1.5, 0, 1, 0 ! O

Vibrational Energy Characteristic Temperatures

1.91870d+03, 1 ! CO₂ 1st mode (1dg)

9.59660d+02, 1 ! CO₂ 2nd mode (2dg)

9.59660d+02, 1 ! CO₂ 2nd mode (2dg)

3.38210d+03, 1 ! CO₂ 3rd mode (1dg)

3.12200d+03, 2 ! CO

3.3950d+03, 3 ! N2

2.2390d+03, 4 ! O2

2.8170d+03, 5 ! NO

Blottner Coefficients for viscosity model

-0.04137200000d+00, 1.32930000000d+00, -1.50160000000d+01 ! CO2

0.01833000000d+00, 0.43609000000d+00, -1.16910000000d+01 ! CO

2.6814200d-02, 3.177838d-01,-1.13155513d+01 ! N2

4.4929000d-02,-0.826158d-01,-0.92019475d+01 ! O2

4.3637800d-02,-0.335511d-01,-0.95767430d+01 ! NO

1.1557200d-02, 6.031679d-01,-1.24327495d+01 ! N

2.0314400d-02, 4.294404d-01,-1.16031403d+01 ! O

Reactant/product species (not including generic collision partners)

1, 2, 7 #1 CO2 + M <—> CO + O + M

3, 6, 6 #2 N2 + M <—> N + N + M

4, 7, 7 #3 O2 + M <—> O + O + M

5, 6, 7 #4 NO + M <—> N + O + M

3, 7, 5, 6 #5 N2 + O <—> NO + N ! Zeldovich

4, 6, 5, 7 #6 O2 + N <—> NO + O ! Zeldovich rever.

1, 7, 4, 2 #7 CO2 + O <—> O2 + CO

Collision constants for each nrd reaction

6.9d18,6.9d18,6.9d18,6.9d18,6.9d18,1.4d19,1.4d19

7.0d18,7.0d18,7.0d18,7.0d18,7.0d18,3.0d19,3.0d19

2.0d18,2.0d18,2.0d18,2.0d18,2.0d18,1.0d19,1.0d19

1.1d14,5.0d12,5.0d12,5.0d12,1.1d14,1.1d14,1.1d14

Arrhenius parameters for each reaction (Cfm,eta,Ea) (Park 90,unless otherwise)

-1.50d+00, 6.3275d+04 #1

-1.60d+00, 1.1320d+05 #2

-1.50d+00, 5.9750d+04 #3
 0.00d+00, 7.5500d+04 #4
 5.690d+09, 0.42d+00, 4.2938d+04 #5 ! D.Bose
 2.490d+06, 1.18d+00, 4.0055d+03 #6 ! D.Bose
 2.100d+10, 0.00d+00, 2.7800d+04 #7

Equilibrium constant curve-fit coefficients (Park 90, $n=10^{16} \rightarrow 0$, Mitcheltree 94 $\rightarrow 1$)

-6.611895e-01, 4.747853e+00, 1.090510e+00,-6.471533e+00, 9.784774e-04 #1
 1.60600d+00, 1.57320d+00, 1.39230d+00,-1.15330d+01,-4.54300d-03 #2
 6.41830d-01, 2.42530d+00, 1.90260d+00,-6.62770d+00, 3.51510d-02 #3
 6.38170d-01, 6.81890d-01, 6.63360d-01,-7.57730d+00,-1.10250d-02 #4
 9.67940d-01, 8.91310d-01, 7.29100d-01,-3.95550d+00, 6.48800d-03 #5
 3.73200d-03, 1.74340d+00, 1.23940d+00, 9.49520d-01, 4.61820d-02 #6
 3.212446e-01, 1.310986e+00, 1.011075e+00, -4.665631e-01, 4.389974e-04 #7

C.1.4 Five Species CO_2 Model

Species Properties : CO₂,CO,O₂,C,O

molwt hform cvs zch
 44.01100d0 -8.9328800d6 2.500000 0 ! CO₂
 28.01100d0 -4.0630824d6 2.500000 0 ! CO
 32.00000d0 0.0000000d0 2.500000 0 ! O₂
 12.01100d0 5.9211889d7 1.500000 0 ! C
 16.00000d0 1.5420000d7 1.500000 0 ! O

Vibrational Energy Characteristic Temperatures

1.9187d3 1 ! CO₂
 9.5966d2 1 ! CO₂
 9.5966d2 1 ! CO₂
 3.3821d3 1 ! CO₂
 3.1220d3 2 ! CO
 2.2390d3 3 ! O₂

Blottner Coefficients for viscosity model

-4.1372000d-02 1.329300d-00 -1.50160000d+01
 0.0183300d+00 0.436090d+00 -1.16910000d+01
 4.4929000d-02 -8.261580d-02 -9.20194750d+00
 0.0161900d+00 0.500740d+00 -1.23110000d+01
 2.0314400d-02 4.294404d-01 -1.16031403d+01

Reactant/product species (not including generic collision partners)

1 2 5
 2 4 5
 3 5 5
 1 5 3 2
 2 5 3 4
 2 2 1 4

Collision constants for each nrd reaction

6.90d18, 6.90d18, 6.90d18, 1.40d19, 1.40d19 #1
 2.30d17, 2.30d17, 2.30d17, 3.40d17, 3.40d17 #2
 2.00d18, 2.00d18, 2.00d18, 1.00d19, 1.00d19 #3

Arrhenius parameters for each reaction (Cfm,eta,Ea) (Park ?)

-1.50d+00, 6.3275d+04 #1 CO₂ + M <—> CO + O + M
 -1.00d+00, 1.2900d+05 #2 CO + M <—> C + O + M
 -1.50d+00, 5.9750d+04 #3 O₂ + M <—> O + O + M
 2.100d+10, 0.00d+00, 2.7800d+04 #4 CO₂ + O <—> O₂ + CO
 3.900d+10, -0.18d+00, 6.9200d+04 #5 CO + O <—> O₂ + C
 2.330d+06, 5.00d-01, 6.5710d+04 #6 CO + CO <—> CO₂ + C

Equilibrium constant curve-fit coefficients (Park 90 type)

-6.611895d-01, 4.747853d+00, 1.090510d+00,-6.471533d+00, 9.784774d-04
 -4.505134e-01, 4.084767e+00, -2.314232e-03, -1.295035e+01, 4.819804e-04

6.41830d-01, 2.42530d+00, 1.90260d+00,-6.62770d+00, 3.51510d-02
 3.212446d-01, 1.310986d+00, 1.011075d+00, -4.665631d-01, 4.389974d-04
 -1.334134d+00, 9.461910d-01,-3.531516d+00,-5.130943d+00,-1.46341d-01
 2.1067608d-01, -6.6308660d-01, -1.0928244d+00, -6.4788131d+00, -4.9649706d-04

C.2 Modified Vibrational Relaxation Parameters

Table C.1: Modified Millikan and White relaxation times

Vibrating Species	Collision Partner	a	b
<i>CO</i>	<i>N</i>	47.7	0.0500
<i>CO</i>	<i>O</i>	47.7	0.0500
<i>CO</i>	<i>C</i>	47.7	0.0500
<i>CO₂</i>	<i>CO₂</i>	36.5	-0.0193
<i>CO₂</i>	<i>CO</i>	45.4	0.0305
<i>CO₂</i>	<i>NO</i>	46.4	0.0308
<i>CO₂</i>	<i>N₂</i>	45.4	0.0305
<i>CO₂</i>	<i>O₂</i>	47.3	0.0311
<i>CO₂</i>	<i>C</i>	33.7	0.0263
<i>CO₂</i>	<i>N</i>	35.8	0.0271
<i>CO₂</i>	<i>O</i>	37.6	0.0278
<i>CO₂</i>	<i>Ar</i>	50.3	0.0321
<i>N₂</i>	<i>O</i>	72.4	0.0150
<i>N₂</i>	<i>C</i>	72.4	0.0150
<i>NO</i>	<i>N₂</i>	49.5	0.0420
<i>NO</i>	<i>O₂</i>	49.5	0.0420
<i>NO</i>	<i>NO</i>	49.5	0.0420
<i>NO</i>	<i>N</i>	49.5	0.0420
<i>NO</i>	<i>O</i>	49.5	0.0420
<i>O₂</i>	<i>Ar</i>	164.3	0.0307
<i>O₂</i>	<i>N</i>	72.4	0.0150
<i>O₂</i>	<i>O</i>	47.7	0.0590

C.3 T5 Shots Simulated

The data for the *CO₂* shots are from Adam[12] and the data from the Air shot are from Jewell (personal communication Joe Jewell). The table consists of the shot number, the freestream gas in the shocktube, the transition location along the cone surface, the reservoir enthalpy, and the reservoir pressure.

Table C.2: List of T5 Tunnel shots simulated in Chapter 6.1.

Shot	Freestream Gas	Trans. Loc. (cm)	Res. Enthalpy (MJ/kg)	Res. Pressure (MPa)
1116	CO_2	37.46	7.96	86.2
1118	CO_2	32.5	5.31	85.8
1119	CO_2	45.72	9.33	71.6
1120	CO_2	10.2	3.91	72.0
1121	CO_2	62.87	9.91	40.8
1123	CO_2	45.509	6.48	55.2
1125	CO_2	35.74	4.64	61.2
1126	CO_2	36.73	4.55	62.2
1131	CO_2	42.8	6.34	79.9
1132	CO_2	41.6	7.74	52.3
1133	CO_2	36.73	5.24	48.2
1148	CO_2	44.79	5.87	44.2
1149	CO_2	46.67	5.06	44.5
2580	Air	22	5.26	50.3
2581	Air	46	6.40	29.9
2582	Air	42	5.69	29.6
2537	Air	37.27	6.84	44.7
2579	Air	35.37	7.13	47.4
2614	Air	69.53	9.46	53.73
2615	Air	58.145	8.85	53.20
2616	Air	48.65	8.29	53.80
2617	Air	52.45	8.51	52.3
2620	Air	60.04	8.65	51.7
2656	Air	39.165	7.59	78.4
2540	Air	60.04	9.47	51.6
2601	Air	58.145	10.45	74.7

C.4 Injection Conditions

C.4.1 Theoretical Injection Conditions

C.4.1.1 Nitrogen Freestream

Table C.3: Injection conditions for the theoretical injection cases with a freestream of N_2

Case	Injection Gas	Temperature (K)	f_w	Mass Flux(g/s)
1	CO_2	293	0.05	1.24
2	CO_2	293	0.1	2.47
3	CO_2	293	0.2	4.96
4	CO_2	293	0.3	7.43
5	CO_2	293	0.4	9.92
6	CO_2	293	0.6	14.88
7	Air	293	0.1	2.47
8	N_2	293	0.05	1.24
9	N_2	293	0.1	2.47
10	N_2	293	0.2	4.96
11	Ar	293	0.05	1.24
12	Ar	293	0.1	2.47
13	Ar	293	0.2	4.96
14	Ar	293	0.3	7.43
15	Ar	293	0.4	9.92
16	CO_2	1000	0.0	0.0
17	CO_2	1000	0.05	1.24
18	CO_2	1000	0.1	2.47
19	CO_2	1000	0.2	4.96
20	CO_2	1000	0.3	7.43
21	CO_2	1000	0.4	9.92
22	CO_2 -No Vib	293	0.1	2.47
23	Air-No Vib	293	0.1	2.47
24	N_2 -No Vib	293	0.1	2.47
25	Ar-No Vib	293	0.1	2.47

C.4.1.2 Air Freestream

Table C.4: Injection conditions for the theoretical injection cases with a freestream of Air

Case	Injection Gas	Temperature (K)	f_w	Mass Flux(g/s)
1	CO_2	293	0.05	1.30
2	CO_2	293	0.1	2.61
3	CO_2	293	0.2	5.22
4	CO_2	293	0.3	7.83
5	CO_2	293	0.6	15.65
6	Air	293	0.1	2.61
7	N_2	293	0.1	2.61
8	Ar	293	0.1	2.61
9	CO_2	1000	0.0	0.0
10	CO_2	1000	0.1	2.61

C.4.2 Porous Injection Conditions

Table C.5: Injection conditions for the porous injection cases with a freestream of Air

Case	Injection Gas	Temperature (K)	Mass Flux (g/s)
1	CO_2	293	0.5
2	CO_2	293	1.0
3	CO_2	293	2.0
4	CO_2	293	3.0
5	CO_2	293	5.0
6	CO_2	293	6.0
7	CO_2	293	7.5
8	CO_2	293	10.0
9	CO_2	293	11.0
10	CO_2	293	12.0
11	CO_2	293	12.5
12	CO_2	293	13.0
13	CO_2	293	13.5
14	CO_2	293	14.0
15	CO_2	293	14.5
16	CO_2	293	15.0
17	CO_2	293	17.0
18	CO_2	293	20.0
19	Air	293	10.93
20	N_2	293	10.77
21	CO_2	1000	9.43
22	CO_2	1500	7.7
23	CO_2	2000	6.9
24	CO_2	2500	6.3

Appendix D

Useful Second Mode Disturbance Trends

Due to its acoustic nature, a couple useful trends can be made regarding the behavior of second mode disturbances. These relationships follow from two general aspects of second mode disturbances. The first is the approximation for most amplified frequency which is

$$f \approx \frac{0.8U_e}{2\delta}.$$

This formula is based on the relationship between the boundary edge velocity and the disturbance phase speed at the location of second mode disturbance growth, which has a ratio of approximately 0.8. This formula also takes into account that the sonic line height is generally half of the boundary layer thickness, as seen in Fig. 7.12a. The second important relationship is that of the amplification rate of a disturbance frequency to the boundary layer thickness. As seen in Fig. D.1, the amplification rate for a particular frequency is approximately a concave-down parabola with respect to boundary layer thickness.

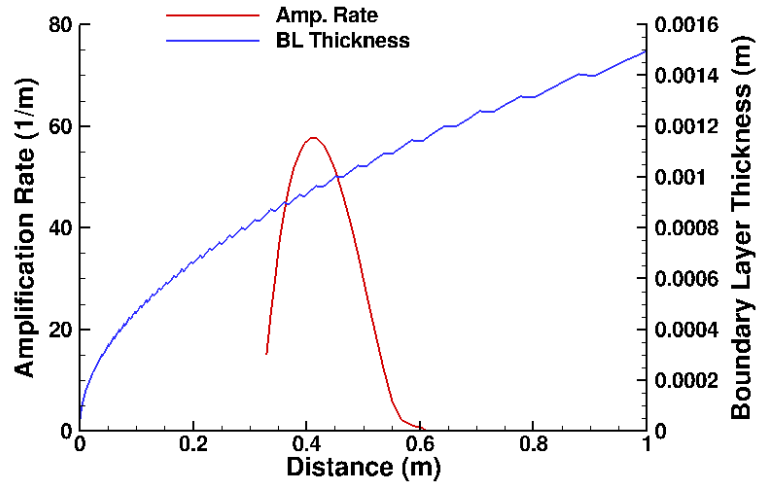


Figure D.1: Amplification rate and boundary layer thickness versus distance along a sharp cone surface. The amplification rate of a particular frequency is approximately a concave-down parabola with respect to boundary layer thickness.

D.1 Disturbance Bandwidth

The first trend that can be determined from these two properties is a relationship between the bandwidth of amplified frequencies and the curvature of the boundary layer. A flatter boundary layer results in a smaller bandwidth of previously amplified frequencies as opposed to a boundary layer with larger curvature. To demonstrate this, the N factors at various locations along a sharp cone boundary layer, as seen in Fig. D.2. The N factor essentially represents the disturbance frequencies that could potentially be present at a given location in a boundary layer. As seen in the plot, the overall disturbance bandwidth is reduced as the distance along the cone increases. This is due to a flattening of the boundary layer.

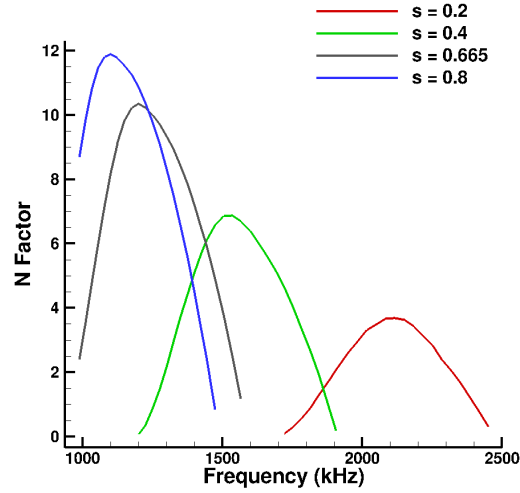


Figure D.2: N factor versus frequency for several locations along a sharp cone boundary layer.

D.2 Relative Amplification

A second trend with second mode disturbances can be determined for the amplification of disturbances between similar boundary layers. Based on the two properties of disturbance amplification discussed above, the overall amplification of a particular frequency also depends strongly on the curvature of the boundary layer thickness. A boundary layer that maintains a thickness near the optimal thickness for a particular frequency will result in a greater amplification of the particular frequency. This gives us the relationship of

$$\frac{\partial \delta}{\partial x} \propto \frac{1}{(-\alpha_i)},$$

where $(-\alpha_i)$, is the amplification rate of a boundary layer disturbance.

We can then determine the parameters that will result in a larger amplification based on the change in boundary layer thickness. Using the formula for boundary layer thickness for a Blasius boundary layer,

$$\delta \propto \frac{x}{\sqrt{\text{Re}_x}} = \sqrt{\frac{\mu}{\rho U x}},$$

where x is the streamwise distance, μ is the dynamic viscosity of the fluid, ρ is the fluid density, and U is the fluid velocity, we can take the find the slope of the boundary layer at a given location,

which is approximately

$$\frac{\partial \delta}{\partial x} \propto \sqrt{\frac{\mu}{\rho U x}} = \frac{1}{\sqrt{\text{Re}_x}} \propto \frac{1}{(-\alpha_i)}.$$

Therefore, given the same boundary layer thickness, thus same most amplified frequency, a boundary layer with a higher Reynolds number will result in larger amplification of the most amplified frequency. In other words, we can state the following about two similar boundary layers

$$(-\alpha_i)_1 > (-\alpha_i)_2 \Leftrightarrow \sqrt{\text{Re}_{x,1}} > \sqrt{\text{Re}_{x,2}}.$$

Evidence for this relationship is also seen in Fig. D.2, in that the disturbances near the end of the cone achieve a larger amount of amplification than those at the front of the cone.